THE FRACTURE TOUGHNESS OF SILICA FUME CONCRETE USING EXPERIMENTAL AND NUMERICAL TECHNIQUES

BY

MOSTAFA ASILI, B.Sc., M.Sc.

Thesis submitted to the CNAA, London, in candidature for the degree of Doctor of Philosophy, 1992.

Department of Civil Engineering and Building
The Polytechnic of Wales
Treforest
Mid. Glamorgan
U.K.

Collaborating Establishment:
Elkem Chemicals Ltd.
High Wycombe
U.K.

TO MY DEAR MOTHER
FOR ALL HER SACRIFICES

AND

TO MY DEAR FATHER
FOR HIS UNWAVERING SUPPORT
AND ENCOURAGEMENT

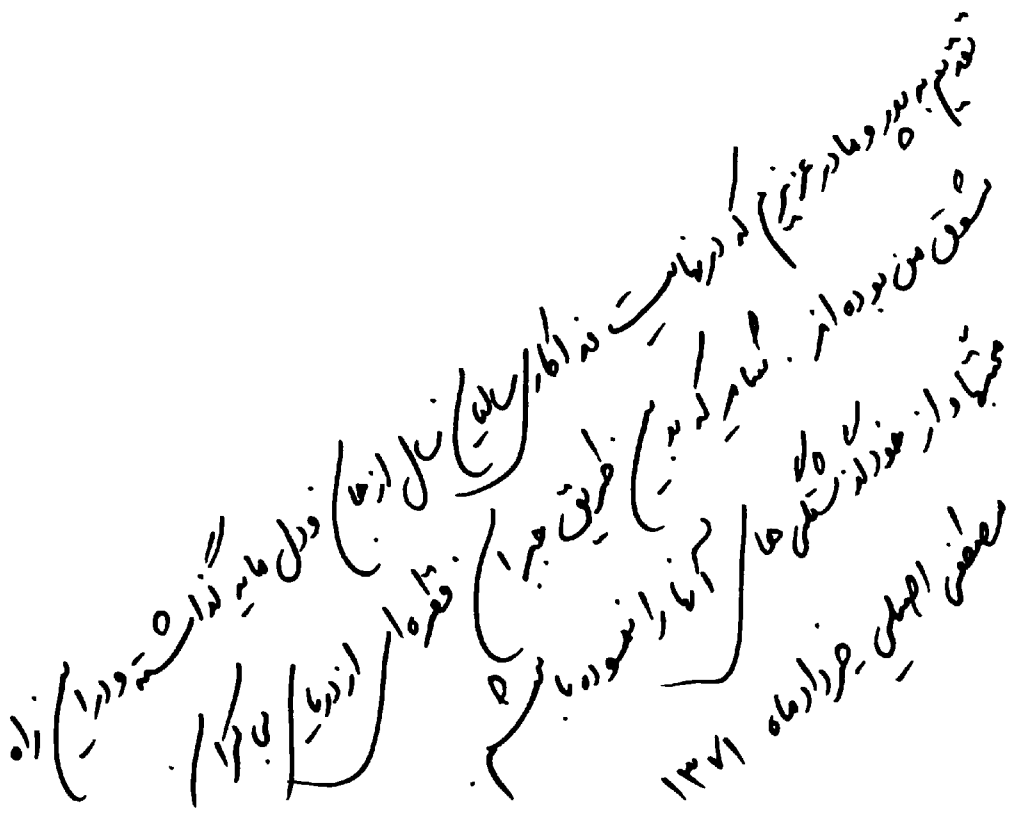

CERTIFICATE OF RESEARCH

This is to certify that, except where specific reference is made, the work described in this thesis is the result of the investigation of the candidate.

M. Asili
.....
M. Asili
(Candidate)

B B Sabir
.....
B.B. Sabir
(Director of Studies)

S. Wild
.....
S. Wild
(Supervisor)

S.D. Summerhayes.
.....
S.D. Summerhayes
(Supervisor)

DECLARATION

This is to certify that neither this thesis, nor any part of it, has been presented or is being concurrently submitted in candidature for any degree at any other academic establishment.

M. Asili

.....

M. Asili
(Candidate)

ACKNOWLEDGEMENTS

The author is indebted to his director of studies Dr. B.B. Sabir for the unceasing help, guidance and encouragement afforded to him during the course of this investigation.

The useful advice and suggestions of Dr. S. Wild and Mr. S.D. Summerhayes, project supervisors, as well as Mr. R. Lewis, Elkem Chemicals' technical advisor, is gratefully acknowledged.

The author also wishes to express his appreciation to the staff of the Department of Information Technology for their cooperation in the running of the programs. Particular thanks are due to Mr. T. Jones and Mr. A. Davies for helpful discussions.

The positive and understanding attitude of the technical staff of the Department of Civil Engineering and Building in design, manufacture and purchase of the testing equipment, as well as assistance in conducting the tests is appreciated.

ABSTRACT

The escalating manufacturing cost of ordinary Portland cement has led to the search for less energy intensive materials. One such material is condensed silica fume (CSF) which is an industrial by-product and until recently was discarded as waste. Research has shown that the addition of CSF to concrete can have the dual benefits of increased strength and improved durability.

In the present study experimental and numerical techniques were employed to investigate the mechanical and fracture characteristics of CSF concrete wet cured at 20° C and 50° C.

Whereas the high temperature curing resulted in increased compressive strength at early age, the specimens cured at 20° C exhibited higher strengths beyond 28 days. It was also found that increasing the CSF content did not significantly increase the tensile strength and, in fact, as with the compressive strength, a small decrease was obtained when the CSF content was increased from 16% to 20%. Furthermore, curing temperature did not appear to have a major influence on the tensile strength, nor did it affect the relationship between the static modulus of elasticity E and the compressive strength. However, a reduction in E was obtained for compressive strengths beyond 90 N/mm^2.

Several geometries, namely the Compact Compression Specimen (CCS) and the Singly and Doubly Notched Axial Splitting Specimens (SNASS and DNASS), were employed in the fracture studies. Detailed finite element analyses for these geometries were carried out using triangular and rectangular isoparametric elements. The results for the stress distributions demonstrated the existence of large tensile stresses at the root of the notch, thus confirming that failure is of the opening (mode 1) type.

In evaluating the fracture toughness, both the stress intensity factor and the energy approaches were used. As no allowance was made for the tortuosity of the fracture surface, the former approach was considered to be more reliable in the present work. This was subsequently used to assess the degree of brittleness of the concrete. It was found that beyond a compressive strength of about 90 N/mm^2, increased brittleness was obtained with increasing strength.

Some of the fracture tests were conducted on concrete reinforced with polypropylene fibres. The post cracking performance of such concrete was assessed using a toughness index evaluated from the area under the load-displacement relationships.

CONTENTS

CHAPTER FOUR

FINITE ELEMENT FORMULATION

CHAPTER FIVE

FINITE ELEMENT ANALYSIS OF THE COMPACT COMPRESSION SPECIMEN

CHAPTER SIX

FINITE ELEMENT ANALYSIS OF THE AXIAL SPLITTING SPECIMEN

CHAPTER SEVEN

FRACTURE TOUGHNESS OF CSF CONCRETE

CHAPTER EIGHT

HIGH STRENGTH CONCRETE

CHAPTER NINE

LIST OF FIGURES

LIST OF TABLES

LIST OF PLATES

NOTATIONS

A	Cross-sectional area, Area to δ
A_{lig}	Area of uncracked ligament
a	Pre-crack length, Semi-major axis of an ellipse
B	Specimen thickness, Additional area to 2δ
b	Semi-minor axis of an ellipse, Breadth of specimen
C	Compliance
C_1, C_2	Constants of integration
c	Notch length in the compression zone
d	Specimen width
ds	An element of arc along contour Γ
E	Modulus of elasticity
e	Eccentricity of force
EI	Flexural rigidity
E_m	Energy absorbed by testing machine in producing a deformation δ
E_s	Energy required to cause fracture of the specimen
F	Work performed by external forces on a body
f	Eccentricity of centre line along y-axis
f_1	Function of Poisson's ratio
$f(a)$	Second order polynomial function of 'a'
f_c	Compressive strength
f_t	Tensile strength
G	Energy release rate, Griffith fracture surface energy per unit area
G_1, G_2, G_3	Energy release rates associated with modes 1, 2 and 3
G_c	Critical strain energy release rate, fracture energy
g	Acceleration due to gravity
h	$\sqrt{(P/2EI)}$
I	Second moment of area
J	Line integral
J_{1c}	Critical value of J associated with mode 1
J_c	Critical value of J
k_1, k_2, k_3	Stress intensity factors in modes 1, 2 and 3
k	Stress intensity factor
k_c	Fracture toughness or the critical stress intensity factor
k_m	Stiffness of testing machine
L	Specimen or element length, Object size
l_{ch}	Characteristic length
M_x	Bending moment
m	Mass
m, n	Orthogonal curvilinear coordinates (local coordinates)
P	Single applied force, Load per unit thickness
P_i	External load acting on a body (i=1, 2, ...n)
Q_x	Shearing force
q	Correction factor
T	Traction vector
t	Thickness
U	Total energy stored in a cracked body
U_a	Change in elastic strain energy caused by introduction of a crack

U_b	Bending strain energy
U_o	Elasticity energy of a loaded uncracked plate
U_p	Potential energy (lost by axial force)
U_s	Shear strain energy
U_t	Total energy stored in a body
U_x	Change in elastic energy caused by the formation of the crack surface
u,v	Radial and tangential displacements
u_{ij}	Derivative of displacement in the i-direction with respect to j
u_x, u_y, w	Displacements in the x, y and z directions
W	Strain energy density
w	Loading platen width
w/c	Water/cementitious ratio
W_o	Energy corrected for nonlinearities
x,y,z	Rectangular coordinates
y	Transverse deflection
Y	Geometrical parameter

GREEK SYMBOLS

α, β	Independent constants of integration
σ_{ys}	Yield strength
$\sigma_x, \sigma_y, \sigma_z$	Normal components of stress parallel to x, y and z axes
r, Θ	Polar coordinates
$\sigma_{xy}, \sigma_{xz}, \sigma_{yz}$	Shearing strain components in rectangular coordinates
Ω	Rigidity modulus, Shear modulus
μ	Poisson's ratio
μ'	Function of Poisson's ratio
σ_o	Uniform tensile stress
$\varepsilon_x, \varepsilon_y, \varepsilon_{xy}$	In-plane strains in the rectangular coordinates
$\varepsilon_r, \varepsilon_\Theta, \varepsilon_{r\Theta}$	In-plane strains in the polar coordinates
$f(\Theta)$	Polynomial function of Θ
ϕ	Shape factor
δ	Deformation
$P(\delta)$	Load producing a deformation δ
	Total displacement
σ_f	Apparent fracture stress
Γ	Closed contour encircling a crack tip
ε	Strain
σ	Stress, Tensile strength
δ_o	Maximum beam deflection

MATRIX SYMBOLS

[Ke]	Element stiffness matrix
[B]	Strain-displacement matrix
[C]	Transformation matrix
[D]	Rigidity matrix
$[\ ]^T$	Transpose of a matrix
$[\ ]^{-1}$	Inverse of a matrix
$\{\delta_e\}$	Element nodal displacements vector
$\{\varepsilon_e\}$	Element nodal strains vector
$\{\sigma_e\}$	Element nodal stresses vector
$\{\alpha\}$	Shape function parameters vector
[K]	Structure stiffness matrix
[F]	Nodal forces vector

CHAPTER ONE

INTRODUCTION

Recent times have shown a rising demand for the production of Portland cement. The escalating manufacturing energy cost and environmental concerns have led to the search for less energy intensive materials for use as partial replacements for ordinary Portland cement (OPC). A notable activity has been in the use of pulverised fuel ash (PFA) where as high as 50% substitutions by mass of OPC have been used without detrimental effects on the resulting concrete.

Other pozzolanic materials which have also received attention include ground granulated blast furnace slag (GGBFS), rice husk ash (RHA) and condensed silica fume (CSF). These materials are largely industrial by-products which are otherwise discarded as waste and their utilisation, therefore, results in additional benefits in terms of environmental protection and preservation. Furthermore, with judicious use, these materials have the potential of extending the use of concrete as a structural material by meeting more stringent durability and strength requirements. The use of high strength concrete can result in lower construction costs due to significant reduction in the size of concrete members. This can be particularly advantageous for columns in meeting long span requirements and to reduce the quantities of reinforcing steel.

The production of high strength concrete employing finely divided mineral admixtures has in the main been achieved by the use of PFA and more recently CSF. The latter is a by-product of the smelting process used to produce silicon metal and ferro-silicon alloys. It has a high proportion of active silica (SiO_2) and extensive research has shown that its addition to the concrete mix can lead to marked improvement in strength. Due to its extremely small particle size, CSF acts as an effective filler and has been used not only for structural purposes but also for floor surfaces and repair materials in situations where high compressive strength and low permeability are advantageous.

It has for some time been appreciated that as the concrete strength increases its behaviour approaches that of a homogeneous material whose response is more linear elastic than that of normal concrete. The failure stress in high strength concrete has been shown to be accompanied by a comparatively low critical strain resulting in a brittle matrix. The increase in brittleness is evident by the steep gradients of both the ascending and descending parts of the stress-strain curves usually obtained for high strength concrete.

The degree of brittleness of a material may be assessed on the basis of mechanical and fracture properties through a non-dimensional parameter called the brittleness number. Using this approach it can be shown that the ductility of the material can be increased by increasing its fracture

energy. In the case of concrete materials this can be done by careful choice of the constituent materials. Another way is by reinforcing the matrix with fibres whose failure strain is greater than that of the concrete matrix, thus providing a crack arresting mechanism and enhancing the fracture toughness characteristics.

The fracture properties of cementitious materials have been studied by many researchers over a period of several decades. Various methods of testing and different specimen geometries have been proposed. The fracture toughness of concrete may be evaluated by one of two basic approaches. In the first, the critical strain energy release rate G_C is evaluated from the area under the load-displacement curve obtained from laboratory tests. In the second, the critical stress intensity factor k_C is obtained directly from a knowledge of the failure load, obtained from experiments, and the stress intensity factor for the geometry. For linear elastic fracture mechanics (LEFM), the two approaches are equivalent and there are simple relationships between k_C and G_C.

Classical solutions for the stress intensity factor exist for some basic geometries. For more practical test geometries, however, numerical techniques such as the finite element method (FEM) have to be employed.

In the present work, numerical and experimental techniques were employed to examine the mechanical and fracture

properties of CSF concrete with compressive strengths up to 120 N/mm^2. Several geometries were investigated to evaluate the fracture properties using both the G_c and k_c approaches. Detailed finite element analyses were carried out using triangular and quadrilateral isoparametric elements which contain the required singularity at the crack tip. Assuming LEFM to be applicable, the stress intensity factors were evaluated using both direct and energy methods. Amongst the energy methods, particular attention was paid to the strain energy release rate (SERR) and J-integral methods.

CHAPTER TWO

REVIEW OF PREVIOUS WORK

The utilisation of condensed silica fume (CSF) in concrete has made it possible to achieve strengths far in excess of those attainable previously using normal methods of production. Concretes with characteristic strengths of 90 N/mm^2 or more can be produced with ease by employing normal aggregates, superplasticizers and moderate levels of CSF [1]. CSF has also been successfully used in lightweight concrete where compressive strengths greater than 70 N/mm^2 have been achieved [2]. Concretes of very high strength have also been produced using high strength aggregates and special techniques. For example, Ohama et al [3] achieved strengths in excess of 250 N/mm^2 using calcined bauxite and CSF replacements up to 30%. Large scale production of such concretes is however difficult and expensive and in practice they are only used in specialised applications on a small scale.

The strength gain pattern of CSF concrete has been studied by several researchers [1, 4-6] who have mostly concentrated on curing at about 20° C. Ronne [7] studied the effect of curing conditions, with temperatures in the range 20°-70° C, on the long term compressive strength (up to two years) of concretes containing CSF and pulverised fuel ash (PFA). The author [7] concluded that good initial curing conditions in the first three days gave an improvement in compressive strength when compared to the samples dried immediately

after demoulding. Aitcin and Laplante [8] carried out long-term field studies on the compressive strength of CSF concrete. They reported that there was no tendency for strength loss for samples tested at up to 4 years.

Several investigators have studied the relationship between the tensile and compressive strengths under different curing regimes. For example, Loland and Hustad [9] reported results of cylinder splitting and flexure tests for CSF concrete both for continuously water cured specimens and for specimens exposed to drying after 7 days. Their tensile strength results showed no systematic influence due to curing conditions but indicated that the water cured reference specimens (0% CSF) gave consistently higher results than those which were subjected to drying. Similar results were obtained from the flexure tests. Maage and Hammer [10] also measured the tensile strength for CSF concrete under both wet and dry curing conditions. In contrast to Loland and Hustad's results they found that water cured CSF concrete produced consistently higher tensile strengths than the air cured specimens.

Some investigators [11-14] proposed mathematical relationships between the tensile and compressive strengths of concrete made with normal materials. These formulations achieved limited success since a number of factors affect the relationship between the two strengths. These factors include the surface texture and grading of the coarse

aggregate, properties of the fine aggregate, age and curing time.

Dewar [15] examined the relationship between the cylinder splitting strength and the cube compressive strength of concretes having 28-day strengths of up to 83 N/mm^2. The author [15] concluded that at low strengths, the tensile strength may be as high as 10% of the compressive strength but at higher strengths this may reduce to 5%.

Similar studies were carried out on the static modulus of elasticity E. For example, Teychenne et al [16] suggested the following relationship for concrete with compressive strengths in the range 20-60 N/mm^2 and for densities in excess of 2300 kg/m^3

$$E = 9.1\ f_c^{0.33} \qquad (2.1)$$

In equation 2.1, f_c is the cube compressive strength. The American Concrete Institute (ACI) [17] proposed a square root relationship between E and the compressive strength obtained from cylinder tests. For normal density (about 2346 kg/m^3) and for compressive strengths up to 41 N/mm^2, the relationship was given as

$$E = 4.78\ \sqrt{f_c} \qquad (2.2)$$

In equations 2.1 and 2.2, f_c is measured in N/mm^2 and the values of E are given in kN/mm^2.

John and Shah [14] tested concretes with strengths in the range 27-110 N/mm^2 and concluded that equation 2.2 was adequate for this range. The high strengths were achieved by using 2-8 mm crushed diabase aggregates and a water/cement ratio, w/c = 0.21.

Swamy [18] examined the properties of high strength concrete, with cube strengths ranging between 80 N/mm^2 and 112 N/mm^2, with w/c ratios $\leq$ 0.35. In his expression for the elasticity modulus the coefficient on the right hand side of equation 2.2 was 4.07. This coefficient is lower than the generally accepted value of 4.5 and the reduction was attributed to the high paste content and the fineness of the cement used.

The above empirical relationships, and others [18, 19] which included the density of the concrete, are valid only for specific conditions and materials and can be sensitive to such factors as the properties of the aggregate and the shape and surface texture of the coarse aggregate.

Following testing a large number of concrete specimens, Loland [20] demonstrated that E for high strength concrete did not increase at the same rate as the compressive strength. The author [20] found no significant difference between E for CSF concrete and that for the reference concrete. Giaccio et al [21] studied the influence of PFA inclusion on E for concretes with w/c = 0.4 and w/c = 0.55 at ages up to one year. The concretes employed had 28-day

compressive strengths in the range 30-70 N/mm^2. They also concluded that there was no significant difference between the PFA concretes and the reference concrete.

Experimental data on the mechanical properties of high strength concrete are limited. However, the references cited above [14-19] and other investigations [22, 23] have generally indicated that the empirical relationships between compressive strength and other properties such as tensile strength, flexural strength and modulus of elasticity established for normal concretes can not always be used for high strength concrete. Caution should, therefore, be exercised in extrapolating data from lower strength to high strength concretes and if necessary, tests should be carried out to develop data for the materials or applications in question. In general it is observed that cracking in high strength concrete is more localised and approaches homogeneous material behaviour as compared to normal concrete. It is also observed that high strength concrete exhibits a relatively more linear elastic behaviour and is comparatively more brittle than normal concrete [14, 22].

The degree of brittleness of a material can be assessed using fracture mechanics principles. The concepts of fracture mechanics were initially developed to characterise the failure process in metals, polymers and ceramic materials. Due to the heterogeneous, anisotropic and discontinuous nature of concrete and other cement based composites, the application of fracture mechanics to

concrete technology has been a matter for debate. This situation, however, has changed in recent years and fracture mechanics is now being increasingly applied to the study of fracture in concrete materials. In fracture mechanics the property which gives structural materials resistance in the presence of cracks and crack-like defects is termed the fracture toughness. Toughness is a measure of the energy required to produce fracture and hence increases with increasing ductility, the latter being a measure of the strain required to produce failure.

There are inherent difficulties in determining the fracture toughness characteristics of cementitious materials. Apart from the fact that almost all factors that influence strength also affect fracture toughness, there are no established testing methods, specimen geometries and dimensions. Furthermore, it is generally agreed that linear elastic fracture mechanics (LEFM) is not directly applicable to cementitious materials because of the slow crack growth that takes place during loading. For example, Swamy [24] states that cementitious materials undergo considerable microcracking under the applied loads and as a result the effective crack length at maximum load is usually underestimated. This in turn leads to an underestimation of the fracture energy of the material [25]. Another factor is the uncertainty of whether crack propagation takes place evenly across the full width of the crack front. By using a stiff testing machine in controlling the load increments and employing a microscope fitted with a micrometer, Swamy

[24] monitored the crack propagation in fibre reinforced concrete beams. He concluded that the crack extension process is far from a simple growth of a single crack. A considerable amount of microcracking characterised by branching cracks, apparent discontinuities and local crushing of the matrix was found to be present. It was suggested, however, that if slow crack growth is accounted for and the pseudo-plastic zone in front of the crack tip is small in relation to the crack size and that of the specimen, then LEFM may be reasonably assumed to apply to small scale tests.

Experimental work has shown that LEFM can be applied to metallic or ceramic materials under plane strain conditions provided that certain minimum specimen size requirements are observed. Ewalds and Wanhill [26] give the specimen width d as

$$d = 5.0\ (k_c/\sigma_{ys})^2 \qquad (2.3)$$

In equation 2.3, σ_{ys} is the yield strength and k_c is the fracture toughness which is defined as the critical value of the stress intensity factor. Cementitious materials do not exhibit yielding like metallic materials and Modeer [27] proposed the following equation for concrete

$$d = 10\ (k_c/f_t)^2 \qquad (2.4)$$

in which f_t is the tensile strength. Taking k_c = 1.0 $MNm^{-3/2}$ and f_t = 4.0 MN/m^2 a minimum specimen width of 625 mm is obtained.

In recent years attention has been paid to the idea of describing the crack tip nonlinearity by a fictitious crack model. In this model cohesive forces in the crack process zone are imposed to account for the microcracking that takes place ahead of the crack tip. These closure forces are varied in accordance with the extent of crack opening. The model was originally proposed by Dugdale [28] for studying ductile fracture in metallic materials. To the author's knowledge this model was first applied to concrete materials by Kesler et al [29]. This was proposed because earlier experimental work [30] suggested that LEFM could not be applied directly to their uniaxially tensioned concrete specimens. More recently Hillerborg et al [31], Bazant and Oh [32] and others [33, 34] used this model to represent a generalised non-yielding stress-strain behaviour for concrete. These developments, however, have taken an impractically complex direction and it is argued that in the absence of LEFM it would be difficult to assess the validity of this approach. Furthermore, Saouma et al [35] re-evaluated Kesler's results and despite the small thickness of their specimens in relation to the crack size concluded that LEFM was applicable. This contradiction was attributed to the inappropriate relationships employed in [30] for evaluating their results.

Swartz [36] carried out an extensive testing program using beams in 3- and 4-point bending. By employing a dye technique it was shown that the process zone ahead of the crack tip was very small. It was concluded that if allowance is made for the slow crack growth then LEFM could be used for concrete materials.

A number of geometries have been employed by different workers in assessing the fracture characteristics of concrete materials. These have traditionally included the beam in 3- or 4-point bending, the double cantilever beam, the double torsion plate and the compact tension specimen [37]. Some of these geometries, however, result in large specimens in relation to the crack size and may be considered inappropriate in practice. In more recent years alternative geometries such as the circumferentially notched round bar in bending [38], the compact compression specimen [39] and the axial splitting specimen [40] have been employed.

The effect of specimen size on the fracture toughness of concrete has been examined by several investigators for different specimen geometries. Mindess [41], for example, tested beams in 3-point bending with sizes in the range 100 mm x 100 mm x 840 mm - 400 mm x 400 mm x 3360 mm and concluded that the fracture energy increased significantly in the case of the large specimens. Nallathambi et al [42] carried out a similar study and reported that the fracture toughness increased substantially with increasing specimen

size when evaluated by an energy approach. However, the increase was only slight when the fracture toughness was evaluated by the stress intensity factor approach. Using this approach, Barr and Sabir [43] examined the effect of specimen size on the fracture toughness using the compact compression specimen. They concluded that specimen lengths in the range 100 mm to 200 mm yielded the same results for the fracture toughness.

Studies on the effect of the notch size on the fracture toughness evaluated by the stress intensity factor approach have also been conducted. Again conflicting results have been reported by different investigators. Whereas Kesler et al [29], Gjorv et al [44] and Nallathambi et al [42] all reported a decrease in fracture toughness with increasing notch size, Petersson [45] concluded that the fracture toughness initially increases and then decreases. Carpinteri [46] also conducted tests on notched beams in flexure and obtained similar results to those of Petersson [45]. Pak and Trapeznikov [47] tested 3000 specimens of different sizes and types and reported that the fracture toughness increases with increasing notch size. Hillemeier and Hilsdorf [48] used wedge loaded compact tension specimens and concluded that the fracture toughness decreases with increasing notch depth and stabilises for the deeper notches. Using beams in 3-point bending, Kitagawa and Suyama [49] reported that the fracture toughness is approximately constant for different notch sizes. A similar conclusion to that of [49] was reported by Brandt [50] for fibre reinforced concrete (FRC).

Almost all of the above relationships between fracture toughness and notch size were reported by different authors when the fracture toughness was evaluated using an energy approach. Petersson [45], Brandt [50], Yokomichi et al [51] and Mazars [52] all tested concrete beams in flexure and found the fracture toughness to be independent of the notch depth. Whereas Desayi [53] concluded that the fracture toughness increased with increasing notch depth, results reported by Nallathambi et al [54] showed the opposite trend.

Mindess [41] studied the effect of self weight of the specimen by testing beams in 3-point bending with lengths ranging between 840 mm and 3360 mm. The author [41] concluded that including the self weight of the beam made very little difference to the calculated values of the fracture energy. Barr et al [55] studied this effect in view of the moments created due to the eccentricity of the loading arrangement. They concluded that in the case of the 100 mm cubes this was negligible but had to be taken into account when using larger test specimens.

The above studies on the effects of specimen size, notch size and self weight on the fracture toughness have largely been conducted on concretes with low to moderate compressive strengths. Some investigators, however, examined the fracture toughness in relation to the strength of the concrete. For example, results obtained by John and Shah [14] indicated that the fracture toughness of concretes with

compressive strengths up to 110 N/mm^2 increased with increasing compressive strength thus implying increased ductility. Similar results were reported by Jenq and Shah [56]. Nallathambi and Karihaloo [57] also showed that the fracture energy of concrete increased with increasing compressive strength. These results are in contrast with those obtained for metals where with increasing strength the fracture toughness decreases thus indicating increased brittleness [58].

As pointed out earlier, it is generally observed that high strength concrete exhibits more linear elastic behaviour and is more brittle than normal concrete. Although, results reported in this thesis support this, to the author's knowledge, this behaviour has not been confirmed by other researchers through fracture studies.

A number of studies have been made to evaluate the post-cracking toughness of FRC materials. This is usually done through a toughness index evaluated from the area under the load-displacement curve. Several definitions for such an index have been proposed. The ACI [59] proposed an index evaluated from tests conducted on beams loaded in flexure. This index was defined as the ratio of the area under load-displacement curve up to a displacement of 1.9 mm to the area up to first crack. Using beams in bending, Johnston [60] evaluated the toughness index from the area under the load-displacement curve up to a displacement which is a multiple of that at first crack. Barr et al [61] defined a

toughness index obtained from tests employing the compact compression specimen. This was calculated from the area up to twice the displacement at first crack. More recently Purkiss [62] evaluated the toughness properties of steel fibre reinforced concrete subjected to elevated temperatures. In the calculation of the toughness index it was not possible to detect the load at first crack at very high temperatures and instead, the point at which nonlinearity occurred in the load-displacement curve was employed.

There are two main approaches for determining the fracture toughness of a material. These are the energy balance approach, which gives the critical strain energy release rate G_c, and the stress intensity factor approach, which gives the critical stress intensity factor k_c. The advantages and disadvantages of these approaches are given by Swamy [37]. In the energy balance approach G_c is determined from the area under the load-displacement curves obtained experimentally. The determination of k_c, however, requires a knowledge of the stress intensity factor k for the geometry used in the test. Expressions for k based on classical solutions have been developed for standard geometries. These are generally expressed as polynomial or trigonometric functions of the notch size. However, in the absence of such expressions, numerical analyses are carried out for the geometries under study. Amongst the numerical methods employed the finite element method (FEM) has received much attention.

Initial efforts [63-65] using conventional finite elements demonstrated clearly that hundreds, or sometimes thousands, of elements are necessary to achieve a solution accuracy within 5%. The number of elements required in a given situation is dependent on the complexity of the problem and the procedure employed in the determination of the fracture parameters. From the outset, the most appealing approach to finite element fracture mechanics analysis is that which takes explicit account of the singular form of the stresses at the tip of the crack. A large number of such formulations employing classical solution functions have been developed in the 1970's. Although some of these have been based on assumed singular stress fields [66], the majority of the singularity formulations are developed from displacement functions which result in the appropriate singularity in the stresses.

Byskov [67] appears to have been the first to formulate a finite element based on classical displacement fields established by Muskhelishvili [68]. The element is triangular in shape with the crack tip at the interior of the triangle. In the analysis, all elements surrounding this special crack element are conventional constant strain triangles. Although continuity of displacements across the element interfaces was not achieved, except at the nodes, the crack element contained terms representing the rigid body modes. A high order circular crack tip element, similar in many respects to that of Byskov was presented by Wilson

[69]. The general formulation for the element was in terms of a stress function, due to Williams [70], which is equivalent to that of Muskhelishvili.

The primary differences between the two approaches of references [67] and [69] are element shape and coupling technique with the surrounding constant strain triangular elements. The circular shape of Wilson's element allowed the stiffness matrix to be expressed explicitly, whereas the stiffness matrix of Byskov's element was determined numerically. To maintain the approximate circular shape of the outer boundary, Wilson found it necessary to surround the tip element by a large number of conventional elements. It was argued, however, that a sufficient number of conventional elements is required in order to reduce the effect of non-compatibility of displacements at the interfaces of the two types of elements. Byskov's element can be surrounded by only three conventional elements and hence no effective control is maintained over the influence of non-compatibility of displacements.

An underlying consideration in the choice of classical solution functions for finite element formulations is that they usually satisfy the relevant conditions of equilibrium within the element. Classical solution functions are, however, usually complex and generally lead to very difficult integration of the stiffness equations and in some cases result in the elements requiring many nodal points with additional degrees of freedom (d.o.f.).

Polynomial type shape functions rather than classical solution functions have been used to produce element stiffness matrices which contain singularities. These usually lead to simpler forms of elements and easier integration of the stiffness equations. Tracey [71] introduced a triangular element for an elastic medium, based on assumed displacement fields, which takes account of the singularity at the crack tip. In the analysis the special near tip elements were surrounded by trapezoidal isoparametric elements. The author [71] points out that the isoparametric elements have a singular stress variation admissible within the element as well as a constant stress state, thus reducing the effects of displacement non-compatibility. In analysing a rectangular bar with symmetrical edge cracks, it was found that stress intensity factors within 4% of an accepted value were obtained using 548 d.o.f.

Polynomial type displacement functions were employed by Wilson [69] to develop a stiffness matrix for a triangular crack tip element in terms of polar coordinates. In the examples considered by Wilson [69], the crack tip region was enclosed by a series of these wedge shaped isosceles triangular elements, all having a common nodal point at the tip of the crack. The crack tip elements were surrounded by conventional constant strain triangular elements [72]. It was pointed out [69] that displacements in the constant strain elements vary linearly with the rectangular coordinates, whereas displacements on the outer boundary of

the singular elements vary approximately linearly with the angular polar coordinate. Although displacements are continuous only at the two common nodal points of the two types of elements, the author [69] suggests that as the wedge angles of the tip elements decrease indefinitely, continuity at the common interface is approached in the limit.

Tracey [71] employed isoparametric formulations to develop an element for an elastic medium which embodied the singular conditions at the crack tip. This element was also triangular in shape and was shown to be equivalent to that of Wilson [69] as the included angle at the crack tip is reduced.

Sabir [73] derived displacement shape functions for partially curved trapezoidal and triangular elements by integrating assumed singular strain functions appropriate for LEFM. The elements were formulated in terms of polar coordinates and they contained all the terms associated with rigid body displacements. In the analysis the special elements were surrounded by constant strain triangular elements. The elements were tested in a number of fracture geometries and were shown to perform well in deriving the stress intensity factors directly from the solution for the displacements.

It has been shown that singular transformations from physical to isoparametric coordinates can be made if node

points along the sides of the element are positioned in a certain way. Henshell and Shaw [74] used the standard 8-noded isoparametric element with mid-side nodes displaced to the quarter points to produce singularity at the tip of the crack. Barsoum [75] pointed out that while producing singularity, as with other special crack tip elements, the modified isoparametric element retained the advantage of producing constant strain and rigid body motion modes. The author [75] reports a solution for the same problem analysed by Tracey [71] with similar accuracy using 700 d.o.f. In a subsequent paper [76], Barsoum extended the approach to obtain an element for fracture analysis of shells based on a 20-noded solid isoparametric element. Isoparametric elements have also been used successfully in nonlinear analysis of fracture problems [77-79].

In a further paper Barsoum [78] pointed out that in using the 8-noded isoparametric elements, the singularity condition prevails only along the edges of the element. The author [78] overcomes this by collapsing a pair of nodes to form a triangular element in which singularity prevails on all lines emanating from the vertex at the tip of the crack.

The use of the singularity isoparametric elements is clearly confined to the elements enclosing the tip of the crack, the elements surrounding them being of the conventional type. In reference [80] it was shown that if a layer of 'transitional' elements surround the tip elements, a significant improvement in the accuracy of the solution is

obtained without increasing the number of d.o.f. In these elements the side nodes are positioned between the quarter and mid-side points.

The above shows that considerable developments have been made in the application of the FEM to fracture mechanics analysis. At present, the most widely used approach is that which employs quarter point isoparametric elements around the crack tip and conventional elements in the remaining part of the structure. Although the quarter-point elements represent the stress condition near the crack tip with considerable accuracy, in order to achieve overall accuracy further conditions should hold. There must be adequate displacement compatibility between the special tip elements and the surrounding conventional elements. These surrounding elements must be small enough to give a close representation of the stresses adjacent to the special elements. This situation can lead to some difficulty in the choice of the size of the tip elements. They should be large enough to cover the region of large stress gradients, yet small enough to interface with a sufficiently fine exterior mesh.

Once a numerical solution has been obtained for a particular finite element representation, the stress intensity factor can be estimated using one of two basic approaches. In the first approach, the stress intensity factor is obtained by direct substitution of the results in the well-known crack tip equations.

The equilibrium and stability of cracks from an energy viewpoint was first discussed by Griffith [81]. Later Irwin [82] presented a more detailed study of the energy analysis and its relationship to the crack tip stress field approach. Since then a number of somewhat different energy analyses have been developed by many authors. These form the basis of the second approach. These approaches are discussed in detail in the ensuing chapter.

CHAPTER THREE

THEORETICAL CONSIDERATIONS

3.1 Introduction

Almost all structures contain cracks or microcracks. These may exist as an inherent defect or be introduced at a later stage during the service life of the structure. The need for a reliable means of assessing the stability of such cracks and the remaining useful life of the structure is of paramount importance. Although analytical solutions exist for comparatively simple geometries and loading conditions, it is often the evaluation of the stress and displacement fields in cracked bodies of far more complex and practical geometries that is required. The finite element technique is now firmly established as the most attractive and practical tool for the numerical solution of such engineering problems. In its application, attempts have ranged from the use of extremely fine meshes with no particular attention to the crack tip region, to the accurate modelling of the singular stress field in the vicinity of the tip. Once the numerical solution has been obtained for a particular finite element representation, the stress intensity factor is estimated using one of two basic approaches, i.e. the direct approach and the energy method.

In this chapter the basic concepts and definitions used in fracture mechanics analysis are introduced. The various numerical techniques employed in the finite element analysis

of fracture problems are also presented.

3.2 Elastic Stress Field Parameters

When a cracked body is subjected to an external load it can deform in various ways. Irwin [82] observed that kinematically three modes of crack surface displacement can be identified, as illustrated in Figure 3.1. These are

Mode 1

This is the opening mode with symmetric extension or bending of cracked surfaces with respect to the plane containing the crack prior to deformation and in which the discontinuity is perpendicular to the plane of crack.

Mode 2

The sliding mode which is characterised by local deformations in which the crack surfaces slide over one another in opposite directions but in the same plane. In this mode the discontinuity is in the plane and parallel to the direction of the crack.

Mode 3

The tearing mode in which the movement of the crack surfaces can be related to the warping action of non-circular cylinders under torsion in which the material points, initially in the same plane, occupy different

planes after deformation. The displacement discontinuity in this mode is parallel to the leading edge of the crack.

The stress intensity factor describes the magnitude of the elastic stress field at the crack tip. The three factors associated with the above mentioned modes of cracking are denoted k_1, k_2 and k_3 respectively. It is generally possible to characterise a crack in a solid by superposition of all of these modes. When k reaches a critical value k_c, sufficient energy is being applied to the crack tip and crack propagation will usually occur catastrophically. This critical value of the stress intensity factor at the onset of unstable crack growth is referred to as the fracture toughness. On a macroscopic scale the opening mode is predominantly experienced in practice and consequently this thesis concerns itself with mode 1 failure only.

3.3 Evaluation of the Stress Intensity Factor

The stress intensity factor can be estimated from results of numerical analysis using one of two basic approaches, namely the direct and the energy balance approaches.

3.3.1 The Direct Approach

In this approach the results of numerical analyses are employed in the classical crack tip equations or other simulations to compute the stress intensity factor. Although both stresses and displacements can be employed for this purpose, it is generally agreed that the displacement approach yields more accurate results as the accuracy of the results for stresses is usually inferior to that for the displacements.

3.3.1.1 Displacement Extrapolation (DE)

In this approach the stress intensity factor is obtained by the direct substitution of the finite element displacement or stress results into the well-known crack tip equations. Starting with the equilibrium equations for plane extension and following the Westergaard method of stress analysis of cracks [83], the stress and displacement fields associated with each mode are obtained. Using the notation shown in

Figure 3.2 and neglecting the higher order terms in r, the equations can be written as:

Mode 1

$$\sigma_x = [k_1/\sqrt{(2\pi r)}] \cos \Theta/2 \, (1 - \sin \Theta/2 \sin 3\Theta/2)$$

$$\sigma_y = [k_1/\sqrt{(2\pi r)}] \cos \Theta/2 \, (1 + \sin \Theta/2 \sin 3\Theta/2)$$

$$\sigma_{xy} = [k_1/(\sqrt{2\pi r})] \sin\Theta/2 \cos \Theta/2 \cos 3\Theta/2 \qquad (3.1)$$

$$u_x = [k_1/(2\Omega)] \sqrt{(r/2\pi)} \cos \Theta/2 \, (\mu' - 1 + 2\sin^2 \Theta/2)$$

$$u_y = [k_1/(2\Omega)] \sqrt{(r/2\pi)} \sin \Theta/2 \, (\mu' + 1 - 2\cos^2 \Theta/2)$$

$$w = 0$$

Mode 2

$$\sigma_x = [-k_2/\sqrt{(2\pi r)}] \sin \Theta/2 \, (2 + \cos \Theta/2 \cos 3\Theta/2)$$

$$\sigma_y = [k_2/\sqrt{(2\pi r)}] \sin \Theta/2 \cos \Theta/2 \cos 3\Theta/2$$

$$\sigma_{xy} = [k_2/(\sqrt{2\pi r})] \cos \Theta/2 \, (1 - \sin \Theta/2 \sin 3\Theta/2) \qquad (3.2)$$

$$u_x = [k_2/(2\Omega)] \sqrt{(r/2\pi)} \sin \Theta/2 \, (\mu' + 1 + \cos^2 \Theta/2)$$

$$u_y = [k_2/(2\Omega)] \sqrt{(r/2\pi)} \cos \Theta/2 \, (1 - \mu' + \sin^2 \Theta/2)$$

$$w = 0$$

Mode 3

$$\sigma_{xz} = [-k_3/\sqrt{(2\pi r)}] \sin \Theta/2$$

$$\sigma_{yz} = [k_3/\sqrt{(2\pi r)}] \cos \Theta/2$$

$$\sigma_x = \sigma_y = \sigma_z = \gamma_{xy} = 0 \qquad (3.3)$$

$$w = (k_3/\Omega)\sqrt{(2r/\pi)}\sin\theta/2$$

$$u_x = u_y = 0$$

In the above equations Ω is the rigidity modulus given by

$$\Omega = E/[2(1+\mu)]$$

and μ' is a function of Poisson's ratio μ given by

$$\mu' = 3-4\mu \quad \text{(plane strain)}$$
$$\mu' = (3-\mu)/(1+\mu) \quad \text{(plane stress)} \qquad (3.4)$$

In equations 3.1-3.3, u_x, u_y and w are the displacements in the x, y and z directions respectively and the stresses are as defined in Figure 3.2. Using the above equations in correlation with the finite element nodal displacements or stresses, k values for a series of nodal points (r,θ) near the crack tip are calculated. Plots of k as a function of r for a given value of θ for the particular displacement or stress component is made and tangential extrapolation is used to estimate the value of k as r approaches zero, i.e. at the crack tip.

This method of calculation has been employed in many investigations including the works based on special crack tip elements [69] and isoparametric elements [74].

3.3.1.2 Conic Section Simulation (CSS)

This method is due to Chow and Lau [84] and is based on mapping the nodal displacements of the crack surface into an elliptical displacement function of the axial coordinates. Consider a crack in an infinite plate, as shown in Figure 3.3, subjected to the opening mode under uniform tension σ_o at infinity and normal to the crack surface. The crack surface displacements derived by Sneddon [85], can be written for plane stress conditions as

$$u_x = -(1-2\mu)\ \sigma_o x/E \tag{3.5}$$

$$u_y = 2\sigma_o a\ (1 - x^2/a^2)^{\frac{1}{2}}/E \tag{3.6}$$

For a finite width plate subjected to uniform tension σ_o as shown in Figure 3.4, the crack surface displacements can be expressed in the form of an elliptical function as

$$u_y = b\ (1 - x^2/a^2)^{\frac{1}{2}} \tag{3.7}$$

where 'a' and 'b' are the semi-major and semi-minor axes of the elliptic surface respectively. Equations 3.6 and 3.7 yield

$$\sigma_o = bE/2a \tag{3.8}$$

The stress intensity factor k_1 is defined as

$$k_1 = \sigma_o \sqrt{(\pi a)} \qquad (3.9)$$

Substitution of equation 3.8 into equation 3.9 gives

$$k_1 = bE \sqrt{(\pi a)}/2a \qquad (3.10)$$

Having obtained the appropriate opening displacement of the crack surface from the finite element analysis, the value of stress intensity factor is deduced. Chow and Lau [86] demonstrated the use of this approach by applying it to the problem of a centre cracked plate of various widths and computing the stress intensity factors directly from the finite element analysis. Satisfactory results were obtained using quarter point singular crack tip elements. It was however noted that for problems where the crack surface displacements do not comply with a single elliptical function, the accuracy of the method becomes questionable. This approach was later modified [87] by mapping only the quarter point displacements into an elliptical function.

The above equations can easily be modified for the case of a plate under plane strain conditions by replacing E and μ in equation 3.5 and 3.6 by $E/(1-\mu^2)$ and $\mu/(1-\mu)$ respectively. On combining the resulting equations with equation 3.7 we have

$$\sigma_o = bE \; / \; [2a \; (1-\mu^2)] \qquad (3.11)$$

Equations 3.9 and 3.11 give the stress intensity factor for plane strain conditions as

$$k_1 = bE \sqrt{\pi a} / [2a (1-\mu^2)] \qquad (3.12)$$

3.3.2. The Energy Approach

Accredited to Griffith [81], in this approach the criterion for propagation of a crack in a body is expressed in terms of the rate of change (with respect to crack extension) of the various energy terms involved in the process. The attractiveness of such an approach lies in the fact that it does not require an exact modelling of the crack tip stress and displacement fields. Hence accurate results can be obtained by employing relatively coarse meshes using conventional elements.

A number of energy methods have been developed to compute the stress intensity factor. These include the strain energy release rate and virtual crack extension methods in which the stress intensity factor is related to the energy release associated with an infinitesimal crack extension. Another is the J-integral method which derives the stress intensity factor from a path independent line integral.

3.3.2.1 Strain Energy Release Rate (SERR)

An elastic body subjected to applied loads and containing an extending crack has a total energy U, where

$$U = U_O + U_a + U_\gamma - F \qquad (3.13)$$

in which U_O is the elastic energy of the loaded uncracked plate, U_a is the change in the elastic strain energy caused by introducing the crack in the plate, U_γ is the change in elastic energy caused by the formation of the crack surfaces, and F is the work performed by the external forces.

The total energy U increases with crack length 'a' until the moment of instability. Thus instability will occur if

$$dU/da \leq 0 \qquad (3.14)$$

since U_O is constant, equation 3.14 can be rearranged to give

$$d/da\ (F-U_a) \geq dU_\gamma/da \qquad (3.15)$$

The left hand side of equation 3.15 represents the energy release rate for an increment of crack extension da and is denoted by G. Referring to Figure 3.5, the work done by the external loads is equivalent to $P_i\ d\delta i$. Therefore

$$G = P_i \, (d\delta i/da) - dU_a/da \qquad (3.16)$$

Where i=1,2,....,n, and n is the number of applied loads. The strain energy in the body is equal to the work done by the loads, i.e.

$$U_a = \tfrac{1}{2} \, P_i \, \delta_i \qquad (3.17)$$

Equations 3.16 and 3.17 give

$$G = P_i \, (d\delta_i/da) - \tfrac{1}{2} \, d/da \, (P_i \, \delta_i) \qquad (3.18)$$

It can be shown that for the particular case of a single applied force P, the energy release rate is given by

$$G = \tfrac{1}{2} \, P \, d\delta/da \qquad (3.19)$$

In the FEM a cracked body is represented by a number of elements connected at the nodal points. Displacements and stresses at these nodal points are the basic result of such an analysis and hence evaluation of the strain energy release rate is possible by employing equations 3.13-3.19. Direct relationships exist between the energy release rate G and stress intensity factor k for each mode of crack extension [88]. For the three modes of crack extension and under plane strain conditions these are

$$G_1 = (1-\mu^2)\, k_1^2/E$$

$$G_2 = (1-\mu^2)\, k_2^2/E \qquad (3.20)$$

$$G_3 = (1-\mu^2)\, k3^2/E$$

where G_1, G_2 and G_3 are the energy release rates associated with these modes. Having found G, the appropriate relationship (equations 3.20) can be used to calculate the stress intensity factor.

3.3.2.2 Virtual Crack Extension (VCE)

The VCE method was proposed by Parks [89] and Hellen [90] as an alternative to the strain energy release rate technique. A finite element analysis is initially performed for the original crack geometry and the strain energy is evaluated. The crack is then extended by releasing the appropriate nodal points ahead of the crack tip and the strain energy is once more calculated. The difference between the two computed values of the strain energy is regarded as the energy released in extending the crack and the stress intensity factors are evaluated from equations 3.20.

3.3.2.3 J-Integral

The concept of the J-integral applies to conditions involving both elastic and plastic deformations. The criterion extends the concepts of LEFM, where only small scale plasticity is permissible, to elastic plastic fracture mechanics (EPFM) in which extensive plastic deformation occurs. The method relies on determining the change in potential energy when a crack is extended by an amount da in a manner comparable to that of the strain energy release rate G in the linear elastic case. An EPFM parameter J, equivalent to the LEFM parameter G, can be defined as

$$J = d/da\ (F-U_a) \qquad (3.21)$$

Returning to equation 3.13, the potential energy U_p is defined as

$$U_p = U_o + U_a - F \qquad (3.22)$$

Thus U_p contains all the energy terms that may contribute to non-linear elastic behaviour. Since U_o is constant, equation 3.22 can be differentiated to give

$$dU_p/da = d/da\ (U_a-F) = -d/da\ (F-U_a) \qquad (3.23)$$

From equations 3.21 and 3.23, it follows that

$$J = -\ dU_p/da \qquad (3.24)$$

It has been shown that a closed contour encircling a crack tip has a constant value of line integral. This important finding enables us to calculate fracture toughness parameters by studying a small area around the crack tip without focusing attention directly at the tip itself. The integral most often used is due to Rice [91] who showed, using Green's theorem [92], that

$$J = -dU_p/da = \int_{\Gamma} (W\, dy - T\, du/dx\, ds) \qquad (3.25)$$

where Γ is a closed contour surrounding the crack tip from the lower lip of the crack to the upper lip in an anti-clockwise manner, as shown in Figure 3.6. W is the strain energy density or the work done on the body in loading to a given condition and is given by

$$W = W(\varepsilon) = \int_0^{\varepsilon} \sigma_{ij}\, d\varepsilon_{ij} \qquad (3.26)$$

For a simple linear elastic body subjected to a tensile strength σ giving a strain ε equation 3.26 becomes

$$W = \int_0^{\varepsilon} \sigma_{11}\, d\varepsilon_{11} = 1/2\ \sigma\ \varepsilon \qquad (3.27)$$

T is the traction vector defined according to the outward normal along Γ and may be written as

$$T_i = \sigma_{ij}\, n_j \tag{3.28}$$

Using the mathematical notation, it follows that

$$\begin{aligned} T_1 &= \sigma_{11}\, n_1 + \sigma_{12}\, n_2 \\ T_2 &= \sigma_{21}\, n_1 + \sigma_{22}\, n_2 \end{aligned} \tag{3.29}$$

n_1 and n_2 are the cosines of angles Θ_1 and Θ_2 created by the vector normal to the surfaces of the contour and the positive x and y directions respectively. It can readily be shown that

$$\begin{aligned} dx &= -\, ds \cos \Theta_2 \\ dy &= ds \cos \Theta_1 \end{aligned} \tag{3.30}$$

u is the vector of displacements and ds is an element of arc length along Γ.

The J-integral, which can be determined numerically with relative ease, provides a practical method for analysing both elastic and plastic fracture behaviour. For linear elastic behaviour J is identical to G and thus, a J-integral failure criterion can be used in a manner similar to that based on the critical stress intensity factor approach. J_C can be regarded as a material constant for the initiation of crack extension and is related to the critical stress intensity factor by the following relationships

$$J_C = G_C = (1-\mu^2)\, k_C^2/E \qquad \text{(plane strain)}$$

$$J_C = G_C = k_C^2/E \qquad \text{(plane stress)} \tag{3.31}$$

in which E is Young's modulus and μ is poisson's ratio.

The J-integral method offers a relatively simple means for determining the energy release rate for cases where the plastic zone near the crack tip is small. It must be noted that in the presence of significant plasticity, equations 3.31 are not valid although some investigators indicate that J_C may still adequately characterise the crack tip condition for fracture initiation. Finally, since the J-integral is expressed only in two dimensions, its applicability is restricted to the problems of plane strain or generalised plane stress.

By numerically evaluating the integral of equation 3.25, using the finite element results, along a path surrounding the crack tip, an estimate of the stress intensity factor can be obtained using equation 3.31.

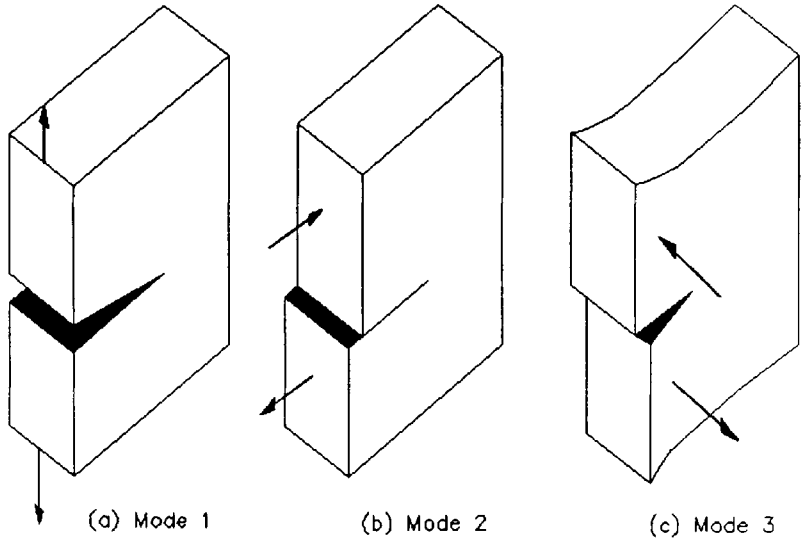

Figure 3.1 The Three Modes of Cracking.

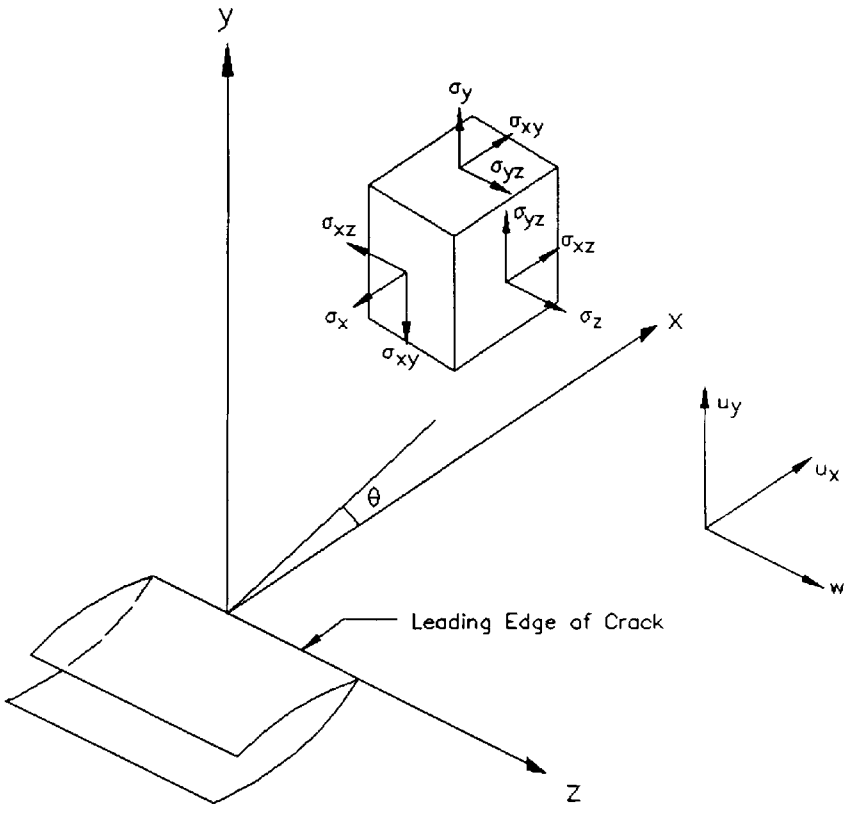

Figure 3.2 Displacement and Stress Components in the Rectangular Coordinates System.

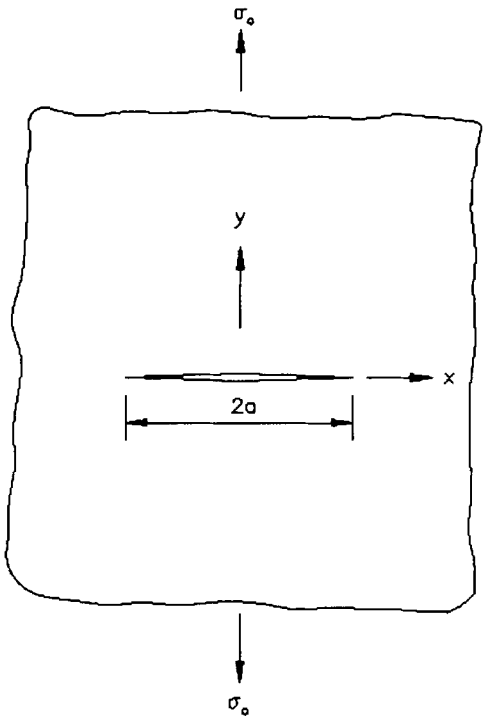

Figure 3.3 An Infinite Plate Under Uniform Tension.

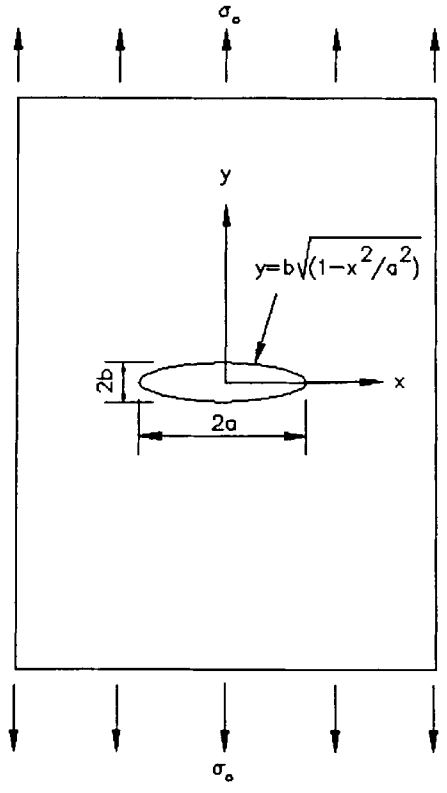

Figure 3.4 The Conic Section Simulation Model.

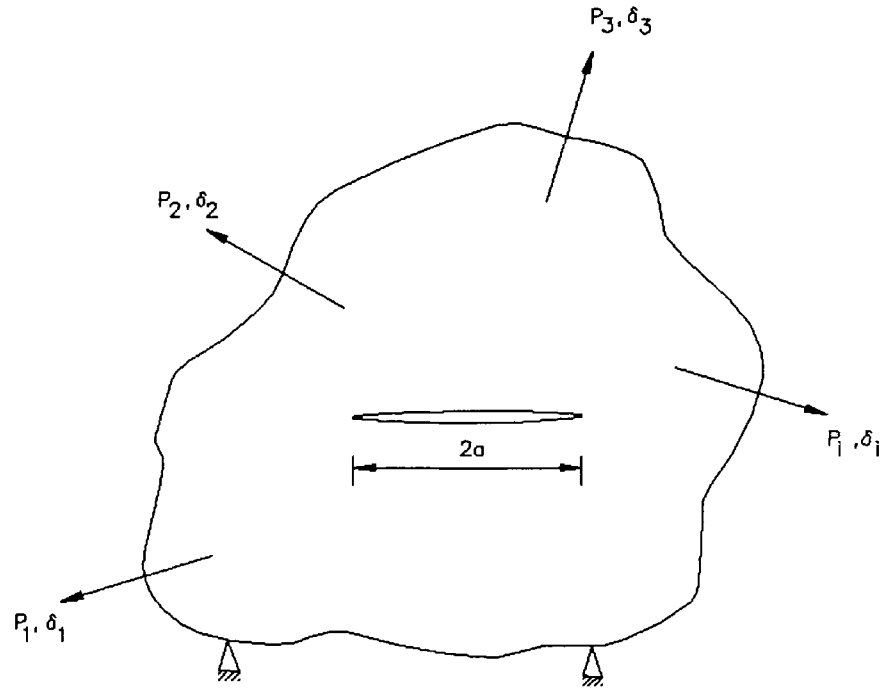

Figure 3.5 A Cracked Body Under Arbitrary System of Applied Loads.

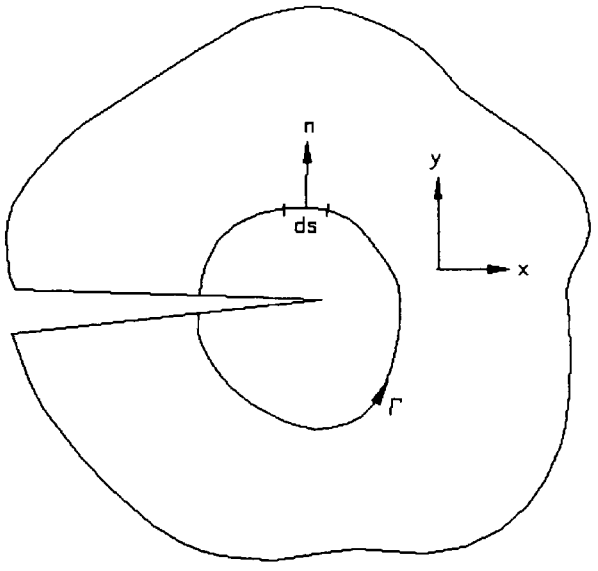

Figure 3.6 The J-Integral Contour Γ.

CHAPTER FOUR

FINITE ELEMENT FORMULATIONS

4.1 Introduction

The finite element method (FEM) has emerged as one of the most powerful tools of numerical analysis. The developments in this field of analysis in the past two decades have been impressive. By means of the FEM, approximate solutions can be obtained for a wide range of structures of complex geometries and loading conditions. In the FEM the continuum is divided by imaginary lines into a number of elements interconnected at discrete points or nodes. A function is chosen to define uniquely the state of displacement within each element in terms of its nodal displacements. These, together with any initial strains and the elastic properties of the material define the state of stress throughout the element. The stiffness matrices are found for the elements and are assembled to obtain the structure stiffness matrix.

In this chapter after a brief outline of the general finite element procedure, the formulations for various elements used in fracture analysis are presented.

4.2 The Finite Element Method

The FEM is described in detail in the literature and will only be outlined briefly here. In this method the structure is divided into a number of sub-regions (elements) connected at discrete points called nodes. For each sub-region a displacement function in terms of discrete parameters α_1, α_2, ...,α_n is prescribed. An approximate solution for these parameters can be obtained by minimising the potential energy of the structure and the loads under the constraints imposed. If the prescribed displacement functions satisfy certain requirements with respect to continuity and conformity, it can be shown that as the size of the elements decrease indefinitely, the solution obtained converges to the exact solution. The minimisation procedure involves the development of the overall structure stiffness matrix from the element stiffness matrices $[K_e]$. For two dimensional analysis and in terms of the rectangular system of coordinates shown in Figure 4.1, $[K_e]$ can be evaluated from

$$[K_e] = [C]^{-1,T} \int\int [B]^T[D][B]\, dx\, dy\, [C]^{-1} \qquad (4.1)$$

In equation 4.1 the index T refers to the transpose of a matrix and the matrices [C], [B] and [D] are defined by the following relationships

$$\{\delta_e\} = [C]\ \{\alpha\} \qquad (4.2)$$

$$\{\varepsilon_e\} = [B]\ \{\alpha\} \qquad (4.3)$$

$$\{\sigma_e\} = [D]\ \{\varepsilon_e\} \qquad (4.4)$$

[C] is a square matrix usually referred to as the transformation matrix. [B] is the strain-displacement matrix containing the element strains given by equations 4.11. [D] is the rigidity matrix given by

$$[D] = Et/(1-\mu^2) \begin{bmatrix} 1 & \mu & 0 \\ \mu & 1 & 0 \\ 0 & 0 & (1-\mu)/2 \end{bmatrix} \qquad (4.5)$$

for plane stress, and

$$[D] = Et/(1+\mu)(1-2\mu) \begin{bmatrix} 1-\mu & \mu & 0 \\ \mu & 1-\mu & 0 \\ 0 & 0 & (1-2\mu)/2 \end{bmatrix} \qquad (4.6)$$

for plane strain, where E is the Young's modulus, t is the thickness and μ is Poisson's ratio.

In equations 4.2 and 4.3, $\{\alpha\}$ is the vector containing the discrete parameters appearing in the assumed shape functions and $\{\delta_e\}$, $\{\varepsilon_e\}$ and $\{\sigma_e\}$ are vectors containing the element nodal displacements, element strains and element stresses respectively.

Once the element stiffness matrix $[K_e]$ is formed the structure stiffness matrix [K] can be assembled. This is a

square matrix, symmetrical about the leading diagonal, relating the nodal forces {F} to the corresponding structure nodal displacements {δ} by the following equation

$$\{F\} = [K]\ \{\delta\} \tag{4.7}$$

For a given system of applied forces and/or displacements a solution may be obtained for the nodal displacements by inverting the structure stiffness matrix. Thus

$$\{\delta\} = [K]^{-1}\ \{F\} \tag{4.8}$$

Once the nodal displacements are calculated the element nodal stresses (or stresses at any point within the element) may be evaluated from

$$\{\sigma_e) = [S_e]\ [C]^{-1}\ \{\delta_e\} \tag{4.9}$$

where $[S_e]$ is an element stress matrix given by

$$[S_e] = [D]\ [B] \tag{4.10}$$

4.3 Strain-Based Finite Elements

As outlined earlier, in the conventional FEM a displacement (or shape) function is assumed for the particular element in terms of the discrete parameters $\{\alpha\}$. This approach, however, does not always satisfy the 'completeness' requirements to ensure convergence to the exact solution. Ideally the chosen displacement function should be such that it does not permit straining of an element to occur when the nodal displacements are caused by rigid body translations. Furthermore, although continuity of displacements is automatically satisfied at the nodes, it is desirable that such continuity is preserved across the interfaces of adjacent elements. Finally, it is also desirable that the resulting functions for the strains and the stresses satisfy the compatibility and equilibrium conditions. These conditions present difficulties in many formulations and may lead to rather sophisticated displacement fields.

In this section a simple procedure for deriving displacement functions from assumed strain functions is described. These functions satisfy the conditions of rigid body modes and can be adjusted to meet the requirements of compatibility and equilibrium.

4.3.1 Rectangular In-plane Equilibrium Element

In cartesian x- and y-coordinates, the relationship between the in-plane strains ε_x, ε_y and ε_{xy} and the translational displacements u_x and u_y, as shown in Figure 4.1, are

$$\varepsilon_x = \delta u_x/\delta x$$

$$\varepsilon_y = \delta u_y/\delta y \qquad (4.11)$$

$$\varepsilon_{xy} = \delta u_x/\delta y + \delta u_y/\delta x$$

If we equate equations 4.11 to zero and then integrate the resulting differential equations, we obtain the following expressions for the displacements

$$u_x = \alpha_1 - \alpha_3\, y$$

$$u_y = \alpha_2 + \alpha_3\, x \qquad (4.12)$$

Equations 4.12 represent the displacements of the element without straining, i.e. the rigid body displacements which are expressed in terms of three independent constants of integration α_1, α_2 and α_3.

To obtain the shape functions for a rectangular element with corner nodes only and having two degrees of freedom u_x and u_y at each node, the shape functions should contain eight

independent constants. The additional five constants may be proportioned among the three strains as follows

$$\varepsilon_x = \alpha_4 + \alpha_5 y$$

$$\varepsilon_y = \alpha_6 + \alpha_7 x \qquad (4.13)$$

$$\varepsilon_{xy} = \alpha_8$$

giving an independent linear variation for the direct strains ε_x and ε_y, and a constant shearing strain ε_{xy}.

The compatibility condition may be written as

$$\delta^2\varepsilon_x/\delta y^2 + \delta^2\varepsilon_y/\delta x^2 = \delta^2\varepsilon_{xy}/\delta x\delta y \qquad (4.14)$$

This differential relationship must be satisfied by the strain components to secure the existence of functions u_x and u_y with the strain components of equations 4.11. To check if the strain element satisfies compatibility within the elements, we substitute equations 4.13 in the compatibility equation 4.14 and find that internal displacement compatibility is satisfied.

If we consider an elemental area dx by dy, as shown in Figure 4.1, the equilibrium equations in the x and y directions may be written as

$$\delta\sigma_x/\delta x + \delta\sigma_{xy}/\delta y = 0$$

(4.15)

$$\delta\sigma_y/\delta y + \delta\sigma_{xy}/\delta x = 0$$

For a plane stress problem the stress components can be expressed as

$$\sigma_x = [E/(1-\mu^2)]\ \{\varepsilon_x + \mu\varepsilon_y\}$$

$$\sigma_y = [E/(1-\mu^2)]\ \{\varepsilon_y + \mu\varepsilon_x\} \qquad (4.16)$$

$$\sigma_{xy} = [E/(1+\mu)]\ \varepsilon_{xy}$$

If equations 4.13 are substituted in 4.16 and these are in turn substituted in equations 4.15, it will be found that equilibrium in neither of the x or y directions is satisfied. The equilibrium equations can be satisfied by introducing a term representing the effect of Poisson's ratio μ in equations 4.13 for the strains. This is achieved at the expense of coupling some of the terms in the assumed strain functions. One possible way of achieving equilibrium within the element is by taking the distribution of the strains to be given by

$$\varepsilon_x = \alpha_4 + \alpha_5\ y - \mu\ \alpha_7\ x$$

$$\varepsilon_y = \alpha_6 + \alpha_7\ x - \mu\ \alpha_5\ y \qquad (4.17)$$

$$\varepsilon_{xy} = \alpha_8$$

In this form the direct strains are linked while the shear strain is left independent. Equations 4.17 can now be substituted into 4.11 and the resulting equations are integrated to obtain the following displacement functions

$$u_x=\alpha_1 - \alpha_3\, y + \alpha_4\, x + \alpha_5\, xy - \alpha_7\, (y^2+\mu x^2)/2 + \alpha_8\, y/2$$

$$u_y=\alpha_2 + \alpha_3\, x - \alpha_5(x^2+\mu y^2)/2 + \alpha_6\, y + \alpha_7\, xy + \alpha_8\, x/2 \qquad (4.18)$$

Displacement functions in terms of polar coordinates were developed from equations 4.18 and an element stiffness matrix was derived. Full details of the matrices encountered for this element are given in [93]. The resulting element was found to be effective in analysing annular plates subjected to in-plane loading.

4.3.2 Singularity Elements

In this section the strain-based approach is used to derive element stiffness matrices for fracture analysis. The displacement functions formulated here are for the 'trapezoidal' element shown in Figure 4.2, and are due to Sabir [94]. The element has four boundaries, two of which are straight in the radial direction and the other two circular. The element is initially considered to be made up of two 'triangular' sub-regions, namely I and II, as shown in Figure 4.2. In terms of the polar coordinates system shown, the strain components for two dimensional analysis are

$$\varepsilon_r = \delta u/\delta r \tag{4.19}$$

$$\varepsilon_\theta = u/r + 1/r\ \delta v/\delta\theta \tag{4.20}$$

$$\varepsilon_{r\theta} = 1/r\ \delta u/\delta\theta + \delta v/\delta r - v/r \tag{4.21}$$

where u and v are the radial and tangential displacements defined in Figure 4.2.

If the strains are equated to zero, equations 4.19 and 4.20 can be integrated to give the following complimentary functions

$$u = \alpha_1 \sin\theta + \alpha_2 \cos\theta$$

$$v = \alpha_1 \cos\theta - \alpha_2 \sin\theta + \alpha_3 r \tag{4.22}$$

where α_1, α_2 and α_3 are independent constants of integration. Equations 4.22 represent displacements with zero strains, i.e. they represent rigid body displacements.

Particular integrals can be obtained from equations 4.19-4.21 by making suitable choices for the strains. Each 'triangular' sub-region will have six degrees of freedom, namely u and v at each node, and thus the shape function must be expressed in terms of six independent constants. Three of these are required for the rigid body displacements (equations 4.22) leaving three constants available for the strain functions. Consideration of the crack tip equations 3.1 suggest functions of the form $f(\theta)/\sqrt{r}$. The following strain functions are thus assumed

$$\varepsilon_r = (\beta_1 + \beta_2\,\theta)/\sqrt{r}$$

$$\varepsilon_\theta = (\beta_3 + \beta_4\,\theta)/\sqrt{r} \qquad (4.23)$$

$$\varepsilon_{r\theta} = (\beta_5 + \beta_6\,\theta)/\sqrt{r}$$

where β_1-β_6 are constants, only three of which must be independent. The three dependent constants are eliminated by satisfying the compatibility equations 4.19-4.21. By substituting the strain functions (equations 4.23) in equations 4.19 and 4.20, the following particular integrals are obtained

$$u = 2\,(\beta_1 + \beta_2\,\theta)\,\sqrt{r}$$

$$v = [(\beta_3 - \beta_1)\,\theta + (\beta_4 - 2\beta_2)\,\theta^2/2]\,\sqrt{r} \qquad (4.24)$$

Substituting for u, v and $\varepsilon_{r\theta}$ in the third of equations 4.23, we have

$$\beta_4 = \beta_5 = 2\beta_2 \qquad (4.25)$$

$$\beta_6 = \beta_1 - \beta_3/2 \qquad (4.26)$$

Eliminating β_4 from equations 4.24, we have

$$u = 2\,(\beta_1 + \beta_2\,\theta)\,\sqrt{r}$$

$$v = (\beta_3 - 2\beta_1)\,\theta\,\sqrt{r} \qquad (4.27)$$

Equations 4.27 can be simplified slightly by observing that:

(i) u requires an independent term containing $\sqrt{r}$ and a term containing $\sqrt{r}\,\theta$

(ii) v requires one independent term containing $\sqrt{r}\,\theta$, (as β_1 is independent of $(\beta_3 - 2\beta_1)$, if β_3 is independent).

Thus

$$u = (\alpha_4 + \alpha_5\theta)\,\sqrt{r} \qquad (4.28)$$

$$v = \alpha_6 \, \theta \, \sqrt{r}$$

The complete solutions for u and v thus become

$$u = \alpha_1 \sin\theta + \alpha_2 \cos\theta + \alpha_4 \sqrt{r} + \alpha_5 \sqrt{r}\,\theta$$

$$v = \alpha_1 \cos\theta - \alpha_2 \sin\theta + \alpha_3 r + \alpha_6 \sqrt{r}\,\theta \qquad (4.29)$$

The corresponding expressions for the strains are

$$\varepsilon_r = (\alpha_4 + \alpha_5 \theta)/2\sqrt{r}$$

$$\varepsilon_\theta = (\alpha_4 + \alpha_6 + \alpha_5 \theta)/\sqrt{r} \qquad (4.30)$$

$$\varepsilon_{r\theta} = (2\alpha_5 - \alpha_6 \theta)/2\sqrt{r}$$

Consideration of these equations indicates that ε_r and ε_θ each contain one independent constant, while $\varepsilon_{r\theta}$ is completely dependent on ε_r and ε_θ. This is the only possibility if terms of $f(\theta)/\sqrt{r}$ are to be used while satisfying the compatibility equations. It is also observed from equations 4.29 that coupling in the displacements is provided only by the rigid body terms.

Equations 4.29 are used to derive stiffness matrices for the two 'triangular' regions, shown in Figure 4.2, from

$$[K_e] = [C]^{-1,T} \int\int [B]^T[D][B] \; r \, d\theta \, dr \; [C]^{-1} \qquad (4.31)$$

Equation 4.31 is the equivalence of equation 4.1 in terms of polar coordinates and [C], [B] and [D] are as defined in section 4.2. The overall stiffness matrix for the 'trapezoidal' element shown in Figure 4.2 is obtained from those for elements I and II by a procedure described in [94]. This element was shown to be effective when combined with constant strain triangular elements in analysing LEFM problems [94].

4.4 Isoparametric Finite Elements

Early attempts at producing finite elements containing the singularity condition at the crack tip were based on classical solution functions. The full series form of the expressions for the stresses (equations 3.1-3.3) contain terms proportional to $r^{-1/2}$, $r^{1/2}$, $r^{3/2}$, etc. The first term ($r^{-1/2}$) predominates at the tip of the crack and is the basis for LEFM. This term represents the singularity in the stress distribution. The corresponding term in the displacement expressions (equations 3.1-3.3) together with the additional terms can, however, be employed as the assumed displacement field of multi-noded finite elements. In this way singular stress fields have been written such as those established by Westergaard [83], Muskhelishvili [68] and Williams [70], among others. A number of finite elements have been developed using this procedure and some of them were cited in Chapter 2.

Simpler forms of element geometry are possible and the integration of the stiffness equation is made easier when elementary polynomials, rather than classical solution functions, are employed in the formulation of elements containing singularities. One of the earliest developments to exploit this approach was that by Levy [95] who demonstrated that by degenerating a bilinear rectangle to a triangle, by coalescing two adjacent vertices, a singularity of 1/r is achieved. This order of singularity is appropriate for inelastic fracture mechanics analysis.

A simple polynomial displacement field which gives $1/\sqrt{r}$ singularity for the triangle shown in Figure 4.3 was presented by Tracey [71]. This was subsequently generalised for a family of elements by Tracey and Cook [96]. With reference to Figure 4.3, the displacement field for this element, in either coordinate direction can be expressed as

$$u = (1 - m^p)\,\delta_1 + m^p\,(1 - n)\,\delta_2 + m^p\,n\,\delta_3 \qquad (4.32)$$

The local coordinates m and n are defined such that m=1 along the edge 2-3 of the element and m=0 at node 1. The radial edges 1-2 and 1-3 correspond to n=0 and n=1 respectively. It can be shown that equation 4.32 gives representation of singularities of the order r^{-p} where r is the radial coordinate with an origin at node 1. Whereas this field preserves inter-element continuity of displacements, the resulting element stiffness matrix does not represent the constant strain conditions required for thermal stress problems.

Blackburn [97] presented a displacement field for a singular 6-noded triangular element (three nodes at the vertices and three along the sides), with a coordinate system as defined in Figure 4.3, as

$$u = \alpha_1 + \alpha_2\,m + \alpha_3\,n + (\alpha_4\,m + \alpha_5\,n + \alpha_6\,mn) \,/\, \sqrt{(m + n)} \qquad (4.33)$$

where the constants α_1-α_6 are associated with the six nodes of the element. It was shown [97] that equation 4.33 gives a linear variation of displacement along the edges which meet at the singular vertex.

It has long been recognised that the transformation from physical to isoparametric coordinates can be singular if node points along the sides of the element are positioned in a certain way. Henshell and Shaw [74], and Barsoum [75] independently perceived that this consideration could be employed to represent the singularity sought in fracture mechanics analysis. This development was employed in some of the work reported in this thesis and a somewhat detailed discussion is presented below.

Consider the case of a side of an element of length L with end nodes 1 and 3 and a mid-side node 2, as shown in Figure 4.4. Introducing the non-dimensional coordinate

$$m = -1 + 2x/L \qquad (4.34)$$

which has values of -1, 0 and 1 at nodes 1, 2 and 3, respectively, the coordinate x can be written in shape function form [98] as

$$x = -\tfrac{1}{2}\,(1-m)\,x_1 + (1-m^2)\,x_2 + \tfrac{1}{2}\,m\,(1+m)\,x_3 \qquad (4.35)$$

If we now move node 2 to the quarter-point, i.e. $x_1=0$, $x_2=L/4$ and $x_3=L$, equation 4.35 becomes

$$x = (1-m^2)\ L/4 + m\ (1+m)\ L/2 = (1+m)^2\ L/4 \qquad (4.36)$$

Equation 4.36 can be re-arranged to give

$$m = -1 + 2\ \sqrt{(x/L)} \qquad (4.37)$$

The transformation from physical to isoparametric coordinates is based upon the inverse of the matrix of derivatives of the former with respect to the latter. Differentiating equation 4.36 we have

$$dx/dm = (1+m)\ L/2 = \sqrt{(Lx)} \qquad (4.38)$$

The derivative in equation 4.38 is zero when m=-1 (or x=0). This result means that the transformation is singular at node 1.

We next examine the consequences of this singularity by expressing the displacement in terms of the shape functions given in equation 4.35 as

$$u = -\tfrac{1}{2}\ m\ (1-m)\ u_1 + (1-m^2)\ u_2 + \tfrac{1}{2}\ m\ (1+m)\ u_3 \qquad (4.39)$$

The direct strain in the x-direction is given by

$$\varepsilon_x = \delta u/\delta x = (\delta u/\delta m)\ (\delta m/\delta x) \qquad (4.40)$$

Evaluation of the above derivatives from equations 4.37-4.39 leads to the following expression for the strain

$$\varepsilon_x = -\tfrac{1}{2}\,[3/\sqrt{(xL)} - u_4/L)\,u_1 + [2/\sqrt{(xL)} - u_4/L)\,u_2$$

$$+\tfrac{1}{2}\,[-1/\sqrt{(xL)} + u_4/L)\,u_3 \qquad (4.41)$$

The strain singularity along edge 1-3 is therefore of the required order for LEFM, i.e. $1/\sqrt{r}$.

The above concept can be applied to generate both two and three dimensional finite elements. For planar conditions, the generalisation of the line (Figure 4.4) to the 8-noded quadrilateral shown in Figure 4.5 was adopted [74, 75]. In this way the strain variation along edge 1-3 is also obtained along edge 1-7 but not along rays within the element emanating from node 1. The latter condition, however, can be enforced by forming a triangular element through coalescing nodes 1, 7 and 8 of the quadrilateral element to give the element shown in Figure 4.6. In this element the mid-side nodes are again moved to the quarter points adjacent to the crack tip node 1. In this element the m and n parameters become directly related to the physical polar coordinates r and Θ, respectively.

For this element the displacement function and the strain distribution along the x-axis are respectively given as [98]

$$u = -(1-m^2)\ (2u_1 + u_3 + u_5)/4 + (1-m^2)\ (u_2 + u_6)/2$$

$$+(1-m)\ (u_1 + u_4)/2 \qquad (4.42)$$

and

$$\varepsilon_x = (2u_1 - 2u_2 + u_3 + u_5 - 2u_6)/L_1$$

$$-(3u_1 - 2u_2 + u_3 + u_4 + u_5 - 2u_6)/2\ \sqrt{(L_1 x)} \qquad (4.43)$$

with $u_1 = u_7 = u_8$.

It is found that equations 4.42 and 4.43 lead to the displacements being inter-element compatible and the resulting element reproduces constant strain conditions as well as satisfying the rigid body mode requirement.

In a finite element analysis the stress intensity factors are calculated from the displacements in the following manner. The displacement along the edge 1-3 of the triangular element of Figure 4.6 can be obtained from equations 4.37 and 4.39 as

$$u_x = u_1 + [-3u_1 + 4u_2 - u_3]\ \sqrt{(r/L)} + [2u_1 - 4u_2 + 2u_3]\ r/L \qquad (4.44)$$

In which x is replaced by the radial distance from the crack tip, r. An identical expression exists for the displacement u_y along the edge 1-3. For the mode 1 type of fracture, the

analytical expression for the u_x displacement along rays emanating from the crack tip in the vicinity of the singularity is given in equations 3.1. The stress intensity factor can then be evaluated by equating the coefficients of $\sqrt{r}$ in equations 4.44 and the fourth of equations 3.1, with θ being the polar angle of element edge 1-3. In this way the following expression is obtained

$$k_1 \cos \theta/2 \, (1 - 2\mu + \sin^2 \theta/2) = [\sqrt{2\pi}/L] \, \Omega \, (-3u_1 + 4u_2 - u_3) \tag{4.45}$$

which gives the stress intensity factor k_1 in terms of the finite element solutions for the displacements at nodes 1, 2 and 3, see Figure 4.6.

4.5 J-Integral Formulation

Considerable use of the J-integral approach is made in the work reported in this thesis to determine the stress intensity factor. This was achieved by making use of the finite element program published by Owen and Fawkes [98]. This program employs the 8-noded isoparametric element discussed in the previous section. The technique employed in this program places restrictions on the finite element mesh employed in the analysis. In particular, the crack geometry must be idealised by a radial fan of elements centred at the crack tip. This technique does not allow automatic mesh generation schemes to be employed.

In order to enable the evaluation of the J-integral along paths within the elements of the uniformly graded meshes preferred in the present work and described in Chapter 5, it was necessary to make some modifications to the Fortran code given in [98].

Consider a symmetrical rectangular path Γ, with sides along the x and y directions, enclosing the crack tip as shown in Figure 4.7. The numerical evaluation of J along this path may be simplified by observing the following considerations.

Equation 3.25 gives J as

$$J = \int_{\Gamma} (W\,dy - T\,du/dx\,ds) \qquad (4.46)$$

In this expression W is the strain energy density given by

$$W = \tfrac{1}{2} (\sigma_x \varepsilon_x + \sigma_y \varepsilon_y + \sigma_{xy} \varepsilon_{xy}) \qquad (4.47)$$

Using Hooke's law (equation 4.16), equation 4.47 may be expressed in terms of the strains as

$$W = \frac{E}{2(1-\mu^2)} (\varepsilon_x^2 + \varepsilon_y^2 + 2 \mu \varepsilon_x \varepsilon_y) + \frac{E}{4(1+\mu)} \varepsilon_{xy}^2 \qquad (4.48)$$

The strains ε_x, ε_y and ε_{xy} are expressed in terms of the displacements u_x and u_y in equations 4.11. Employing the notations

$$u_{xx} = \delta u_x / \delta x$$
$$u_{xy} = \delta u_x / \delta y$$
$$u_{yx} = \delta u_y / \delta x$$
$$u_{yy} = \delta u_y / \delta y$$

the strain energy may be expressed in terms of the displacements as

$$W = E [u_{xx}^2 + u_{yy}^2 + 2 \mu u_{xx} u_{yy}] / 2(1-\mu^2)$$

$$+ E [u_{xy}^2 + u_{yx}^2 + 2 u_{xy} u_{yx}] / 4(1+\mu) \qquad (4.49)$$

The second term of the integral in equation 4.46 is evaluated as follows

$$T_{ij} \frac{\delta u_i}{\delta x} = (\sigma_x n_1 + \sigma_{xy} n_2) \frac{\delta u_x}{\delta x} + (\sigma_{xy} n_1 + \sigma_y n_2) \frac{\delta u_y}{\delta x} \quad (4.50)$$

Using Hooke's law equation 4.50 may be re-written in terms of the displacements as

$$T_{ij} \frac{\delta u_i}{\delta x} = \frac{E}{(1-\mu^2)} [u_{xx} (u_{xx} + \mu u_{yy}) n_1 + u_{yx} (u_{yy} + \mu u_{xx}) n_2]$$

$$+ \frac{E}{2(1+\mu)} [u_{xx} (u_{yx} + u_{xy}) n_2 + u_{yx} (u_{yx} + u_{xy}) n_1] \quad (4.51)$$

Utilising equations 4.46-4.51 J is evaluated along the lines 1-2, 2-3 and 3-4 in Figure 4.7 using the following equations

Line 1-2

$$ds = dy \ , \ n_1=1 \ , \ n_2=0$$

$$J_{1-2} = \frac{E}{2(1-\mu^2)} [u_{yy}^2 - u_{xx}^2] dy + \frac{E}{4(1+\mu)} [u_{xy}^2 - u_{yx}^2] dy \quad (4.52)$$

Line 2-3

$$ds = dx \ , \ n_1=0 \ , \ n_2=1$$

$$J_{2-3} = - [E/(1-\mu^2)] [u_{yx} u_{yy} + \mu u_{xx} u_{yx}) dx$$

$$+ [E/2(1+\mu)] [u_{xx} u_{yx} + u_{xx} u_{xy}] dx \qquad (4.53)$$

Line 3-4

$$ds = dy , n_1=-1 , n_2=0$$

$$J_{3-4} = [E/2(1-\mu 2)] [3u_{xx}^2 + u_{yy}^2 + 4 \mu u_{xx} u_{yy}] dy$$

$$+ [E/4(1+\mu)] [u_{xy}^2 + 3u_{yx}^2 + 4 u_{xy} u_{yx}] dy \qquad (4.54)$$

The simplified relationships (equations 4.52-4.54) were implemented in the finite element code [98]. The total value of J is given by adding the contributions of the elements through which the integral path is chosen and the stress intensity factor is then calculated using equations 3.31.

4.6 The Finite Element Programs

The numerical analyses carried out in the work reported in this thesis were based on two finite element programs. The first is a commercial product marketed under the name PAFEC (Program for Automatic Finite Element Calculations) which was originally developed at Nottingham university [99]. The second, published by Owen and Fawkes [98], is a plane stress/strain program specifically written for analysis of fracture problems and modified during the present study to include the formulations for the J-integral described in the previous section. This program is referred to, in the present work, as STRESS.

Both programs are installed on a VAX 8650 Mainframe at the Information Technology Centre at the Polytechnic of Wales. A brief description of the main features of the programs is given in this section.

4.6.1 Program PAFEC

This is a general purpose program which enables 2- and 3-dimensional analysis of beams, plates, shells and other solid geometries [99]. The program facilitates the use of one or a combination of different finite elements developed for various applications. Amongst these applications are static, dynamic, thermal and fracture analyses. The main feature of this program is the ease with which complex

meshes are generated. Another feature is that the package provides an interactive environment which provides full graphical display of output including mesh generation and verification.

The program provides for fracture analysis using a 6-noded triangular element with the mid-side nodes adjacent to the crack tip moved to the quarter points as described in section 4.4. The program outputs the value of the stress intensity factor evaluated by the displacement approach as described in section 3.3. Another estimate of the stress intensity factor is computed from J (section 4.5) through equations 3.31. In computing J a path is taken through the elements immediately surrounding the crack tip and therefore no control on the choice of the J-integral path is provided.

The input data for this program is organised into modules and Appendix I gives a sample data file for a problem discussed in Chapter 5.

4.6.2 Program STRESS

In their book [98], Owen and Fawkes give a comprehensive treatment of the subject of fracture mechanics analysis by the method of finite elements. They include Fortran codes for a number of modules which may be employed in a finite element program. Program STRESS was assembled from a number of the above modules, some of which were extensively revised

to enable the handling of automatically generated finite element meshes, thus simplifying the task of data preparation. The equations developed in section 4.5, for J-integral calculations, were also implemented in the Fortran code. The resulting program facilitates the calculation of the stress intensity factor using all the approaches described in Chapter 3. Appendix II gives the data preparation manual for program STRESS which is available in the department of Civil Engineering and Building at the Polytechnic of Wales.

4.7 J-Integral Evaluation

The attractiveness of the J-integral approach lies in the fact that the integral is path independent and thus enables one to choose a path remote from the tip of the crack and avoid the steep gradients of the strains in that vicinity. In the determination of J by the finite element method, therefore, it may be considered unnecessary to employ special elements at the crack tip which more accurately characterise the singularity conditions there. In practice, however, the path independency of J cannot always be guaranteed. This appears to be influenced by the finite element mesh employed. Considerably smaller elements are required near the crack tip and many workers have used element topologies requiring a considerable amount of data preparation. It is clearly advantageous to be able to use uniformly graded meshes which can be generated automatically. In the absence of analytical solutions, for guidance, it is necessary to carry out convergence studies before reliance on the results can be assumed. It is felt that this can only be effectively made by the employment of uniform meshes.

Sabir [100] carried out a detailed study on the use of the J-integral approach for determining the stress intensity factor. This was done by analysing several basic geometries such as the Single Edge Cracked Specimen (SECS) shown in Figure 4.8. The analytical solution for this geometry can be written in the form

$$k_1 = \gamma \sigma_o \sqrt{(\pi a)} \qquad (4.55)$$

where γ is a correction factor applied to the solution of the stress intensity factor for an infinite plate given by equation 3.9. The solution for γ as a function of a/d, where d is the width of the plate, is given as [26]

$$\gamma = 1.12 - 0.231\ a/d + 10.55\ (a/d)^2$$

$$- 21.72\ (a/d)^3 + 30.39\ (a/d)^4 \qquad (4.56)$$

This solution is due to Brown and Srawley [101] and is accurate to within 0.5% for $a/d \leq 0.6$.

Numerical solutions were obtained for the SECS using 8-noded plane stress isoparametric elements. Three finite element idealisations were considered. In the first a regular mesh, i.e. one with identical size elements, employing standard isoparametric elements was used. The second solution utilised the same mesh with singularity elements (mid-side nodes moved to the quarter points) either side of the crack tip. The third analysis employed a graded mesh in which the size of the elements was made progressively smaller as the crack tip was approached. One such mesh (8 by 8 elements) is shown in Figure 4.8b.

Having obtained the J values using the above idealisations, the stress intensity factor and corresponding correction

factors were obtained from equations 3.31 and 4.55. The convergence characteristics for the case a/d = 0.5 are given in Figure 4.9a. In general good convergence is obtained using regular meshes of 8 by 8 or smaller. Improvement in the results is obtained by employing graded meshes with smaller elements in the vicinity of the crack tip.

Variation of γ with the radial distance, averaged for the contours enclosing the crack tip, is shown in Figure 4.9b. Here r is defined as the average distance from the crack tip to the lines describing the half contour. The results demonstrate that path independency of the J-integral can be confirmed using the crack tip elements in the present analysis. Finally, the effect of a/d on the correction factor γ is shown in Figure 4.9c. It is evident that, except for very small cracks, good agreement with the analytical solution of equation 4.56 is obtained.

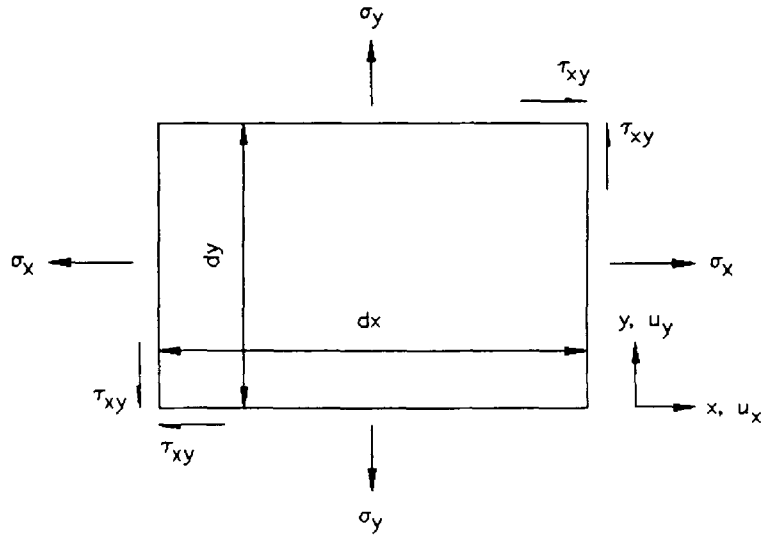

Figure 4.1 Two Dimensional Rectangular System of Coordinates.

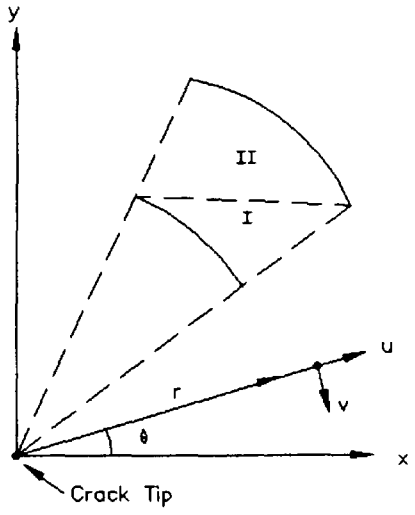

Figure 4.2 The Singularity Elements Due to Sabir [94].

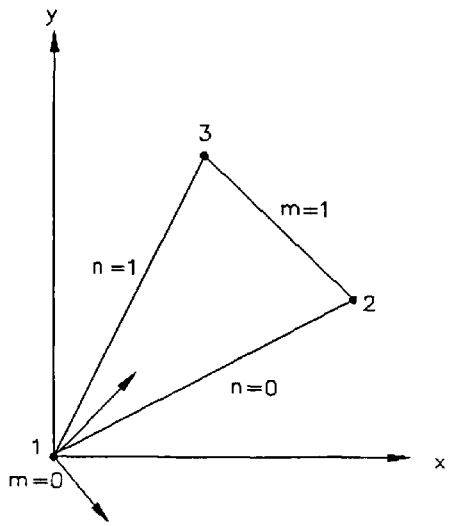

Figure 4.3 Triangular Isoparametric Element with Singularity at Node 1.

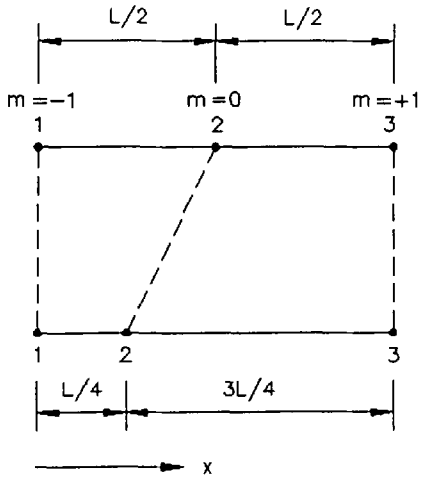

Figure 4.4 Uniaxial Isoparametric Coordinates.

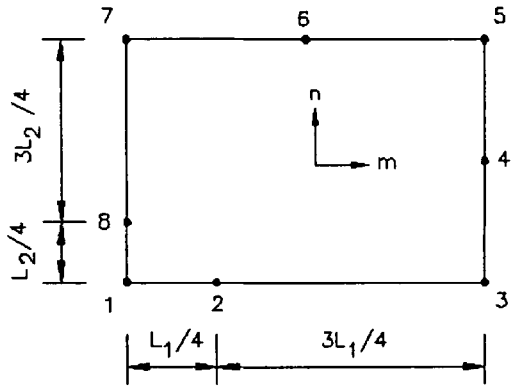

Figure 4.5 Rectangular Isoparametric Element with Side Nodes at the Quarter-Points.

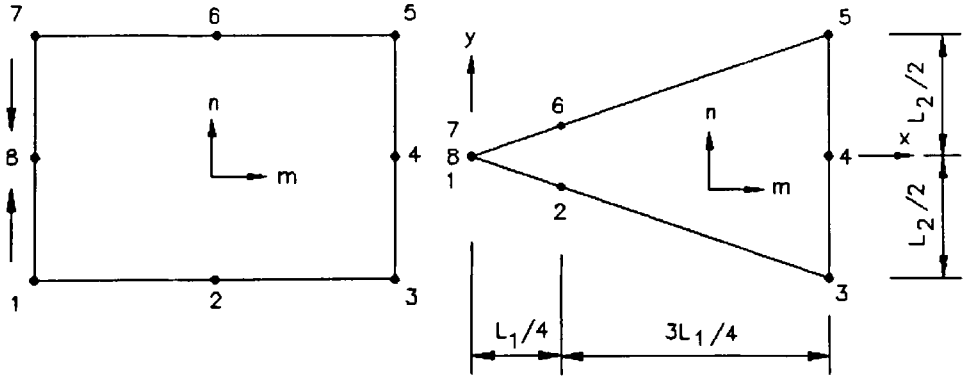

Figure 4.6 Triangular Isoparametric Element with Side Nodes at the Quarter-Points.

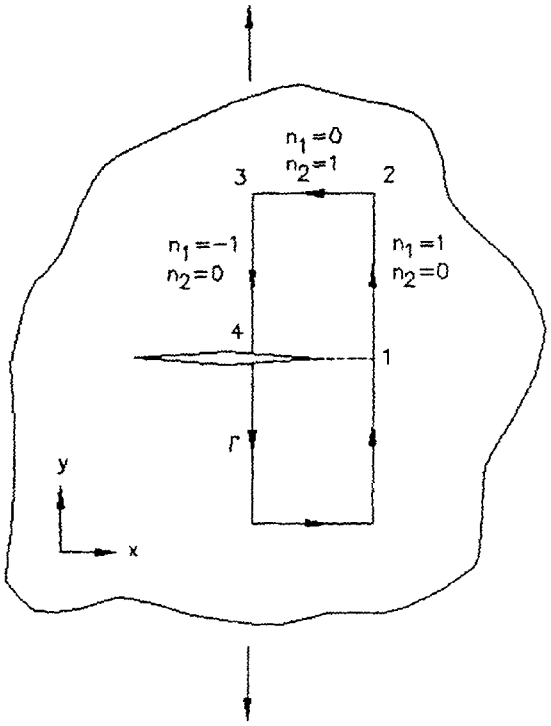

Figure 4.7 Rectangular J-Integral Path Enclosing the Crack Tip.

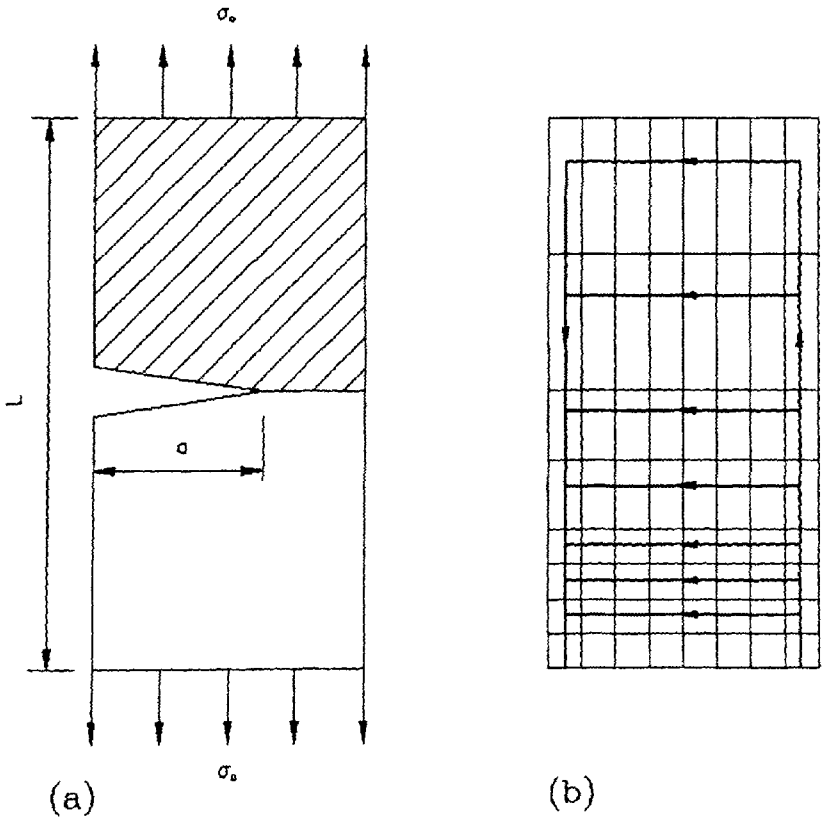

Figure 4.8 (a) The Single Edge-Cracked Specimen. (b) Finite Element Mesh and J-Integral Paths for Half the Specimen.

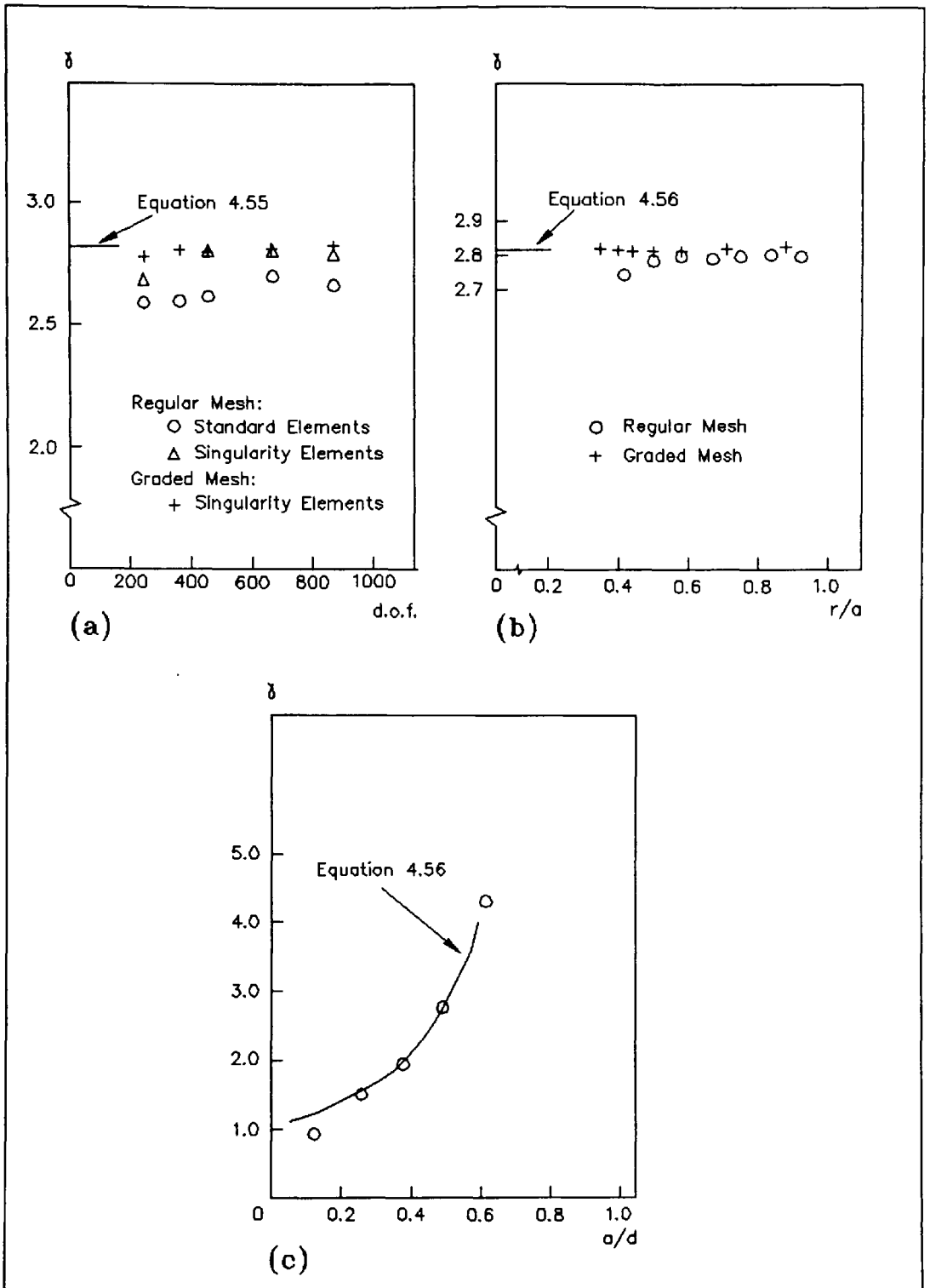

Figure 4.9 (a) Convergence of Correction Factor δ .
(b) Variation of δ with Radial Distance of the J-Contour from the Crack Tip.
(c) Variation of δ with Crack Size.

CHAPTER FIVE

FINITE ELEMENT ANALYSIS OF THE COMPACT COMPRESSION SPECIMEN

5.1 Introduction

The double edge notched cube geometry for fracture toughness evaluation of concrete materials was first proposed by Barr et al [39]. Later Sabir and Barr [94] carried out finite element analysis of the specimen to determine the stress intensity factors for a number of crack geometries. This was done using a displacement approach and the special crack tip elements [102] cited in Chapter 3. Although this approach gives accurate estimates for the stress intensity factor, it was suggested [103] that in cases when the stress distribution is required or when evaluating other fracture parameters such as energy release rates or J-integrals, it would be more economical to use isoparametric representations. This chapter gives the results of a detailed study of the specimen using triangular and rectangular isoparametric elements. Details of these elements and the special crack tip elements which contain the required singularity together with the finite element programs used were given in Chapter 4. As all the problems considered in the remainder of the thesis are predominantly of the opening mode of fracture, the stress intensity factor will be simply referred to by k.

5.2 Description of the Specimen Geometry

The specimen is a 100 mm or 150 mm cube modified by the introduction of two central notches on opposite faces and loaded eccentrically as shown in Figure 5.1. The attractiveness of this specimen lies in the fact that it is based on standard quality control samples requiring little additional preparation and that the test is simple to perform. In the actual test the load is applied via two 5 mm square steel bars placed along the edges of the specimen. It was observed that as the test was conducted the load was concentrated on the inner edges of the loading bars. This loading position was used in the numerical analysis.

The specimen has similarities in terms of both geometry and loading with that of the compact tension specimen used in fracture toughness testing and is therefore referred to as the Compact Compression Specimen (CCS).

5.3 Stress Analysis

The main objective of the geometry under consideration is to produce a suitable test for determining the fracture toughness of concrete materials. This depends on sufficiently large tensile stresses being developed at the root of the notch remote from the loading. This is clearly influenced by the size of the notches (a and c) introduced into the specimens. Although in most of the tests carried out in this study the specimens failed in the opening mode of fracture, it was considered desirable to confirm the existence of such stresses by numerical analysis.

Finite element analysis of a 100 mm cube containing two symmetrical cracks of lengths 30 mm (i.e. a=c=30 mm) was carried out using the program PAFEC [99] described in Chapter 4. For stress intensity factor evaluation the program allows the use of triangular elements only and taking advantage of symmetry, these were employed to model half the specimen as shown in Figure 5.2. The element has three corner nodes and three mid-side nodes with two degrees of freedom (d.o.f.), namely u_x and u_y, prescribed at each node. The middle nodes of the sides with a common corner node at the tip of the crack were moved to the quarter points to yield the $1/\sqrt{r}$ singularity pertaining to the crack tip. Plane strain conditions were assumed, with E=30 kN/mm^2 and Poisson's ratio μ=0.2. The symmetry condition was achieved by supporting the uncracked ligament on rollers as shown in Figure 5.2, i.e. by restraining the uncracked

ligament in the y-direction. The specimen was subjected to a unit load applied at the node which is 5 mm away from the edge. To simulate no slipping between the steel loading bars and the specimen, a horizontal restraint was imposed at the loading point.

5.3.1 Finite Element Idealisation

The finite element mesh generation for the half-specimen shown in Figure 5.2 was developed by dividing the area into 10 blocks as shown in Figure 5.3. Each block is automatically subdivided into triangular elements. In the analysis only the root of the notch remote from the loading was specified as a crack tip and the area in this vicinity was represented by a fine mesh of elements.

The use of element blocks not only reduces the amount of data required to generate the finite element mesh, but also provides a facility for implementing different element subdivisions for convergence studies. Using this approach, two meshes were generated, namely a coarse mesh with 220 elements and 952 d.o.f. and a fine mesh with 880 elements and 3664 d.o.f. Figure 5.4 gives the details of the fine mesh in which the elements on either side of the crack tip in the tensile zone had sizes of a/18 and a/24, where 'a' is the crack size. Appendix I gives the data file used to generate this mesh. This data file contains all the modules required for the complete solution of this problem.

5.3.2 Stress Distribution

The deformed finite element mesh (obtained from the coarse mesh analysis for clarity) and contours of the σ_y stress (in N/mm^2) normal to the crack, are shown in Figures 5.5a and 5.5b respectively. By examination of the stress contours in Figure 5.5b it is evident that tension zones develop around the crack tip remote from the loading. As expected larger compressive stresses are developed under the load and in the vicinity of the root of the notch below the load. The maximum and minimum stresses, as obtained from the stress contours, together with their approximate locations are given in Table 5.1. These give a ratio of maximum compressive σ_y stress under the load to maximum tensile σ_y stress near the crack tip (in the tension zone) of 2.5. The corresponding principal stress ratio is 2.4. These conditions demonstrate that, for this geometry, if failure is to occur as the applied load is increased, then this will take place in a tensile mode normal to the crack.

Figure 5.6 gives the results for the σ_y stress and the shear stress σ_{xy} along the crack line of the specimen. It is clear that σ_y is the dominant stress along the uncracked ligament and that σ_{xy} almost vanishes along this line. This shows that the specimen will fail in an entirely tensile (opening) mode and that the sliding mode of fracture does not make a significant contribution to the eventual failure. The results also demonstrate the asymptotic behaviour of the stress as the crack tips are approached. All the stresses

are given for a unit applied compressive load and can be factored for any other load.

5.3.3 Evaluation of Stress Intensity Factor

5.3.3.1 Displacement Extrapolation (DE)

It is well established that the most reliable estimates for the stress intensity factor are given by extrapolation of the results obtained from the y-displacements of the free surface of the crack. Equation 3.1 can be re-arranged to give

$$k = 2\Omega\ (2\pi/r)^{\frac{1}{2}}\ f_1^{-1}\ (\mu,\Theta)\ u_y \qquad (5.1)$$

where f_1 is a function of Poisson's ratio μ and the angular coordinate Θ as given in the fifth of equations 3.1. Equation 5.1 was employed to evaluate the stress intensity factor k at points along the line $\Theta = 180°$ (see figure 5.7) using the results obtained from the coarse and fine mesh analyses. The results are shown as a function of the radial distance from the crack tip in Figure 5.7. It is seen that if the values near the crack tip are disregarded, then the results approach a line of constant slope. By extrapolation to the crack tip i.e. r=0, estimates for k of 116.2 $m^{-3/2}$ and 120.0 $m^{-3/2}$ per unit load are obtained from the coarse and fine mesh analyses respectively.

5.3.3.2 Conic Section Simulation (CSS)

The CSS method described in Chapter 3 was next employed to obtain the stress intensity factor k. For plane strain conditions it can be shown that k is given by

$$k = \frac{bE}{2a\ (1-\mu^2)} \sqrt{(\pi a)} \qquad (5.2)$$

where

$$b = \frac{u_y}{(1 - x^2/a^2)^{\frac{1}{2}}} \qquad (5.3)$$

'a' and 'b' being the semi-major and semi-minor axes of the elliptic surface respectively. Figure 5.8 shows the variation of the stress intensity factor along the crack surface as obtained from the two mesh idealisations. It is clear that the results do not give a constant value and that by extrapolation of the results to x=a, estimates for the stress intensity factor which are close to those obtained by the DE process are obtained. A similar behaviour was obtained in [87] for an edge-cracked plate subjected to uniform tension.

Table 5.2 summarises the results for the stress intensity factor obtained from the two mesh idealisations together with those obtained in the previous section.

5.4 Stress Intensity Factors

The performance of the 8-noded quadrilateral isoparametric elements in obtaining stress intensity factors was demonstrated in Chapter 4. There, it was shown that accurate estimates for k can be obtained for standard geometries using the J-integral approach by employing relatively coarse meshes. Considerable improvement in the results was obtained by moving the mid-side nodes of the crack tip elements to the quarter points. In the remainder of this chapter detailed assessment of the performance of isoparametric elements in evaluating k is carried out. The half-specimen shown in Figure 5.2 was analysed using two types of meshes. In the first, the crack geometry was idealised by a fan arrangement of elements encircling the crack tip as shown in Figure 5.9. This idealisation results in a relatively coarse mesh having 44 elements and 326 d.o.f. In order to facilitate the use of this mesh for analysis of several geometries with varying notch depths, both crack tips were enclosed by 5 mm square elements which were surrounded by progressively larger elements arranged in a fan-like pattern. While such an approach allows some control over the number of elements employed and the choice of element sizes throughout the geometry, it places a considerable restriction on the mesh topology particularly when automatic mesh generation schemes are to be employed. Nevertheless, the mesh shown in Figure 5.9 can be used for analysing geometries with the crack in the tension zone varying

between 25 mm and 40 mm. Appendix III gives the data file for the fan mesh arrangement with a=c=30 mm.

In the second type of mesh, an arrangement of regular rectangular elements as shown in Figure 5.10 was employed. This idealisation results in 55 elements and 396 d.o.f. representing one half of the specimen. The mesh was progressively refined as the elements approached the crack tip in the tension zone. The size of elements in the x- and y-directions, with increasing distance from the crack tip in the tension zone, were chosen in the ratios a/30, a/15, a/5, and a/3. Several notch geometries were considered and Figure 5.10 gives the finite element idealisation for the case a=c=30 mm. The data file for this problem is given in Appendix IV.

In order to carry out convergence studies the analysis was repeated for three other mesh idealisations with element sizes according to the ratios

a/15, a/5, a/3 (36 elements, 270 d.o.f.)

a/60, a/30, a/15, a/5, a/3 (78 elements, 546 d.o.f.)

a/100, a/60, a/30, a/15, a/5, a/3 (105 elements, 720 d.o.f.).

The above idealisations were implemented by the use of an automatic mesh generation scheme which was incorporated in

the finite element program STRESS, discussed in Chapter 4. In this way the data preparation work was greatly reduced over that required for generating the fan mesh discussed earlier. This is apparent when comparing the two data files given in Appendices III and IV. Although this approach offers little control over the choice of element numbers and sizes, this did not prove to be of considerable disadvantage as accurate estimates for k could be obtained using relatively coarse meshes. This was particularly true when using evaluation methods which do not rely on raw data for points near the crack tip.

5.4.1 Convergence Studies

Several solutions for the geometry analysed in section 5.3 were obtained using the idealisations described in the previous section. The stress intensity factor was evaluated using all of the methods outlined in Chapter 3, i.e. DE, CSS, SERR and the J-integral. The results for the stress intensity factor are summarised in Table 5.3. Figure 5.11 gives the variation of the stress intensity factor with the radial distance from the crack tip. It can be seen that, within the limits of accuracy imposed by the DE method, the extrapolated results for the stress intensity factor from the regular mesh idealisations are all in agreement with that obtained in section 5.3.3, Table 5.2. However considering the most accurate estimate to be 120.0 $m^{-3/2}$ per

unit load, the result yielded by the fan mesh analysis (Table 5.3) is an underestimate which is 4.8% in error.

Figure 5.12 gives the stress intensity factor as obtained by the CSS method. Here again the results do not give a constant value and an extrapolation process is necessary. Although the regular meshes yield acceptable values, the extrapolated result obtained from the fan mesh analysis is now 9.2% in error. It is clear that for this geometry there is no advantage in evaluating the stress intensity factor by the CSS method.

In Figure 5.13 the results obtained by the SERR and J-integral methods are presented as a function of the total number of d.o.f. used in analysing half the specimen and employing the various regular mesh idealisations. The result of the DE method obtained in section 5.3 (Table 5.2) using triangular isoparametric elements is also indicated. It can be seen that the estimates for the stress intensity factor rapidly converge to that obtained by the DE method irrespective of whether the SERR or J-integral approach is used. Both approaches yield results with less than 1% error using 720 d.o.f.

5.4.2 Variation of the Stress Intensity Factor with Notch Geometry

The SERR and J-integral approaches were employed to examine the relationship between the stress intensity factor and the size of the notches. Solutions were obtained for specimens with notch sizes in the tensile zone ranging between a=25 mm and a=40 mm in increments of 5 mm. The size of the notch in the compressive zone was varied between c=20 mm and c=40 mm, in increments of 5 mm. In all the analyses a unit compressive load was applied and the results for k obtained by employing the various regular mesh idealisations are given in Tables 5.4-5.7.

Convergence curves for the stress intensity factor are presented in Figure 5.14. It can be seen that for all the cases considered both approaches yield results which converge rapidly. Using a relatively small total number of d.o.f., accurate estimates for the stress intensity factors are obtained.

The variation of the stress intensity factor with the size of the notch in the tension zone is shown in Figure 5.15 for c=20, 25, 30 and 35 mm. The indicated values are those obtained from analyses employing the fine mesh with 105 elements and 720 d.o.f. It is seen that for all a/d ratios considered, the SERR and J-integral methods yield results which are in close agreement. These results enabled expressions to be found which give the stress intensity

factor k as a function of the a/d ratio. In the case of the symmetrically notched specimens the following expressions were obtained

SERR method

$$k = \frac{P}{t\, d^{\frac{1}{2}}} [-87.5(a/d)^{1/2} + 952.0(a/d)^{3/2} - 3405.8(a/d)^{5/2} + 4273.2(a/d)^{7/2}] \qquad (5.4)$$

J-integral method

$$k = \frac{P}{t\, d^{\frac{1}{2}}} [-108.1(a/d)^{1/2} + 1147.1(a/d)^{3/2} - 4016.8(a/d)^{5/2} + 4901.1(a/d)^{7/2}] \qquad (5.5)$$

Both expressions give estimates for k which are within 1% of the finite element results.

The results for the stress intensity factors presented in this section will be employed in the laboratory tests, reported in Chapters 7 and 8, for evaluating the fracture toughness of concrete.

5.5 Conclusions

In this chapter detailed finite element analyses of the Compact Compression Specimen (CCS) using triangular and quadrilateral isoparametric elements were carried out. The results for the stresses in a specimen with a=c=30 mm, using triangular isoparametric elements incorporated in a commercially available program (PAFEC), demonstrated that the test specimen fails in a predominantly tensile (opening) mode of fracture and that the sliding mode does not make a significant contribution. The stress intensity factor was evaluated by the two methods, i.e. the displacement extrapolation (DE) and conic section simulation (CSS) methods, using two mesh idealisations. In the first idealisation half the specimen was represented by 220 triangular elements and in the second the number of elements was 880. These idealisations resulted in a total number of d.o.f. of 952 and 3664, respectively. Using the DE method, the estimates for the stress intensity factor obtained from the two analyses were within 3% of each other. It was found that the CSS method did not give constant values for the stress intensity factor and in order to obtain reasonable estimates an extrapolation process was necessary.

The performance of the quadrilateral isoparametric element was next examined. Using program STRESS, outlined in Chapter 4, the above problem was analysed using two types of mesh idealisations. In the first, the mesh was generated manually with the elements around the crack tip arranged in a fan-

like pattern. In the second an arrangement of regular rectangular elements was employed. The regular meshes were generated automatically using a mesh generation scheme which was coded into program STRESS. Using the latter type of idealisation it was possible to analyse the problem using several meshes with ease. Using a regular mesh the results for the stress intensity factor demonstrated that the DE method yields similar accuracy to that obtained by employing the triangular elements using about 300 d.o.f. The result obtained using a fan-like mesh was 9.2% in error for a similar total number of d.o.f.

Convergence studies were carried out by analysing the problem using four regular mesh idealisations with a total number of d.o.f. ranging between 270 and 720. The stress intensity factor was computed using all of the methods described in Chapter 3. Rapid convergence was obtained in all cases and in particular, using 720 d.o.f., the SERR and J-integral methods yielded values which were less than 1% in error when compared to that obtained using triangular elements with 3664 d.o.f.

Convergence studies were also carried out for a further sixteen geometries of the CCS. In these the notch size in the tension zone was varied between 25 mm and 40 mm and that in the compression zone varied between 20 mm and 40 mm. Again rapid convergence of the results for the stress intensity factor was obtained for all the geometries considered using both the SERR and J-integral methods.

Finally the effect of the notch size on the stress intensity factor was examined. In all cases, the stress intensity factor increased with increasing notch size. Two expressions for the stress intensity factor as a power series in a/d were developed for the symmetrically notched specimens using the results obtained from the SERR and J-integral methods. Both expressions yield values for the stress intensity factor which are within 1% of their numerical (finite element) values.

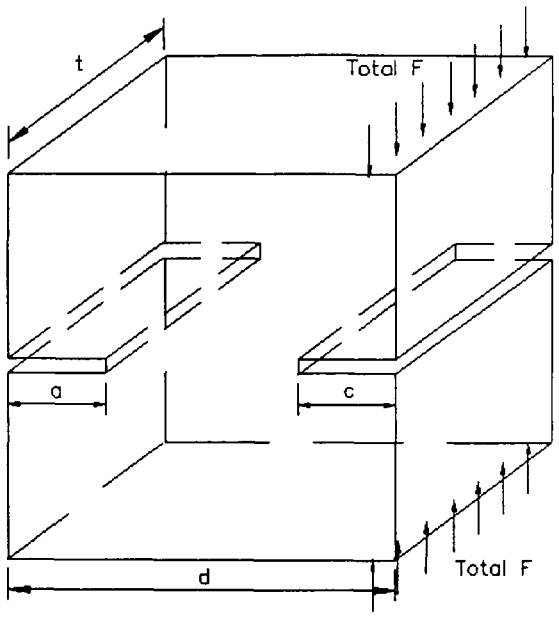

Figure 5.1 The Compact Compression specimen (CCS).

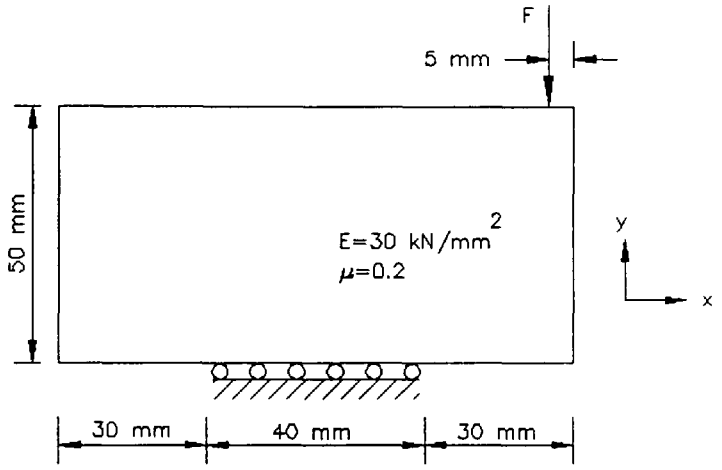

Figure 5.2 The Half-Specimen Analysed (CCS).

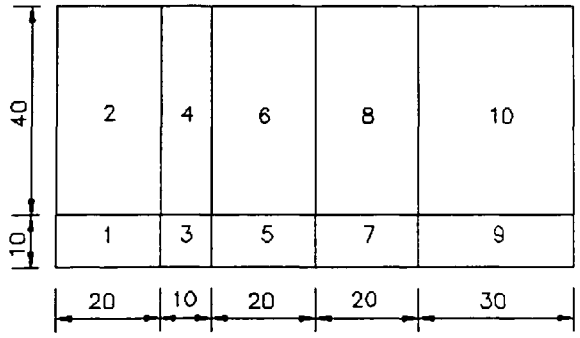

Figure 5.3 Element Blocks Used in Analysing Half the Specimen (CCS). All Dimensions are in mm.

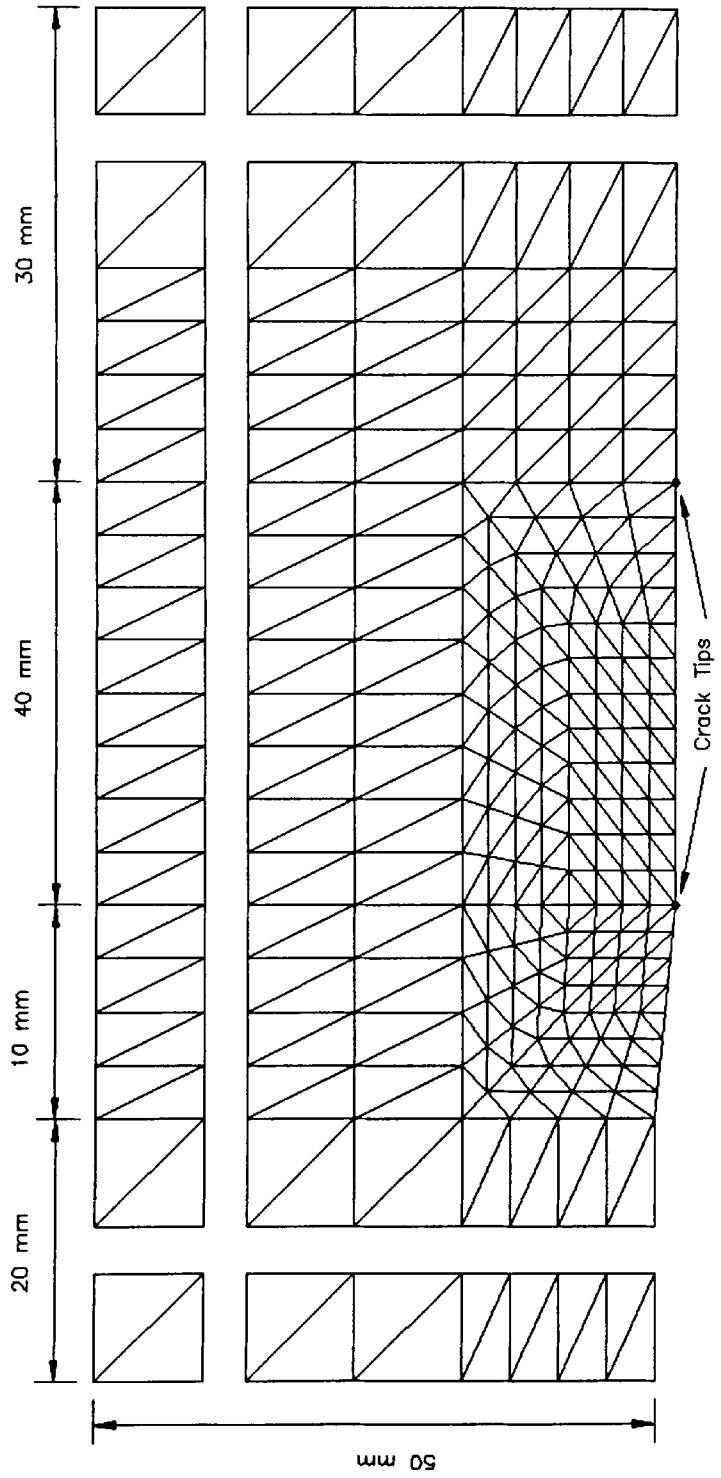

Figure 5.4 Finite Element Mesh for the Half-Specimen Using 880 Triangular Elements (3664 d.o.f.).

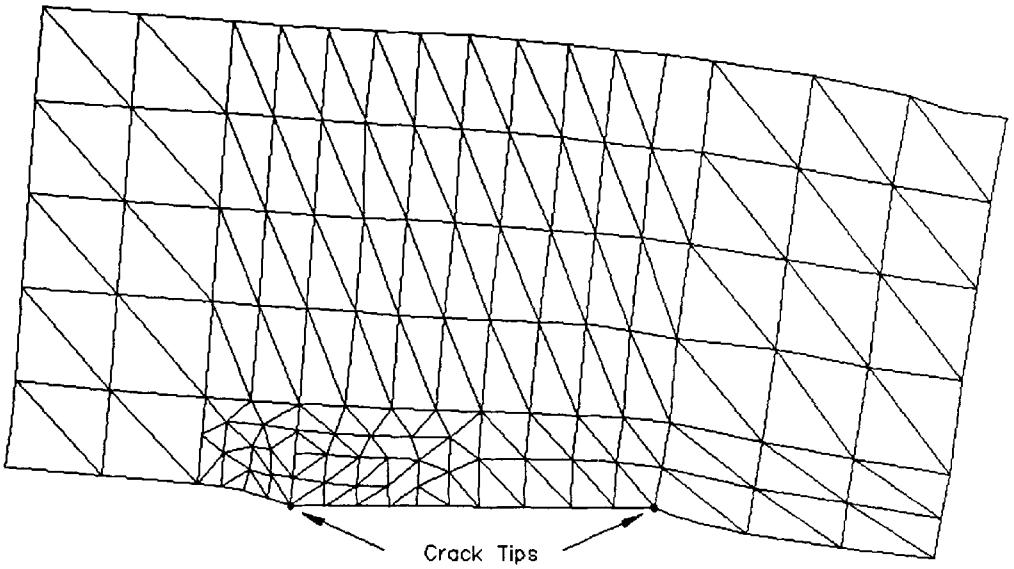

(a)

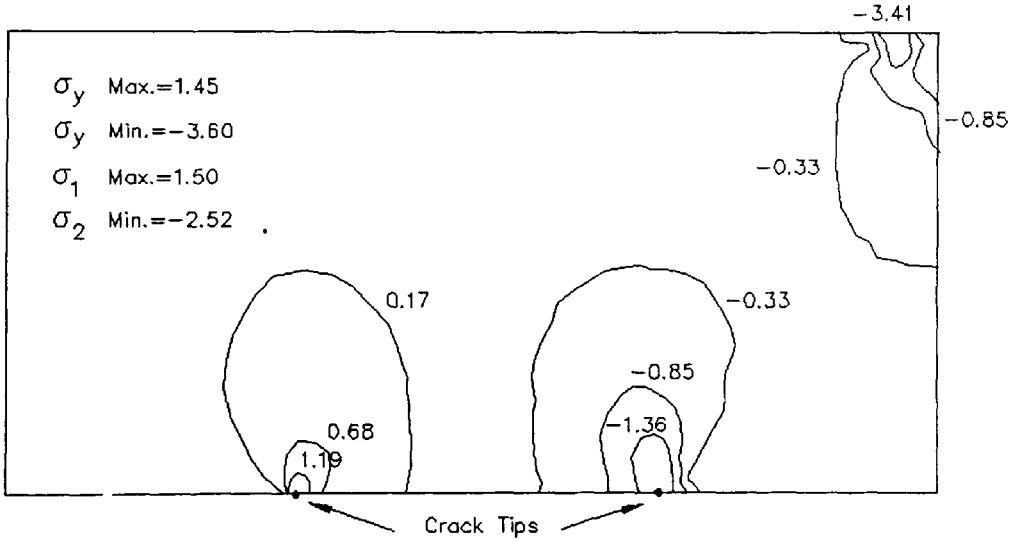

(b)

Figure 5.5 (a) Deformed Shape for CCS Using 220 Triangular Elements (952 d.o.f.).
(b) Contours of σ_y ($N/mm^2 x10^{-3}$) for Unit Applied Load.

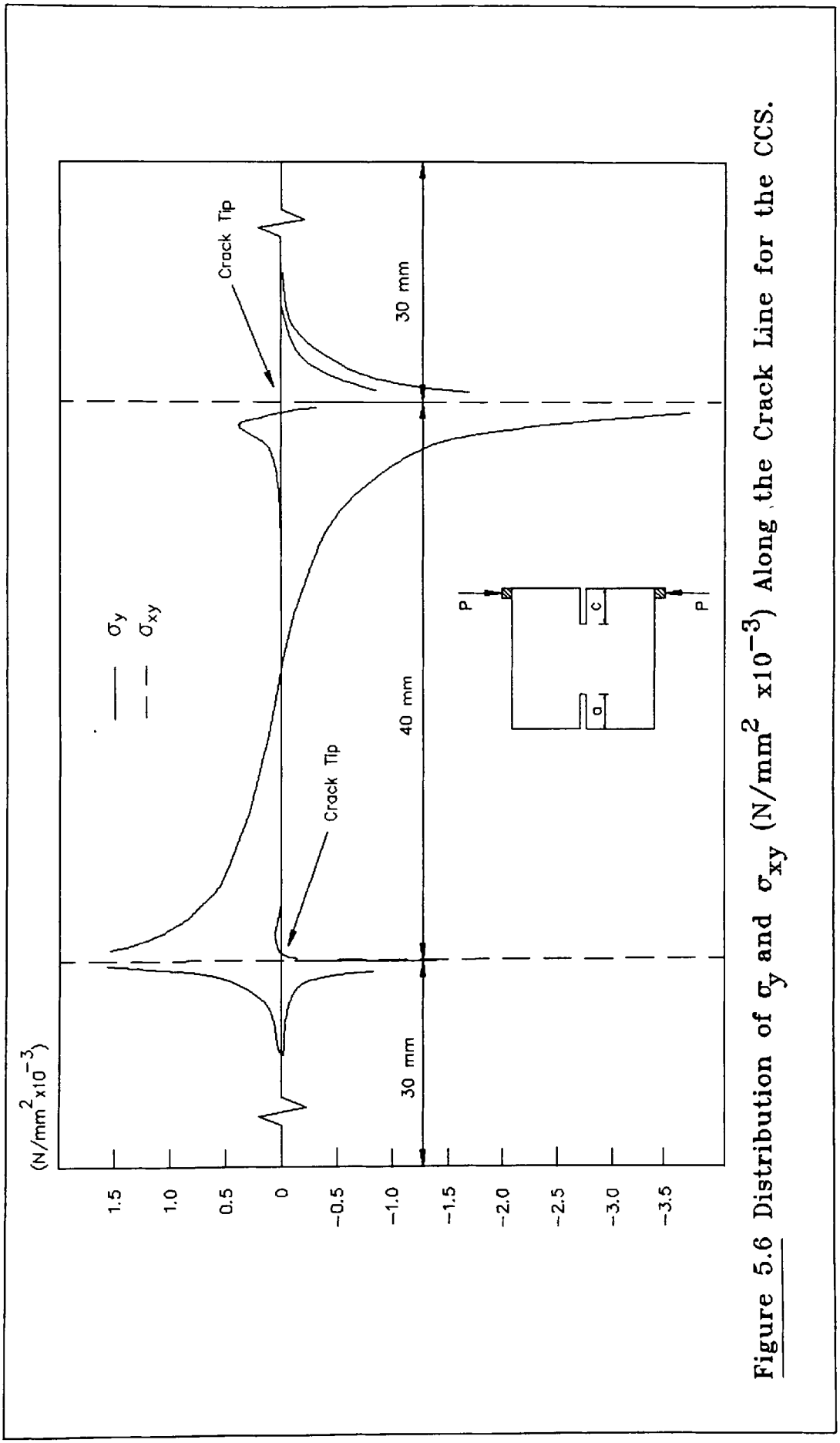

Figure 5.6 Distribution of σ_y and σ_{xy} (N/mm^2 $x10^{-3}$) Along the Crack Line for the CCS.

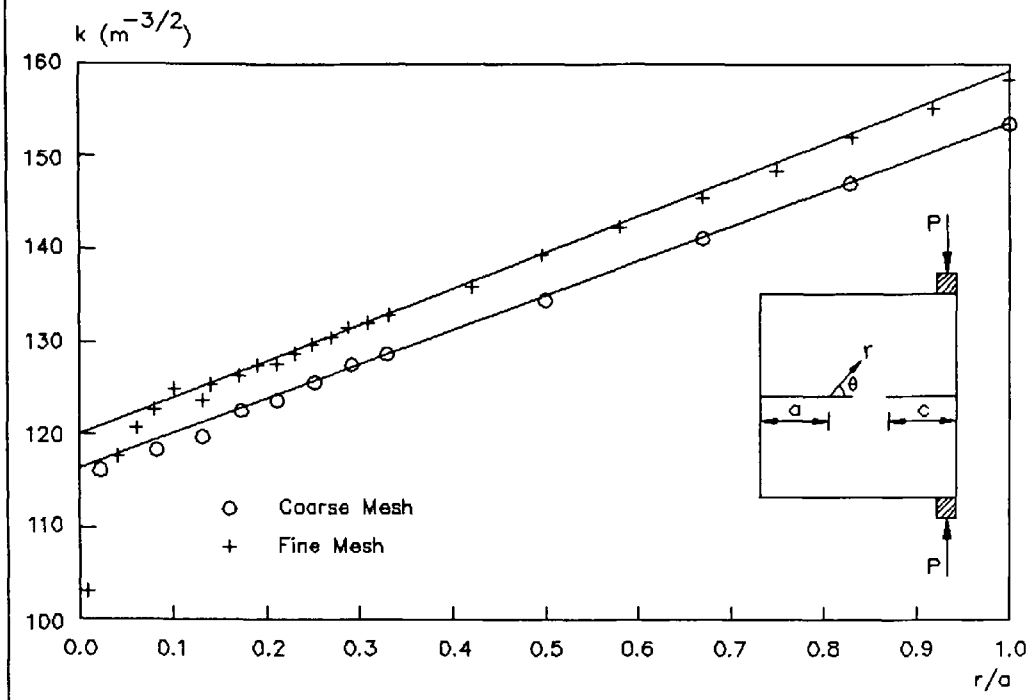

Figure 5.7 Variation of k with Radial Distance from the Crack Tip (CCS, a=c=30 mm) - Triangular Elements.

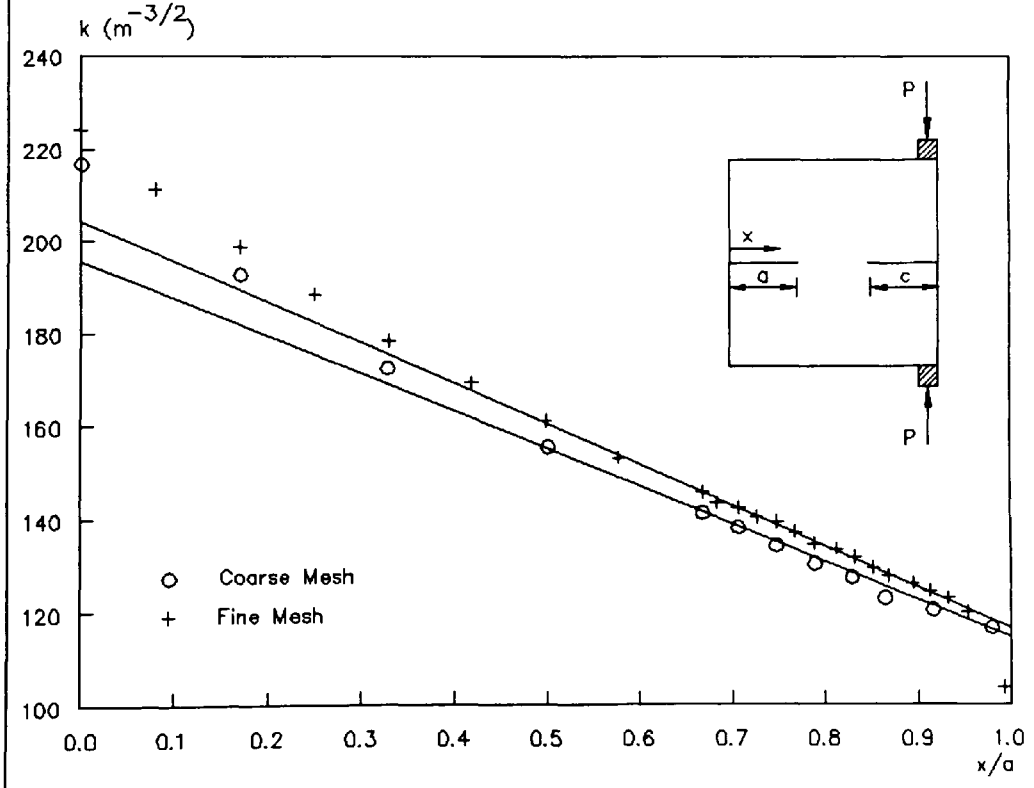

Figure 5.8 Variation of k with x/a (CCS, a=c=30 mm) - Triangular Elements.

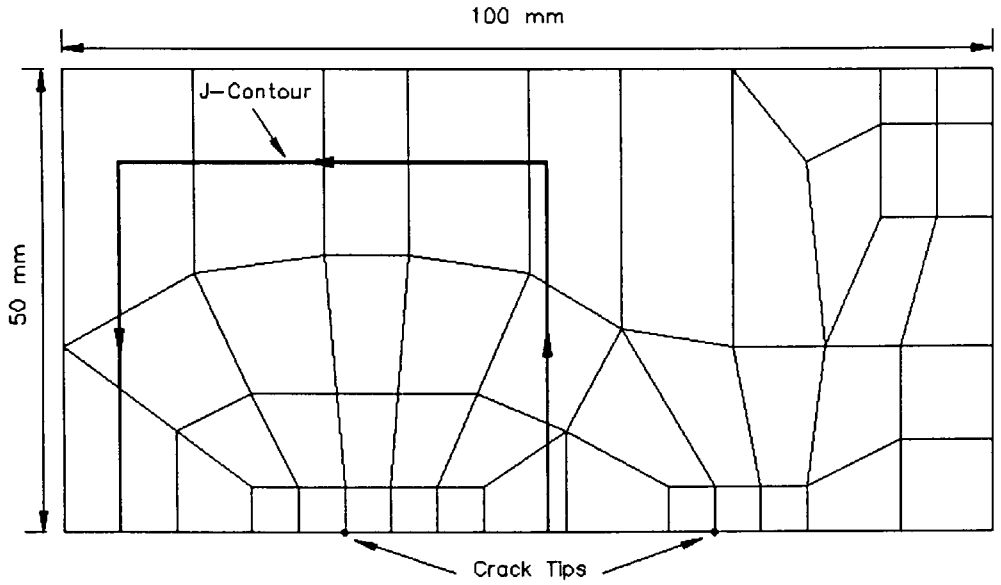

Figure 5.9 Finite Element Mesh for the Half-Specimen Using 44 Quadrilateral Elements (326 d.o.f.).

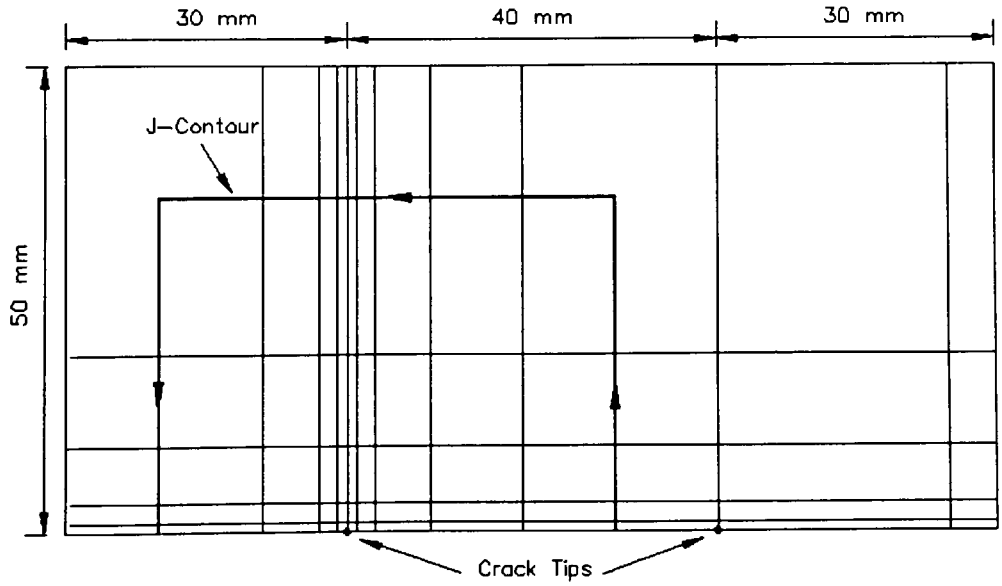

Figure 5.10 Finite Element Mesh for the Half-Specimen Using 55 Rectangular Elements (396 d.o.f.).

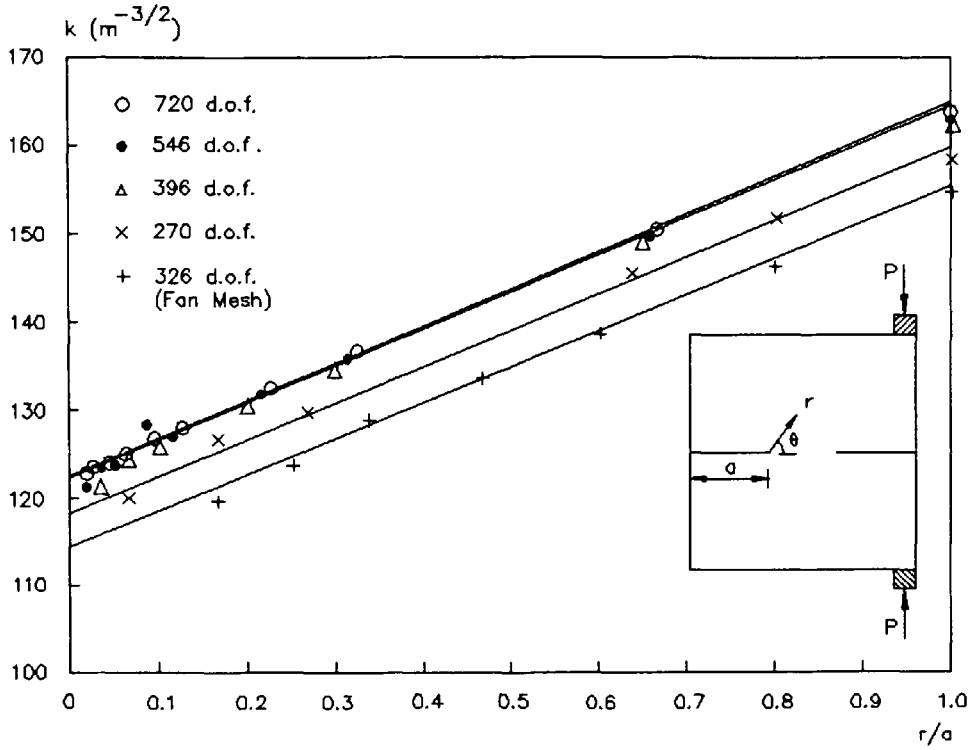

Figure 5.11 Variation of k with Radial Distance from the Crack Tip (CCS, a=c=30 mm) - Quadrilateral Elements.

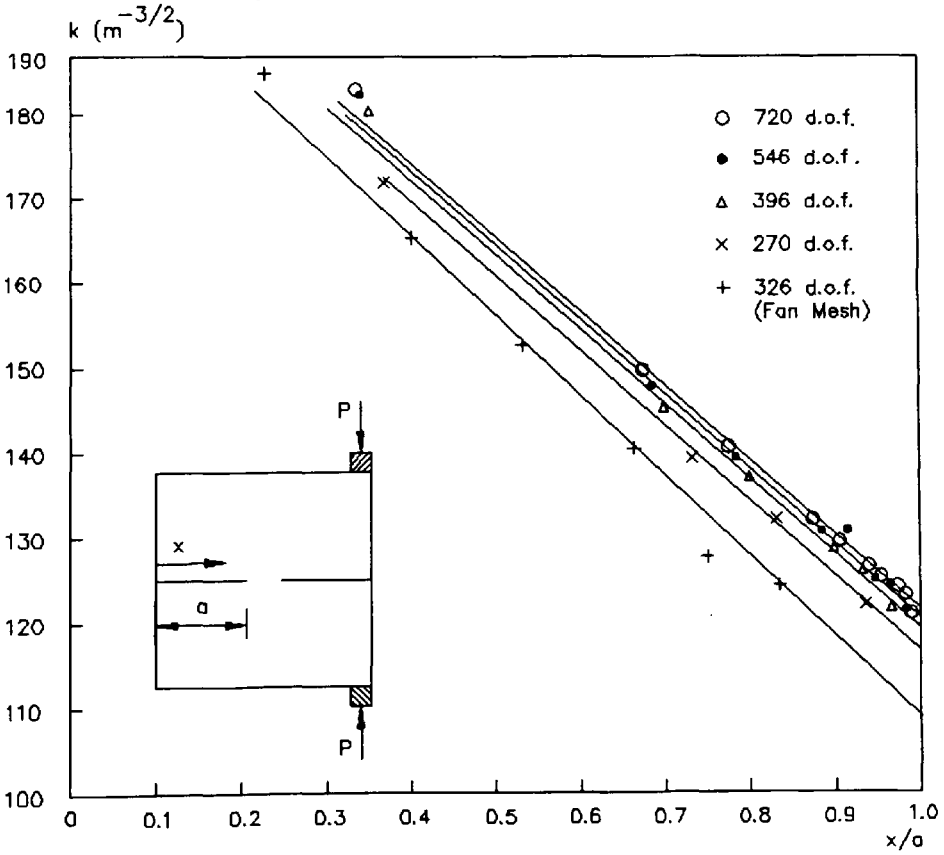

Figure 5.12 Variation of k with x/a (CCS, a=c=30 mm) - Quadrilateral Elements.

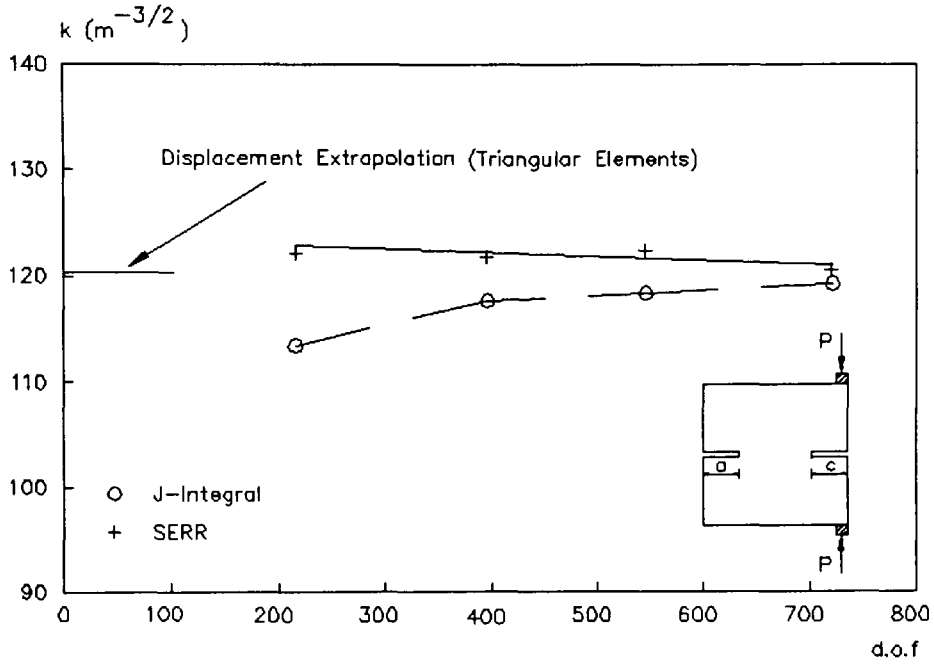

Figure 5.13 Convergence Curves for k (CCS, a=c= 30 mm) Using SERR and J-Integral Methods - Rectangular Elements.

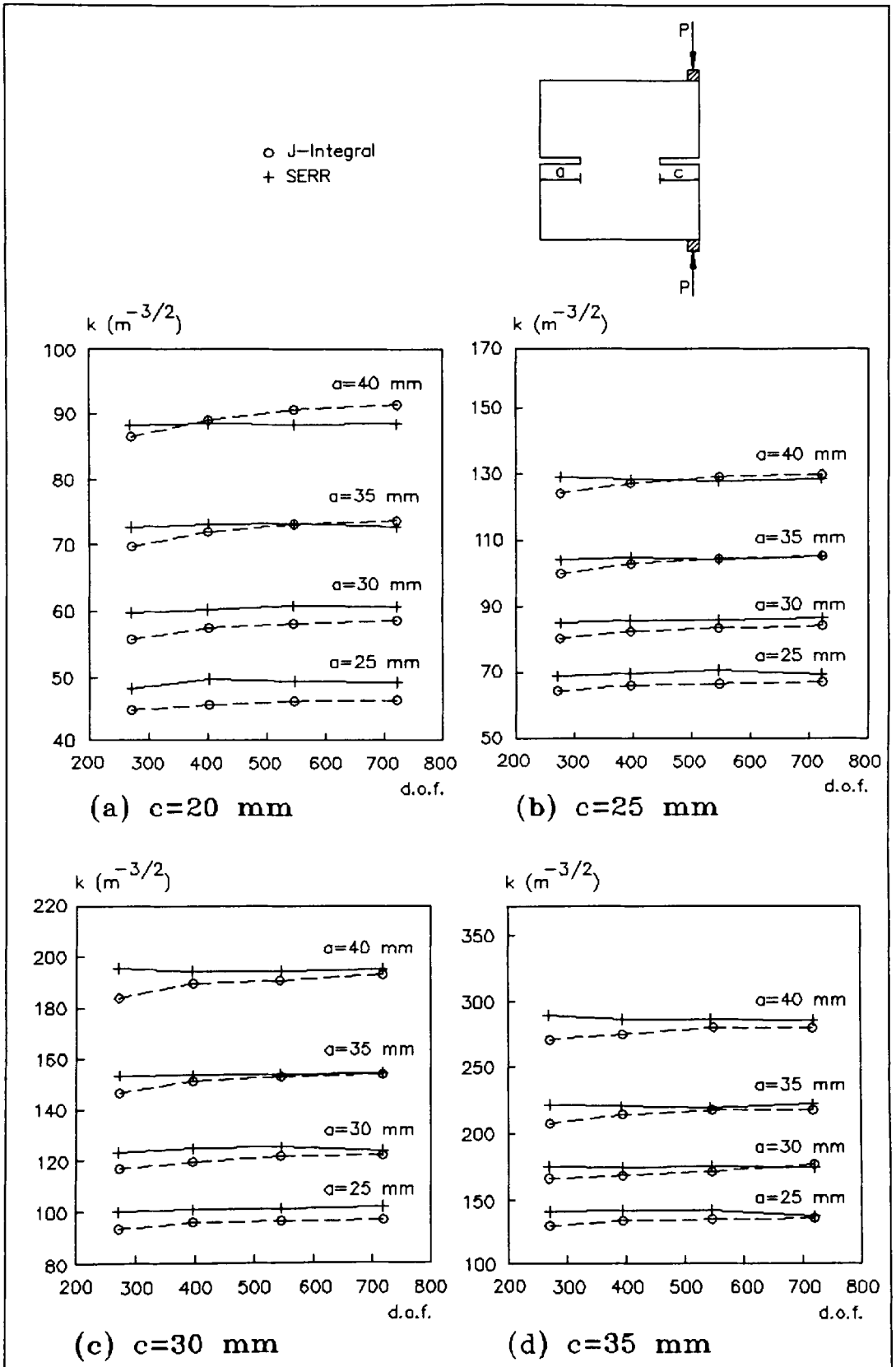

Figure 5.14 Convergence Curves for k (CCS) Using SERR and J-Integral Methods - Rectangular Elements.

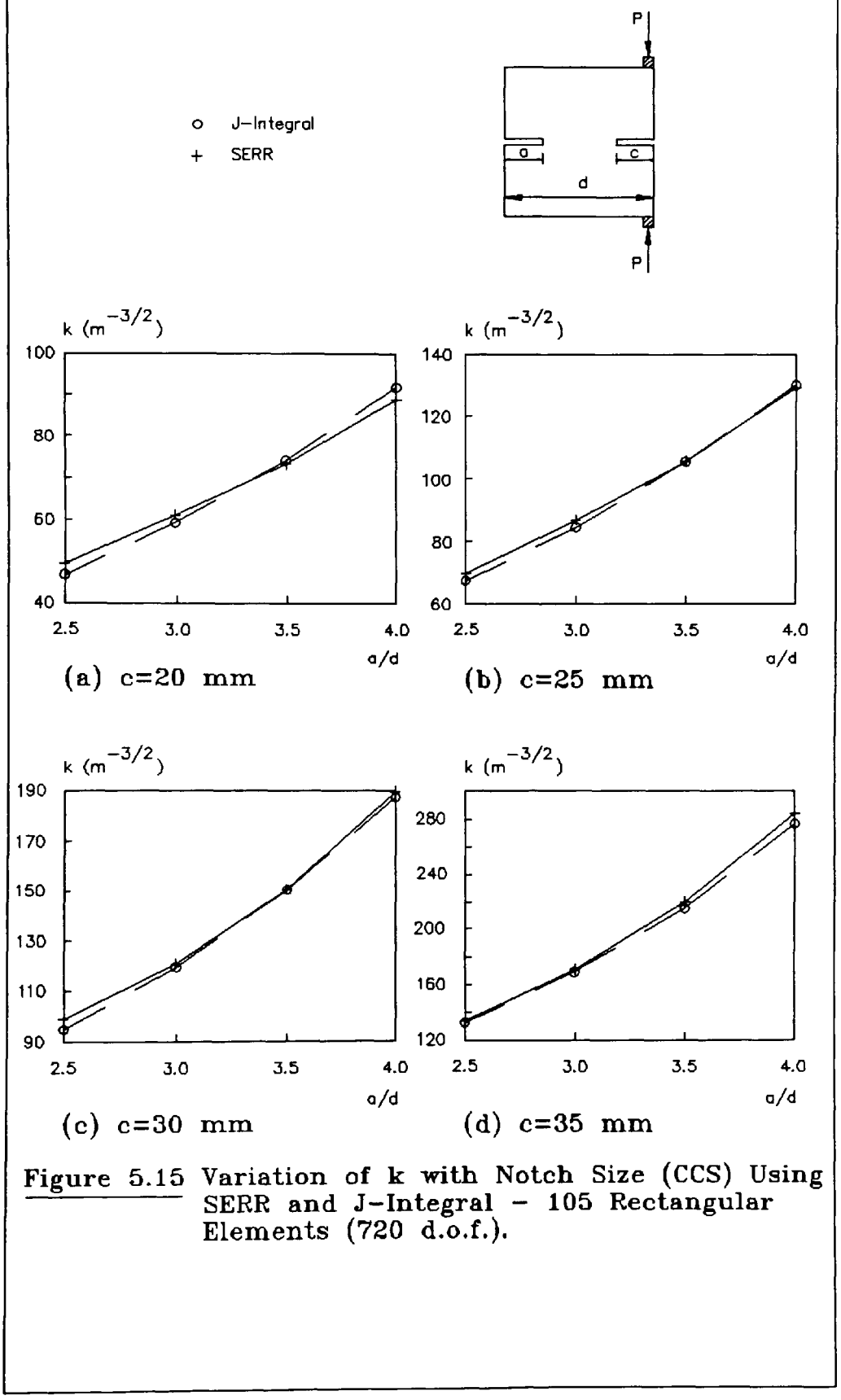

Figure 5.15 Variation of k with Notch Size (CCS) Using SERR and J-Integral - 105 Rectangular Elements (720 d.o.f.).

	Maximum	Location	Minimum	Location
σ_x	0.91	tension crack tip	-2.82	compression crack tip
σ_y	1.45	tension crack tip	-3.60	compression crack tip & load point
σ_{xy}	0.76	load point	-0.86	compression and tension crack tips & load point
principal stress	1.50	tension crack tip	-3.60	compression crack tip & load point
Maximum shear from principal stress	1.40	compression crack tip & load point	-	-

Table 5.1 Maximum and Minimum Stresses ($N/mm^2 x 10^{-3}$) for the Problem of Figure 5.2 (CCS, a=c=30 mm).

d.o.f.	k ($m^{-3/2}$)	
	DE	CSS
952	116.2	114.2
3664	120.0	116.6

Table 5.2 Comparison of Stress Intensity Factor Values (CCS, a=c=30 mm) - Triangular Elements.

d.o.f.	k ($m^{-3/2}$)			
	DE	CSS	SERR	J-integral
326 (fan mesh)	114.3	109.0	125.3	126.6
270	118.0	116.6	121.0	113.8
396	121.2	119.4	122.4	117.4
546	122.0	120.7	122.3	118.6
720	122.2	121.8	120.5	119.3

Table 5.3 Comparison of Stress Intensity Factor Values Using Various Mesh Idealisations (CCS, a=c=30 mm) - Quadrilateral Elements.

a (mm)	c (mm)	k ($m^{-3/2}$)	
		SERR	J-integral
25	20	48.6	45.1
	25	69.2	64.7
	30	97.8	91.3
	35	137.3	128.1
30	20	60.1	56.2
	25	85.5	80.3
	30	121.0	113.8
	35	172.0	161.3
35	20	73.2	70.2
	25	104.7	100.2
	30	150.4	143.0
	35	219.1	205.7
40	20	88.6	87.1
	25	129.2	124.7
	30	190.7	179.6
	35	286.9	267.4
	40	455.0	409.3

Table 5.4 Variation of Stress Intensity Factor with Notch Depth (CCS) Using 36 Rectangular Elements (270 d.o.f.).

a (mm)	c (mm)	k ($m^{-3/2}$)	
		SERR	J-integral
25	20	49.3	46.1
	25	70.3	66.2
	30	99.0	93.4
	35	138.4	131.0
30	20	60.7	57.9
	25	86.3	82.9
	30	121.9	117.4
	35	171.1	165.8
35	20	73.5	72.4
	25	105.0	103.2
	30	150.3	147.1
	35	217.9	211.4
40	20	88.6	89.7
	25	128.8	128.1
	30	189.6	184.6
	35	282.9	272.4
	40	448.3	426.0

Table 5.5 Variation of Stress Intensity Factor with Notch Depth (CCS) Using 55 Rectangular Elements (396 d.o.f.).

a (mm)	c (mm)	k ($m^{-3/2}$)	
		SERR	J-integral
25	20	49.7	46.6
	25	71.1	66.8
	30	99.4	94.4
	35	138.0	132.4
30	20	61.2	58.6
	25	86.4	83.7
	30	122.3	118.6
	35	172.1	167.9
35	20	73.6	73.5
	25	104.7	104.7
	30	149.8	149.1
	35	217.5	214.2
40	20	88.8	91.0
	25	128.5	129.9
	30	189.3	187.2
	35	283.2	277.5
	40	445.8	434.3

Table 5.6 Variation of Stress Intensity Factor with Notch Depth (CCS) Using 78 Rectangular Elements (546 d.o.f.).

a (mm)	c (mm)	k ($m^{-3/2}$)	
		SERR	J-Integral
25	20	49.5	46.8
	25	69.7	67.1
	30	99.2	94.8
	35	134.3	133.1
30	20	61.1	59.1
	25	86.6	84.3
	30	120.5	119.3
	35	170.7	168.8
35	20	73.2	74.0
	25	105.4	105.3
	30	150.1	149.9
	35	219.2	215.2
40	20	88.9	91.6
	25	129.3	130.6
	30	190.0	188.0
	35	285.0	277.5
	40	437.2	435.3

Table 5.7 Variation of Stress Intensity Factor with Notch Depth (CCS) Using 105 Rectangular Elements (720 d.o.f.).

CHAPTER SIX

FINITE ELEMENT ANALYSIS OF THE AXIAL SPLITTING GEOMETRY

6.1 Introduction

Compression splitting tests have been employed in a variety of forms to obtain the strength of brittle materials. An early example dates to 1947 when Carneiro [104] tested a disc in compression producing cracking in the direction of the applied force. Kendall [105] introduced the idea of initiating a single sharp starting notch to induce stable crack propagation. Karihaloo [106, 107] improved the model by applying a lateral restraint under the loading platen.

In this chapter finite element analyses of a Singly Notched Axial Splitting Specimen (SNASS), due to Karihaloo, are carried out. A modified version of Karihaloo's geometry, i.e. a Doubly Notched Axial Splitting Specimen (DNASS) is also examined.

6.2 Analytical Solution

Kendall [108] discussed the complexities of compression failure and argued that the compressive strength is not the most suitable parameter for measuring compression cracking of brittle materials since the stress at failure varies with geometry and manner of application of the force. Using Griffith's energy balance [81], he expressed the equation for the cracking force P, as

P = function (fracture surface energy, geometry, elasticity)

with the particular function being dependent on the crack path and the mode of failure. The fracture surface energy was suggested as the more suitable material parameter since it remains the same both in tension and in compression irrespective of geometry and loading arrangement. Kendall [108] tested rectangular blocks of a glassy brittle polymer in compression. Sharp starting cracks were introduced in order to prevent catastrophic failure, and make it possible to study the slow compression crack propagation. The theory proposed was that the crack effectively divided the specimen into two short struts bending outwards under the compression. Following detailed theoretical and experimental investigations, it was concluded that the compressive splitting force, as well as the mode of failure, depended on the specimen dimensions, its elastic properties and the loading platen size.

Griffith's theory predicts an essentially unstable crack propagation in compression. Although Kendall's experiments displayed this phenomenon, his theory failed to explain it. Karihaloo [106, 107] improved the model, to give a better approximation to the experimentally observed behaviour, by recognising that in compression testing a certain lateral constraint under the loading platen exists. He also discovered that a crucial factor, namely the length of the pre-crack, has a major influence on the magnitude of the failure load as well as the mode of failure.

Referring to Figure 6.1, the pre-crack divides the specimen into two short struts which bend when compressed. The deformation of each strut can be described by the action of a cantilever strut of length a/2 loaded eccentrically with a force P/2 as shown in Figure 6.2. The bending moment M_x can be expressed as

$$EI\ d^2y/dx^2 = -M_x = \tfrac{1}{2}\ P(e+f-y) \qquad (6.1)$$

where y is the transverse deflection and EI is the flexural rigidity. Equation 6.1 can be re-arranged to give

$$d^2y/dx^2 + h^2y = h^2(e+f) \qquad (6.2)$$

in which

$$h^2 = P/2EI\ ,\ I = bd^3/96\ ,\ \text{and}\ e = (d-w)/4$$

is the eccentricity of the force P/2.

The general solution of equation 6.2 consists of two parts, i.e. the homogeneous solution and the particular solution. It can be shown that the equation can be satisfied by the solution

$$y = C_1 \sin hx + C_2 \cos hx + (e+f) \qquad (6.3)$$

Applying the boundary conditions, x=0: y=0, and x=0: dy/dx=0, and subsequently substituting the values of C_1 and C_2 in equation 6.3, the equation for the transverse deflection of the strut can be written as

$$y = (e+f)\ (1-\cos hx) \quad \text{for } 0 \leq x \leq \tfrac{1}{2} a \qquad (6.5)$$

The bending moment M_x, and the shear force Q_x at any section are thus

$$M_x = -\tfrac{1}{2} P(e+f) \cos hx$$

$$Q_x = \tfrac{1}{2} Ph(e+f) \sin hx. \qquad (6.6)$$

Using the above equations the bending strain energy U_b, the shear strain energy U_s and the potential energy lost by the axial force U_p can all be calculated for one half of each of the two struts. These are

$$U_b = 2\int_0^{a/2} \frac{M_x^2\, dx}{2EI} = \frac{P^2B^2}{16EIh}(ha + \sin ha) \qquad (6.7)$$

$$U_s = 2\phi\int_0^{a/2} \frac{Q_x^2\, dx}{2A\Omega} = \frac{0.3P^2B^2h\,(1+\mu)}{2AE}(ha - \sin ha) \qquad (6.8)$$

$$U_p = 2\int_0^{a/2} \frac{P}{4}(dv/dx)^2\, dx = 1/4\ PhB^2\,(ha - \sin ha) \qquad (6.9)$$

where

$$B = e/\cos(ha/2),\ A=bd/2,\ \Omega = \text{shear modulus} = E/[2(1+\mu)],$$

and $\phi=1.2$, being the shape factor for a rectangular section. The total energy U_t stored in the strut is made up of the above three components, i.e.

$$U_t = U_b + U_s - U_p \qquad (6.10)$$

The criterion for propagation of the crack by an infinitesimal amount δa, according to Griffith energy conservation principle, is

$$2Gb\ \delta a = \delta U_t \qquad (6.11)$$

or in differential form

$$\delta U_t/\delta a = 2Gb \qquad (6.12)$$

where G is the Griffith fracture surface energy per unit area.

After substituting equations 6.7, 6.8, and 6.9 in equation 6.10 and employing the result in equation 6.12, the following expression is obtained

$$G = \frac{p^2e^2}{32EIb} (2 - ha \tan ha/2) \sec^2 ha/2 \qquad (6.13)$$

Assuming conditions of plane strain to prevail in the specimen and that LEFM is applicable, the surface energy G may be expressed in terms of the stress intensity factor k, by

$$EG = k^2(1-\mu^2) \qquad (6.14)$$

Equations 6.13 and 6.14 yield the following result for the stress intensity factor

$$k^2 = \frac{p^2e^2}{32Ib\ (1-\mu^2)} (2 - ha \tan ha/2) \sec^2 ha/2 \qquad (6.15)$$

As e = (d-w)/4, it is clear that the stress intensity factor k depends on both the platen width w and the pre-crack length 'a'. Furthermore, tests conducted by Karihaloo [107] on polymer specimens demonstrated that failure by yielding under the loading platen could be avoided when $w/d \leq 1/2$. It was also found that stable crack propagation, leading to

failure by splitting along the crack line, could be achieved for sufficiently large pre-cracks, i.e. $1 \leq a/d \leq 3/2$, under narrow compression platens. It was observed that for long pre-cracks, i.e. $a/d \geq 3/2$, buckling of the specimen occurred. It is therefore emphasised that equation 6.15 is only valid when $w/d \leq 1/2$ and $1 \leq a/d \leq 3/2$, i.e. when axial splitting occurs without yielding under the platen, or buckling.

Kendall's test specimens were 20 mm long and had rectangular 3 mm by 6 mm sections. Karihaloo used larger specimens of 100 mm length and 40 mm by 40 mm square or 40 mm by 18 mm rectangular sections. Later Guest and Karihaloo [109] presented further experimental and finite element results using 50 mm long perspex specimens of 10 mm by 10 mm square sections. Their results support the two-strut model outlined above and confirm that in the compression splitting mode the polymer behaviour is essentially elastic on the condition that the pre-crack is sufficiently deep and the loading platen is sufficiently narrow. Violation of these conditions would yield an elastic plastic behaviour, requiring a different approach. More recently Karihaloo [40] calculated the fracture toughness of plain concrete by employing prisms of rectangular section with a central built-in notch introduced using a mild steel strip milled to a very sharp edge.

In the next section finite element analyses of the SNASS are carried out. Estimates of the stress intensity factor are

obtained using the DE, CSS and J-integral methods.

6.3 Finite Element Analysis

Analysis of a prism 400 mm long and 100 mm by 100 mm in cross section containing a 100 mm pre-crack centrally placed at one end was carried out using the 6-noded triangular element described in Chapter 4. Plane strain conditions were assumed to prevail and the stress intensity factor was determined for a unit compressive load applied uniformly through a 25 mm loading platen. Due to symmetry only one-half of the specimen, as shown in Figure 6.3, was considered.

The symmetry condition was simulated by restraining the nodes along the uncracked ligament in the y-direction. The nodes along the edge of the specimen remote from the crack were fully restrained. A restraint in the y-direction was also applied to the nodes under the loading platen to ensure that no slipping takes place between this and the specimen.

6.3.1 Idealisation of the Specimen Geometry

The finite element mesh for the half-specimen was generated by dividing the whole area into 8 regions as shown in Figure 6.4, each being subdivided into a number of triangular elements. The areas under the loading platen, and in the vicinity of the crack tip, were represented by small elements when compared to those employed in the remainder of the body. Two meshes were used namely, a coarse mesh with

368 elements and 1608 d.o.f. and a fine mesh with 1472 elements and 6158 d.o.f. Details of the fine mesh are presented in Figure 6.5. The elements either side of the crack tip had sizes of a/80, where 'a' is the crack size.

6.3.2 Stress Distribution

The deformed half-specimen demonstrating the strutting action over the crack line as obtained from the coarse mesh analysis is shown in Figure 6.6a. Figure 6.6b gives the contours of the σ_y stress. It can be seen that large tensile stresses are present in the vicinity of the crack tip. It can also be seen that compressive stresses of similar magnitudes exist under the loading platen. Figure 6.7 presents the distribution of the σ_y stress along the crack line and the uncracked ligament. Figures 6.6b and 6.7 clearly show that the high compressive stresses are confined to a very small area under the loading platen.

Table 6.1 gives the maximum and minimum values of σ_x, σ_y, σ_{xy}, and the principal stresses together with their locations. Comparison of these results with those for the CCS presented in Table 5.1 reveals that the stresses for the SNASS are generally one order of magnitude lower than those for the CCS. Furthermore, the ratio of the maximum compressive stress (under the load) to the maximum tensile stress (in the vicinity of the crack tip) is 0.65. In the case of the CCS analysed in the previous chapter this ratio

was 2.5. This is due to the fact that the SNASS geometry is considerably stiffer than the CCS. This is confirmed by studying and comparing the relative deformations for the two geometries. These results suggest that the SNASS analysed here is even more susceptible to tensile failure at the crack front than the CCS.

Figure 6.7 also gives the distribution of the shear stress σ_{xy}. It can be seen that, except for very small localised values under the loading platen and near the crack tip, these are virtually non-existent along the uncracked ligament. This indicates that there is no significant mode 2 contribution to the fracture process.

6.3.3 Displacement Extrapolation (DE) and Conic Section Simulation (CSS) Methods

Estimates for the stress intensity factor along the line $\Theta=180°$ (see Figure 6.8) emanating from the crack tip are obtained by substituting the appropriate finite element results for the u_y displacements in equation 5.1. These estimates obtained from the fine and coarse mesh analyses are given in Table 6.2. Figure 6.8 shows a plot of k as a function of the radial distance from the crack tip. If the values for the points near the crack tip are ignored, extrapolation of the line of constant slope gives estimates for k of 13.95 $m^{-3/2}$ and 14.06 $m^{-3/2}$ per unit load for the coarse and fine mesh analyses respectively.

Equation 5.2 is next employed to obtain estimates for the stress intensity factors by the CSS method. The results are shown in Table 6.3 and presented graphically against the ratio x/a in Figure 6.9. Extrapolation of the results to x=a yields values of 13.89 $m^{-3/2}$ and 13.96 $m^{-3/2}$ for the coarse and fine meshes respectively.

Using mesh idealisations similar to those used for w=25 mm results were obtained for the cases of w=20 mm and w=30 mm. The k estimates for the three platen widths as obtained by the DE and CSS methods together with those yielded by equation 6.15 are presented in Table 6.4. Accepting the DE method to be the most reliable, the estimate of 14.06 $m^{-3/2}$ for the 25 mm plate is 5.1% in error when compared with that of Karihaloo's equation 5.15. The CSS analysis yields an estimate of 13.96 $m^{-3/2}$ which is 5.8% in error.

The 8-noded isoparametric element used in Chapter 5 is next employed in analysing the geometry with w=25 mm. The mesh employed is made up of rectangular elements as shown in Figure 6.10. In this idealisation a total of 266 elements and 1778 d.o.f. were used in analysing one half of the specimen. The mesh was made progressively finer as the elements approached the crack tip. The sizes of the elements, either side of the crack tip, in the x-direction were calculated according to the ratios a/150, a/100, a/60, a/30, a/15, (each pair of adjacent elements having the same size), followed by a row of elements of size a/5. In the y-direction under the half-platen width of 12.5 mm, the

element sizes varied according to the ratios a/150, a/100, a/60, and a/30. The unloaded area was divided into two elements in the y-direction. Care was taken to ensure that the maximum element aspect ratios did not exceed those used in the CCS analysis. In this idealisation not only the elements were of similar sizes to those used for the CCS but also any geometrical errors introduced were kept the same for both analyses.

Using the above idealisation the stress intensity factor was determined by the DE and the CSS methods. The results for k for the various platen widths are shown in Table 6.5. Figures 6.11 and 6.12 present the variation of the stress intensity factor along a section of the crack for the case w=25 mm using the DE and CSS methods respectively. The DE method gives a value of 14.59 $m^{-3/2}$ while the CSS method yields a lower value of 14.30 $m^{-3/2}$ which is 3.5% in error when compared to that obtained from equation 6.15. The DE value is within 1.5% of that given by the same equation.

6.3.4 J-Integral Method

The J-integral method was next employed to obtain the stress intensity factor. J-integrals were computed along the three paths indicated in Figure 6.10 and the results for the stress intensity factor k are presented in Table 6.5. The J-integral results demonstrate the path independency and give

stress intensity factors which are in good agreement with those obtained by the DE method, with the maximum difference being less than 2%.

6.4 Effect of Loading Platen Width, Crack Size, and Specimen Length

A parametric study of the SNASS geometry was carried out by obtaining solutions for specimens with different loading platen widths, crack sizes and specimen lengths. This was done using both triangular and rectangular finite elements. Table 6.4 gives the results for the stress intensity factor k for L=400 mm, a=100 mm and loading platen widths w=20 mm, 25 mm and 30 mm obtained by the DE and CSS methods and employing the triangular elements. The table also gives the results obtained using equation 6.15. It can be seen that all methods yield similar values. The results obtained using the rectangular elements and graded meshes similar to that shown in Figure 6.10 are shown in Table 6.5. Using such idealisations k was evaluated by the J-integral method as well as the DE and CSS methods. Again it can be seen that all approaches yield similar results. The variation of k with the size of the loading platen is shown in Figure 6.13. As expected k decreases with increasing platen size.

Further solutions were obtained for specimens with crack sizes ranging between 50 mm and 150 mm and a loading platen width of 25 mm. The results for k obtained from these solutions are summarised in Table 6.6. Figure 6.14 gives the variation of k with crack size. It is seen that k increases with increasing crack size. The rate of increase, however, slows down considerably for $a/d \geq 1$. It is also seen that, for the range of values of 'a' considered here, equation

6.15 is not crack size sensitive and can lead to an overestimate for $a/d \leq 1$.

Next the effect of the specimen length L on k was investigated. Several solutions were obtained using both triangular and rectangular elements with loading platen width w=25 mm and crack size a=100 mm. Using the DE method it was found that for the range L=250 mm to L=500 mm studied, the values of stress intensity factor were well within 1% of those reported in Tables 6.4 and 6.5 and were therefore independent of the specimen length. This is due to the fact that the tensile stresses are confined to the areas surrounding the crack tip and increasing the size of uncracked ligament beyond a certain limit has no bearing on these stresses. This is reflected by equation 6.15 which is independent of the specimen length.

6.5 The Doubly Notched Axial Splitting Specimen (DNASS)

In an attempt to develop an axial splitting specimen for fracture toughness evaluation employing standard quality control samples the SNASS geometry was modified by employing 100 mm cubes and introducing an additional notch on the opposite face as shown in Figure 6.15. The additional notch not only encourages the splitting more readily but also results in the specimen being doubly symmetric which allows simpler analysis using one-quarter of the specimen as depicted in Figure 6.16. In the analysis the conditions of symmetry were implemented by restraining the nodes along the uncracked ligament in the y-direction and those along the y-direction line of symmetry, in the x-direction. Furthermore, the movement in the y-direction of the nodes under the loading platen was prevented in order to simulate no slip between the platen and the specimen. As a result reactive forces in the y-direction were induced at these nodes. Taking the coefficient of friction between steel and concrete as 0.25, care was taken to ensure that the value of this reaction did not exceed 0.25P. If this condition occurred, the force was set equal to the above product and the analysis repeated. This procedure was found necessary in only a few of the cases considered.

Two sets of analyses were carried out under plane strain conditions. In the first, the geometry with a=30 mm and w=20 mm was represented by triangular elements. Two mesh idealisations were used, i.e. a coarse mesh with 136

elements and 578 d.o.f., and a fine mesh with 544 elements and 2245 d.o.f. Due to the considerable reduction in the specimen length it was found desirable to study the stress distribution. Contours of σ_y stress obtained by employing the fine mesh confirmed the existence of large tensile stresses in the vicinity of the crack tip as well as larger compressive stresses under the loading platen. The maximum and minimum values of the stresses together with their locations are given in Table 6.7. This gives a value of 1.7 for the ratio of the maximum compressive σ_y stress to the maximum tensile σ_y stress. This is more favourable than the value of 2.5 obtained in the case of the CCS and confirms the suitability of the DNASS for fracture testing.

The distributions of the direct stress σ_y and the shear stress σ_{xy} along the crack line are shown in Figure 6.17. As in the case of the SNASS, this reveals that large tensile σ_y stresses in the region of the crack tip are accompanied by negligible shear stresses σ_{xy}, thus indicating the mode of failure to be that of the opening mode.

In the second analysis the geometry was represented by rectangular isoparametric elements using program STRESS. Again two idealisations were considered, a coarse mesh with 40 elements and 294 d.o.f. and a fine mesh comprising 60 elements and 426 d.o.f. for the quarter-geometry. In the case of the fine mesh elements either side of the crack tip had sizes of a/30.

Using both of the idealisations described above the stress intensity factor k was evaluated by the DE method. Figures 6.18 and 6.19 show the variation of k along the line of the notch $\theta=180°$ for the coarse and the fine mesh analyses using the two element idealisations. The extrapolated results for k are presented in Table 6.8. The fine mesh idealisation utilising the triangular elements yields a value for k of 10.8 $m^{-3/2}$ per unit load. It can be seen that using rectangular elements, with a much reduced total number of d.o.f., an estimate for k which is within 2% of the above value is obtained.

Finally it was considered of interest to compare the deformations of the specimens examined in this chapter to those of the CCS studied in Chapter 5. Table 6.9 gives the results for the maximum displacements for the three geometries namely, the SNASS, DNASS and the CCS. In these the crack size 'a' had values 100 mm, 30 mm and 30 mm respectively. The length L was 400 mm for the SNASS and 100 mm for the other two geometries. The table also gives the ratios of the maximum compressive σ_y stress to the maximum tensile σ_y stress for the above geometries. The results provide further numerical proof that both the SNASS and DNASS are stiffer than the CCS and more importantly confirm the mode of failure in all three cases to be that of the opening mode.

6.6 Conclusions

In this chapter finite element analyses of singly and doubly notched axial splitting specimens (SNASS and DNASS) were carried out. In these, several idealisations employing the triangular and rectangular isoparametric elements discussed in Chapter 4 were employed. The results for the stress distributions, for the geometries and loading arrangements considered, confirmed the existence of large tensile stresses in the vicinity of the crack tip demonstrating their suitability for fracture studies in concrete materials.

Estimates for the stress intensity factor k were obtained by the DE, CSS and J-integral methods. In the case of the SNASS good agreement was obtained when these estimates were compared with those obtained by the analytical solution established by Karihaloo [107]. As with the case of the Compact Compression Specimen (CCS), analysed in Chapter 5, it was found that no advantage was gained by using the CSS method as it required an extrapolation process.

A parametric study of the SNASS geometry was carried out by varying the loading platen width, crack size and specimen length. For a given crack size the analytical expression, given by equation 6.15, and the finite element analyses indicated that the stress intensity factor k decreased with increasing platen width with good agreement being obtained from both approaches. For a given platen width, the finite

element results demonstrated that k increased with increasing crack size up to an a/d ratio of 1.0. For $a/d \geq 1$ equation 6.15 yielded results which were in good agreement with those obtained in the present work. It was found, however, that this equation was not crack size sensitive and gave considerably overestimated values for $a/d < 1$. The finite element analysis confirmed that k is independent of the specimen length L which is absent in equation 6.15.

In all the solutions obtained in this chapter it was found that the rectangular isoparametric finite elements are more efficient than the triangular elements and it is possible to obtain accurate estimates for k using a relatively small number of elements.

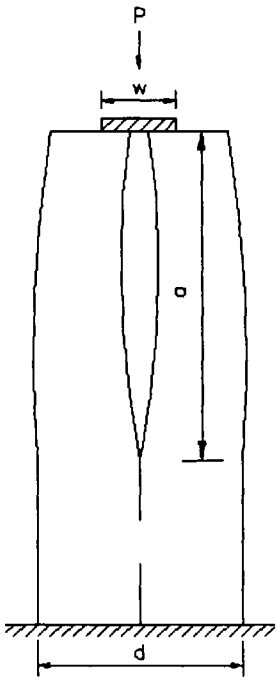

Figure 6.1 The Two-Strut Model – Karihaloo [107].

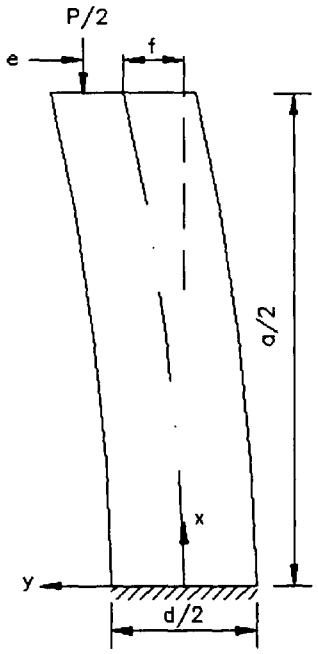

Figure 6.2 Isolated Half-Strut Under the Eccentric Compressive Force P/2.

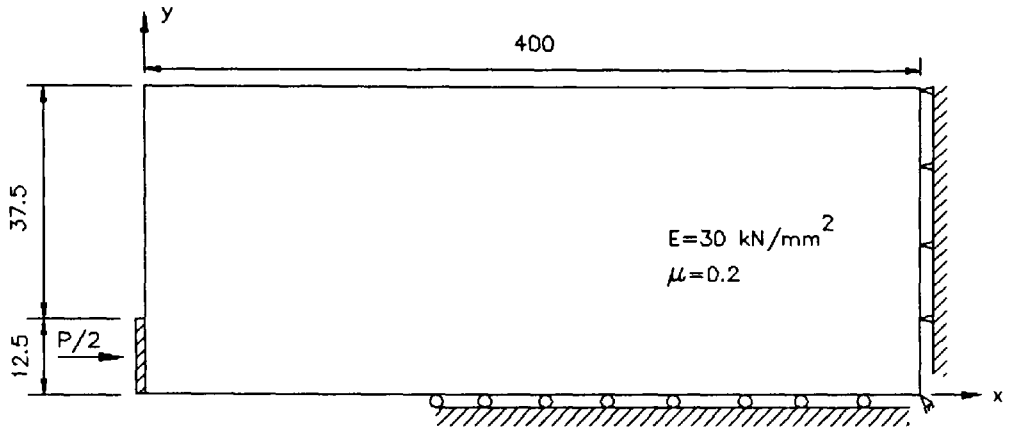

Figure 6.3 The Half-Strut Analysed (SNASS). All Dimensions are in mm.

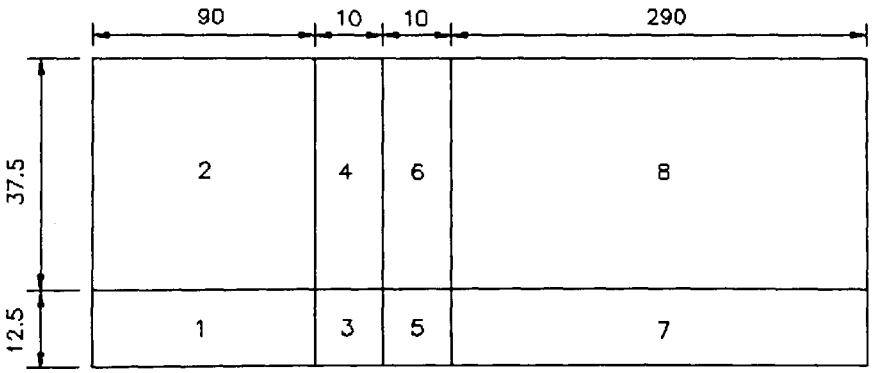

Figure 6.4 Element Blocks Used in Analysing the Half-Strut (SNASS). All Dimensions are in mm.

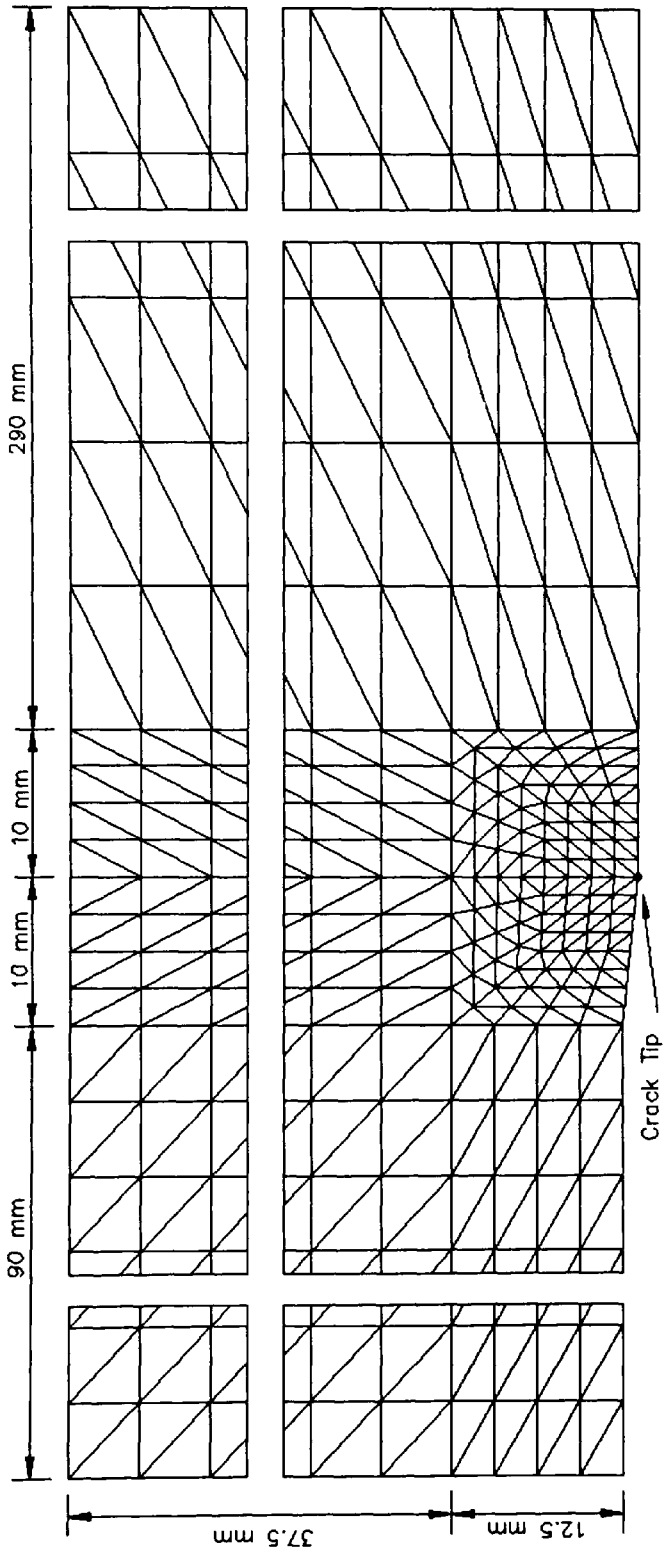

Figure 6.5 Finite Element Mesh for the Half-Strut Using 1472 Triangular Elements (6158 d.o.f.).

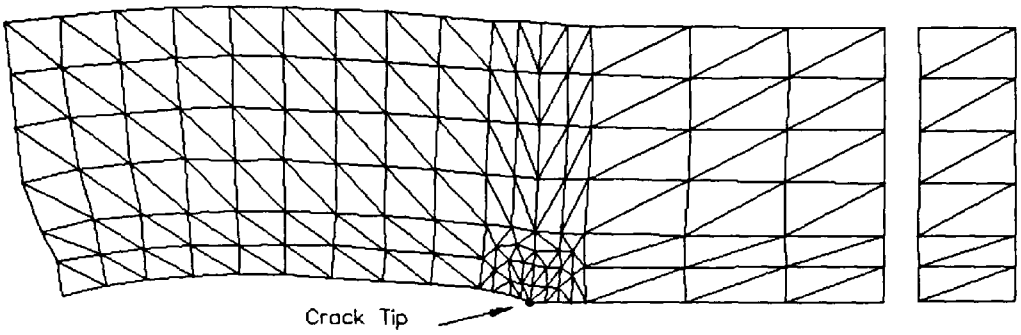

Figure 6.6a Deformed Shape for SNASS Using 368 Triangular Elements (1608 d.o.f.).

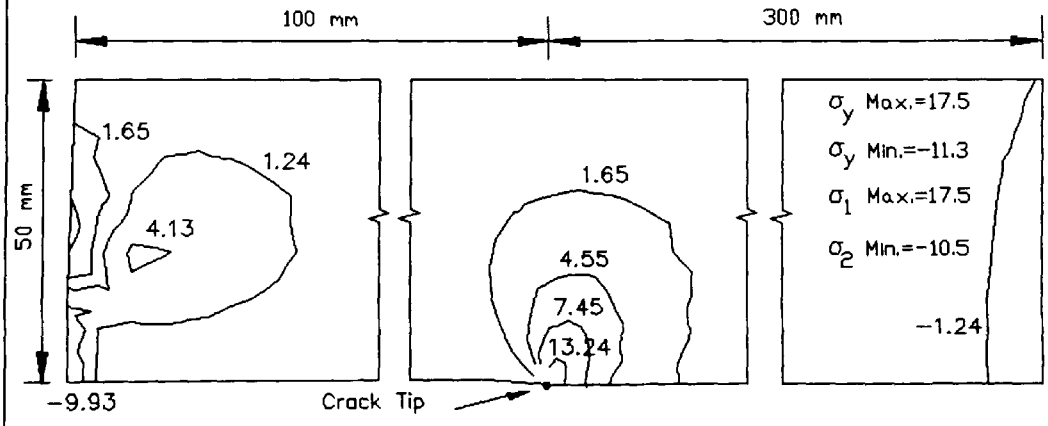

Figure 6.6b Contours of σ_y (N/mm^2 $x10^{-5}$) for Unit Applied Load.

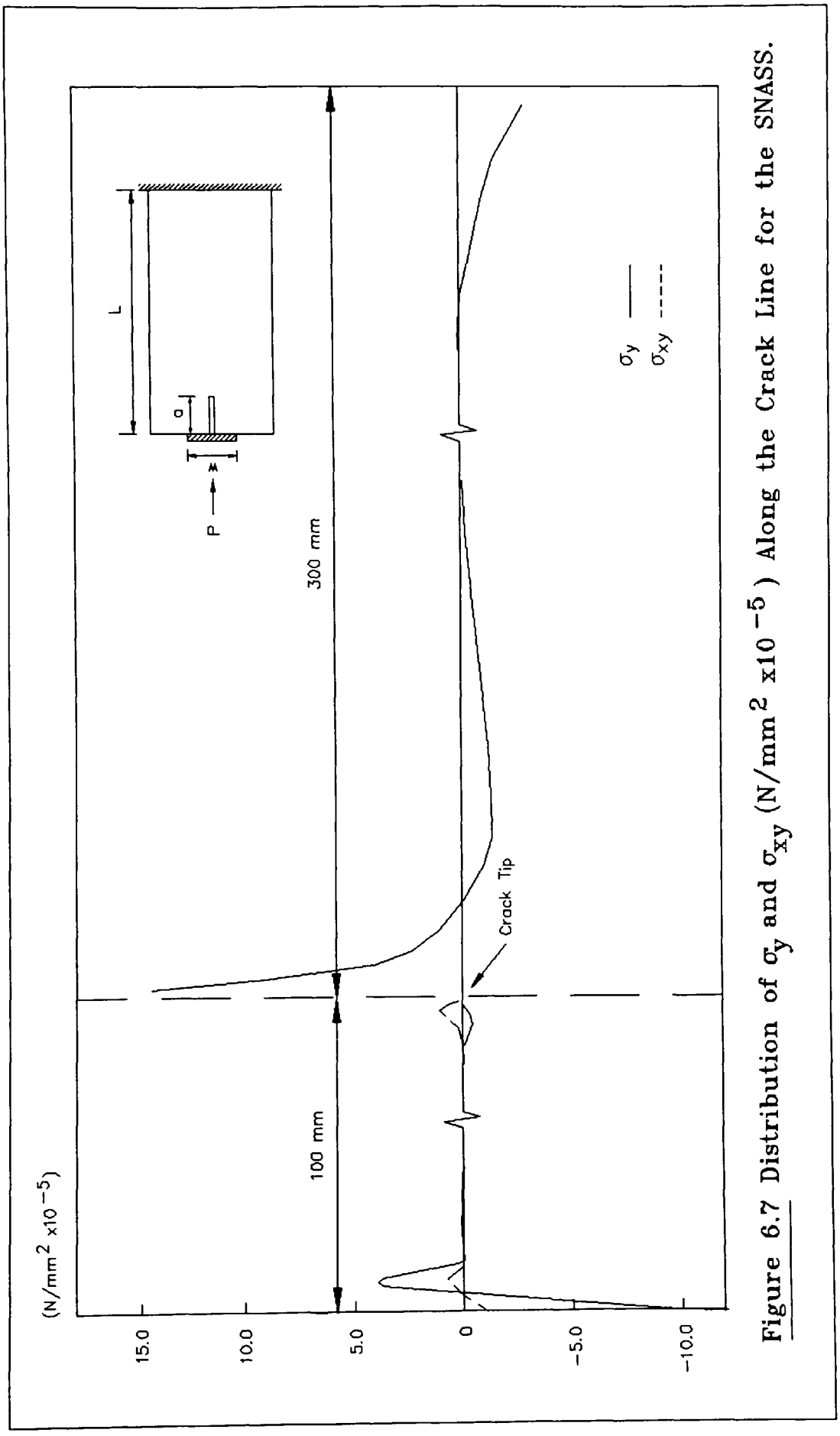

Figure 6.7 Distribution of σ_y and σ_{xy} (N/mm^2 x10^{-5}) Along the Crack Line for the SNASS.

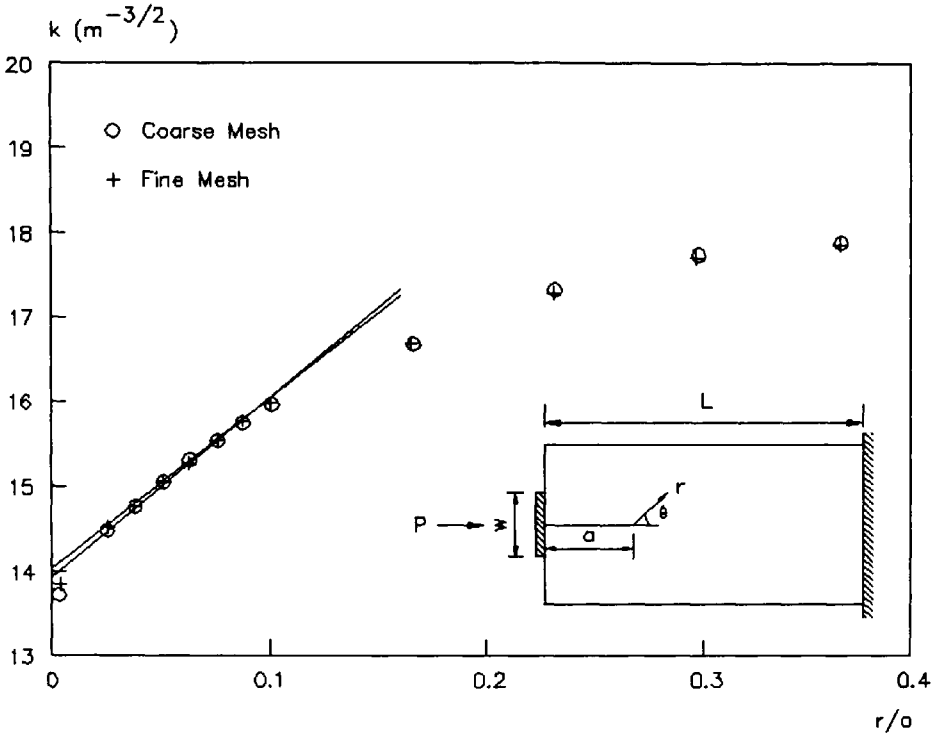

Figure 6.8 Variation of k with Radial Distance from the Crack Tip (SNASS, a=100 mm, w=25 mm) - Triangular Elements.

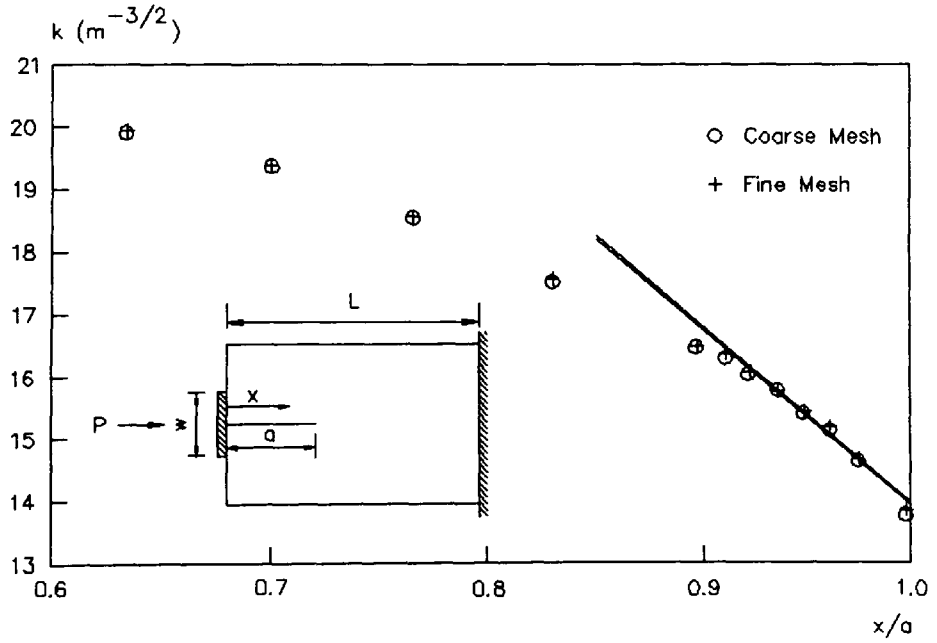

Figure 6.9 Variation of k with x/a (SNASS, a=100 mm, w=25 mm) - Triangular Elements.

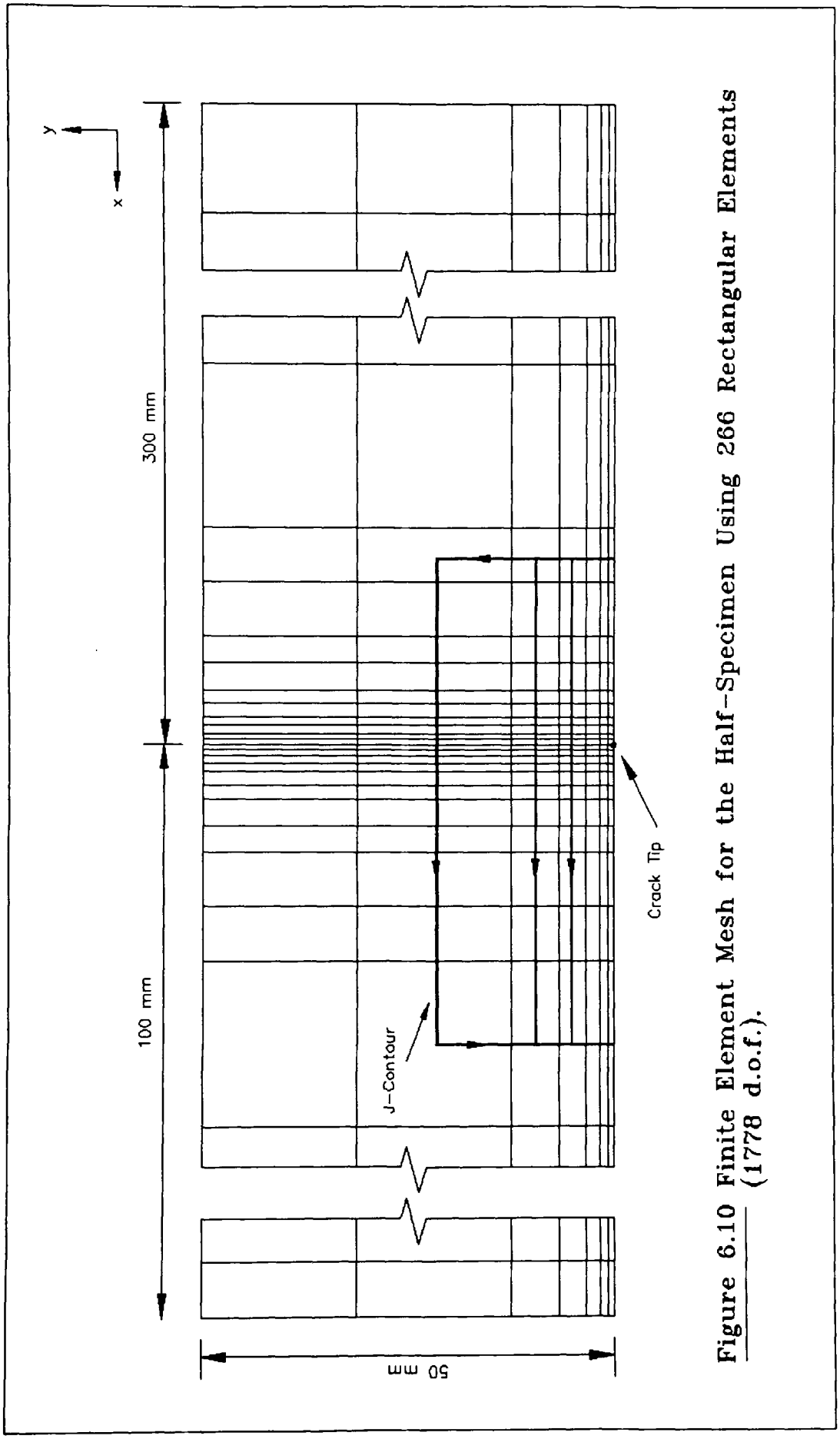

Figure 6.10 Finite Element Mesh for the Half-Specimen Using 266 Rectangular Elements (1778 d.o.f.).

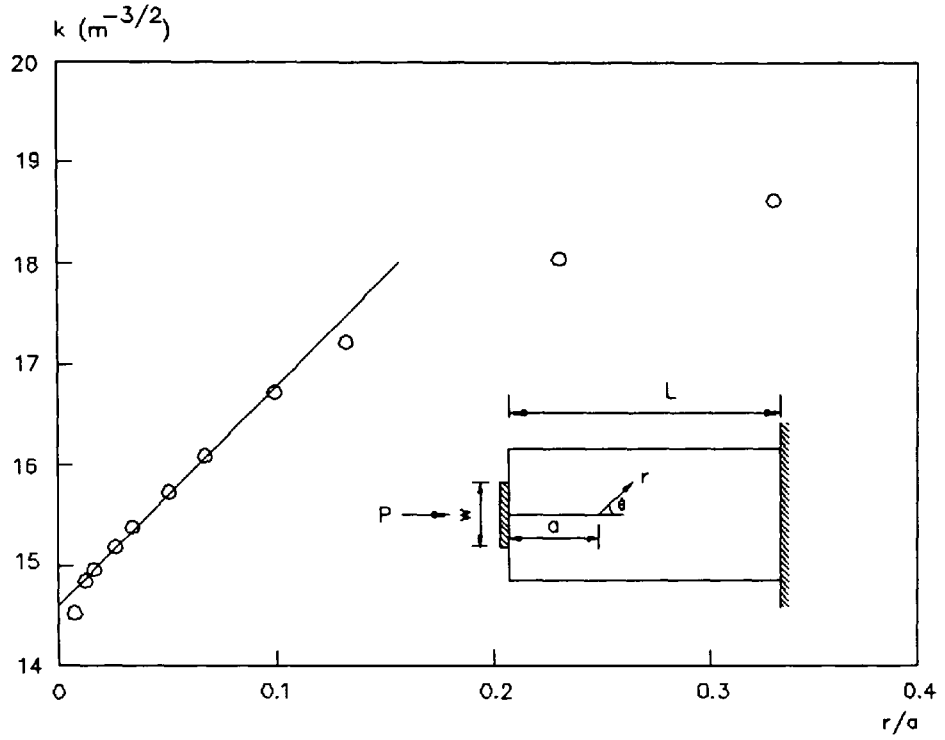

Figure 6.11 Variation of k with Radial Distance from the Crack Tip (SNASS, a=100 mm, w=25 mm) – Rectangular Elements.

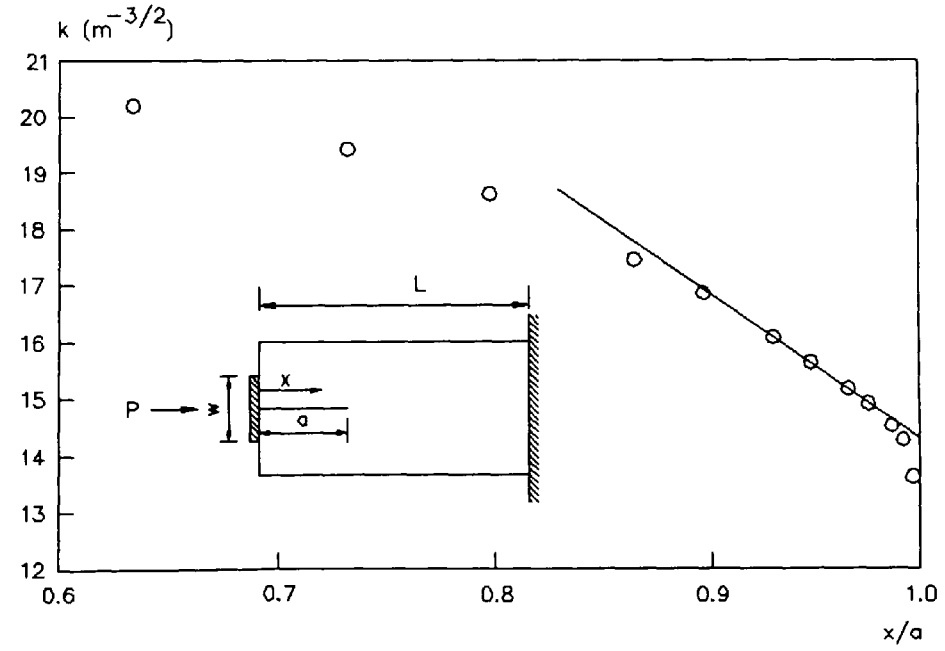

Figure 6.12 Variation of k with x/a (SNASS, a=100 mm, w=25 mm) – Rectangular Elements.

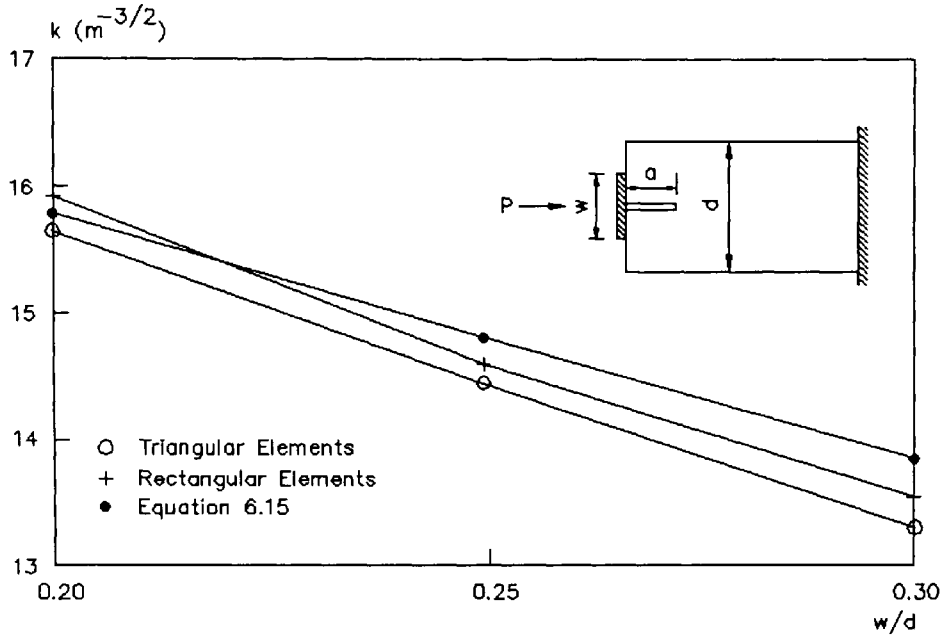

Figure 6.13 Variation of k with Loading Platen Width (SNASS, a=100 mm).

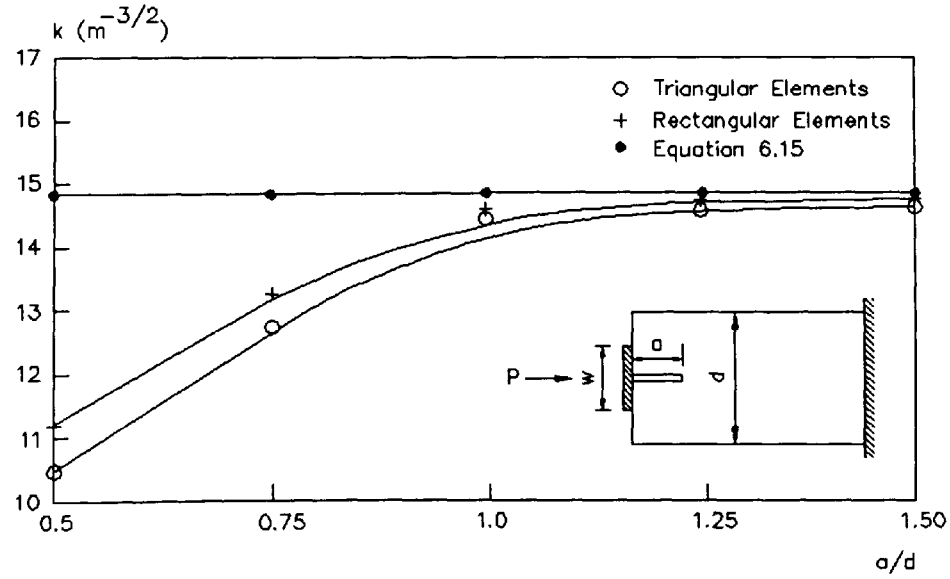

Figure 6.14 Variation of k with Notch Size (SNASS, w=25 mm).

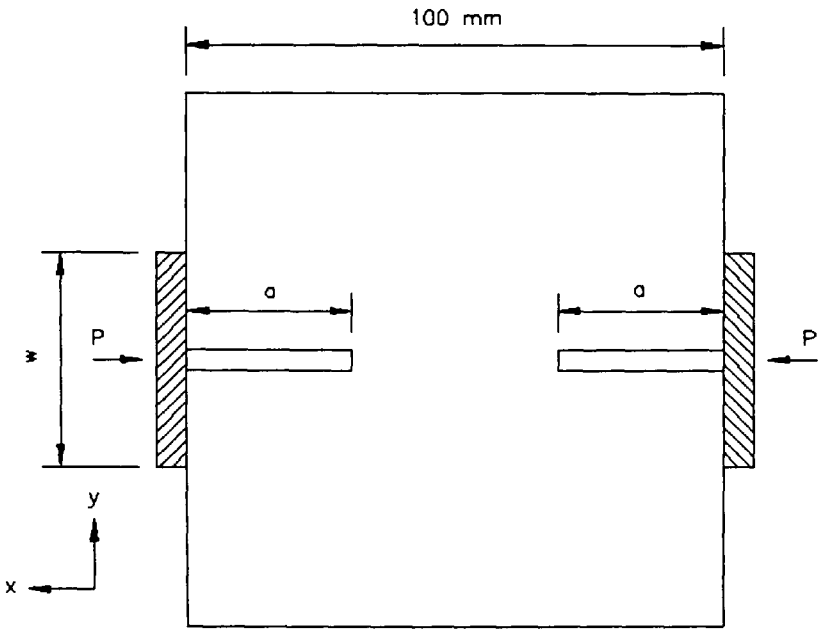

Figure 6.15 The Doubly Notched Axial Splitting Specimen (DNASS).

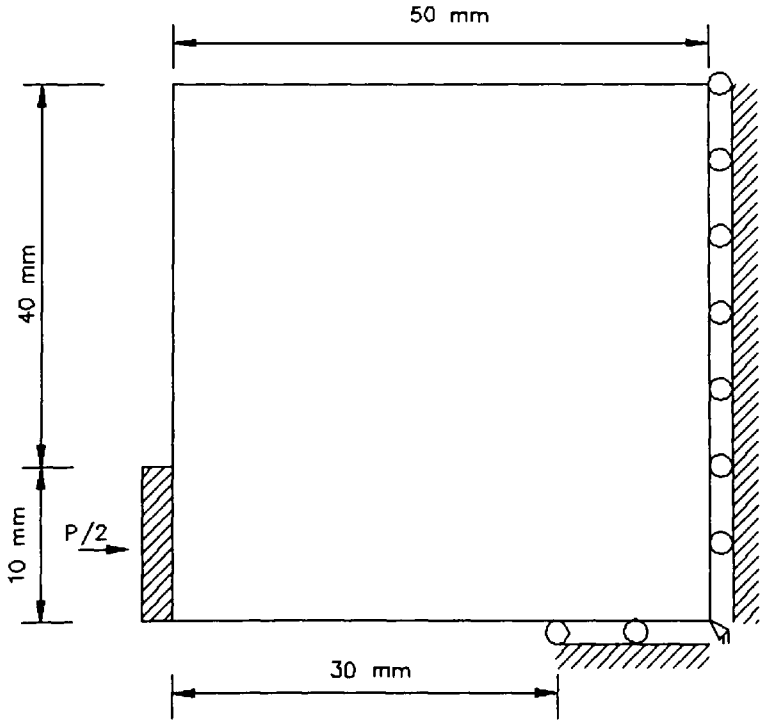

Figure 6.16 The Quarter-Specimen Analysed (DNASS).

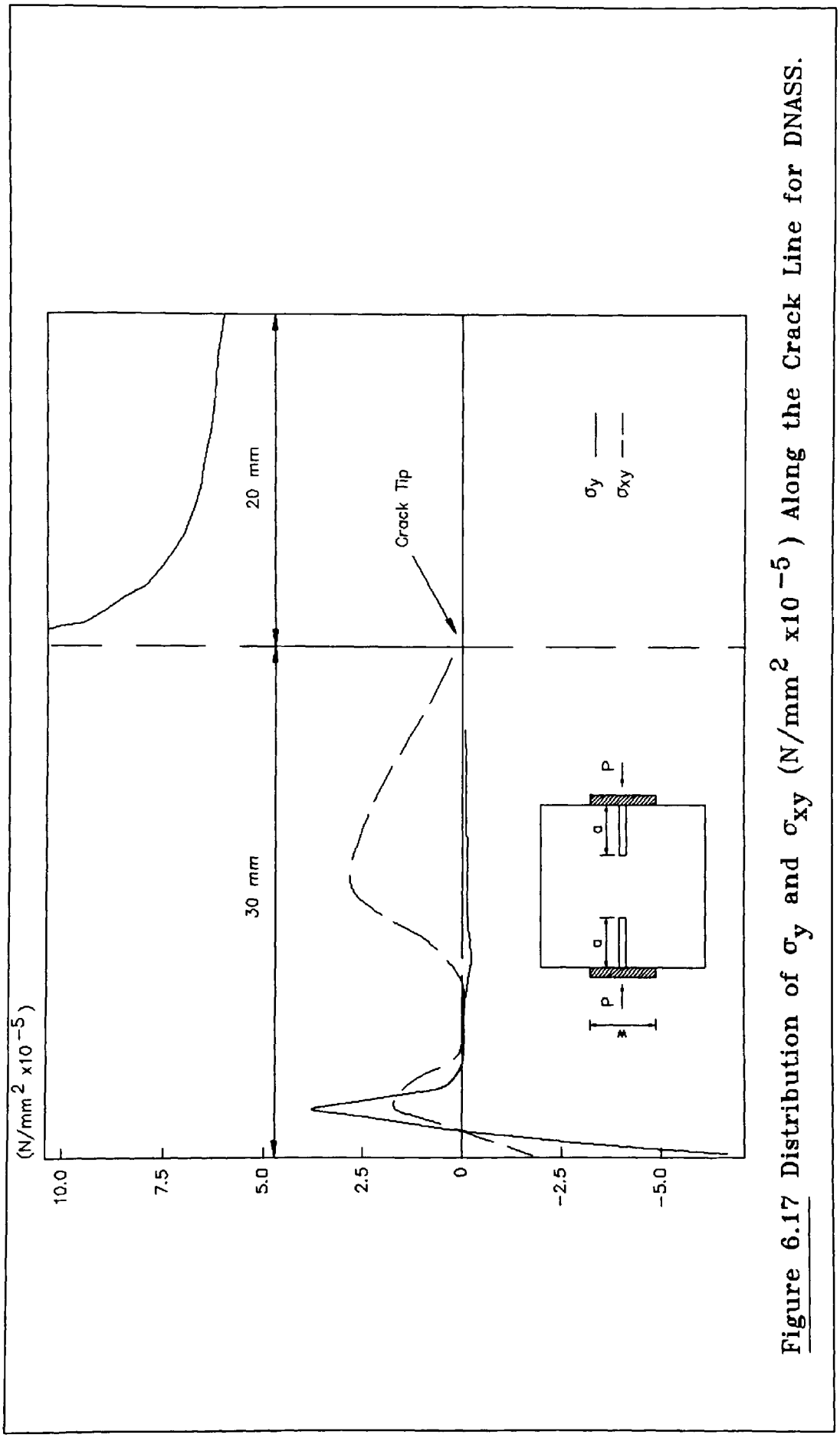

Figure 6.17 Distribution of σ_y and σ_{xy} (N/mm^2 x10^{-5}) Along the Crack Line for DNASS.

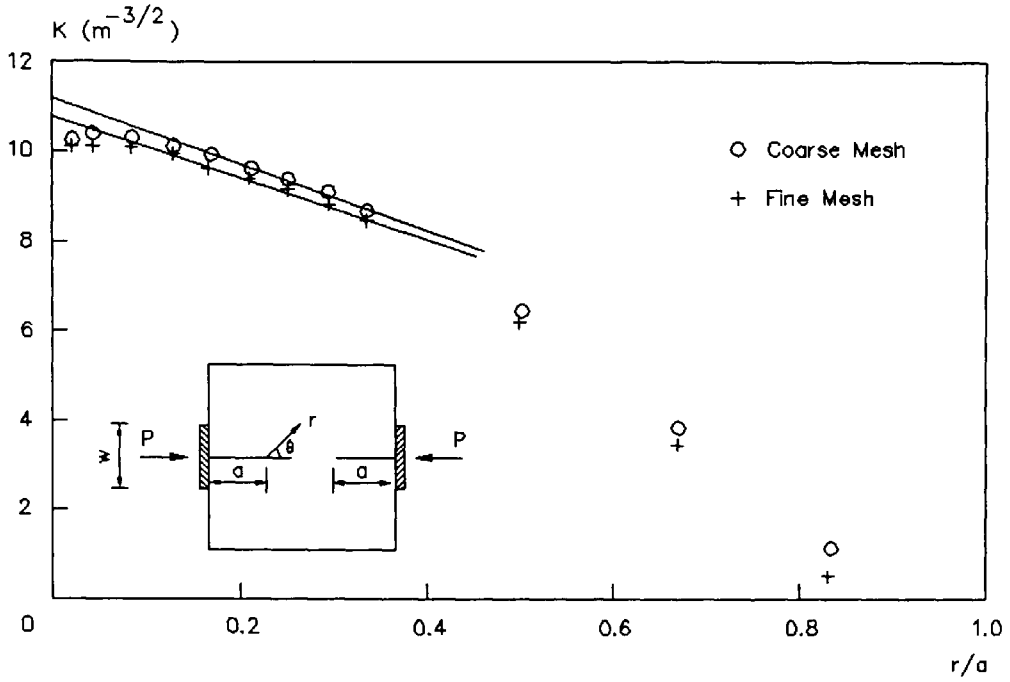

Figure 6.18 Variation of k with Radial Distance from the Crack Tip (DNASS, a=30 mm, w=20 mm) – triangular Elements.

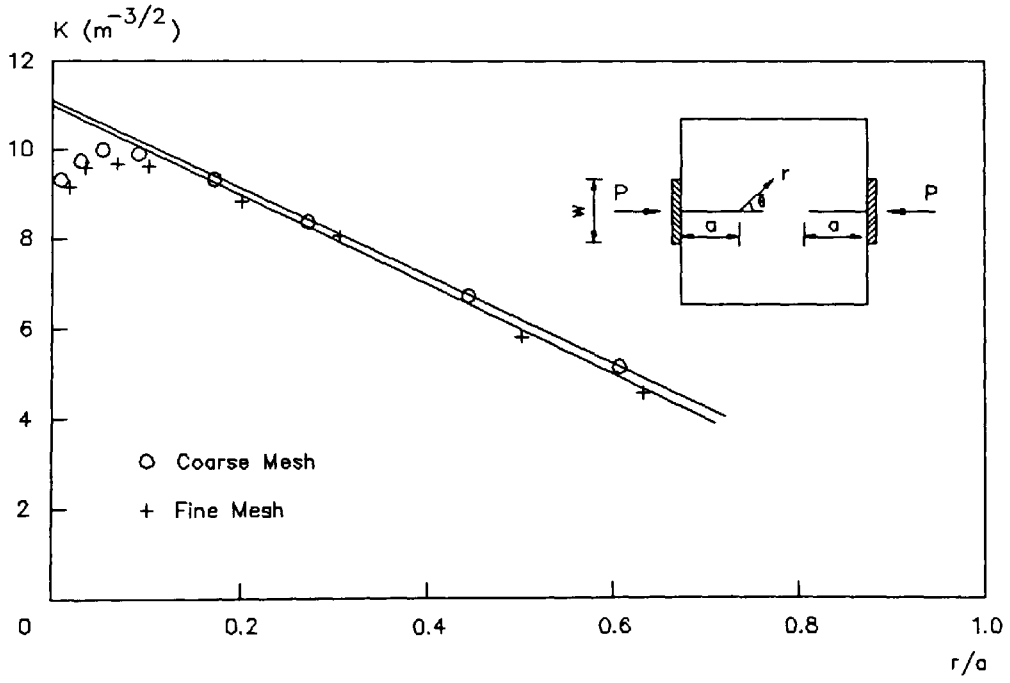

Figure 6.19 variation of k with Radial Distance from the Crack Tip (DNASS, a=30 mm, w=20 mm) – Rectangular Elements.

	Maximum	Location	Minimum	Location
σ_x	0.043	crack tip	-0.450	under loading platen
σ_y	0.175	crack tip	-0.113	"
σ_{xy}	0.192	under loading platen	-0.192	"
Principal Stress	0.175	crack tip	-0.450	"
Maximum Shear from Principal Stress	0.210	under loading platen	-	-

Table 6.1 Maximum and Minimum Stresses ($N/mm^2 x10^{-3}$) for the Problem of Figure 6.3 (SNASS, L=400 mm, a=100 mm, w=25 mm).

r (mm)	Coarse Mesh		Fine Mesh	
	$u_y (x10^{-9})$ (mm)	k $(m^{-3/2})$	$u_y (x10^{-9})$ (mm)	k $(m^{-3/2})$
0	-	-	-	-
0.3	12.1	13.70	12.2	13.81
2.5	36.9	14.46	37.0	14.50
3.8	46.4	14.75	46.5	14.78
5.0	54.3	15.05	54.3	15.05
6.3	62.1	15.33	62.0	15.30
7.5	68.8	15.55	68.8	15.56
8.8	75.5	15.77	75.7	15.81
10.0	81.6	15.98	81.7	16.00
16.7	110.5	16.74	110.6	16.76
23.3	135.6	17.40	135.5	17.38
30.0	157.5	17.81	157.4	17.80
36.7	175.8	17.97	175.7	17.96

Table 6.2 Variation of k with Radial Distance from the Crack Tip (SNASS, L=400 mm, a=100 mm, w=25 mm).

x (mm)	k ($m^{-3/2}$)	
	Coarse Mesh	Fine Mesh
63.3	19.88	19.87
70.0	19.32	19.30
76.7	18.51	18.49
83.3	17.48	17.50
90.0	16.39	16.41
91.3	16.22	16.26
92.5	15.91	15.92
93.8	15.70	15.67
95.0	15.37	15.39
96.3	15.06	15.14
97.5	14.58	14.61
99.7	13.71	13.81

Table 6.3 Variation of Stress Intensity Factor with x (SNASS, a=100 mm, w=25 mm).

Loading Platen Width w (mm)	k ($m^{-3/2}$)		
	DE	CSS	Eqn. 6.15
20	15.67(15.56)	15.01(14.83)	15.81
25	14.06(13.95)	13.96(13.89)	14.82
30	13.29(13.18)	12.91(12.64)	13.83

The figures in brackets are those obtained from the coarse mesh analyses.

Table 6.4 Comparison of Stress Intensity Factor Values (SNASS, L=400 mm, a=100 mm) - Triangular Elements.

Loading Platen Width w (mm)	k ($m^{-3/2}$)			
	DE	CSS	J-Integral	
20	15.92	15.87	15.56 15.63 15.58	15.59
25	14.59	14.30	14.36 14.43 14.37	14.39
30	13.54	13.32	13.30 13.34 13.35	13.33

Table 6.5 Comparison of k Values Using Different Loading Platen Widths (SNASS, L=400 mm, a=100 mm) - Rectangular Elements.

Crack Length a (mm)	k ($m^{-3/2}$)			
	Triangular Elements (DE)	Rectangular Elements		Eqn. 6.15
		(DE)	J-Integral	
50	10.44	11.17	10.87	14.82
75	12.72	13.23	12.94	14.82
100	14.06	14.59	14.39	14.82
125	14.57	14.72	14.69	14.82
150	14.63	14.78	14.82	14.82

Table 6.6 Comparison of k Values Using Different Crack Lengths (SNASS, L=400 mm, w=25 mm).

	Maximum	Location	Minimum	Location
σ_x	0.044	crack tip	-0.510	under loading platen
σ_y	0.126	crack tip	-0.208	"
σ_{xy}	0.027	under loading platen	-0.028	"
Principal Stress	0.126	crack tip	-0.550	"
Max Shear from Principal Stress	0.295	under loading platen	-	-

Table 6.7 Maximum and Minimum Stresses ($N/mm^2 x10^{-3}$) for the Problem of Figure 6.16 (DNASS, a=30 mm, w=20 mm).

Mesh Type	k ($m^{-3/2}$)	
	6-Noded Triangular	8-Noded Rectangular
Coarse	11.2	11.1
Fine	10.8	11.0

Table 6.8 Comparison of k Values (DNASS, a=30 mm, w=20 mm) - Triangular and Rectangular Elements.

Geometry Analysed	SNASS 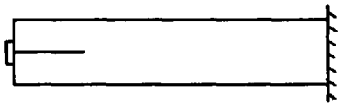 L=400 mm , a=100 mm	DNASS 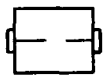 L=100 mm , a=30 mm	CCS  L=100 mm , a=30 mm
δ_{max} (mm) ($x10^{-7}$)	2.3	0.93	33.0
δ_{max}/a	0.023	0.031	1.1
δ_{max}/L	0.006	0.009	0.33
$\sigma_{y(c)}/\sigma_{y(t)}$ *	0.65	1.7	2.5

* Maximum compressive σ_y stress / maximum tensile σ_y stress

Table 6.9 Comparison of the Maximum Displacements / Stresses for Various Geometries Analysed - Triangular Elements.

CHAPTER SEVEN

FRACTURE TOUGHNESS OF CSF CONCRETE

7.1 Introduction

The process of fracture in cementitious materials is probably amongst the most complex of processes known in construction materials. Well over half a century ago Richart et al [110] reported test results of concrete failure under compressive loading. Since then numerous investigations have been carried out in this field and as a result there is now a fairly well established understanding of the physical process of cracking in concrete systems in the form of a relatively new field of study commonly known as fracture mechanics.

Kaplan [111] was the first to apply the principles of fracture mechanics to mortar and concrete. He employed rectangular beams containing sharp v-notches and subjected them to 3- and 4-point bending. During the past two decades a large number of attempts have been made by many researchers to develop test specimens and testing procedures for fracture toughness evaluation of concrete materials. Amongst the specimen geometries used are the double cantilever beam, the double torsion beam, the compact tension specimen and the notched beam in 3- and 4-point bending. Some of these geometries were discussed in Chapter 2 and a more comprehensive review of them is given by Swamy [37]. Work at the Lund Institute of Technology has led

to the RILEM recommendations [112] for fracture energy evaluation for concrete materials from the notched beam geometry. These specimens are large in relation to the uncracked ligament and it is desirable to develop more compact specimens, preferably based on standard quality control samples such as cubes.

Barr et al [39] introduced a specimen based on a cube modified by the introduction of two notches on opposite faces and used it to determine the fracture toughness of fibre reinforced concrete (FRC) materials. This work was based on a finite element solution employing constant strain triangular elements [72]. A more efficient solution for this geometry was developed by Sabir [73] which was later employed in the fracture toughness evaluation [43]. Another development, due to Kendall [105], is that of the compression splitting specimen incorporating a single axial notch. Although this specimen was initially modelled from glassy brittle materials, Karihaloo [106, 107] improved the model and more recently [40] used it to obtain the fracture toughness of concrete. Sabir et al [103] modified the model by introducing an additional notch at the opposite end which resulted in the specimen geometry and loading being symmetrical.

In this chapter results for the fracture toughness obtained from tests carried out on the Compact Compression Specimen (CCS) presented in Chapter 5 are reported. This geometry together with the SNASS and DNASS (Chapter 6) form the basis

basis of the experimental work on fracture toughness carried out during the course of this study. These tests resulted in unstable (sudden) failure of all the specimens employed and in order to control this fibres were introduced into some of the specimens. High modulus polypropylene fibres were used for this purpose and an assessment of the post-cracking behaviour was made through a toughness index based on the area under the load-displacement graph.

7.2 Constituent Materials and Definitions

7.2.1 Constituents

The following materials were used throughout the course of the present investigation.

Cement (OPC)

Ordinary Portland cement (OPC) type 1, commonly used in the UK and complying with BS 12: 1989. The physical properties and chemical composition of the OPC used are presented in Table 7.1.

Fine Aggregate

Fine natural sea dredged sand was used. The sieve analysis showed that the sand compiled with grade F of BS 882: 1983. The results of the sieve analysis and the physical properties are given in Tables 7.2 and 7.3, respectively.

Coarse Aggregate

The coarse aggregate was 10 mm single size crushed limestone supplied by a local quarry. The grading and physical properties of the aggregates are given in Tables 7.2 and 7.3, respectively.

Condensed Silica Fume (CSF)

In recent years growing interest has been shown in the use of CSF as a partial replacement material or as an additive in concrete. The material is a by-product of the silicon alloy industry and is composed of ultra-fine solid amorphous glassy spheres of silicon dioxide (SiO_2). It is produced during the manufacture of silicon or silicon alloys in arc furnaces at 2000° C. It originates from the condensation of SiO vapour, which mixes with oxygen in the upper cooler parts of the furnace, and is blown into bag-house filters. The fine particles have a size similar to tobacco smoke and are on average 80-100 times smaller than cement grains. The purity of the material can be affected by many factors such as the source, the type of alloy produced and the operating temperature of the furnace.

Due to its extremely fine particle size CSF fresh from the filters is very difficult to handle, transport and store. Dust control and mixing would cause further problems. To overcome this the CSF particles are mixed with an equal mass of water and are slurrified using high energy mixers. The pH of the mix is adjusted to lie between 4.5-5.5 to stabilise the slurry both physically and chemically. The slurry can be left at room temperature for prolonged periods without any significant settlement of solids occurring.

CSF affects the concrete in two major ways. Firstly due to its high pozzolanicity it contributes to the hydration

reaction between Portland cement and water by reacting with the calcium hydroxide producing additional gel

OPC + water ————————> CSH gel + calcium hydroxide

CSF + calcium hydroxide + water ————————> CSH gel

Calcium silicate hydrate (CSH) gel is the glue that binds the aggregates together and gives concrete its strength whereas calcium hydroxide makes little contribution to the development of strength.

Due to the reduced calcium hydroxide content, CSF concrete is less prone to sulphate attack and alkali-aggregate reaction than ordinary concrete. Furthermore, by virtue of their extreme fineness the CSF particles occupy the minute voids between the cement grains and on reaction produce cementitious gel which fills the pores thereby reducing the permeability and increasing the strength of concrete. Using normal mixing and curing conditions and a low percentage of CSF, 28-day strengths of 100 N/mm^2 or more have been obtained [113]. Burge [114] reported a 1-day strength of 100 N/mm^2 by employing a water/cementitious material ratio of 0.2 in a rich mix containing 30% CSF and 3% superplasticizer cured at room temperature.

An example of the durability of CSF concrete is the stilling basin of the Kinzua dam in the USA which has been the subject of severe abrasion erosion. Repairs were carried

out using steel fibre reinforced concrete which later proved totally inadequate. Following extensive studies it was decided that CSF concrete might offer a solution to the problem. Recent inspections [115] indicated that the new concrete is indeed performing well.

The CSF employed in the present study was supplied in the form of a slurry in which the mass ratio of CSF solids to water is 1:1. The physical properties and chemical composition of the CSF particles are given in Table 7.1.

Superplasticizer

Due to it's enormous surface area, CSF has a high water demand and in some cases it is necessary to employ superplasticizers to compensate for this and achieve workable concrete. In the second stage of the experimental work (Chapter 8) where high percentages of CSF were employed, Cormix SP1 which is a polymeric sulphonate based dark brown liquid was used. It has a specific gravity of 1.14 at 20° C, contains no chloride and does not induce air-entrainment.

Polypropylene Fibres

Fibres have increasingly been used in concrete and mortars to control cracking. Brittle materials, such as concrete, have small values of work of fracture. If they are reinforced with fibres having a greater tensile strain than

that of cement, the fibres will remain in place and bridge the cracks. In effect the fibres delay and control the tensile cracking of the material resulting in slow and stable crack growth. It is this characteristic of the fibres that gives the composite the properties of post-cracking tensile resistance, increased tensile capability and enhanced energy absorption [116].

There is a variety of fibres available for use in concrete. Amongst these are glass, steel, polypropylene and nylon fibres. Polypropylene fibres became commercially available in a new strong form in the 1960's. They were first suggested as an admixture to concrete by Goldfein [117] for the construction of blast-resistant buildings for the US corps of engineers. These were available in two forms, i.e. monofilament fibres and film fibres. The former suffers from low pull-out strength as a result of the poor bond between the fibre and the matrix. The use of film fibres in concrete is made possible by the process of fibrillation, which is the generation of splits in the longitudinal direction of the fibres [118]. This process leads to better bonding and results in a more effective composite action. The modulus of elasticity of these fibres ranges between 1-8 kN/mm^2, depending on the rate of loading, and is thus much lower than that of concrete.

The fibrillated polypropylene fibres used in the present investigation are the result of a development programme initiated in the late 1970's and aimed at producing stronger

fibres with much improved elastic modulus. These fibres have an elastic modulus of around 18 kN/mm^2. Their roughened surface provides a mechanical key which leads to effective bonding with the cement. Furthermore, it was found that the fibres can be dispersed easily into the mix. This may be the result of the surface lubrication treatment the fibres receive during manufacture. The effectiveness of these fibres in controlling the post cracking resistance of concrete is examined in the fracture tests discussed later in this chapter.

7.2.2 Definitions

In the work presented in this thesis, the following definitions are applied.

Water/Cement Ratio

In all the concrete mixes incorporating CSF, the water/cement ratio (w/c) is based on the total cementitious materials, i.e. OPC + CSF solids. In calculating the w/c ratio allowance was made for the water included in the CSF slurry.

CSF Content

The CSF content is defined as the mass ratio of CSF solids to the OPC particles employed in the reference mix, expressed as a percentage.

Fibre Content

The fibre content is defined as the ratio of the mass of fibres in the mix to the total wet mass, expressed as a percentage.

7.3 Mix Details

The reference mix was designed in accordance with the DoE publication [119] for a 28-day compressive strength of 35-40 N/mm^2. Tests were carried out in accordance with BS 812: part 2: 1975 to determine the moisture content and water absorption of both fine and coarse aggregate. The results are presented in Table 7.3. Prior to use, the aggregates were saturated with the required amount of water in air-tight containers under constant temperature conditions for 24 hours. The saturation of these materials prior to use ensures that the effect of any variation in moisture content is minimised. No problems were encountered in using the CSF slurry which was added to the freshly mixed concrete.

Two series of mixes were prepared for compressive strength and fracture toughness tests. The first (mixes A1-A6) was used for the plain concrete tests. In the second series (mixes B1-B12) fibres were added in order to asses the post-cracking performance.

Batch A (mixes A1-A6)

Six mixes with CSF contents varying between 0-12% all having a constant w/c ratio of 0.47 were prepared. Throughout the work presented in this thesis the CSF content is expressed as a percentage by mass of the cement in the reference mix (i.e. without CSF). The water/cement ratio is based on the total water (including that in the slurry) and total

cementitious material, i.e. cement plus CSF. The quantities per m^3 used in the reference mix were as follows

cement:	497 kg
water:	233 kg
fine aggregate:	770 kg
coarse aggregate:	835 kg

Table 7.4 gives the details of these mixes.

Batch B (Mixes B1-B12)

In this batch nine mixes were prepared. The mix proportions were identical to those of mixes A1, A2 and A4 (Table 7.4) with fibres in the range 0.05-0.15% by weight of the total wet mix being added. The details of these mixes are given in Table 7.5.

The dry ingredients were mixed together for ½ minute after which a mixture of the CSF slurry and water was added. The mixing was then continued for a further 1½ minutes. In the case of the FRC the fibres were added at this stage and mixing was continued for a total time of 2½ minutes. Effective dispersion of the fibres was achieved when these were introduced to the mix through a 26 mm sieve. In this way no problems with 'balling' of the fibres were encountered

The fresh concrete was subjected to slump tests in accordance with BS 1881: Part 102: 1983. The results of these tests for the concretes of batches A and B are given in Tables 7.4 and 7.5, respectively. In addition to the fracture toughness test specimens, 100 mm cube samples were prepared for compressive strength tests at 7 days and 28 days. In all cases the specimens were left in the steel moulds for about 24 hours and were subsequently demoulded and cured in water at 20° C for the specified period prior to testing.

7.4 Compressive Strength

In this section the results obtained from compressive strength tests are reported for the plain and fibre concretes described in the previous sections. Table 7.6 gives the results for the 7-day and 28-day cube strengths together with the densities for the plain concretes. Each result represents the average of those obtained from testing three samples. It is seen that CSF plays a significant role in enhancing the strength at both ages and that there is a consistent increase in strength for increasing CSF content. It can also be seen that the 7-day strengths are in the region of 65-70% of the 28-day values.

The results for the fibre concrete mixes are given in Table 7.7. Here additional cubes were prepared for compressive strength tests at 91 days. Again CSF improves the strength at both 7 days and 28 days. As with standard concretes, the addition of fibres (with few exceptions) appears to lead to slight reductions in the strength. It is also interesting to note that strength gain beyond 28 days decreases with increasing CSF content.

It is seen from Tables 7.6 and 7.7 that the density of the concrete decreases with increasing CSF content. This is considered to be largely a direct result of substitution of the less dense CSF particles for OPC and may be an indication of increased porosity.

The above results are in line with those generally obtained for CSF concrete [6]. However, a detailed study of the influence of CSF addition on the compressive strength, tensile strength and Young's modulus under different curing conditions is carried out in Chapter 8.

7.5 Fracture Parameters

When concrete materials are subjected to external loading, the initial response is largely linear elastic. However, due to their heterogeneous composition and the progressive growth of microcracks during loading, at some stage the load-displacement behaviour exhibits a nonlinear relationship. The linear elastic relationship for a pre-notched specimen, prior to catastrophic failure, is easily produced in the laboratory under both load and displacement control. It is also possible to obtain the post failure relationship if certain conditions are met. This is usually achieved by reducing the straining rate in the displacement control mode just before the anticipated failure load is reached. In this way if the straining rate is sufficiently slow during the post failure stage, the complete load-displacement relationship can be recorded. Nallathambi et al [54], for example, employed cross-head speeds between 0.1-0.5 mm/min for testing beams loaded in 3-point bending. For the larger specimens (600 mm by 80 mm by 76 mm) they reduced the straining rate to as low as 0.05 mm/min in order to obtain the complete load-displacement behaviour.

An idealised load-displacement curve for a notched concrete beam specimen is shown in Figure 7.1 [120]. In general, three distinct regions are observed. In region A the displacements increase approximately linearly with load, i.e. elastic response. Any small deviations are probably due to micro-cracking and/or pre-existing bond cracks in the

entire body. In region B slow and stable growth of micro-cracks takes place resulting in a strain hardening type of behaviour similar to that obtained with metallic materials. At the upper limit of this region the extensive micro-cracks ahead of the pre-existing crack front coalesce and progressively lead to large scale macro-cracking. This results in the inherently unstable growth of the pre-existing crack proceeded by catastrophic failure. The strain softening type of behaviour exhibited in the final stage of the loading (region C) can only be recorded by systematic reduction of the straining rate. To facilitate this control a stiff machine capable of loading in the displacement mode is necessary.

The above behaviour more or less encompasses all the major stages of crack propagation leading to failure in concrete materials as outlined by Swamy [121]. Whereas linear elastic fracture mechanics (LEFM) can be successfully applied to region A of the load-displacement behaviour, the contribution to the fracture toughness by the nonlinear regions must be assessed by a nonlinear approach. Amongst these approaches are the crack opening displacement (COD), J-integral and crack extension force.

Several investigations have been carried out to evaluate the fracture toughness parameters of concrete materials using LEFM and/or nonlinear analysis. In the present work LEFM is employed to evaluate the fracture toughness parameters by two approaches. In the first, the critical stress intensity

factor k_c is evaluated by employing the load at failure in the finite element analysis described in Chapter 4. In the second approach, the area under the linear part of the load-displacement curve recorded directly from the testing machine is utilised to estimate the critical strain energy release rate G_c.

In the case of the fibre concrete tests the above fracture toughness parameters are augmented by a toughness index evaluated from the area under the load-displacement curve.

7.6 Fracture Toughness Test - (CCS)

The compact compression specimens (CCS) for the fracture toughness tests were prepared by means of standard 100 mm cube moulds. The notches were introduced using a specially adapted horizontal milling machine and a 1 mm thick diamond impregnated cutting disc. Great care was exercised in the preparation of the notches. This was achieved by manufacturing a steel housing containing slits on two opposite walls thus enabling the cutting disc to descend through it during notching. Accurate alignment of the concrete cube inside the housing was made possible by introducing a 1.5 mm thick steel plate between the cube and one of the housing walls held tightly in place by means of a screw. The provision and subsequent tightening of an additional screw on the adjacent side ensured that the specimen was held firmly while being notched. This arrangement facilitated the introduction of notches up to 45 mm in depth. The details of the housing are shown in Plate 7.1.

Plate 7.2 shows a specimen positioned in the machine ready for notching. Using this arrangement it was possible to produce notches to an accuracy of ±0.25 mm and hence all fracture toughness results are based on nominal notch-depth values. The concrete cubes were cured in water at 20° C for a period of 21 days at which time the notches were introduced. The samples were then returned to the curing tank until they were tested at 28 days. Specimens with 25

mm, 30 mm, 35 mm and 40 mm deep symmetrical notches were prepared. For each geometry three specimens were made giving a total of 72 samples for the plain concrete tests and 108 for the fibre concrete tests.

The fracture tests were carried out at nominal room temperature by means of a 250 kN Instron testing machine. Plate 7.3 shows a specimen in position ready for testing. The modified cubes were subjected to eccentric compressive loads applied via two 110 mm long steel bars having a 5 mm square cross section positioned along two opposite edges of the specimen. Prior to the application of the load the specimen was placed in a horizontal position by supporting it at the base with an additional steel bar.

The load was applied under displacement control with a cross-head speed of 0.4 mm/min. This is close to the RILEM recommended speed of 0.3 mm/min. As deformation took place the load was concentrated at the inside edges of the loading steel bars and consequently in the finite element analysis the points of application of the load were taken to be located 5 mm from the edge of the specimen. Some specimens failed in shear under the load. The results presented here are for those specimens whose tensile failure occurred at the crack tip, remote from the line of loading, in the opening mode of fracture.

Figure 7.2 gives an example of load-displacement curves up to failure for the three plain concrete specimens with 30 mm

symmetrical notches prepared from mix A4. In all cases there is a significant amount of interaction between the specimen and the testing machine during the early stages of loading. After the initial bedding-in which is characterised by the initial curved parts of the graphs, the results follow linear relationships until sudden failure into halves. The average load at failure for this geometry (mix A4, a=c=30 mm) is 5.80 kN. The coefficient of variation for the failure loads of the three specimens is 3.7% which is well within the accepted range for results of tests conducted on concrete materials. Plate 7.4 shows a typical failed specimen in which failure takes place along the initially uncracked ligament in the plane containing the pre-notches.

The load-displacement graphs for samples of the same geometry (a=c=30 mm) with 0.15% fibres prepared from mix B12 are shown in Figure 7.3. It is seen that the load-displacement relationship is similar to that for plain concrete up to first cracking. At this point the load drops to a level which represents additional strength imparted by the fibres to the brittle matrix. The fibres control the fracture process and maintain the integrity of the specimen after first cracking and the residual strength gives the concrete further load carrying capacity. Whereas in this test cracking is accompanied by a relatively low level of noise, in the case of the plain concrete tests failure was accompanied by a loud noise which is a characteristic of brittle failure.

The loads at failure for this geometry (mix B12, a=c=30 mm) shown in Figure 7.3 give an average of 4.99 kN with a coefficient of variation of 6.0%. This represents a reduction in the failure load of about 14% due to the inclusion of the fibres. As will be seen in the next section this leads to a corresponding 14% reduction in k_c when it is evaluated by the stress intensity factor approach. However, the reduction in k_c is more than compensated for by the obvious benefits of the fracture propagation control provided by the residual strength imparted by the fibres.

7.7 Fracture Toughness - Stress Intensity Factor Approach

Detailed finite element analyses of the compact compression specimen (CCS) geometry were presented in Chapter 5. The results for the stress distributions confirmed the existence of relatively high tensile stresses in the vicinity of the crack tip remote from the loading and normal to the plane containing the crack. These stresses lead to crack propagation and failure of the specimen in the opening mode of fracture which was evident in the majority of the tests conducted. The finite element solutions given in Chapter 5 were employed to produce values for the stress intensity factors for the range of notch sizes employed in the testing programme.

The fracture toughness k_c of a material can be defined as the critical value of the stress intensity factor corresponding to the load which causes failure in the specimen. Typical load-displacement graphs obtained from the fracture tests were discussed in the previous section. These give the loads at failure which can be employed in the finite element analyses to compute k_c. The results for the stress intensity factors given in Chapter 5 were obtained for a unit compressive load which if multiplied by the load at failure would give the corresponding values of the fracture toughness k_c.

Tables 7.8 and 7.9 give the failure loads obtained for the plain concrete (mixes A1-A6) tests conducted at 28 days. It

can be seen that the test yields reproducible results for the failure load with coefficients of variation well below 10%. These tables also give the fracture toughness values obtained by following the above procedure and employing the average load at failure. In Figure 7.4 the results for k_c are shown as a function of the CSF content for the range of a/d ratios considered. It can be seen that although there is a small tendency for k_c to increase with increasing CSF content, the variation is not significant. For a given a/d ratio the coefficients of variation for the range of CSF contents employed range between 2.8% and 4.6%. These results are in contrast to those obtained for the compressive strength (Table 7.6) where it was shown that increasing CSF content leads to consistent increase in the strength.

Figure 7.5 gives the results expressed in terms of the a/d ratio. Here, it is seen that increasing the notch size beyond 30 mm leads to a significant decrease in k_c. The coefficients of variation for the fracture toughness results for a given a/d ratio range between 8.1% and 13.1%.

Further tests were carried out on samples made from the series B mixes. In these the concretes contained polypropylene fibres in the range of 0.05-0.15%. The results are presented in Tables 7.10-7.12. Once more, the low coefficients of variation show that reproducible results for the loads at failure are obtained. The tables also give the fracture toughness values obtained by employing the average loads in the finite element analyses. Close examination of

these reveals that the roles of the CSF and the a/d ratio are not influenced by the inclusion of the fibres. Figure 7.6 gives a comparison between the fracture toughness values for the plain and fibre concretes expressed as a function of the a/d ratio. Here the results for the plain concrete are shown as the average of those obtained from mixes A1-A6, and those for the fibre concretes are the averages determined from the series B mixes. Generally the inclusion of fibres causes a reduction in the load at first failure. The effect of the fibre content on the k_c values evaluated from these failure loads and the finite element analyses is demonstrated in Figure 7.7. Here the values are averaged for the three CSF contents (0-8%) and shown as a function of the fibre content. It can be seen that for all the a/d ratios considered, increasing the fibre content leads to a small reduction in the values of the fracture toughness when evaluated in this way. This, clearly, can be misleading and in order to quantify the complete behaviour of fibre concretes, a toughness index is introduced (section 7.10) to take account for the additional toughness imparted by the fibres during the post-cracking stage.

7.8 Critical Strain Energy Release Rate G_c

In this section the fracture toughness is determined using an energy approach. Table 7.13 gives the failure loads and the corresponding maximum displacements, each being the average of three results, for the various geometries. The critical strain energy release rate (SERR) G_C is evaluated from the area under the load-displacement curve up to the failure load. This is considered to give the energy required to cause the pre-crack to extend over the initially uncracked ligament area. The critical SERR, G_C, evaluated in this way, i.e. the SE1 method, is also given in Table 7.13. It is seen that, for all concretes, G_C decreases rapidly with increasing notch size with the values ranging between approximately 20 Nm/m^2 and 120 Nm/m^2.

It is well known that the utilisation of the load-displacement results in this way without accounting for the interaction that takes place between the machine and the specimen can lead to erroneous results. The extent of the inaccuracies will largely depend on the relative stiffness of the specimen under test to that of the testing machine. Under the applied load the total displacement of the machine-specimen system is the sum of the displacements of the specimen and the machine. The stiffness of the test specimen will clearly depend on the size of the pre-notch and the specimen's geometry in relation to the loading. In the case of the CCS, the stiffness of the testing machine, k_m, is higher than the stiffness of the test specimen

resulting in an increase in the overall flexibility of the system. Figure 7.8 gives a schematic representation of the load-displacement relationships for the testing machine and the machine-specimen system obtained from the fracture tests. The machine stiffness is determined from the load-displacement relationship obtained by compressing the loading platens (in displacement mode) against each other. Under a given load k_m is related to the deformation of the testing machine δ by

$$k_m = \frac{P(\delta)}{\delta} \tag{7.1}$$

Where $P(\delta)$ is the load which produces the displacement δ. The work done during this deformation is given by the area under the load-displacement curve, i.e.

$$E_m = \frac{P(\delta)\ \delta}{2} \tag{7.2}$$

Where E_m gives the energy absorbed by the testing machine in producing the deformation δ. Substituting for the displacement δ from equation 7.1 into equation 7.2 we obtain

$$E_m = \frac{[P(\delta)]^2}{2\ k_m} \tag{7.3}$$

If the total displacement of machine and sample, under the load P, is Δ then the energy required to cause the specimen to fracture over the ligament area is

$$E_S = \tfrac{1}{2} P(\Delta)\ \Delta - \frac{[P(\delta)]^2}{2\ k_m} \qquad (7.4)$$

The second term in the right hand side of equation 7.4 represents the correction that should be applied due to the deformation of the testing machine. Equation 7.4 demonstrates the need for a stiff testing machine in order to obtain accurate estimates of the fracture energy from the load-displacement relationships. On the other hand, the more flexible the test specimen, the less interaction will take place between the specimen and the machine under the load, and hence a greater proportion of the expanded energy will be absorbed by the failed test specimen.

Figure 7.9 gives the load-displacement relationship for the testing machine (in displacement control) for a cross-head speed of 0.4 mm/min. The stiffness k_m obtained from the slope of the straight line is found to be 175 N/m. In this way several values for k_m were evaluated for a series of cross-head speeds and the results are shown in Figure 7.10. These results suggest that less inaccuracies will result as the loading rate is increased.

The critical strain energy release rate G_C is obtained from the estimates for E_S (equation 7.4) at the failure load divided by the ligament area, viz

$$G_C = \frac{E_S}{d\ (d-2a)} \qquad (7.5)$$

The procedure outlined above for calculating G_C is referred to as the SE2 method and the results are given in Table 7.13. In all cases it was found that the corrections that were applied to take account of the energy absorbed by the testing machine were higher for the specimens with the smaller notch sizes. This correction was of the order of 50% for the 25 mm notched specimens decreasing to about 8% for the specimens with 40 mm symmetrical notches. This indicates that the larger the notch size, the more flexible the specimen and hence the less the interaction between the specimen and the testing machine. This was expected and is in agreement with the discussion presented earlier. Figure 7.11 gives the load-displacement graphs for the various a/d ratios employed in mix A4. It is evident that the apparent specimen stiffness decreases as the notches increase in size.

It can be seen that the influence of the notch size on G_C (Table 7.13) is significantly higher than that on the fracture toughness k_C, (Tables 7.8 and 7.9). The G_C values obtained by the SE2 method range between 18 Nm/m^2 and 67.8 Nm/m^2.

Finally G_C was calculated indirectly (SE3 method) from the fracture toughness values given in Tables 7.8 and 7.9. This is done by employing equation 3.15 in which E=30 kN/mm^2 was considered appropriate for the range of strengths given in Table 7.6 [122]. Figure 7.12 gives the results for G_C, as obtained from the SE2 and SE3 methods, expressed as a function of the a/d ratio. It can be seen that whereas the indirect method (SE3) yields more or less constant values, those obtained from the load-displacement relationships (SE2 method) show considerable decrease in G_C as the pre-notch increases in size. Similar results were obtained by Nallathambi et al [54] who tested concrete beams of various sizes in 3-point bending. They employed a w/c ratio of 0.5 and coarse aggregates ranging between 5 mm and 20 mm. Their results for concrete containing 10 mm coarse aggregates are shown in Figure 7.13, together with those obtained in the present study averaged over the range of CSF contents. For the range of specimen sizes employed by Nallathambi et al, G_C values in the range 40-130 Nm/m^2 were obtained. Petersson [45] gives values in the range 60-100 Nm/m^2 for beams in 3-point bending, compared to 30-60 Nm/m^2 reported by Hilsdorf and Ziegeldorf [123]. Following an exhaustive testing program, Go and Swartz [124] reported a 'true estimate' for G_C to be 67 Nm/m^2 ± 3%. The present work yields values in the range 18-68 Nm/m^2 using the SE2 method and 9.3-17.5 Nm/m^2 employing the SE3 method.

One of the problems involved in calculating G_C through an energy approach is that associated with the true fracture

surface area. Nallathambi and Karihaloo [120] estimated that due to the tortuosity of the fracture path in their specimens the fracture area is about 10% more than the area measured in the plane of the crack. Swamy [37] suggested that the true area can be several times greater than the theoretical area. This uncertainty is considered to be one of the major factors leading to the wide scatter of results obtained by different investigators. In the present work no allowance was made for this and the measured area under the load-displacement graphs were divided by the plane area of the uncracked ligament. It is therefore expected that the results obtained using the SE2 method are overestimated by a factor which represents the ratio of the true fracture area to the theoretical area. An estimate of the tortuosity of the fracture path may be obtained from the relationship between the results obtained using the SE2 and SE3 methods. In this way the tortuosity factor may be considered as the ratio of the G_C values obtained by the two aforementioned methods. The tortuosity factors (TF) thus determined are included in Table 7.13. It is tentatively concluded that the true fracture area is of the order of 2-5 times that of the plane area, and as expected this factor increases with increasing uncracked ligament. This may be explained by the fact that with the larger areas available for crack extension the advancing crack front will encounter more of the coarse aggregates responsible for the tortuosity during the fracture propagation process.

Table 7.14 gives the results for G_C for the fibre concrete samples of the series B mixes obtained by the three aforementioned methods. It can be seen that as with plain concrete the indirect method (SE3) yields results for G_C which are lower than those of the SE2 method. This difference is again attributed to the tortuosity factors which are also included in Table 7.14. As with the case of plain concrete the tortuosity factors are in the range 2-5. Figure 7.14 shows the results for both the plain and fibre concretes as evaluated by the SE2 method. It is seen that no significant influence is caused by the introduction of the fibres. In Figure 7.15 the critical strain energy release rate G_C is shown as a function of the fibre content for the various a/d ratios. The results demonstrate that for a given pre-notch size, the weight fractions of fibres employed in the present work have little influence on G_C.

7.9 Toughness Index

The definition of toughness index (TI) due to Barr is illustrated in Figure 7.16a. The test specimen is loaded until a displacement which is twice that at first crack is produced. The toughness index is evaluated from

$$TI = \frac{A + B}{4A} \qquad (7.6)$$

where A is the area under the load-displacement curve up to first crack (displacement δ) and B is the additional area up to twice the displacement at first crack, 2δ. The latter area represents the energy absorbed by the fibres. According to this definition the TI varies from 0.25 for plain concrete to a theoretical maximum value of unity with an elastic plastic response giving 0.75. The alternative definition shown in Figure 7.16b gives the toughness index TI as

$$TI = \frac{A + B}{3A} \qquad (7.7)$$

In this case the TI varies from 0.33 to a maximum of unity for an elastic plastic material.

In the present work the influence of the inclusion of the fibres on the post cracking behaviour is evaluated through the TI obtained from equation 7.6. The results for the various geometries and CSF additions are given in Tables

7.15-7.17. It was found that for a given crack geometry there were no significant differences in the values of the TI for the range of CSF contents used. In Figure 7.17, the toughness indices are averaged for each a/d ratio and presented as a function of the fibre content. It is seen that even with small additions of fibres, the post-cracking performance is increased appreciably.

7.10 Conclusions

The work presented in this chapter is the result of laboratory tests conducted to determine the strength and toughness characteristics of CSF concrete. Two series of concrete mixes were investigated. In the first partial replacements of cement by CSF up to 12% by mass of cement in the reference mix were employed. In the second series polypropylene fibres in the range 0.05-0.15% by mass of the wet mix were introduced. As expected, it was confirmed that CSF plays an important role in enhancing the compressive strength at all ages and that the strength increases with increasing CSF content. It was also found that the rate of strength gain beyond 28 days decreased with increasing CSF content. As with standard concrete, the inclusion of fibres led to a slight reduction in the compressive strength.

LEFM principles were employed to evaluate the toughness characteristics of the concretes employed. This was done by two distinct approaches. In the first, the critical stress intensity factor (or the fracture toughness) k_c was obtained using experimental and numerical techniques. In contrast to the results for the compressive strength, it was found that k_c did not increase appreciably with increasing CSF content up to 12%.

Upon examination of the results for k_c in relation to the pre-notch size it was found that as the pre-notch increased in size, k_c increased and then decreased beyond a notch size

of 30 mm. Similar results were obtained by Petersson [45] and Carpinteri [46] from flexure tests conducted on notched beams. In viewing the literature, however, it was found that almost all possible trends of variation in k_c with increasing notch size have been encountered by independent workers employing flexure tests.

In the second approach the areas under the load-displacement curves obtained from the laboratory tests were used to evaluate the critical strain energy release rate or the fracture energy G_c with due allowance being made for the machine-specimen interaction. G_c evaluated in this way showed a considerable decrease with increasing pre-notch size. When the results are expressed as a function of the ratio of notch size 'a' to uncracked ligament size d, it was found that other investigators [45, 54] encountered similar behaviour when using 3-point bend specimens. Petersson [45] gives values for G_c in the range 60-100 Nm/m^2 for a/d values between 0.2 and 0.4. For the same range of a/d values, the present work yields values for G_c in the range 18-68 Nm/m^2. Whilst it is recognised that the differences in the results are attributable to the methods of testing and materials employed, it is considered that a major factor influencing this is the fracture path and its tortuosity for which no allowance is made in the present study.

G_c was also calculated indirectly through k_c. The results obtained were several times smaller than those evaluated using the load-displacement relationships. The difference

between the results is attributed to the fact that the fracture path is tortuos and can be several times greater than the plane fracture area assumed in the calculation. The ratio of the G_C values obtained by the SE2 and SE3 methods was used to estimate the degree of tortuosity. This was found to be of the order 2-5 times the plane area for both plain and fibre concretes.

The inclusion of fibres (up to 0.15%) generally led to slight decreases in the calculated values of k_C and G_C. Because of the procedures employed in calculating k_C and G_C, these reductions are direct results of the reductions taking place in the maximum loads recorded during the fracture tests. The reductions in the maximum loads, due to fibre inclusion, can only be explained in terms of incomplete bonding between the fibres and the concrete matrix resulting in increased flaw sizes. It is obvious, however, that fibres enhance the toughness characteristics of brittle materials and this is evident from the residual strength exhibited by the load-displacement curves after first cracking. In the present work this enhanced toughness was assessed by a toughness index evaluated from the load-displacement relationship. It was found that increased toughness was obtained as the fibre content was increased. The toughness index also increased with increasing notch depth.

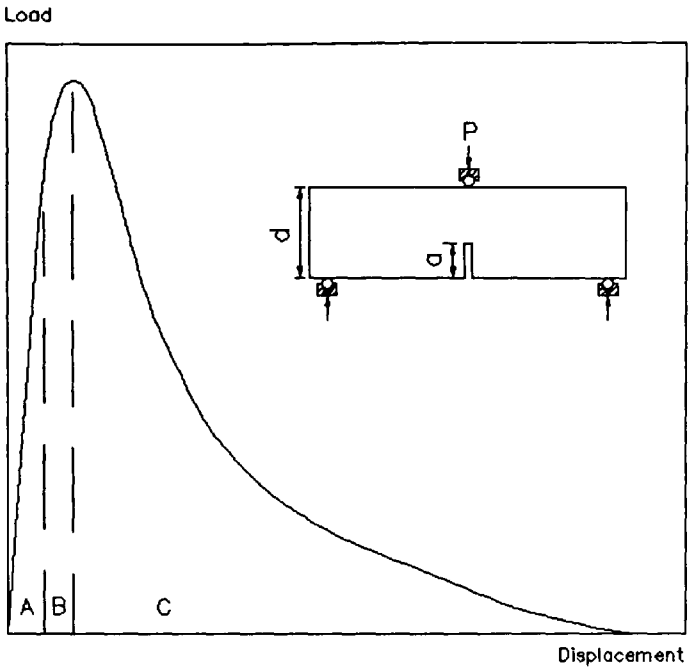

Figure 7.1 Idealised Load–Displacement Relationship for a Notched Beam.

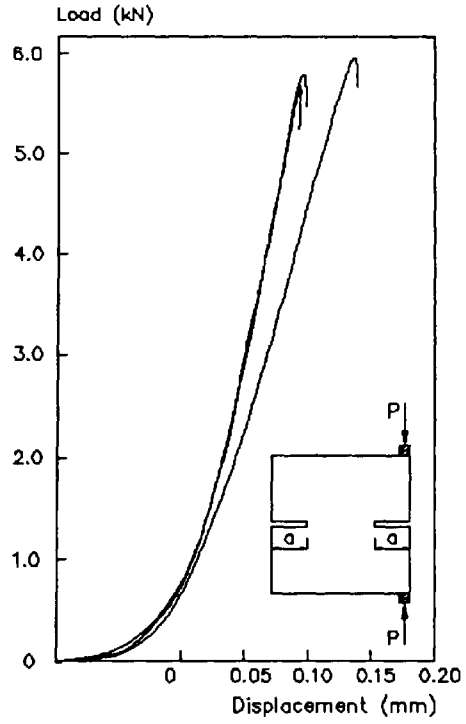

Figure 7.2
Typical Load–Displacement Graphs for the CCS (Mix A4, a=30 mm).

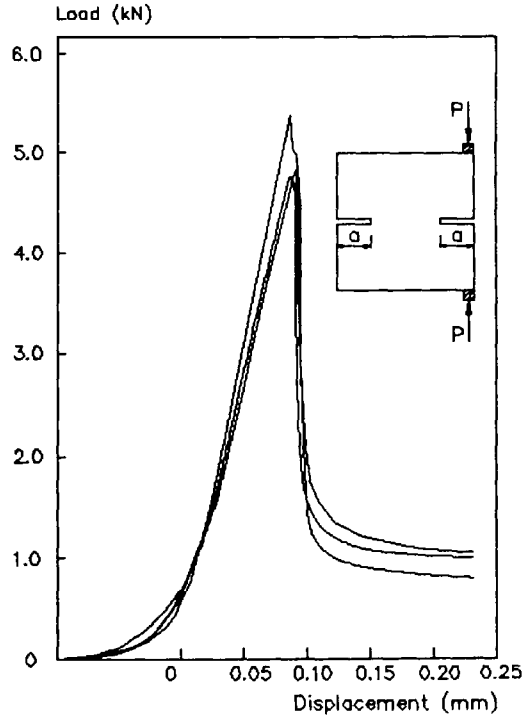

Figure 7.3
Typical Load–Displacement Graphs for the CCS (Mix B12, a=30 mm).

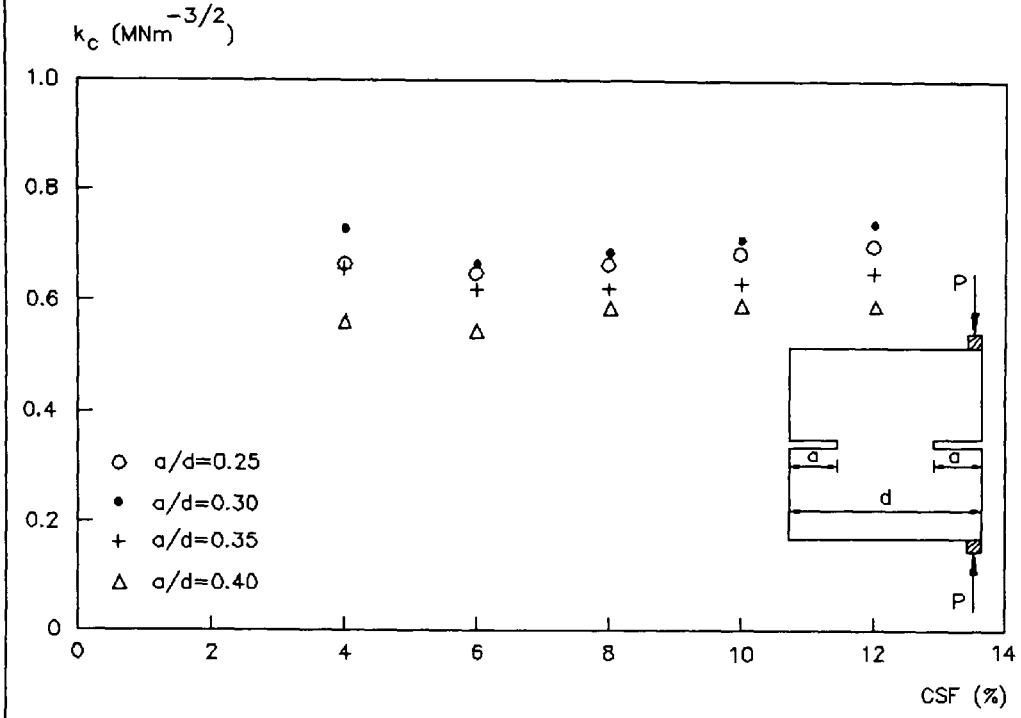

Figure 7.4 Variation of k_c with CSF Content for Different a/d Ratios (CCS).

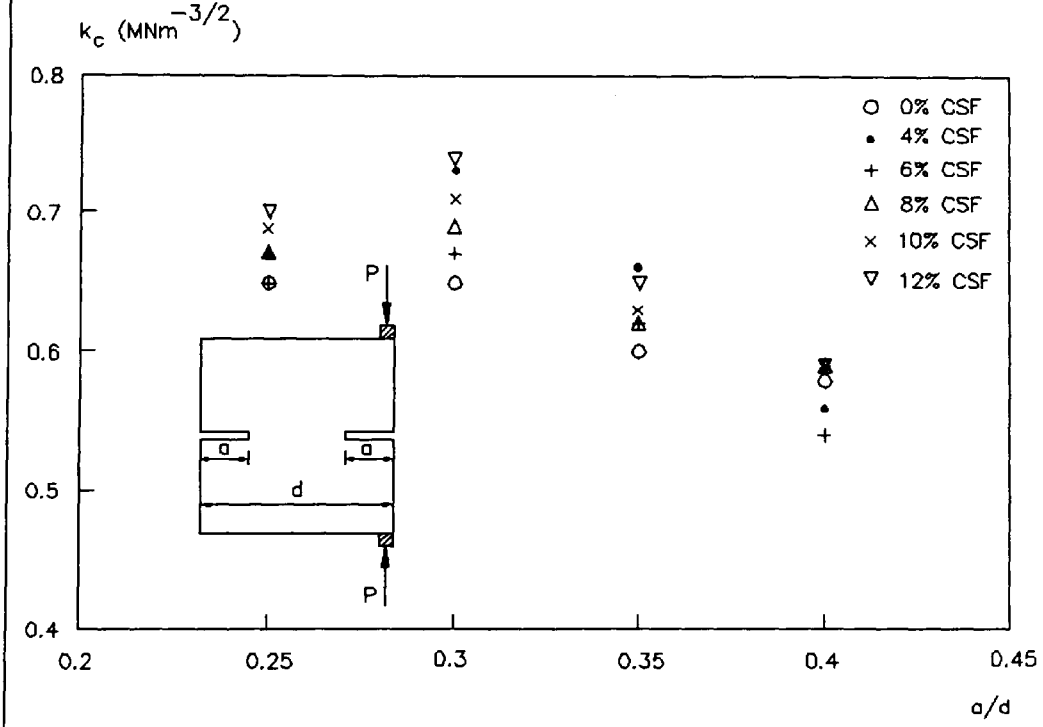

Figure 7.5 Variation of k_c with Notch Size for Different CSF Contents (CCS).

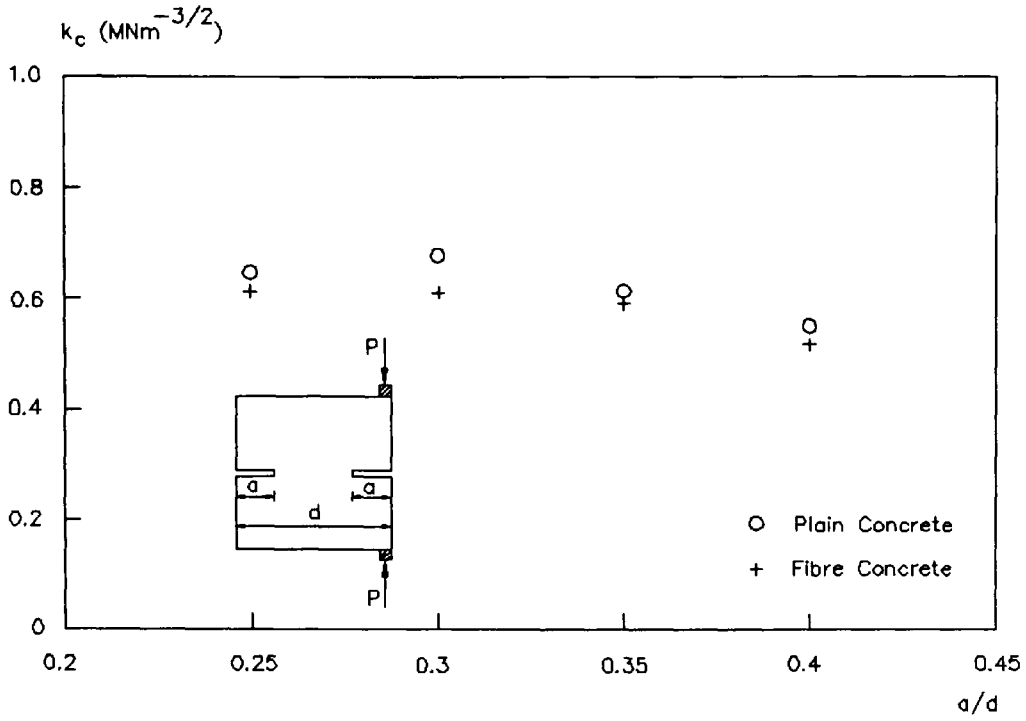

Figure 7.6 Variation of k_c with Notch Size for Plain and Fibre Concrete (CCS).

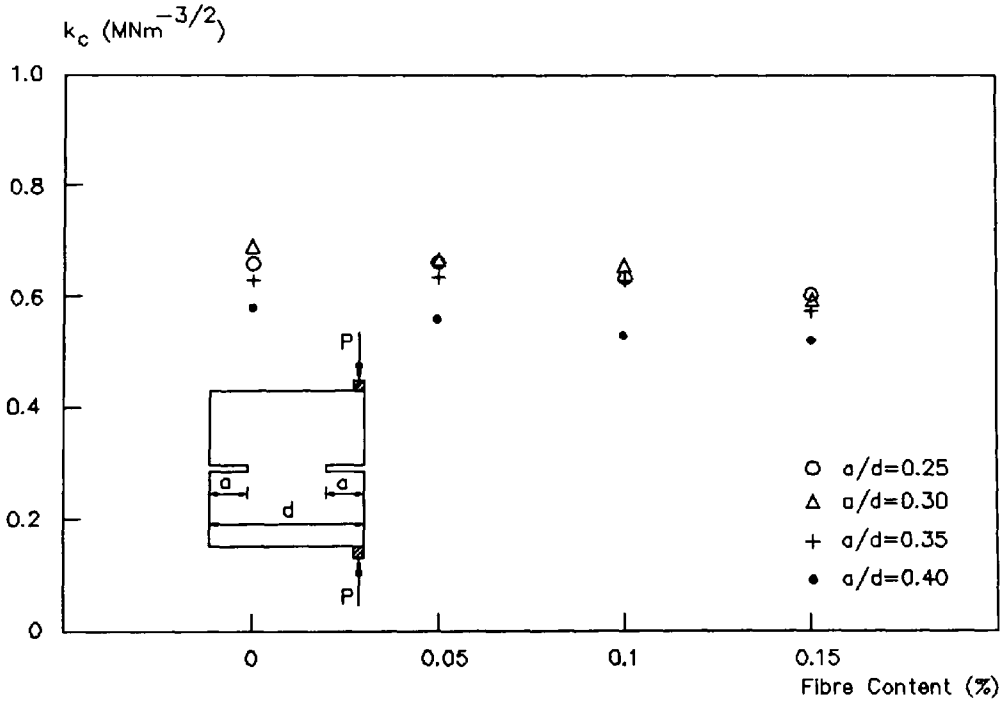

Figure 7.7 Variation of k_c with Fibre Content for Different a/d Ratios (CCS).

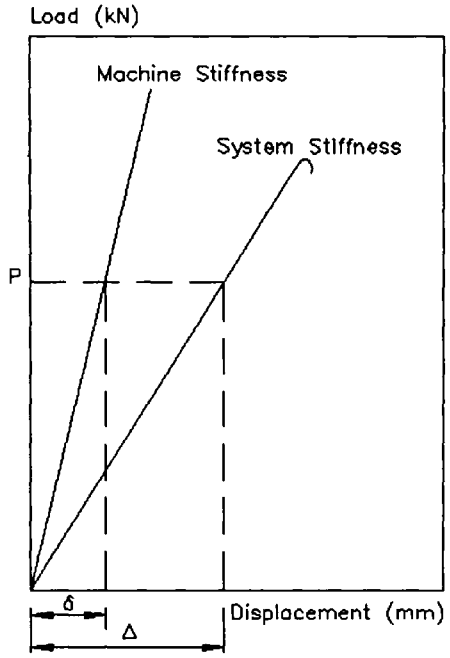

Figure 7.8 Schematic Load-Displacement Curves for Machine and Machine-Specimen System.

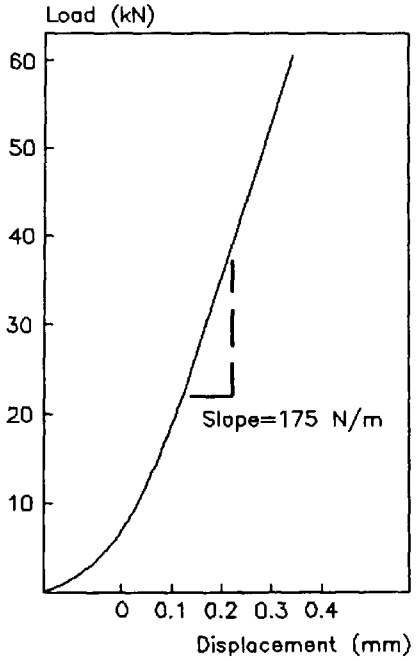

Figure 7.9 Load-Displacement Graph for Testing Machine - Cross-Head Speed=0.4 mm/min.

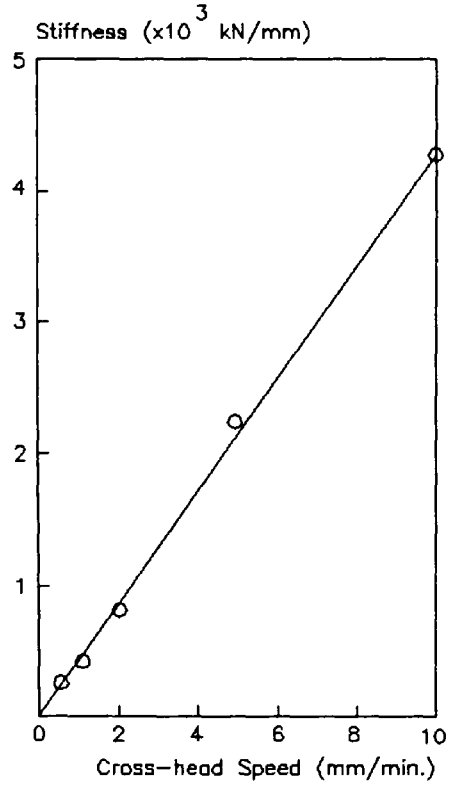

Figure 7.10 Variation of Machine Stiffness with Cross-Head Speed.

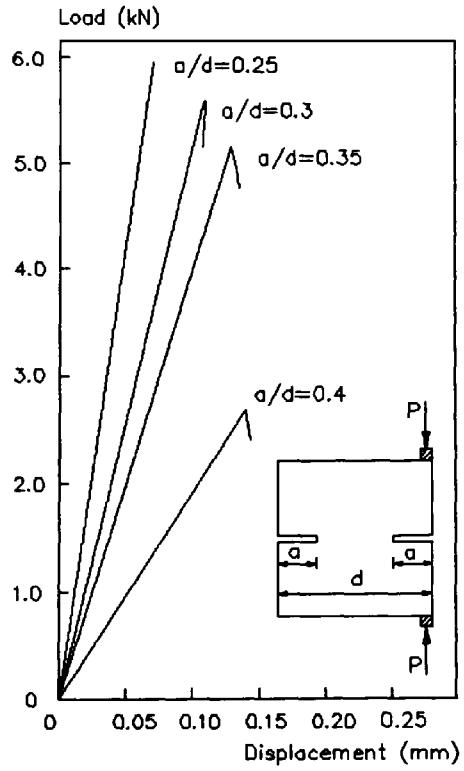

Figure 7.11 Typical Load-Displacement Graphs for the CCS for Different Notch Sizes (Mix A4).

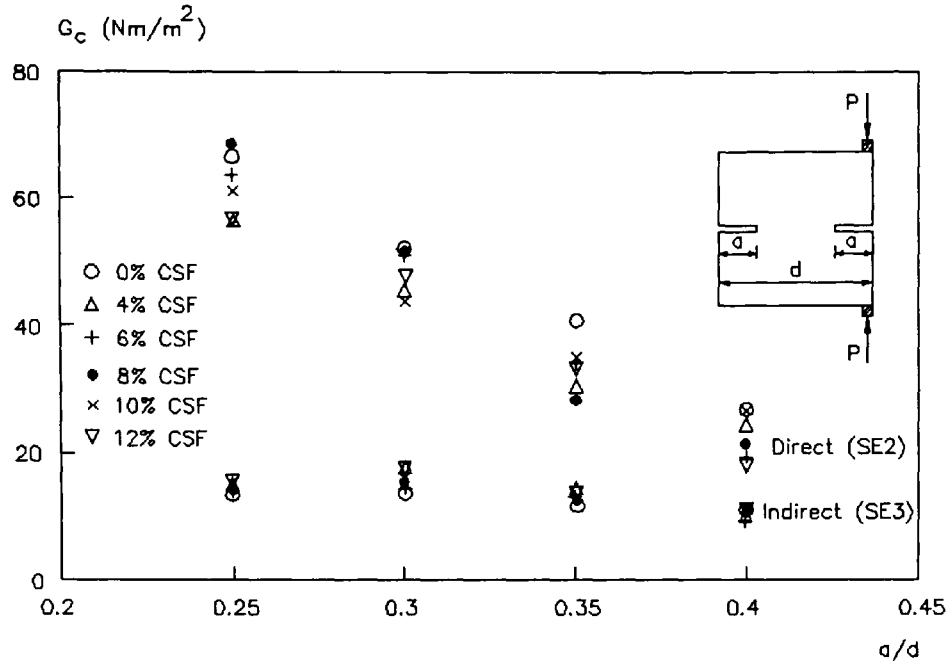

Figure 7.12 Variation of G_c with Notch Size for Different CSF Contents (CCS).

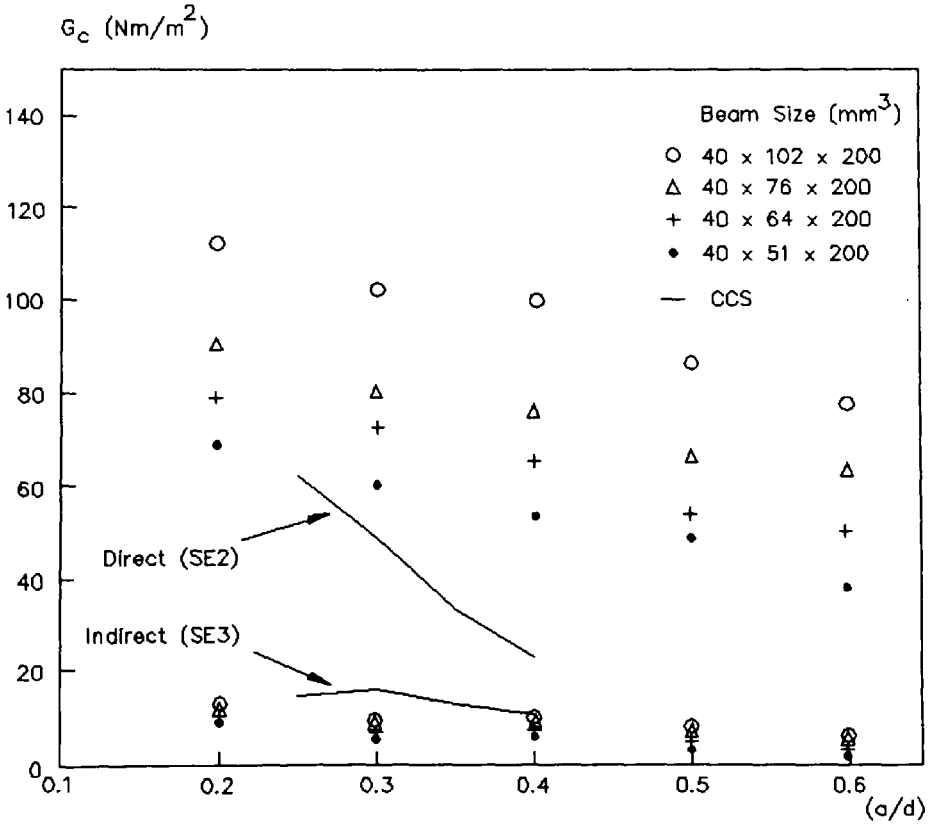

Figure 7.13 Comparison of G_c Obtained from Beams in Bending [54] and CCS (Present Work).

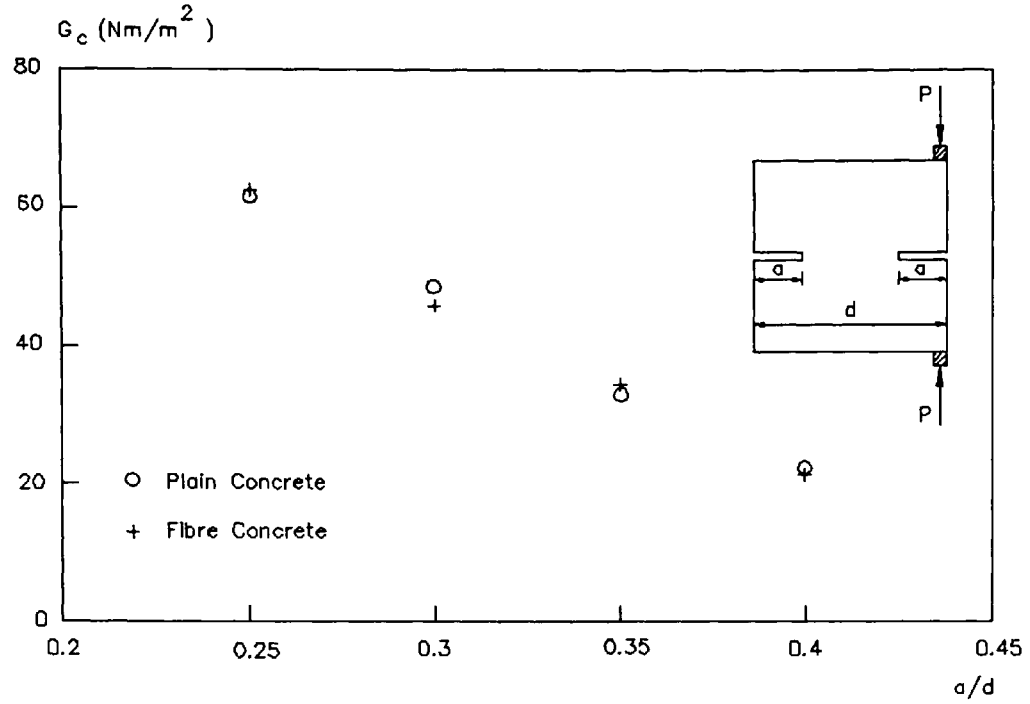

Figure 7.14 Variation of G_c with Notch Size for Plain and Fibre Concrete (CCS).

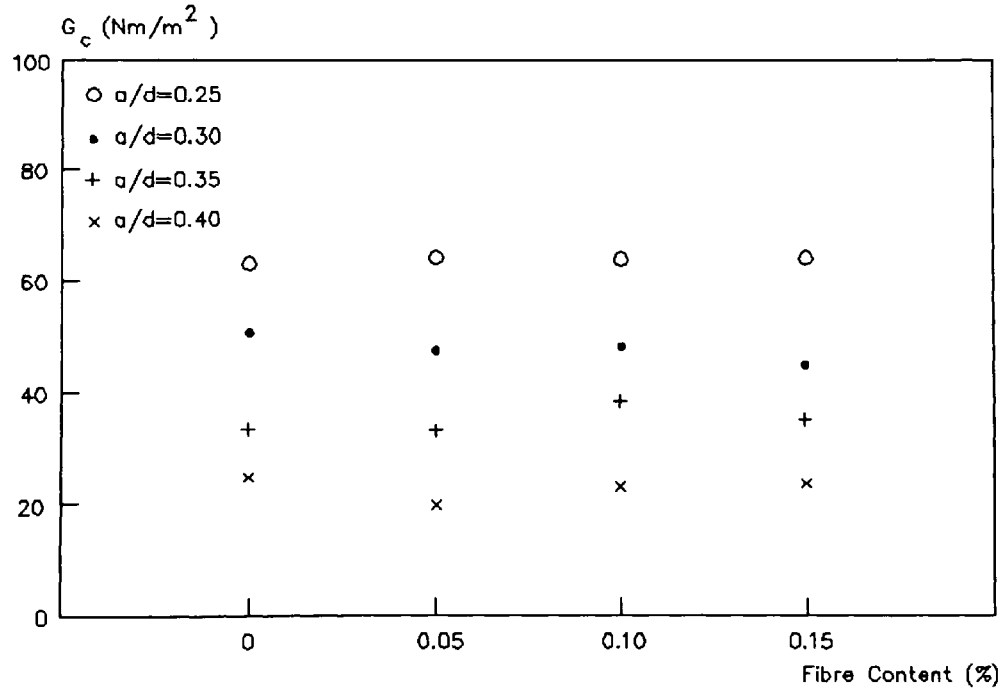

Figure 7.15 Variation of G_c with Fibre Content for Different a/d Ratios (CCS).

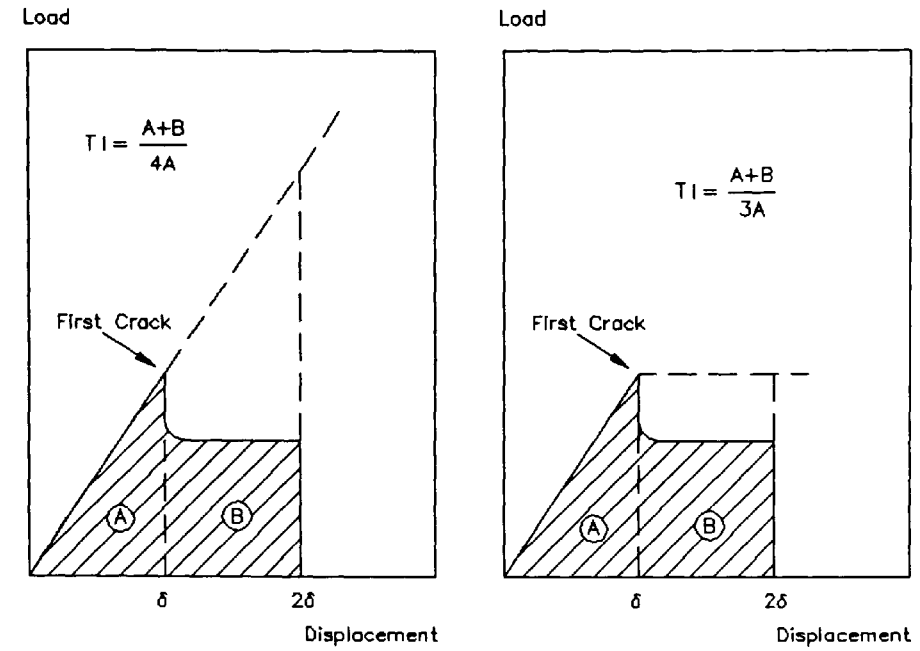

Figure 7.16 Toughness Index Definition –
(a) Elastic Response [61].
(b) Elastic Plastic Response.

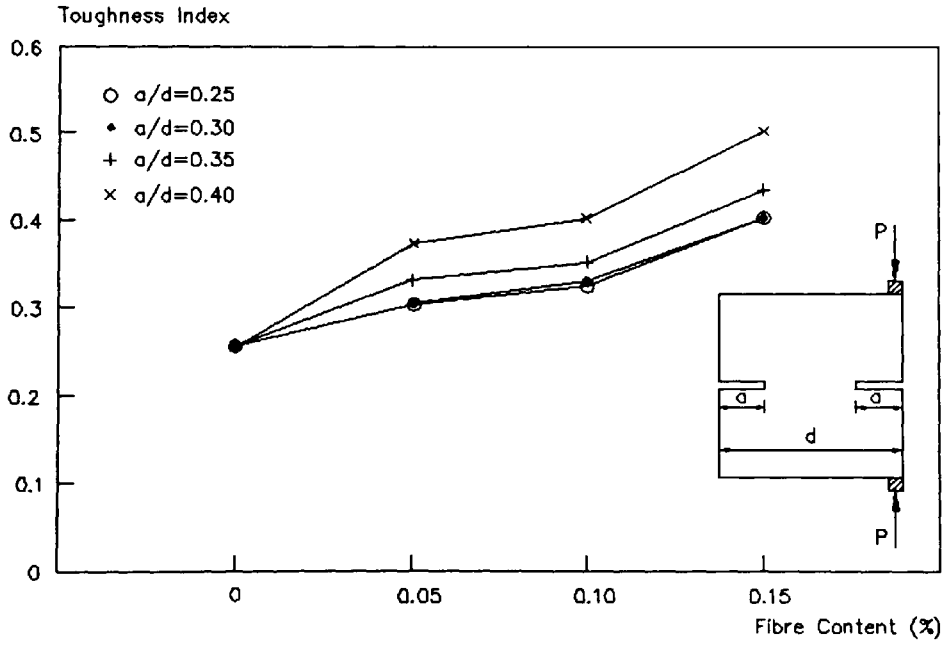

Figure 7.17 Variation of Toughness Index with Fibre Content for Different a/d Ratios (CCS).

CHAPTER FIVE

FINITE ELEMENT ANALYSIS OF THE COMPACT COMPRESSION SPECIMEN

5.1 Introduction

	OPC	CSF
Particle Size (μm)	15	0.15
Surface Area (m^2/kg)	350-500	15000-20000
Bulk Density (kg/m^3)	1300-1400	200-300
Specific Gravity	3.14	2.2
Composition (%)		
SiO_2	20.9	92.0
Fe_2O_3	2.2	1.2
Al_2O_3	4.5	0.7
CaO	64.0	0.2
MgO	2.3	0.2
Na_2O+K_2O	0.9	2.0
Impurities + LOI	4.7	2.7

Table 7.1 Physical and Chemical Properties of OPC and CSF.

Sieve Size	% Passing	
	Fine Aggregate	Coarse Aggregate
10 mm	100.0	99.4
5 "	97.0	4.6
2.36 "	90.9	1.1
1.18 "	88.3	-
600 μm	78.2	-
300 "	6.1	-
150 "	-	-

Table 7.2 Grading of Fine and Coarse Aggregates.

	Fine Aggregate	Coarse Aggregate
Relative Density (SSD)	2.70	2.65
Water Absorption (% of dry mass)	2.96	0.34
Moisture Content	0.70	0

Table 7.3 Physical Properties of Aggregates.

Mix Ref.	CSF (%)	CSF Slurry (kg/m^3)	Water* (kg/m^3)	Cement (kg/m^3)	Slump (mm)
A1	0	0	233.3	496.5	240
A2	4	39.7	213.4	476.6	200
A3	6	59.6	203.5	466.7	190
A4	8	79.4	193.6	456.8	165
A5	10	99.3	183.7	446.9	125
A6	12	119.2	173.7	436.9	100

* 20.2 kg/m^3 Water was added for Absorption.

Table 7.4 Mix Proportions per m^3, w/c=0.47.

Mix Ref.	CSF (%)	Water* (kg/m^3)	Cement (kg/m^3)	Fibres (%)	Fibres (kg/m^3)	Slump (mm)
B1(A1)	0	233.3	496.5	0	0	240
B2		"	"	0.05	1.17	230
B3		"	"	0.10	2.33	220
B4		"	"	0.15	3.50	220
B5(A2)	4	213.4	476.6	0	0	200
B6		"	"	0.05	1.17	190
B7		"	"	0.10	2.33	210
B8		"	"	0.15	3.50	190
B9(A4)	8	193.6	456.8	0	0	165
B10		"	"	0.05	1.17	160
B11		"	"	0.10	2.33	155
B12		"	"	0.15	3.50	140

* 20.2 kg/m^3 Water was added for Absorption.

Table 7.5 Mix Proportions per m^3 for Fibre Concrete, w/c=0.47.

Mix Ref.	CSF (%)	Compressive Strength (N/mm^2) 7-day	Compressive Strength (N/mm^2) 28-day	Density (kg/m^3)
A1	0	23.7	36.7	2365
A2	4	32.2	49.5	2350
A3	6	33.2	53.1	2335
A4	8	37.1	56.0	2325
A5	10	41.3	62.6	2310
A6	12	44.7	64.8	2300

Table 7.6 Properties of CSF Concrete.

Mix Ref.	CSF (%)	Fibre (%)	Compressive Strength (N/mm^2)			Density (kg/m^3)
			7-day	28-day	91-day	
B1(A1)	0	0	23.7	36.7	-	2365
B2		0.05	25.0	36.5	47.0	2360
B3		0.10	24.4	33.9	48.1	2345
B4		0.15	23.4	32.4	42.4	2305
B5(A2)	4	0	32.2	49.5	-	2350
B6		0.05	31.9	50.5	58.2	2310
B7		0.10	34.6	48.0	55.5	2270
B8		0.15	29.2	42.0	46.3	2220
B9(A4)	8	0	37.1	56.0	-	2325
B10		0.05	40.6	60.6	63.8	2300
B11		0.10	35.3	49.8	52.6	2225
B12		0.15	32.5	44.5	47.9	2205

Table 7.7 Properties of CSF Fibre Reinforced Concrete.

Mix Ref.	CSF (%)	Notch (mm)	Failure Load (kN)		V (%)	k_c ($MNm^{-3/2}$)
A1	0	25	9.49 - 9.75	9.62	1.9	0.65
		30	5.67 5.31 5.47	5.48	3.3	0.65
		35	2.80 2.70 2.93	2.81	4.1	0.60
		40	1.43 1.30 1.30	1.34	5.6	0.58
A2	4	25	10.35 9.84 9.70	9.96	3.4	0.67
		30	6.25 6.17 5.85	6.09	3.5	0.73
		35	3.04 3.20 3.04	3.09	3.0	0.66
		40	1.33 1.30 1.24	1.29	3.5	0.56
A3	6	25	9.52 - 9.80	9.66	2.0	0.65
		30	5.72 5.73 5.41	5.62	3.2	0.67
		35	3.03 - 2.70	2.86	8.1	0.62
		40	1.22 1.27 1.19	1.23	3.3	0.54

V = Coefficient of Variation

Table 7.8 Failure Loads and Fracture Toughness Values (CCS) - Mixes A1-A3 (Plain Concrete).

Mix Ref.	CSF (%)	Notch (mm)	Failure Load (kN)		V (%)	k_c ($MNm^{-3/2}$)
A4	8	25	9.80 10.25 9.99	9.99	2.1	0.67
		30	5.66 5.97 5.87	5.80	3.7	0.69
		35	2.98 2.90 2.75	2.88	4.1	0.62
		40	1.45 1.25 1.36	1.35	4.1	0.59
A5	10	25	10.12 10.42 10.13	10.22	1.8	0.69
		30	6.15 5.63 6.14	5.97	5.0	0.71
		35	3.07 2.83 2.95	2.95	4.1	0.63
		40	1.40 1.27 1.38	1.36	3.9	0.59
A6	12	25	10.98 9.66 10.68	10.44	6.6	0.70
		30	6.13 6.43 6.03	6.20	3.4	0.74
		35	2.94 3.11 2.95	3.00	3.2	0.65
		40	1.35 1.38 1.36	1.36	1.1	0.59

V = Coefficient of Variation

Table 7.9 Failure Loads and Fracture Toughness Values (CCS) - Mixes A4-A6 (Plain Concrete).

Mix Ref.	Fibre (%)	Notch (mm)	Failure Load (kN)		V (%)	k_c ($MNm^{-3/2}$)
B2	0.05	25	9.65 9.79 9.66	9.70	0.8	0.65
		30	5.43 5.47 5.42	5.44	0.6	0.65
		35	2.82 2.85 2.93	2.87	2.0	0.62
		40	1.25 1.33 1.29	1.29	3.1	0.57
B3	0.10	25	8.97 8.63 9.22	8.94	3.3	0.60
		30	5.18 5.51 5.40	5.36	3.1	0.64
		35	2.84 2.89 2.59	2.77	5.8	0.60
		40	1.16 1.17 1.09	1.14	3.8	0.50
B4	0.15	25	8.98 8.50 8.35	8.61	3.8	0.58
		30	4.96 4.48 4.57	4.67	5.5	0.56
		35	3.07 2.18 2.56	2.60	17	0.56
		40	1.20 1.12 1.21	1.18	4.2	0.51

V = Coefficient of Variation

Table 7.10 Failure Loads and Fracture Toughness Values (CCS) - Mixes B2-B4, 0 CSF (FRC).

Mix Ref.	Fibre (%)	Notch (mm)	Failure Load (kN)		V (%)	k_c ($MNm^{-3/2}$)
B6	0.05	25	9.87 9.98 9.85	9.90	0.7	0.66
		30	5.42 5.50 5.40	5.44	1.0	0.65
		35	3.03 2.70 3.10	2.94	7.2	0.63
		40	1.23 1.20 1.30	1.24	4.1	0.54
B7	0.10	25	9.44 10.08 9.64	9.72	3.4	0.65
		30	5.90 5.42 5.46	5.59	4.8	0.67
		35	2.82 2.93 2.79	2.85	2.6	0.61
		40	1.12 1.32 1.26	1.23	8.3	0.54
B8	0.15	25	9.32 8.66 9.42	9.13	4.5	0.61
		30	5.25 5.30 5.01	5.19	3.0	0.62
		35	2.88 2.95 2.35	2.73	1.2	0.59
		40	1.21 1.25 1.30	1.25	3.6	0.54

V = Coefficient of Variation

Table 7.11 **Failure Loads and Fracture Toughness Values (CCS) - Mixes B6-B8, 4% CSF (FRC).**

Mix Ref.	Fibre (%)	Notch (mm)	Failure Load (kN)		V (%)	k_c ($MNm^{-3/2}$)
B10	0.05	25	- 9.68 9.90	9.79	1.6	0.66
		30	5.81 5.77 5.70	5.76	1.0	0.69
		35	2.95 2.88 3.08	2.97	3.4	0.64
		40	1.26 1.30 1.45	1.34	7.5	0.58
B11	0.10	25	- 9.04 10.30	9.67	9.2	0.65
		30	5.31 5.52 5.55	5.46	2.4	0.65
		35	3.26 2.99 3.09	3.11	4.4	0.67
		40	1.31 1.21 1.32	1.28	4.7	0.56
B12	0.15	25	9.25 - 9.21	9.23	0.3	0.62
		30	4.87 5.33 4.77	4.99	6.0	0.60
		35	2.58 2.70 2.59	2.62	2.6	0.56
		40	1.15 1.19 1.20	1.18	3.1	0.51

V = Coefficient of Variation

Table 7.12 Failure Loads and Fracture Toughness Values (CCS) - Mixes B11-B12, 8% CSF (FRC).

Mix Ref.	CSF (%)	Notch (mm)	Max. Load (kN)	Max. Displ (mm)	G_c (Nm/m^2)			TF
					SE1	SE2	SE3	
A1	0	25	9.62	0.124	119.2	66.4	13.5	4.9
		30	5.48	0.107	73.2	51.8	13.5	3.8
		35	2.81	0.102	47.7	40.3	11.5	3.5
		40	1.34	0.087	29.0	26.5	10.8	2.5
A2	4	25	9.96	0.113	112.6	55.8	14.4	3.9
		30	6.09	0.094	71.5	45.1	17.1	2.6
		35	3.09	0.076	39.0	30.0	13.9	2.2
		40	1.29	0.082	26.5	24.0	10.0	2.4
A3	6	25	9.66	0.121	116.8	63.5	13.5	4.7
		30	5.62	0.105	73.7	51.2	14.4	3.6
		35	2.86	0.087	41.3	33.7	12.3	2.7
		40	1.23	0.069	21.0	19.0	9.3	2.1
A4	8	25	9.99	0.125	124.8	67.8	14.4	4.7
		30	5.80	0.104	75.5	51.4	15.2	3.4
		35	2.88	0.075	36.0	28.0	12.3	2.3
		40	1.35	0.072	24.5	21.5	11.1	2.0
A5	10	25	10.22	0.118	120.6	60.9	15.2	4.0
		30	5.97	0.093	69.5	44.0	16.1	2.7
		35	2.95	0.088	43.3	35.0	12.7	2.8
		40	1.36	0.085	29.0	26.5	11.1	2.4
A6	12	25	10.44	0.114	119.0	56.8	15.7	3.6
		30	6.20	0.097	75.2	47.7	17.5	2.7
		35	3.00	0.083	41.7	33.0	13.5	2.5
		40	1.36	0.060	20.5	18.0	11.1	1.6

Table 7.13 Variation of Critical Strain Energy Release Rate with Notch Depth (CCS) - Mixes A1-A6.

Mix Ref.	CSF (%)	Fibre (%)	Notch (mm)	Max. Load (kN)	Max. Displ (mm)	G_c (Nm/m^2) SE1	SE2	SE3	TF
B2	0	0.05	25	9.70	0.120	116.4	62.6	13.5	4.6
			30	5.44	0.106	72.1	50.9	13.5	3.8
			35	2.87	0.085	40.7	32.7	12.3	2.7
			40	1.29	0.076	24.5	22.0	10.4	2.1
B3		0.10	25	8.94	0.115	102.8	57.1	11.5	5.0
			30	5.36	0.095	63.7	43.1	13.1	3.3
			35	2.77	0.086	39.7	32.4	11.5	2.8
			40	1.14	0.076	21.7	20.0	8.0	2.5
B4		0.15	25	8.61	0.130	112.0	69.6	10.8	6.4
			30	4.67	0.104	60.7	45.1	10.0	4.5
			35	2.60	0.082	35.7	29.0	10.0	2.9
			40	1.18	0.076	22.4	20.5	8.3	2.5
B6	4	0.05	25	9.90	0.125	123.8	67.7	13.9	4.9
			30	5.44	0.096	65.2	44.2	13.5	3.3
			35	2.94	0.078	38.3	30.0	12.7	2.4
			40	1.24	0.060	18.6	16.5	9.3	1.8
B7		0.10	25	9.72	0.130	126.4	72.3	13.5	5.4
			30	5.59	0.111	77.5	55.3	14.4	3.8
			35	2.85	0.088	41.7	34.0	11.9	2.9
			40	1.23	0.075	23.1	21.0	9.3	2.3
B8		0.15	25	9.13	0.121	110.4	62.8	11.9	5.3
			30	5.19	0.101	65.5	46.3	12.3	3.8
			35	2.73	0.104	47.3	40.3	11.1	3.6
			40	1.25	0.093	29.1	27.0	9.3	2.9
B10	8	0.05	25	9.79	0.115	112.6	57.8	13.9	4.2
			30	5.76	0.095	68.5	44.7	15.2	2.9
			35	2.97	0.084	41.7	33.3	13.1	2.5
			40	1.34	0.066	22.1	19.5	10.8	1.8
B11		0.10	25	9.67	0.115	111.2	57.7	13.5	4.3
			30	5.46	0.094	64.2	42.8	13.5	3.2
			35	3.11	0.106	55.0	45.7	14.4	3.2
			40	1.28	0.085	27.2	25.0	10.0	2.5
B12		0.15	25	9.23	0.113	104.2	55.6	12.3	4.5
			30	4.99	0.092	57.5	39.6	11.5	3.4
			35	2.62	0.089	38.9	32.3	10.0	3.2
			40	1.18	0.078	23.0	21.0	8.3	2.5

Table 7.14 Variation of Critical Strain Energy Release Rate with Notch Depth for Fibre Concrete (CCS) - Mixes B2-B12.

Mix Ref.	Fibre (%)	Notch (mm)	Area A (Nmm)	Area B (Nmm)	Toughness Index		V (%)
B2	0.05	25	587	85	0.29		
			560	108	0.30	0.29	0.4
			604	106	0.29		
		30	276	48	0.29		
			287	60	0.30	0.30	1.9
			301	65	0.30		
		35	134	34	0.31		
			108	46	0.36	0.33	8.0
			122	36	0.32		
		40	52	21	0.35		
			41	20	0.37	0.36	2.8
			56	25	0.36		
B3	0.10	25	510	169	0.33		
			526	130	0.31	0.32	3.1
			505	140	0.32		
		30	220	61	0.32		
			226	83	0.34	0.33	3.5
			316	88	0.32		
		35	144	56	0.35		
			131	51	0.35	0.36	3.2
			120	59	0.37		
		40	43	23	0.38		
			47	24	0.38	0.38	1.5
			40	23	0.39		
B4	0.15	25	531	310	0.40		
			572	384	0.42	0.41	3.1
			575	375	0.41		
		30	274	254	0.48		
			230	188	0.45	0.45	7.1
			248	170	0.42		
		35	118	119	0.50		
			106	104	0.50	0.48	5.5
			137	111	0.45		
		40	47	57	0.55		
			44	52	0.54	0.54	0.6
			43	50	0.54		

V = Coefficient of Variation

Table 7.15 Variation of Toughness Index with Fibre Content (CCS) - Mixes B2-B4, 0 CSF.

Mix Ref.	Fibre (%)	Notch (mm)	Area A (Nmm)	Area B (Nmm)	Toughness Index		V (%)
B6	0.05	25	530	109	0.30		
			595	140	0.31	0.30	1.9
			624	124	0.30		
		30	253	58	0.31		
			275	52	0.30	0.30	2.0
			254	54	0.30		
		35	119	38	0.33		
			124	30	0.31	0.32	4.4
			101	25	0.31		
		40	37	16	0.36		
			35	17	0.38	0.37	2.0
			39	19	0.37		
B7	0.10	25	590	122	0.30		
			645	160	0.31	0.31	1.6
			660	165	0.31		
		30	263	74	0.32		
			295	62	0.30	0.31	4.2
			360	75	0.30		
		35	98	36	0.34		
			121	41	0.33	0.33	3.6
			153	43	0.32		
		40	40	22	0.39		
			56	25	0.36	0.38	4.2
			42	24	0.39		
B8	0.15	25	521	288	0.39		
			578	349	0.40	0.40	1.9
			579	355	0.40		
		30	226	115	0.38		
			281	141	0.37	0.38	2.6
			285	156	0.39		
		35	127	92	0.43		
			139	74	0.38	0.40	5.6
			154	90	0.40		
		40	58	51	0.47		
			59	39	0.42	0.46	7.0
			56	52	0.48		

V = Coefficient of Variation

Table 7.16 Variation of Toughness Index with Fibre Content (CCS) - Mixes B6-B8, 4% CSF.

Mix Ref.	Fibre (%)	Notch (mm)	Area A (Nmm)	Area B (Nmm)	Toughness Index		V (%)
B10	0.05	25	557	110	0.30		
			526	100	0.30	0.30	0.7
		30	291	45	0.29		
			258	37	0.29	0.29	1.7
			300	58	0.30		
		35	109	42	0.35		
			112	36	0.33	0.34	4.0
			154	63	0.35		
		40	39	17	0.36		
			39	21	0.38	0.38	4.0
			55	30	0.39		
B11	0.10	25	488	154	0.33		
			635	262	0.35	0.34	5.2
		30	228	89	0.35		
			258	104	0.35	0.35	0.7
			281	126	0.36		
		35	187	74	0.35		
			144	71	0.37	0.37	4.4
			163	87	0.38		
		40	47	41	0.47		
			53	47	0.47	0.45	7.2
			65	43	0.41		
B12	0.15	25	525	342	0.41		
			541	288	0.38	0.38	6.1
			498	222	0.36		
		30	245	133	0.39		
			217	96	0.36	0.38	4.5
			229	127	0.39		
		35	116	78	0.42		
			108	73	0.42	0.42	1.1
			124	89	0.43		
		40	47	43	0.48		
			45	48	0.52	0.50	5.6

V = Coefficient of Variation

Table 7.17 Variation of Toughness Index with Fibre Content (CCS) - Mixes B11-B12, 8% CSF.

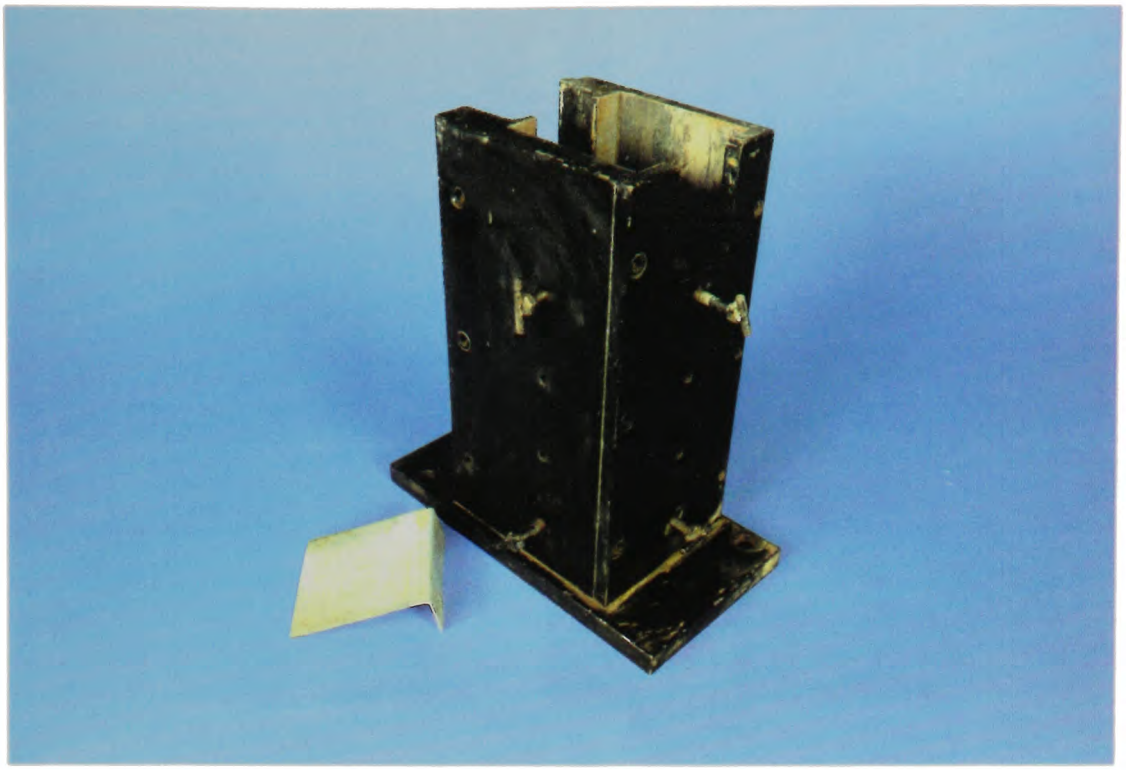

Plate 7.1 Housing for Notching of the Specimens.

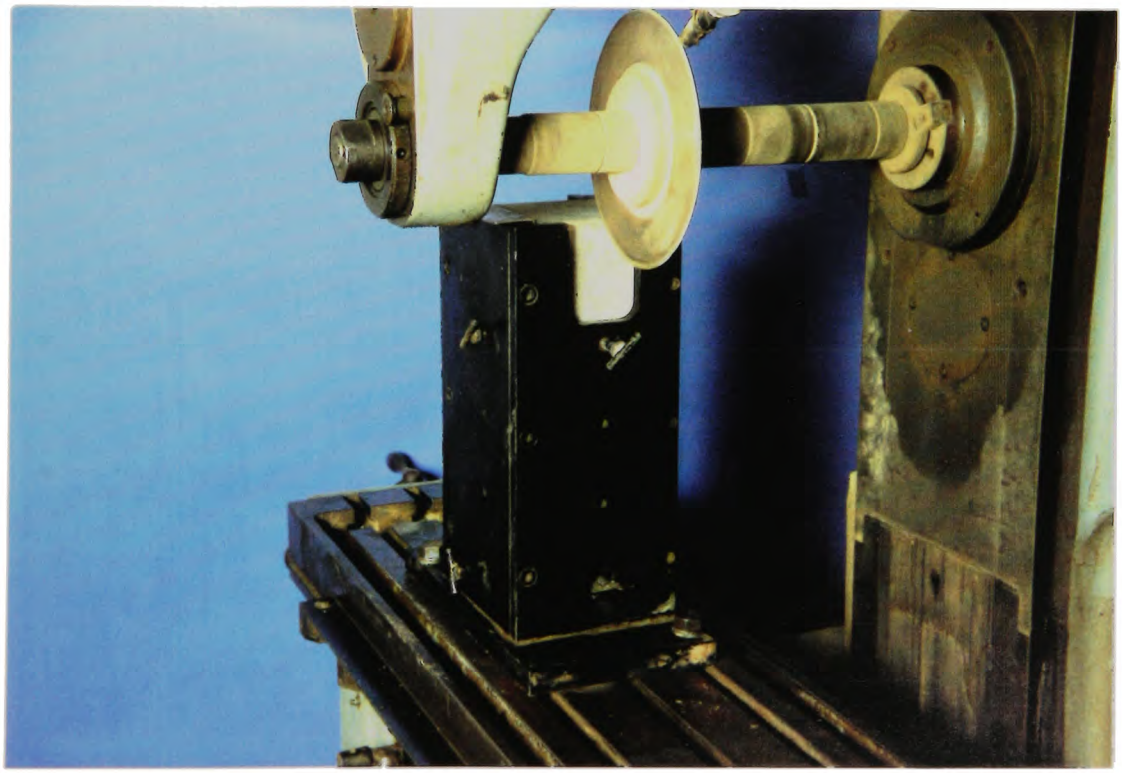

Plate 7.2 A Specimen Positioned in the Machine Ready for Notching.

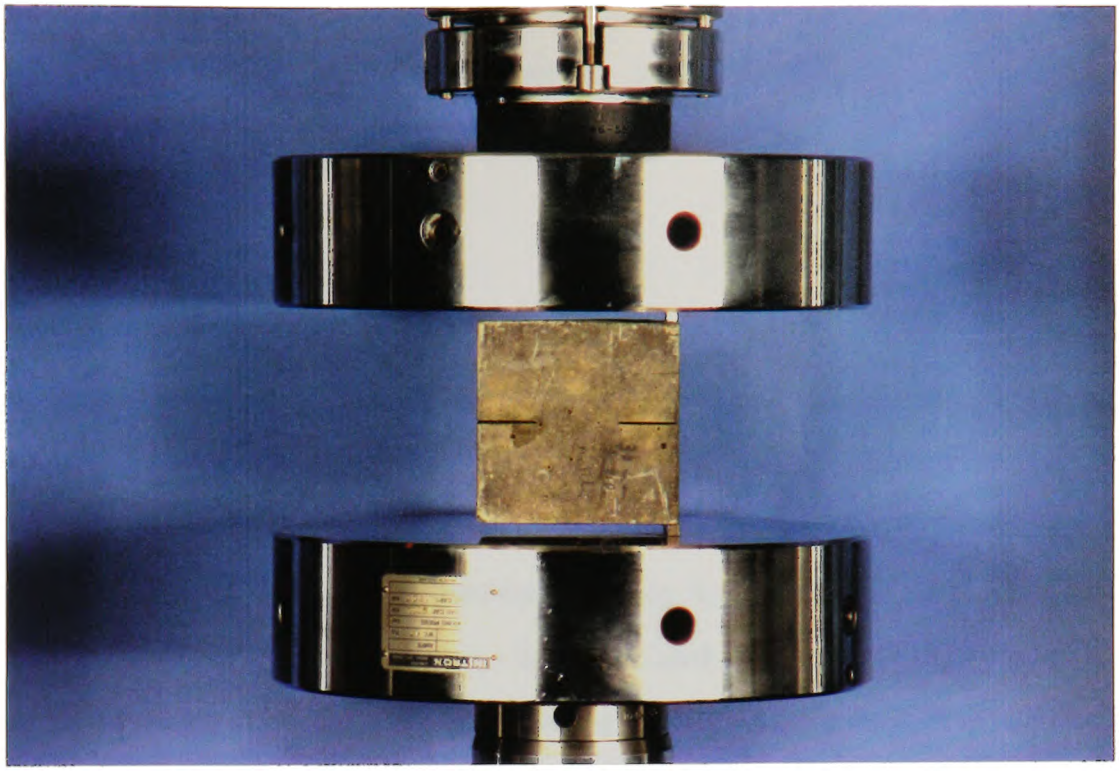

Plate 7.3 Specimen in Position Ready for Testing (CCS).

Plate 7.4 A Typical Failed Specimen Showing Failure Along the Uncracked Ligament (CCS).

CHAPTER EIGHT

HIGH STRENGTH CONCRETE

8.1 Introduction

In this chapter a study of the mechanical properties of high strength concrete (74.0-110.5 N/mm^2) with CSF contents in the range 12-28% is carried out. Results are presented for compressive strength development up to 91 days for two water curing temperatures, i.e. 20° C and 50° C. Tests were also carried out to determine the static modulus of elasticity and the tensile strength at 28 days.

The chapter also reports on the results of fracture tests conducted on the Compact Compression Specimen (CCS) and the Double and Single Notched Axial Splitting Specimens (DNASS and SNASS). The test failure loads were employed in the finite element analyses presented in Chapters 5 and 6 to estimate the fracture toughness. The areas under the load-displacement graphs were utilised to evaluate the strain energy release rate G_c.

8.2 Mixing Procedure

In view of the high dosages of CSF planned for the concretes employed in this chapter and in order to effect optimum dispersion of the CSF particles a different mixing procedure to that of Chapter 7 was adopted. In this all the liquids namely, water, CSF slurry and superplasticizer were first thoroughly mixed together and then poured onto the coarse aggregates which were already placed in the pan mixer. After mixing for 20 seconds the fine aggregate was introduced and mixed in for a further period of 20 seconds. This was followed by the cement which was mixed in until a total mixing time of 2 minutes was achieved.

Although the above procedure may be considered inappropriate from a large scale production point of view, it was found helpful if clusters occurring in the mix as a result of the fast reaction between the cement and CSF were to be avoided. Carette and Malhotra [4] overcame this problem by adding large dosages of superplasticizer. These dosages together with high CSF contents resulted in the concrete having a gluey consistency. Because of this and due to the rapid loss of slump, their concrete required intensive vibration in order to achieve proper compaction.

8.3 Trial Mixes (A-F)

CSF concrete has a high water demand when compared to OPC concrete. For high CSF contents the use of superplasticizers is necessary in order to achieve the desired workability. Because of this a number of trial mixes with varying amounts of CSF and superplasticizer were made.

The reference mix was designed in accordance with the DoE publication [119] with the aim of producing concrete of high strength (70 N/mm^2). The proportions of cement : fine aggregate : coarse aggregate for the mix were 1 : 1.4 : 2.2. Several mixes were prepared using different water/cement (w/c) ratios and incorporating varying amounts of CSF. Table 8.1 gives the details of the trial mixes together with the slump, density and 7-day compressive strengths. As in the previous chapter, the water/cement ratio is based on the total water including that in the slurry and the total cementitious material, i.e. (OPC + CSF). The superplasticizer is expressed as percentage by mass of (OPC + CSF).

8.4 Mechanical Properties

With the experience gained from the trial mixes of the previous section it was considered feasible to produce workable concretes with a w/c = 0.35 having a maximum CSF content of 30%. However, to achieve this as much as 3-4% superplasticizer would be necessary. Although this might be considered excessive, it is found that such dosages of superplasticizer are used in some commercially available CSF slurries. The quantities per m^3 used in the reference mix (i.e. without CSF) were as follows

cement : 470 kg
water : 165 kg
fine aggregate : 675 kg
coarse aggregate: 1015 kg.

The results for compressive strength development as well as the tensile strength and the static modulus of elasticity are reported in the following sections.

8.4.1 Compressive Strength

In this section the results of compressive strength tests carried out on 100 mm cubes wet cured at 20° C and 50° C for up to 91 days are reported. Table 8.2 gives the details for the six mixes employed, with CSF contents ranging between 0 and 28%, together with the results for the slump tests. Two

sets of such mixes, i.e. mixes (1-6) and (7-12), were prepared, the first set being for the 20° C curing and the second for the 50° C curing. Amongst the specimens prepared from each mix, fifteen 100 mm cubes were cast for the compressive strength tests, three cubes being tested at each of the ages of 4, 7, 14, 28 and 91 days.

The results for the compressive strengths are presented in Table 8.3, each being the average of the test results of three samples. Figures 8.1a-8.1f give the variation of the compressive strength with age for the two curing temperatures and for different CSF contents. These show that CSF substitutions for cement by as much as 28% can have a marked improvement on the compressive strength. Whereas the 20° C cured specimens with 12% and 16% CSF contents achieve their maximum strength at about 28 days, the specimens with 20-28% CSF continue to gain strength beyond 28 days. This behaviour is demonstrated further in Figure 8.2 where the strength is expressed as a percentage of that developed at 28 days. Figure 8.2 also indicates that the strength development for CSF concrete is faster than that for the reference concrete up to 28 days.

Figure 8.3 gives the results for the compressive strengths for the specimens cured at 50° C. Here, it can be seen that high temperature curing accelerates strength development of CSF concrete when compared to that of the reference concrete up to 28 days. Beyond this age, however, the strength gain is slower than that for the reference concrete.

The pattern of strength gain of CSF concrete is different to that of OPC concrete. Whereas it is generally accepted that the 7-day strength of normal OPC concrete is of the order of 60-70% of the 28-day strength, the results obtained here (high strength concrete) give a 7-day strength which is 86% of the 28-day strength for curing at 20° C with this proportion being 93% for the 50° C curing. In the case of the CSF concretes employed here the ratio of the 7-day to 28-day strengths range between 70% and 80% for the 20° C curing and 90% and 100% for the 50° C curing.

The effect of the curing temperature on the compressive strength development is further examined in Figures 8.4a-8.4e. Here, the strengths are shown as a function of the CSF content. It can be seen that whereas high temperature curing results in higher strengths at the early ages, this trend is reversed with increasing age. In contrast to the strength development pattern at early ages, the 91-day strengths are higher for the specimens cured at 20° C than those cured at 50° C. The transition period appears to start at an age of about 14 days. It is also noted (see Figures 8.1e-8.1f) that this transition takes place at an earlier age for the lower CSF contents. Close examination of Figures 8.4a-8.4e also reveals that at the early ages the influence of the curing temperature is more pronounced for the concretes with the higher CSF contents. It is interesting to note that for ages up to 28 days the specimens cured at 20° C exhibit a marked drop in compressive strength when the CSF content is increased from 16% to 20%. Yogendran et al [1] tested 150 mm

diameter by 300 mm long cylinders in compression and found that the strength increased up to 15% CSF content and then decreased up to the maximum employed CSF content of 25%. Their results for concretes with a w/c = 0.34 are shown in Figure 8.5. They reported the loss in the strength to be due to the improper compaction in the given range. For the higher CSF replacements (20-28%) the present work yields results for compressive strength at early ages which decrease and then increase (see table 8.3). This was unexpected and a possible explanation for this behaviour is given in section 8.10. A similar behaviour was observed by Carette and Malhotra [4] using CSF replacements of up to 30%.

Skurdal [125] examined strength development for moist curing at 20° C, 30° C and 50° C for concretes with 0, 10% and 20% CSF. His concretes had 28-day strengths at 20° C varying between 30 N/mm^2 and 65 N/mm^2. He reported a 20% reduction in the 28-day strength for cubes cured at 50° C when compared to those cured at 20° C. The 28-day results obtained here (Figure 8.4d) for the high strength concretes (75-100 N/mm^2 when cured at 20° C) show that for up to about 16% CSF replacement, the reduction caused by high temperature curing is of the order 4-10%. However, beyond 16% CSF replacements the higher temperature curing causes an increase in the 28-day strength ranging between 8% and 17%. Maage and Hammer [10] also reported on an investigation of the compressive strength of cement/PFA mixes with 0, 5% and 10% CSF. The mixes were water cured at 5° C, 20° C and 35° C

and were maintained at these temperatures for 28 days after which they were stored in water at 20° C for up to one year. Their results for the mean values of four cement blends for 20° C curing are shown in Figure 8.6. For 20° C curing, CSF had the same influence on strength development as that reported in the present work. Furthermore, at 5° C the strength of the blended cements lagged behind that of the OPC up to 28 days. This lag increased for the concrete with 10% CSF. At 35° C the CSF concrete exhibited higher strengths than that cured at 20° C. These results are in agreement with those found in the present investigation.

From the foregoing it is clear that increased temperature can have a beneficial effect on the early strength development of CSF concrete. In practice, this can be implemented by using warm, insulated concrete or by heat curing for the initial 14 days.

8.4.2 Tensile Strength

Although the tensile strength of concrete is normally ignored for design purposes, an appreciation of its magnitude can be advantageous in design calculations and estimation of loads under which fracture takes place.

Due to the fact that concrete is a highly brittle material with a heterogeneous and porous structure, a direct application of a tensile force to give a uniform stress is

difficult. Thus only marginal success has been achieved by employing this method by, for example, the use of epoxy bonded end pieces [122]. It is more convenient to measure the tensile strength of concrete by indirect methods such as tensile splitting or flexural testing. Although both of these methods are known to overestimate the tensile strength of concrete, it is widely accepted [122] that the splitting test gives results closer to the true tensile strength. Moreover the tensile splitting test is simple to perform and gives more uniform results than other tests.

In the present work tests were carried out according to BS 1881: Part 117: 1983 to obtain the tensile splitting strength of the various concretes used. The specimens were subjected to wet curing at two temperatures, namely 20° C and 50° C until they were tested at 28 days. The results are presented in Table 8.4, each being the average obtained from two tests. Figure 8.7 gives a plot of the tensile strength against the 28-day compressive strength obtained here, together with those obtained by Maage and Hammer [10] for the water cured specimens. It can be seen that no significant influence on the observed relationship between compressive and tensile strength is exhibited by the two curing regimes employed in the present work. It is also apparent that the rate of increase of tensile strength with increasing compressive strength is less for high strength concrete (75-100 N/mm^2 when cured at 20° C) than that observed by Maage and Hammer [10] for low strength concrete (20-55 N/mm^2). Figure 8.8 shows a plot of the tensile

strength expressed as a percentage of the compressive strength. As compressive strength increases the tensile strength forms a decreasing percentage of the compressive strength. This percentage in the present work ranges between 4% and 6%, and in the work of Maage and Hammer [10] it ranges between 6% and 10%.

The relationship between the tensile strength and the compressive strength at 28 days (up to 84 N/mm^2) was studied by Dewar [15]. He concluded that at low strengths the tensile strength may be as high as 10% of the compressive strength but at higher strengths this was found to be about 5%. This is exactly what is obtained in the current work and is apparent from Figure 8.8. It is also in line with results usually reported for conventional OPC concrete [122].

Figure 8.9 gives the variation of the tensile strength with CSF content. The tensile strength does not increase significantly with increasing CSF content and the only systematic change is a small reduction in strength for concretes with CSF contents between 16% and 20%. Beyond this CSF content the concrete continues to show a gradual increase in strength. In Figure 8.10 the ratio of the tensile to compressive strength is shown as a function of the CSF content. It can be seen that increasing CSF content leads to decrease in the ratio of tensile to compressive strength. This might be expected with respect to the previous results in that increasing CSF contents produce

higher compressive strengths and that higher strengths are associated with lower ratios. The lower ratio (%) of tensile to compressive strength at 20% CSF contents and above for the 50° C cured material is explained by the fact that the 28-day compressive strengths (see Figure 8.4d) are significantly higher than those for the 20° C cured material.

8.4.3 Young's Modulus of Elasticity

Tests were carried out in accordance with BS 1881: Part 121: 1983 to determine the static modulus of elasticity at 28 days for the CSF concrete mixes used in this study. The results which are the average of two cylinder tests are given in Table 8.4 for both curing temperatures. The variation of Young's modulus with the compressive strength is presented in Figure 8.11. It can be seen that the curing temperature does not have a significant effect on the relationship between the Young's modulus and the compressive strength and that compressive strengths beyond 90 N/mm^2 are associated with marked reductions in the values of Young's modulus.

John and Shah [14] tested normal concrete with strengths ranging between 27 N/mm^2 and 110 N/mm^2 and found that the ACI expression [17] given in equation 2.2, which was originally proposed for strengths up to 41 N/mm^2, was adequate for evaluating the Young's modulus. Equation 2.2 is

also shown in Figure 8.11. When compared with the results obtained here for the CSF concrete this gives an underestimate in the values of the modulus of elasticity of about 9% for compressive strengths up to about 90 N/mm^2. However, comparison with normal concrete may not be valid as CSF concretes result in the formation of additional cementitious gel with lower calcium/silicate ratios than the gel formed in hydrated cement alone. Increased CSF contents lead to increasing amounts of this gel with progressively lower calcium/silicate ratios. The amount of gel formed will depend in part on the amount of calcium hydroxide produced from the hydrated cement which is available to react with the CSF. Thus at each particular curing time there will be a critical level of CSF above which the CSF will be in excess. This excess CSF will make no contribution to the strength development. These factors will clearly have a profound effect on the way the elasticity modulus and the strength develop.

Figure 8.12 gives the calculated values for the Young's modulus as a function of the CSF content. The values show a small increase, up to 16% CSF, peaking to 44.2 kN/mm^2 for the 20° C curing and 45.0 kN/mm^2 for the 50° C curing and then fall for CSF contents between 16% and 20%. In general CSF contents beyond 16% lead to reductions in the modulus of elasticity with the high temperature curing showing a decrease of about 16% from it's peak value.

8.5 Fracture Toughness Tests

The fracture toughness tests conducted on the high strength concretes discussed in this chapter are described in the present section. This section also gives the details of the specimen geometries and loading conditions used.

8.5.1 The Compact Compression Test - (CCS)

Finite element analyses for the Compact Compression Specimen (CCS) were presented in Chapter 5 and a full description of the laboratory testing arrangement was given in Chapter 7. For the testing program employing this geometry and that described in the next sub-section (8.5.2), six mixes (R1-R6) were prepared by duplicating mixes 1-6 given in Table 8.2. Amongst the specimens prepared from each mix, six 100 mm cubes were prepared for the CCS tests, three for curing at 20° C and the remaining three for curing at 50° C. All cubes were symmetrically notched to a nominal depth of 30 mm using the procedure outlined in Chapter 7. After notching, at 21 days, the specimens were returned to the curing tanks until testing at 28 days.

8.5.2 The Axial Splitting Tests - (DNASS and SNASS)

Finite element analyses for the Doubly and Singly Notched Axial Splitting Specimens (DNASS and SNASS) were described

in Chapter 6. The results for the stress distributions indicated that high tensile stresses exist near the notch tips provided that the loading platens are sufficiently narrow.

Laboratory tests were performed on 100 mm cubes modified by the introduction of two symmetrical notches as shown in Figure 8.13. The notches were cut in the same manner as that adopted for the CCS in Chapter 7. Two notch sizes were employed, i.e. a=30 mm and a=35 mm. In all twenty four specimens were prepared from each of the mixes (R1-R6). Three specimens of each of the two geometries were tested with the load applied through steel platens of two different sizes. The loading platens had widths w=15 mm in the first test and w=20 mm in the second. In this way twelve specimens were tested at each of the two curing regimes, i.e. 20° C and 50° C. In all cases the loading platens were 110 mm long and 10 mm thick. The loading platens were carefully aligned in order to ensure symmetry. Plate 8.1 shows a DNASS (a=30 mm, w=20 mm) ready for testing.

The Instron testing machine employed in the fracture toughness tests is capable of applying the load under both 'displacement' and 'load' control. In the displacement mode, it is possible to apply loads up to 100 kN. While this was sufficient for the CCS test, in view of the anticipated larger failure loads for the axial splitting tests, the latter tests were conducted under load control. In the load control mode the test machine has a maximum capacity of 200

kN and a cross-head speed of 0.5 mm/min was employed. This was the nearest available straining rate to that used for the CCS test under displacement control, i.e. 0.4 mm/min. All specimens failed by splitting into halves in the plane containing the notches.

Additional tests were conducted using the Singly Notched Axial Splitting Specimen (SNASS) analysed in Chapter 6, see Figure 6.1. The specimens were 100 mm by 100 mm in cross section and had lengths ranging between 150 mm and 330 mm. These specimens were prepared in standard 500 mm long prism moulds provided with an adjustable steel plate partition 20 mm in thickness as shown in Plate 8.2. All specimens had 100 mm notches introduced using one of two methods. In the first, the notches were formed by a 5 mm thick steel plate milled to a very sharp edge, fixed to the centre of each end of the mould, see Plate 8.2. In this method the steel plates forming the pre-notches were pulled out from the mould immediately after the initial setting time which was approximately five hours. This was found necessary in order to avoid the risk of premature cracking. In the second, the prisms were notched at 21 days using the procedure adopted in Chapter 7. Plate 8.3 shows a 250 mm long specimen prepared using this method. All the prisms were tested on removal from the curing tank at 28 days using 25 mm wide loading platens.

8.5.3 The 3-Point Bend Specimen

The notched beam shown in Figure 8.14 loaded in 3-point (or 4-point) bending is the most commonly used geometry for the evaluation of the fracture toughness or the fracture energy of concrete. A wide range of specimen dimensions has been employed by various researchers. The failure can be unstable, semi-stable or stable depending on the notch depth and the stiffnesses of the specimen and the testing machine. In the present work this geometry was employed to enable direct comparison of the fracture toughness values with those obtained using the CCS and DNASS tests.

The beams employed had square cross sections 100 mm by 100 mm and were 500 mm long. The notches were introduced by means of a clipper cutting machine equipped with a 2.5 mm disc. Plate 8.4 shows the arrangement used for this test.

8.6 Fracture Toughness and Fracture Energy Results - (CCS)

All the compact compression specimens failed in an identical manner to those presented in Chapter 7. Table 8.5 gives the results for the failure loads and the fracture toughness for the two curing temperatures. In general the fracture toughness is approximately 30% greater than those obtained for the concretes employed in Chapter 7, Tables 7.8 and 7.9. It is also seen that high temperature curing (50° C) causes a 10% reduction in k_c. A similar effect was also observed in the results for the tensile strength shown in Figure 8.9. The variation of k_c with the 28-day compressive strength for both curing regimes is presented in Figure 8.15. The fracture toughness values increase with increasing strength (up to 85 N/mm^2) and then decrease. Figure 8.16 shows the variation of fracture toughness with CSF content. Whereas k_c initially increases, beyond certain CSF contents this appears to decrease. Both of the above behaviours are somewhat unexpected and can only be possible if at the high CSF contents (which give high strength values) the critical flaw size in the cement matrix is rapidly decreasing at the same time as either E or G_c is decreasing.

Next the strain energy release rate G_c is calculated. The results obtained using the direct approach (i.e. the SE2 method, Chapter 7) together with those of the indirect approach (SE3 method, Chapter 7) are presented in Table 8.6.

As was found for the results presented in Chapter 7, because of the tortuosity of the fracture path, the fracture energy values obtained using the SE2 method are significantly higher than those of the SE3 method. The tortuosity factors presented in Table 8.6 are of the same order as those obtained in Chapter 7. In Figure 8.17 the results are presented as a function of the CSF content. These show that the values of G_c calculated by the SE2 method exhibit a much greater degree of variation than those calculated by the SE3 method, particularly for the specimens cured at 50° C. Furthermore, the results from the SE3 method, suggest that G_c is little affected by the CSF content.

In view of the difficulties associated with the determination of G_c, outlined in Chapter 7 (section 7.8), and the possible inaccuracies in recording the displacements directly from the testing machine, in the present work the k_c approach is considered to be more reliable.

8.7 Fracture Toughness Results - (DNASS and SNASS)

Figure 8.18 gives the load-displacement graphs for the three DNASS specimens prepared from mix R2 (20° C curing) with a=30 mm and a loading platen width w=15 mm. The curves follow a similar pattern to those obtained from the CCS tests. After an initial bedding-in, they exhibit a linear behaviour up to sudden and unstable failure characterised by a sharp drop in the value of the load. On comparison of these curves with those obtained for the CCS (Figure 7.2) it can be seen that in relation to the total energy absorbed up to failure, the proportion of the work done during the bedding-in process is smaller for the DNASS tests than that for the CCS. For the results presented in Figure 8.18 the average failure load is 82.0 kN and the corresponding coefficient of variation is 7.3%. It was observed that the coefficients of variation for the DNASS were generally higher than those obtained for the CCS. A finite element analysis of a DNASS geometry with a=30 mm and w=20 mm was carried out in Chapter 6 and the stress intensity factor k was reported in Table 6.8. Additional analyses using 8-noded rectangular isoparametric elements were carried out to provide the values for k for the other geometries considered here. For completeness all the results are presented in Table 8.7.

Tables 8.8-8.11 give the results for the failure loads and the corresponding fracture toughness values employing the results for k given in Table 8.7, for the two curing

temperatures considered. In Figures 8.19 and 8.20 the fracture toughness is shown as a function of the 28-day compressive strength given in Table 8.3 for the 20° C and 50° C curing respectively. It is observed that as with the results obtained from the CCS tests (section 8.6), the fracture toughness initially increases with increasing strength and then decreases. The decrease in the fracture toughness occurs at strengths of 92 N/mm^2 in the case of 20° C curing and 98 N/mm^2 for the samples cured at 50° C. It is further observed that when the results for the fracture toughness, obtained from the DNASS, are expressed as a function of the CSF content a similar behaviour to that shown in Figure 8.16 is obtained. In this case the decrease in the fracture toughness with increasing CSF content occurs at levels greater than 16%.

Finite element analyses of the SNASS (section 6.4) demonstrated that k was independent of the specimen length L in the range 250 mm < L < 500 mm. In order to study the effect of the specimen length and the type of notch, i.e. blunt (machine cut) or sharp (cast in), on the fracture toughness, repeats of reference mix 1 (Table 8.2) were made. In total five pairs of prisms of varying lengths with a 100 mm notch were prepared. These were loaded through 25 mm wide platens. The failure loads and fracture toughness values are given in Table 8.12. These increase with increasing specimen length for both notch types. The rate of increase, however, slows down beyond L=230 mm. It is noted that sharp notches produce k_c values which are in the order of 4-7% lower than

those obtained by employing a blunt notch. Nadeau et al [126] obtained k_c results for machine notched and cast notched specimens which varied by less than 10%.

The testing arrangement adopted for the DNASS and the SNASS (i.e. load control) did not yield results for displacements which could be relied upon in calculating the critical strain energy release rate from the areas under the load-displacement graphs. Furthermore, it was evident that this geometry results in a highly stiff specimen in relation to the stiffness of the testing machine. As a result the correction required to account for the machine-specimen interaction would be of such an order that might invalidate the calculation method.

8.8 Verification Tests

The work on fracture toughness presented in this thesis is largely based on laboratory tests conducted on two geometries namely the CCS and the DNASS. It was considered desirable to assess these results in the light of those obtained from a standard test geometry commonly used for concrete materials. The geometry chosen is that of the 3-point bend specimen shown in Figure 8.14. For this purpose a repeat of mix 2 (Table 8.2) was made from which three specimens for each of the geometries shown in Table 8.13 were prepared. In accordance with the RILEM recommendations [112], 50 mm notches were introduced into the centre of the 3-point bend specimens at 21 days. The compact compression specimens and the beams in 3-point bending were tested under displacement control with a cross-head speed of 0.4 mm/min while the DNASS's were tested under load control with a cross-head speed of 0.5 mm/min. The fracture toughness from the flexural tests was calculated using the expression

$$k_c = Y \sigma_f a^{\frac{1}{2}} \qquad (8.1)$$

Where σ_f is the apparent fracture stress, 'a' is the notch depth and Y is a geometrical parameter obtained from the following expression given by Brown and Srawley [101]

$$Y = 1.93-3.07(a/d)+14.53(a/d)^2-25.11(a/d)^3+25.8(a/d)^4 \qquad (8.2)$$

Table 8.13 gives the results for the loads at failure and the corresponding fracture toughness k_c. These show that all three test geometries give similar results for the fracture toughness thus demonstrating the validity of the geometries employed here.

8.9 Brittleness

The results shown in Figures 8.15, 8.19 and 8.20 indicated that whereas initially the fracture toughness increases with compressive strength, beyond certain levels of strength (>85 N/mm^2) it decreases suggesting an increase in brittleness. This is similar to the observed behaviour for metals where the fracture toughness decreases with increasing tensile strength [58]. Carrasquillo et al [11] observed that the cracking in high strength concrete is more localised and tends to approach more homogeneous material behaviour than that in normal concrete. This was observed from the stress-strain relationships they obtained for concretes with different strengths. These relationships did not only result in a more linear elastic behaviour but also indicated increased brittleness during the post-cracking stage. Such behaviour is characterised by the steepness of both the ascending and descending parts of the stress-strain curves for concretes with high strength [11-13, 22, 127].

In order to quantify the behaviour of concrete in terms of brittleness it is possible to make use of a dimensionless parameter called the Brittleness Number (BN). The degree of brittleness of an object may be considered to depend on the material properties, i.e. tensile strength f_t, modulus of elasticity E, fracture energy G_c and on the dimension L. In calculating the brittleness number L was arbitrarily taken to be the size of the cube. The BN is expressed as

$$BN = \frac{f_t^2 \, L}{E \, G_c} \tag{8.3}$$

The BN of an object has also been defined as the ratio L/l_{ch} in which l_{ch} is the characteristic length which is a material parameter taking into account the effects of f_t, E and G_c [128]. Thus

$$\frac{L}{l_{ch}} = \frac{f_t^2 \, L}{E \, G_c} \tag{8.4}$$

giving

$$l_{ch} = \frac{E \, G_c}{f_t^2} \tag{8.5}$$

Equation 8.3 was used to determine the BN for the concretes employed in the present study. For the purpose of this calculation the relevant properties obtained from the various tests are summarised in Table 8.14. In calculating the BN, using equation 8.3, the object size L was taken to be 0.1 m, i.e. the cube size.

Assuming plane strain conditions the brittleness number may also be expressed in terms of the fracture toughness k_c by the following equation

$$BN = \frac{f_t^2 \, L}{k_c^2 \, (1-\mu^2)} \tag{8.6}$$

The values obtained using equation 8.6, i.e. from k_c, with μ=0.2 are also shown in Table 8.14. The values yielded by equation 8.6 are several times greater than those obtained using the experimental values of G_c and E through equation 8.3. On the basis of the previous discussions the BN values yielded by equation 8.6 are adopted as the more reliable.

Table 8.15 gives k_c obtained from the DNASS tests and the corresponding BN calculated using equation 8.6. In Figure 8.21 the BN is plotted against the 28-day compressive strength given in Table 8.3. It can be seen that the BN calculated from k_c has a value of about 2.5 for strengths up to 90 N/mm^2. Beyond this strength the BN appears to increase suggesting an increase in the concrete's brittleness. Carpinteri [46] reports a value for the BN of approximately 4 for concretes made with w/c = 0.5-0.6 and having a tensile strength of 3.6-4.6 N/mm^2.

Notwithstanding the reasons given above for adopting the k_c approach, it is of interest to note that the values of BN calculated by equation 8.3 show little variation due to increasing compressive strength. This is particularly significant as the BN evaluated in this way utilises results for G_c and E determined independently by experiment.

Table 8.16 summarises the results for the mechanical and fracture properties for the high strength concrete examined in the present work. The table also gives the results for the characteristic length l_{ch} as determined by equation 8.5.

For comparison purposes the corresponding properties for concrete reported by Petersson [45] as well as those for various cement based materials reported by Hillerborg [128] and Bache [129] are given. It can be seen that the values obtained here are of the same order as those reported in [45] and [128].

8.10 Conclusions

In this chapter a study of the mechanical and fracture properties of high strength CSF concrete wet cured at 20° C and 50° C was carried out. For w/c = 0.35, 28-day cube strengths in the range 74-110 N/mm^2 were obtained with CSF replacements for cement up to 28%. Whereas high temperature curing resulted in increased early strength for all the CSF contents employed, the strength beyond 14 days was increased only for concretes with CSF contents greater than 16%.

The 20° C cured specimens with the lower CSF contents showed a levelling off in strength gain at about 28 days. However, those with CSF contents greater than 16% continued to gain strength beyond 28 days. The results also indicated that the early strength reduced markedly when the CSF content was increased from 16% to 20%. Although, this was unexpected, in reviewing the literature it was found that Yogendran et al [1] obtained similar behaviour from compression cylinder tests. Although the authors [1] attributed the loss in strength to improper compaction, this problem was not evident in the present work as the specimens cured at 50° C, which were prepared from the same batch as those cured at 20° C, did not exhibit this behaviour. A possible explanation for the reduction in strength could be that at some CSF replacement levels there are less hydration products which not only lead to a reduction in the cementitious gel but also smaller quantities of accessible calcium hydroxide for reaction with the CSF. The abundance

of CSF particles at the higher levels (28%) leads to greater dispersal and hence increased reaction rates with the calcium hydroxide which, in turn, produces additional gel for strength enhancement.

The results obtained from the cylinder splitting tests showed that no significant influence on the relationship between the tensile and compressive strengths is exhibited by the two curing regimes employed in the present investigation. The results also indicated that for high strength concrete the rate of increase in tensile strength with increasing compressive strength is lower than that for normal concrete. Whereas for low strength concrete (< 70 N/mm^2), the tensile strength is approximately 10% of the compressive strength, for the high strength concretes employed in this investigation this value is in the range 4-6%. These findings are in agreement with those of Dewar [15].

The tensile strength did not increase significantly with increasing CSF content. As with the compressive strength it was found that a small decrease in the tensile strength was obtained when the CSF content was increased from 16% to 20%.

As with the tensile strength, the curing temperature did not significantly affect the relationship between the static modulus of elasticity and the compressive strength. Furthermore, compressive strengths greater than 90 N/mm^2 were associated with significant reductions in the modulus

of elasticity at both curing temperatures. The relationship between the modulus of elasticity and the CSF content revealed that OPC replacements by CSF greater than 16% lead to marked reductions in the calculated values of the modulus of elasticity. Although this behaviour is unexpected it may be explained if an increase in the CSF content above a critical level results in an increase in the porosity. This increase in porosity may, in part, be responsible for the reductions in the densities reported in Tables 7.6 and 8.3.

The fracture toughness k_c was evaluated using two tests, namely the CCS and DNASS tests. Both tests yielded k_c values which increased with increasing compressive strength up to 85 N/mm^2 for the CCS and 97 N/mm^2 for the DNASS. Beyond these strengths, k_c showed a reduction with increasing compressive strength. A similar trend was also observed when the results were viewed in relation to the CSF content. Whereas initially k_c increased with increasing CSF content, this decreased beyond CSF contents of 16% for the 50° C cured specimens and 20% for the 20° C cured specimens. These results suggest that at the higher CSF contents (which give high compressive strength values) the critical flaw size in the cement matrix is rapidly decreasing at the same time as either E or G_c is decreasing. It was pointed out earlier that E did, indeed, show a reduction at high CSF levels.

The load-displacement relationships obtained from the CCS tests were employed to determine the critical strain energy release rate or fracture energy G_c. G_c was also evaluated

from k_c by employing equation 3.31 and the experimental values for E given in Table 8.4. It was found that G_c evaluated from the load-displacement relationship is several times that evaluated from k_c. This difference is considered to be largely due to the fact that no allowance was made for the tortuosity of the fracture surface when calculating G_c from the area under the load-displacement curves. For this reason and because of the possible inaccuracies involved in the displacements recorded directly from the testing machine, the stress intensity factor approach in evaluating k_c is considered to be more reliable in the present work. The validity of this approach using the CCS and the DNASS was confirmed by comparing the k_c values with that obtained using the 3-point bend test usually employed for concrete materials.

It is of particular significance to note that both E and k_c, which are determined independently, decrease with increasing compressive strength beyond 85 N/mm^2 (CSF > 16%). This, in fact, is the reason for the almost constant values for G_c reported earlier and obtained by the SE3 method, i.e. from k_c.

The stress intensity factor approach was used to assess the degree of brittleness of the high strength concrete. It was shown that both the CCS and DNASS tests yielded similar results for the brittleness number. It was also noted that beyond a strength of about 90 N/mm^2 the brittleness number increased with further increase in strength. This increase

in brittleness was anticipated in view of the results obtained for k_c which decreased with increasing compressive strength. In calculating the brittleness number the object size L was taken to be the size of the test cube. This is arbitrary and other parameters including the aggregate size and the diameter of the reinforcing bars, when present, have been suggested [129].

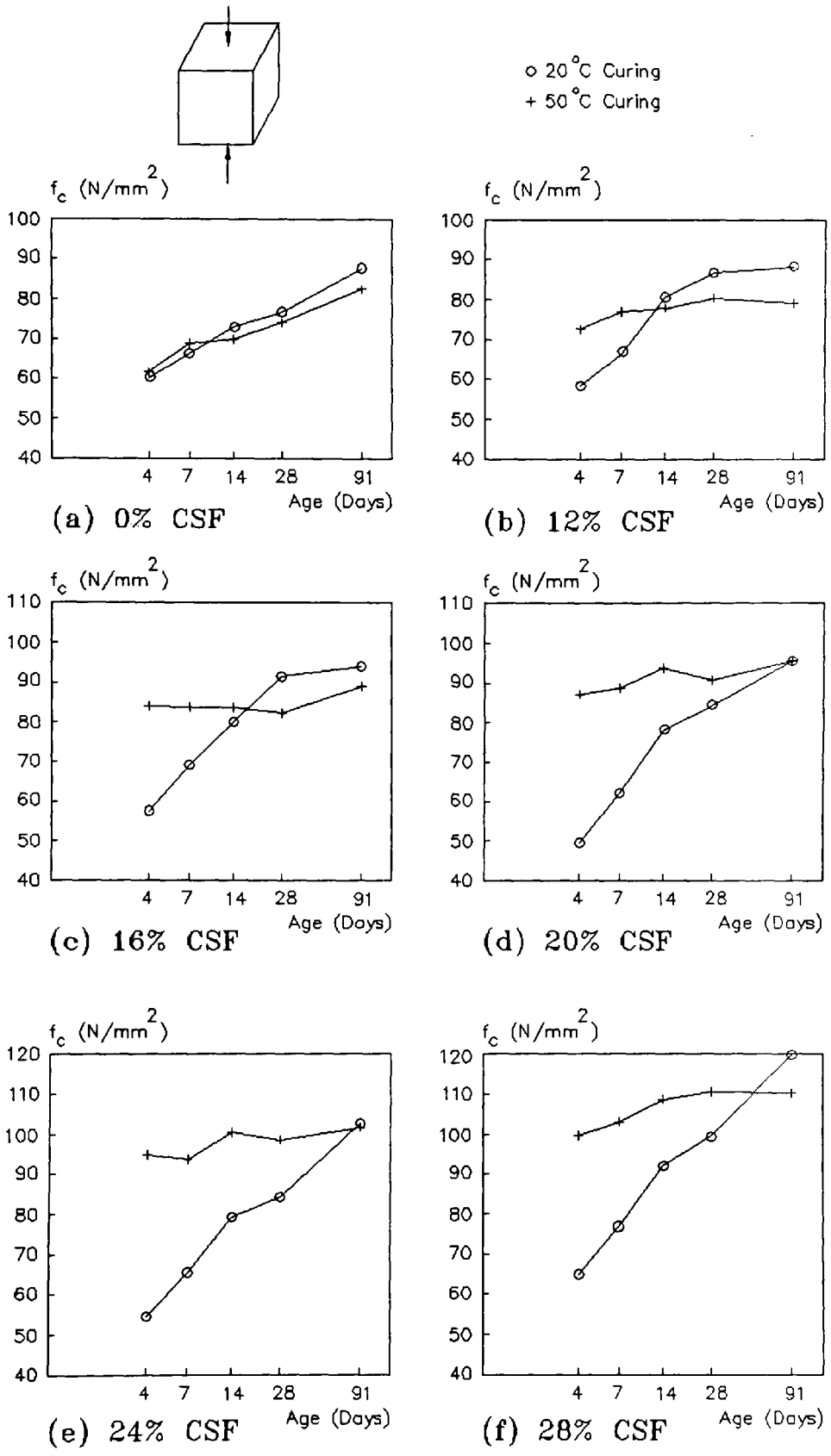

Figure 8.1 Variation of Compressive Strength with Age for Different CSF Contents - w/c=0.35.

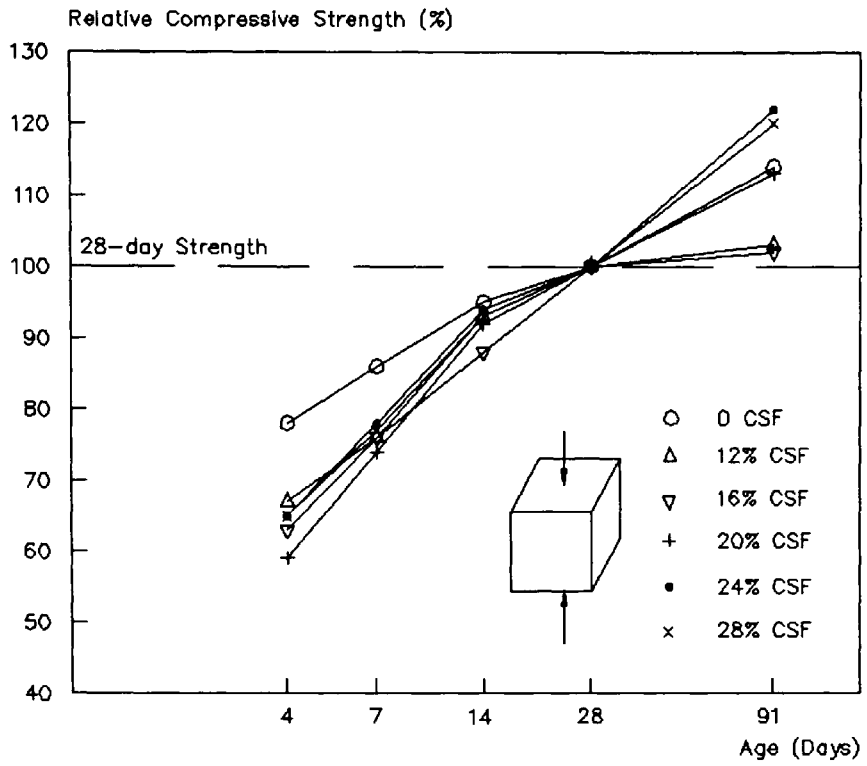

Figure 8.2 Compressive Strength Development of CSF Concrete Cured at 20° C - w/c= 0.35.

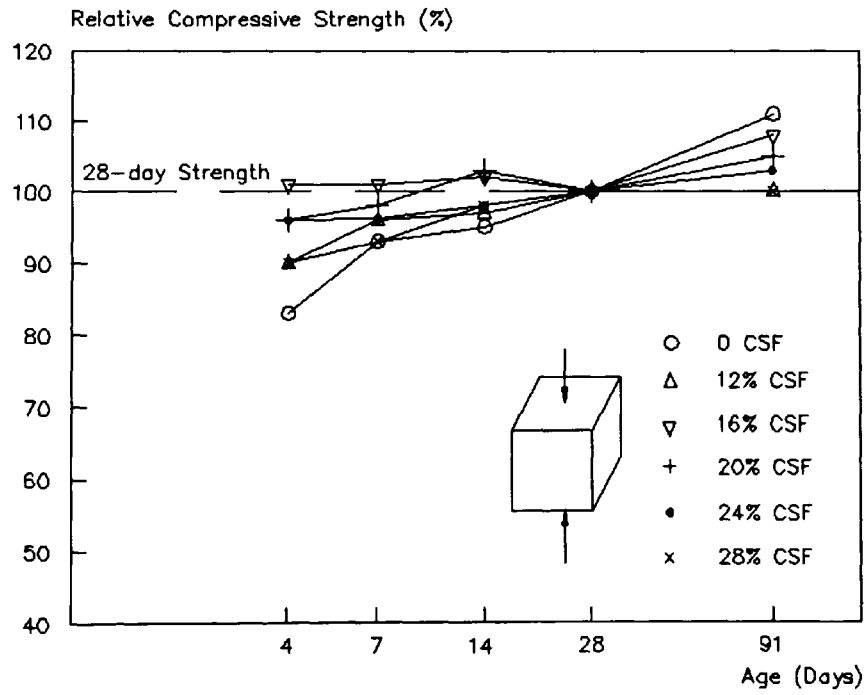

Figure 8.3 Compressive Strength Development of CSF Concrete Cured at 50° C - w/c= 0.35.

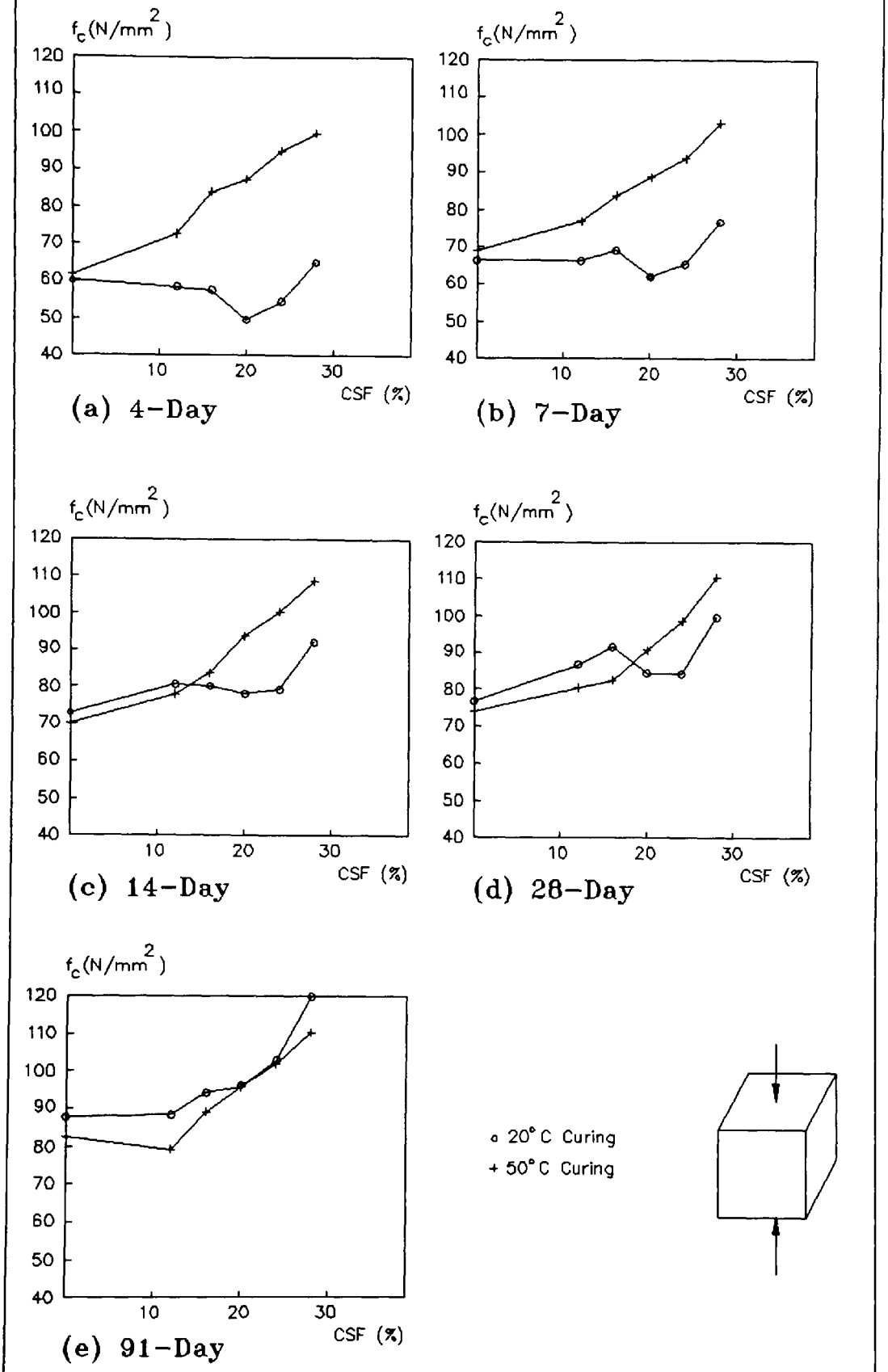

Figure 8.4 Variation of Compressive Strength with CSF Content for Different Ages - w/c= 0.35.

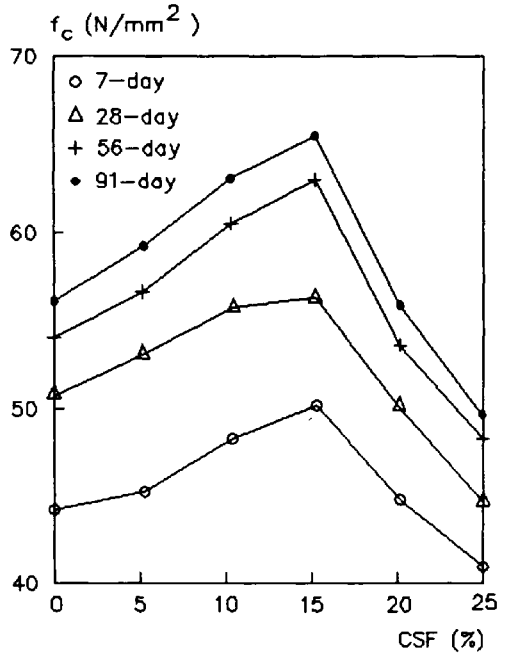

Figure 8.5 Variation of Compressive Strength with CSF Content for Different Ages – w/c= 0.34 [1].

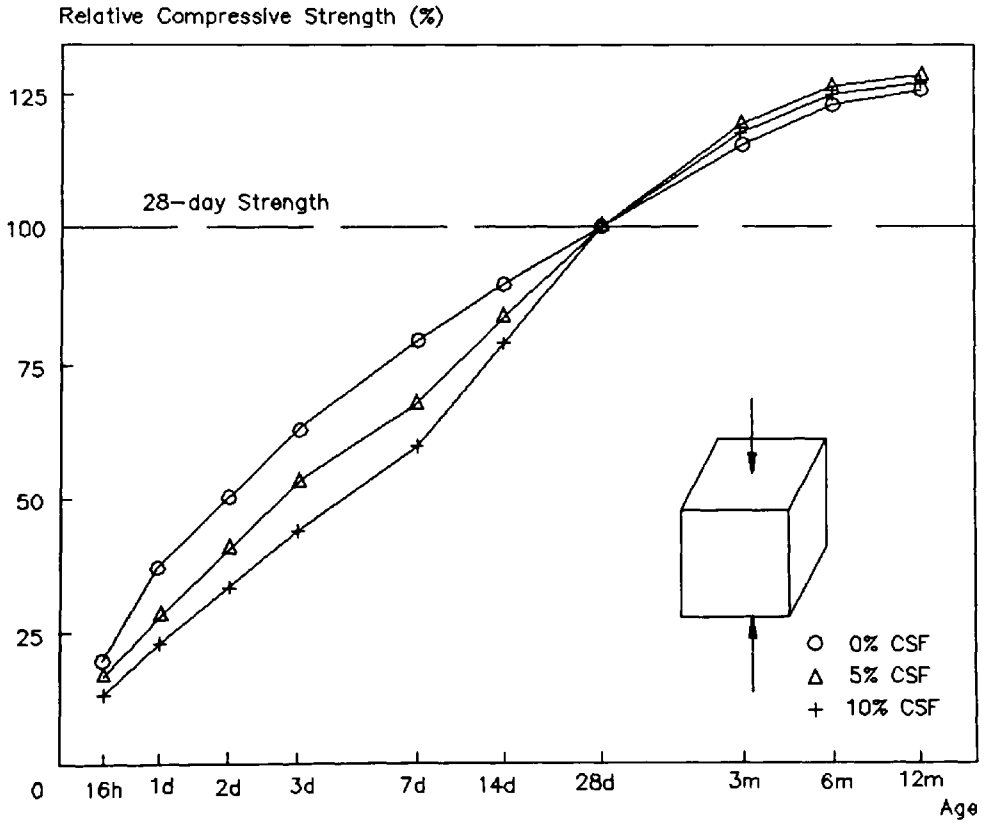

Figure 8.6 Compressive Strength Development of CSF Concrete Cured at 20° C [10].

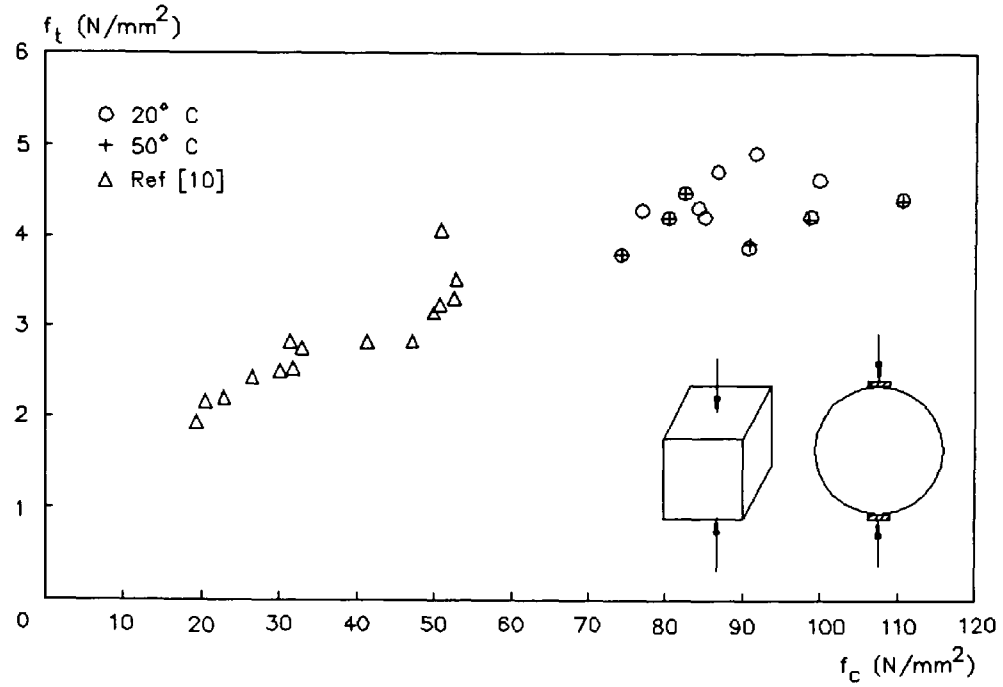

Figure 8.7 Variation of Tensile Strength with Compressive Strength of CSF Concrete at 28 Days - w/c=0.35.

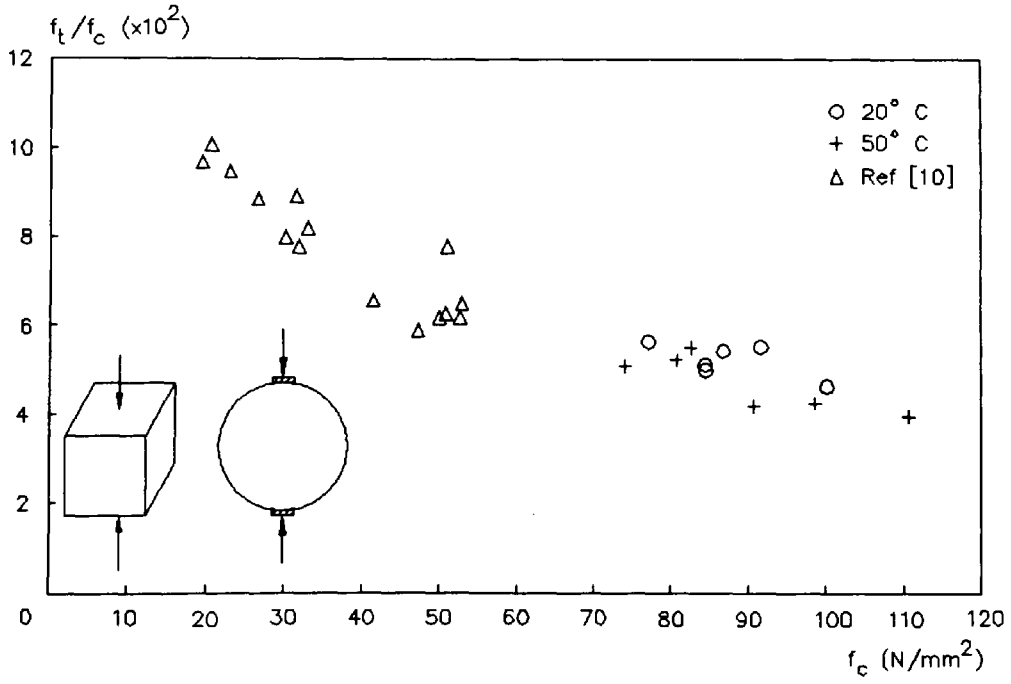

Figure 8.8 Variation of Compressive Strength with the Ratio of Tensile to Compressive Strengths at 28 Days - w/c=0.35.

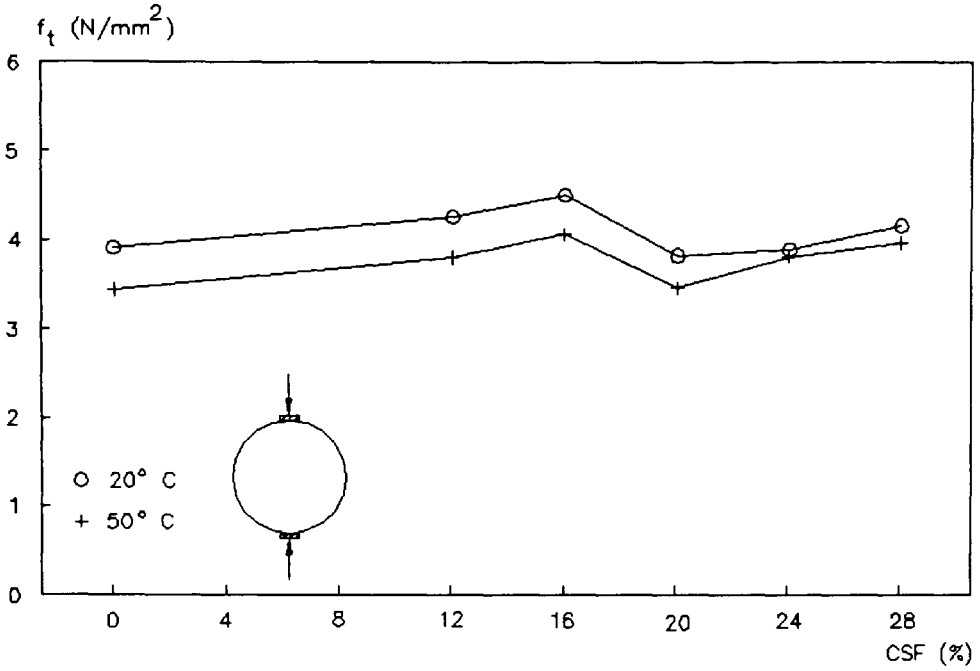

Figure 8.9 Variation of Tensile Splitting Strength with CSF Content - w/c=0.35.

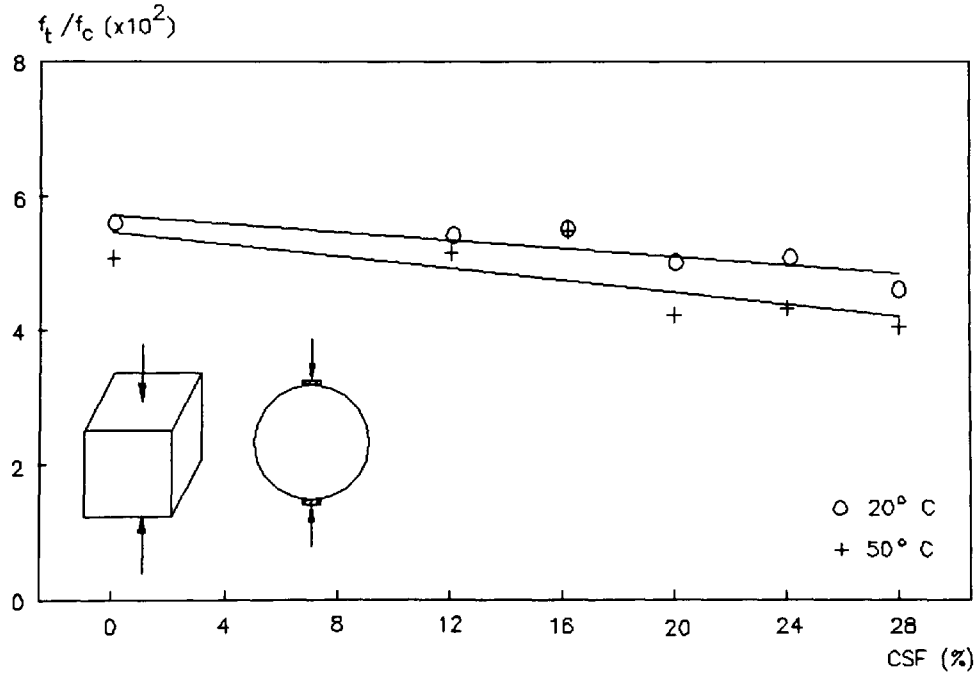

Figure 8.10 Variation of the Ratio of Tensile to Compressive Strengths with CSF Content - w/c=0.35.

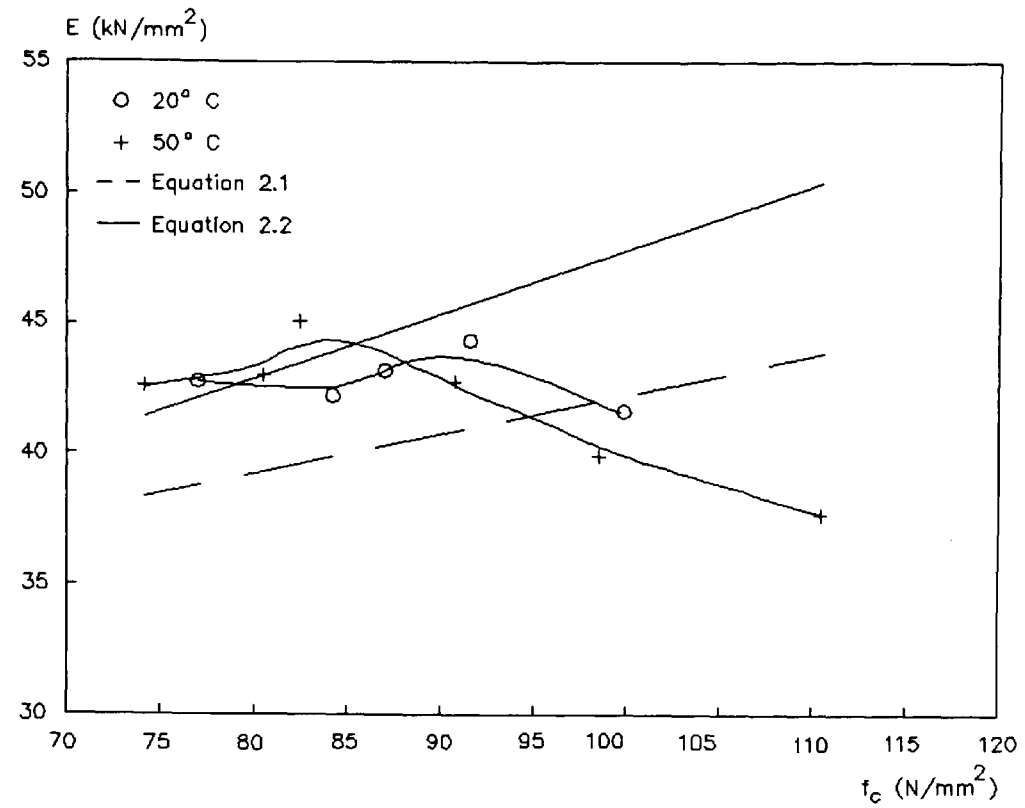

Figure 8.11 Variation of Modulus of Elasticity with Compressive Strength at 28 Days – w/c=0.35.

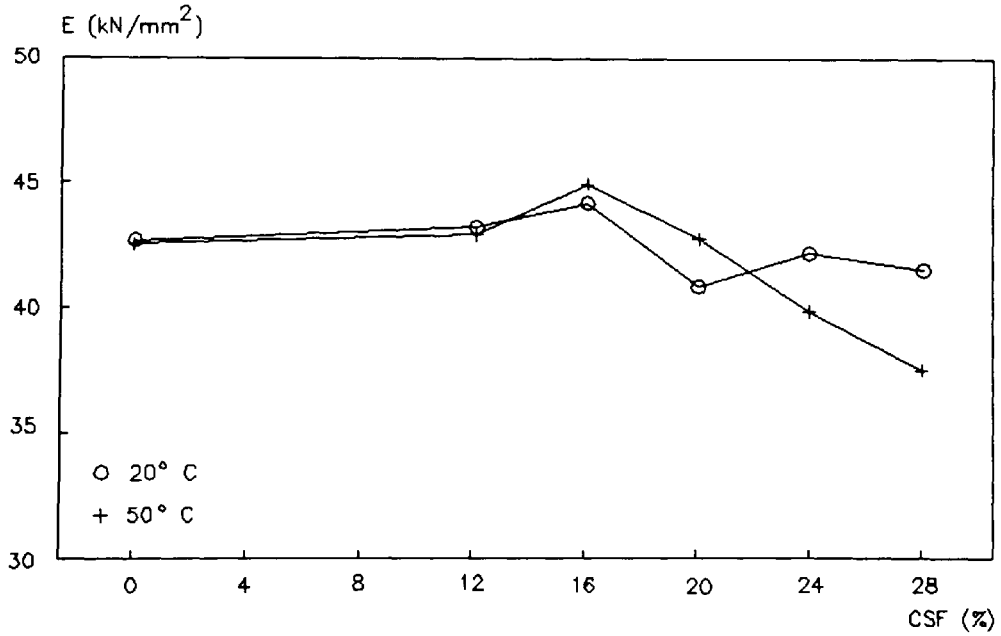

Figure 8.12 Variation of Modulus of Elasticity with CSF Content at 28 Days – w/c=0.35.

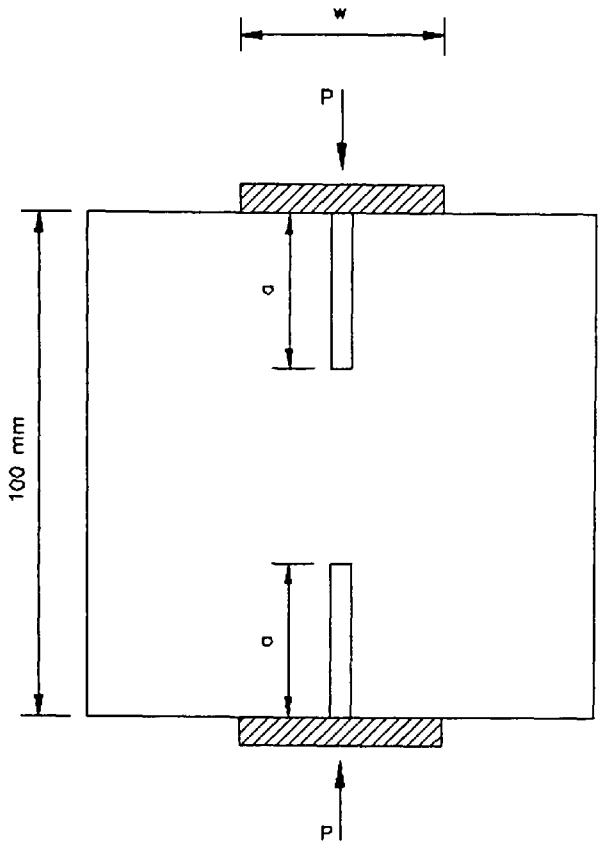

Figure 8.13 The Doubly Notched Axial Splitting Specimen (DNASS).

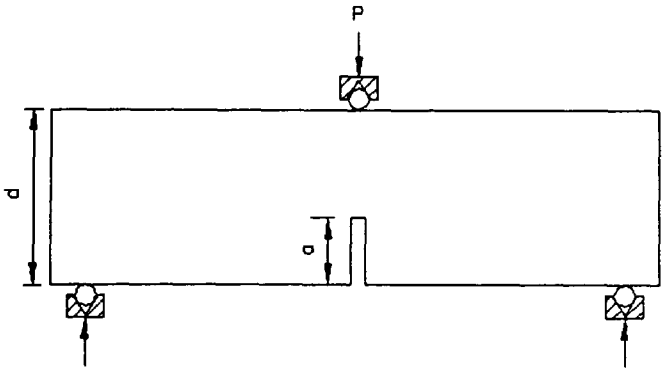

Figure 8.14 The 3-Point Bend Specimen.

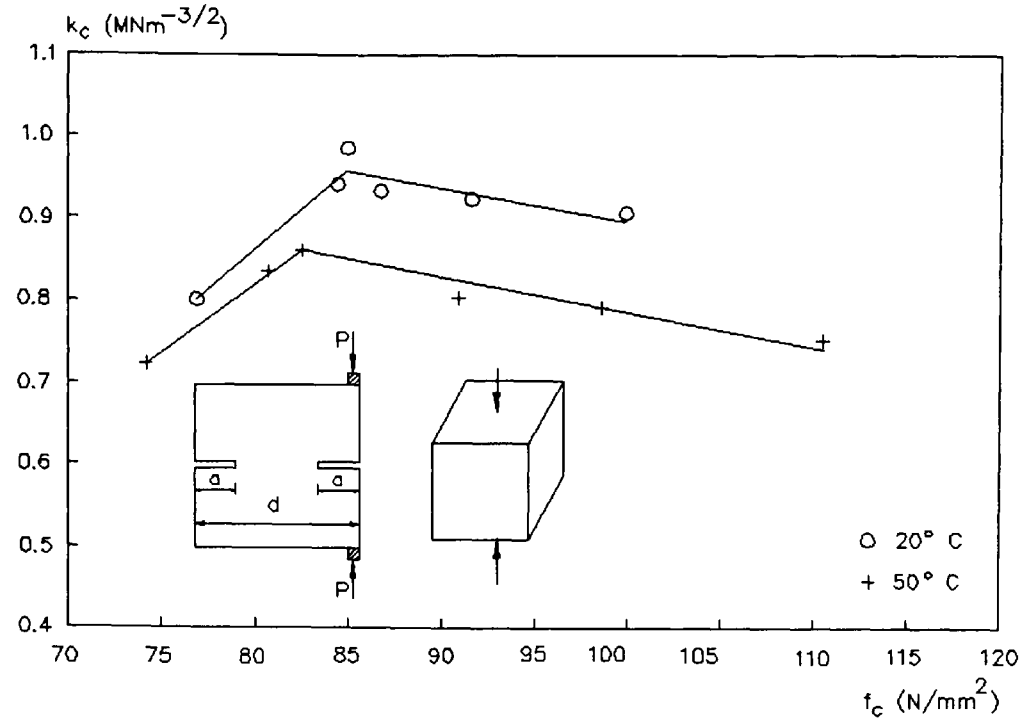

Figure 8.15 Variation of k_c (CCS, a=30 mm) with Compressive Strength of CSF Concrete at 28 Days.

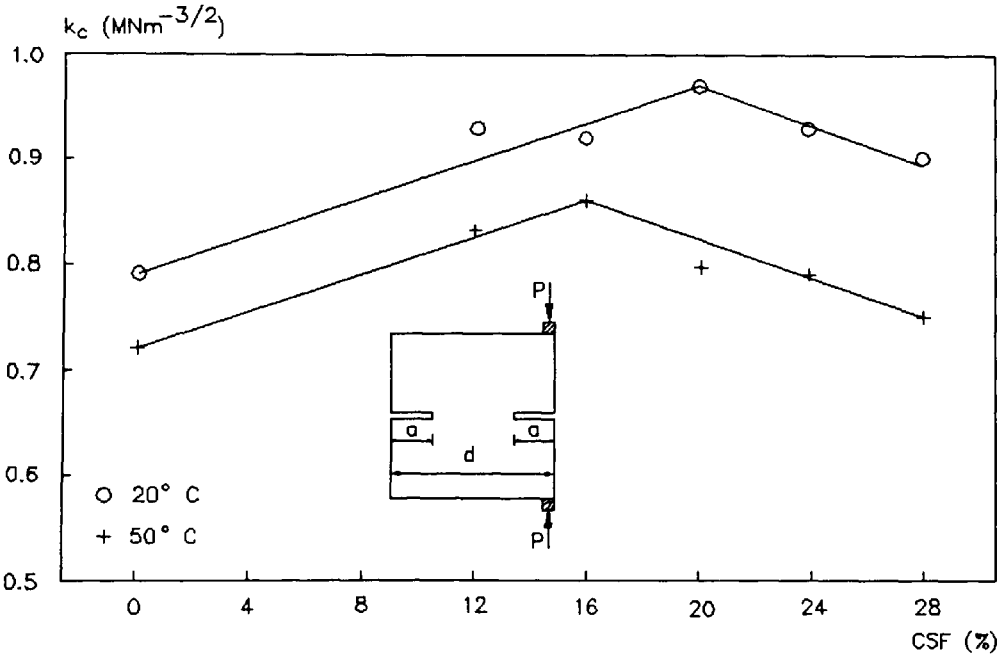

Figure 8.16 Variation of k_c (CCS, a=30 mm) with CSF Content.

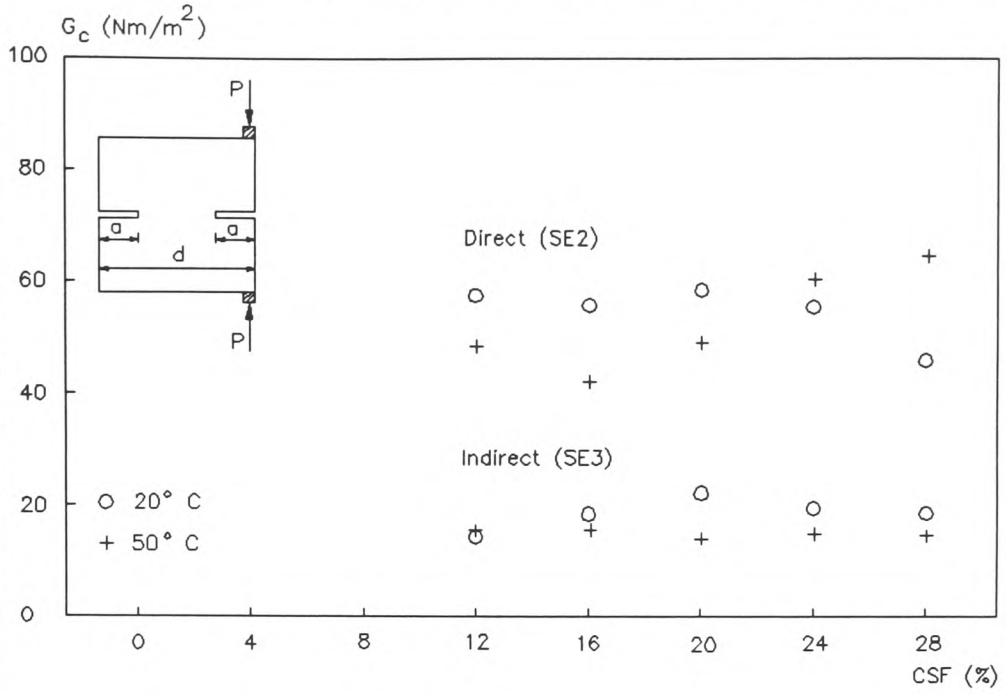

Figure 8.17 Variation of G_c (CCS, a=30 mm) with CSF Content for High Strength Concrete.

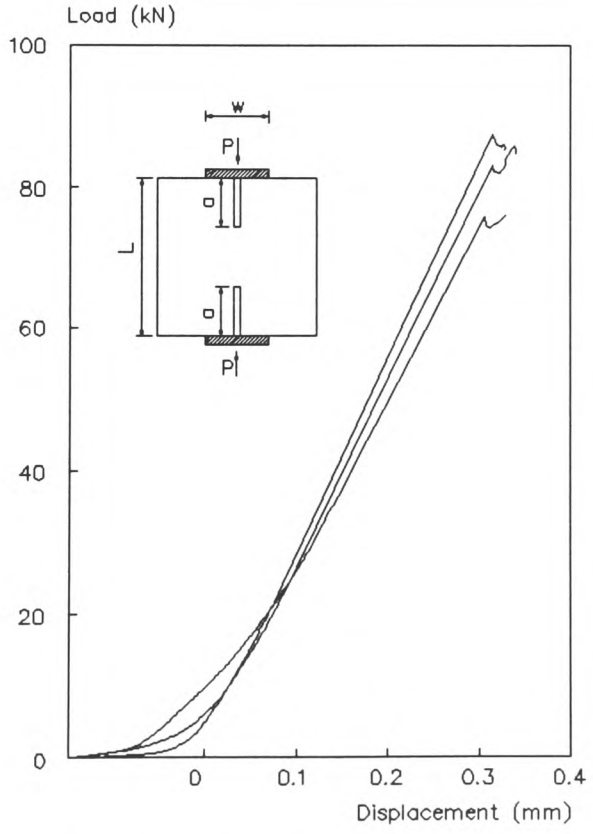

Figure 8.18 Typical Load–Displacement Graphs for the DNASS (Mix R2, 20° C, a=30 mm).

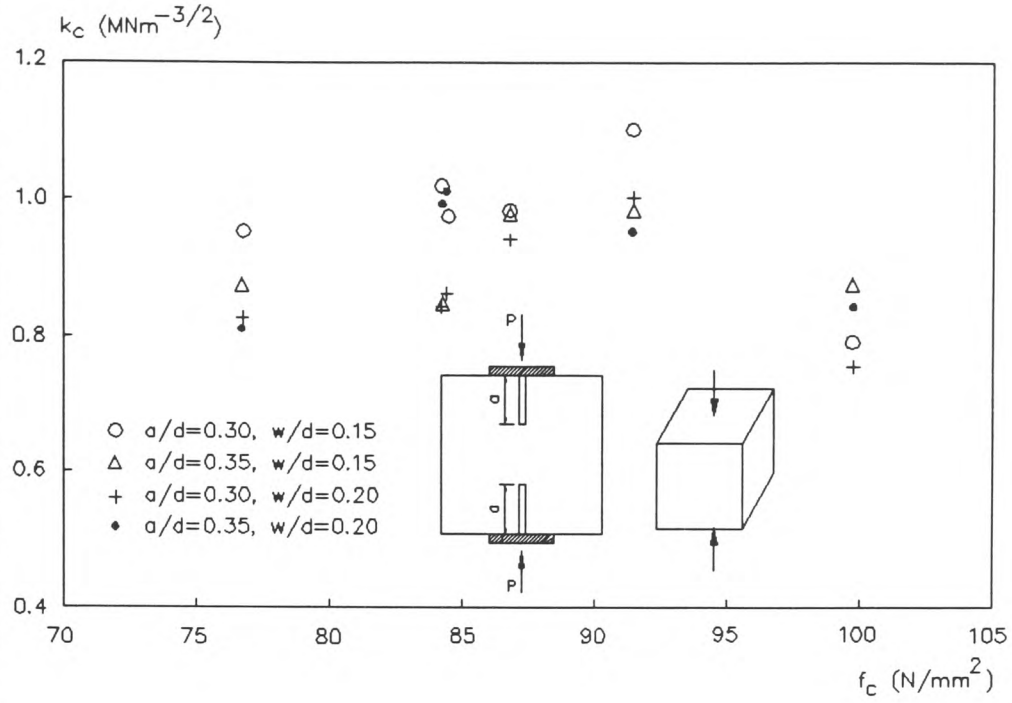

Figure 8.19 Variation of k_c (DNASS) with Compressive Strength for High Strength Concrete Cured at 20° C.

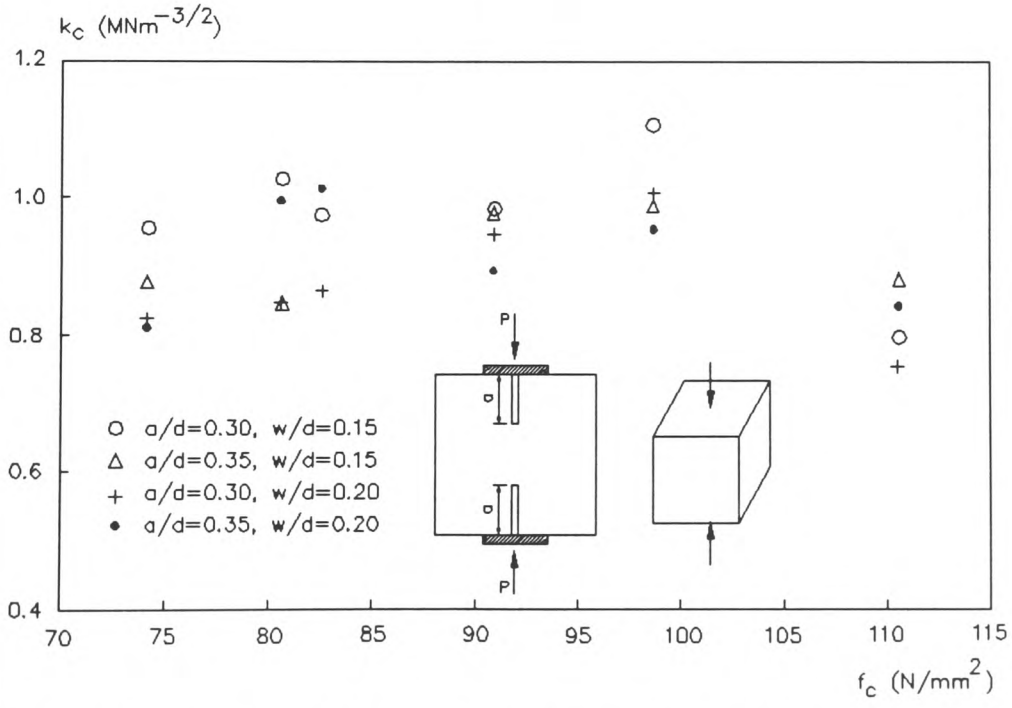

Figure 8.20 Variation of k_c (DNASS) with Compressive Strength for High Strength Concrete Cured at 50° C.

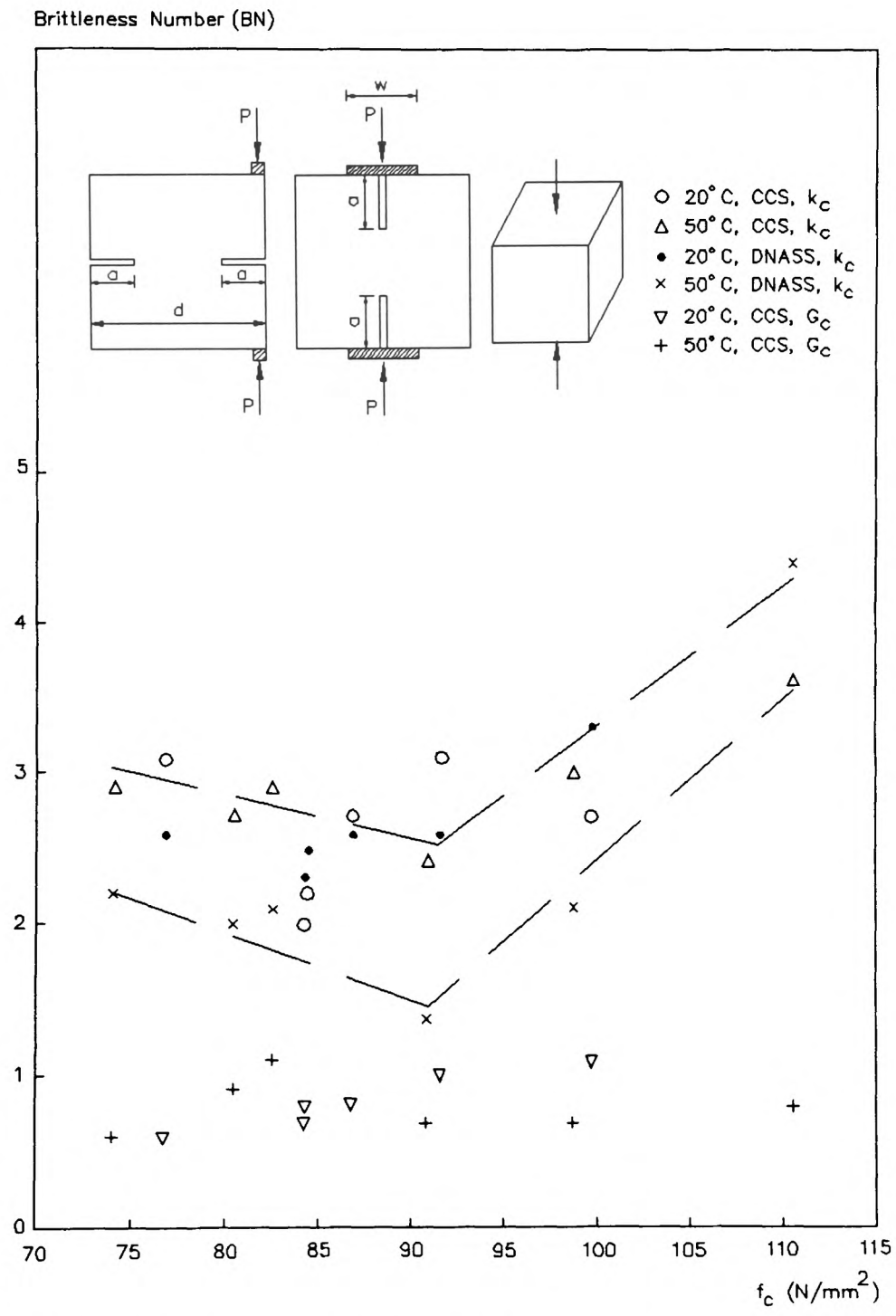

Figure 8.21 Variation of Brittleness Number with Compressive Strength of High Strength Concrete Cured at 20° C and 50° C - (CCS and DNASS).

Mix Ref	w/c ratio	CSF (%)	SP1 (%)	Slump (mm)	Density (kg/m^3)	f_c (N/mm^2)
A	0.40	0	0	95	2430	54.8
B	0.37	0	0	30	2410	55.4
C	0.35	0	0	20	2470	67.3
D	0.35	30	2 3 4	100 130 155	2410 2440 2445	79.1 85.3 82.6
E	0.35	20	2.5 3	120 155	2460 2455	64.4 67.7

Table 8.1 Details of the Trial Mixes.

Mix No.	CSF (%)	CSF Slurry (kg/m^3)	Water (kg/m^3)	Cement (kg/m^3)	SP1 (%)	SP1 L/m^3	Slump (mm)
1	0	0	165.0	470.0	0	0	15
2	12	112.8	108.6	413.6	2.0	8.2	74
3	16	150.4	89.8	394.8	2.5	10.3	110
4	20	188.0	71.0	376.0	3.0	12.4	141
5	24	225.6	52.2	357.2	3.5	14.4	156
6	28	263.2	33.4	338.4	4.0	16.5	170

Table 8.2 Mix Proportions per m^3, w/c=0.35.

Mix No.	CSF (%)	28-day Density	Temp. (°C)	Compressive Strength, f_c (N/mm^2)				
				4-day	7-day	14-day	28-day	91-day
1	0	2440	20	60.2	66.3	72.9	76.7	87.7
2	12	2430		58.4	66.3	80.6	86.7	88.2
3	16	2405		57.5	69.1	80.1	91.5	94.1
4	20	2425		49.6	62.1	78.1	84.4	95.5
5	24	2410		54.5	65.5	79.2	84.2	102.7
6	28	2405		65.0	76.8	92.1	99.7	119.8
7	0	2445	50	61.7	68.8	70.0	74.0	82.4
8	12	2420		72.6	77.0	77.9	80.4	79.2
9	16	2390		83.9	83.8	83.7	82.4	89.0
10	20	2415		87.2	88.8	93.8	90.7	95.5
11	24	2405		94.8	95.8	100.4	98.6	101.7
12	28	2410		99.6	103.1	108.7	110.5	110.3

Table 8.3 Cube Compressive Strength for CSF Concrete Cured at 20° C and 50° C.

Mix No.	CSF (%)	SP1 (%)	TEMP. (° C)	E (kN/mm^2)	f_t (N/mm^2)
1	0	0	20	42.6	4.3
2	12	2.0		43.1	4.7
3	16	2.5		44.2	5.0
4	20	3.0		40.8	4.2
5	24	3.5		42.1	4.3
6	28	4.0		41.4	4.6
7	0	0	50	42.5	3.8
8	12	2.0		42.9	4.2
9	16	2.5		45.0	4.5
10	20	3.0		42.7	3.8
11	24	3.5		39.8	4.2
12	28	4.0		37.6	4.4

Table 8.4 Modulus of Elasticity and Tensile Strength of CSF Concrete Cured at 20° C and 50° C.

Mix Ref.	CSF (%)	SP1 (%)	Temp. (° C)	Failure Load (kN)		V (%)	k_C ($MNm^{-3/2}$)
R1	0	0	20	6.61 – 6.69	6.64	1.0	0.79
R2	12	2.0		7.84 7.43 7.97	7.75	3.6	0.93
R3	16	2.5		7.70 8.01 7.35	7.69	4.3	0.92
R4	20	3.0		7.95 7.75 8.80	8.16	6.8	0.97
R5	24	3.5		7.35 7.88 8.21	7.81	5.5	0.93
R6	28	4.0		7.51 7.90 7.13	7.51	5.1	0.90
R1	0	0	50	5.72 5.75 6.64	6.03	8.6	0.72
R2	12	2.0		7.03 6.77 6.95	6.92	1.9	0.83
R3	16	2.5		6.77 7.51 7.13	7.14	7.3	0.85
R4	20	3.0		7.06 6.38 6.45	6.63	5.6	0.79
R5	24	3.5		6.87 6.23 6.65	6.58	4.9	0.78
R6	28	4.0		6.12 6.08 6.57	6.26	4.3	0.75

V = Coefficient of Variation

Table 8.5 Failure Loads and Fracture Toughness Values (CCS, a=30 mm).

Mix Ref.	CSF (%)	Temp. (° C)	Max. Load (kN)	Max. Displ (mm)	G_c (Nm/m^2)		TF
					SE2	SE3	
R1	0	20	6.64	0.122	69.8	14.4	4.8
R2	12		7.75	0.107	60.8	14.3	4.3
R3	16		7.69	0.102	55.8	18.4	3.0
R4	20		8.16	0.104	58.5	22.6	2.6
R5	24		7.81	0.101	55.0	20.1	2.7
R6	28		7.51	0.092	46.1	18.8	2.5
R1	0	50	6.03	0.115	60.7	11.7	5.2
R2	12		6.92	0.095	48.0	15.4	3.1
R3	16		7.14	0.088	42.1	15.8	2.7
R4	20		6.63	0.097	49.0	14.4	3.4
R5	24		6.58	0.111	60.4	15.1	4.0
R6	28		6.26	0.118	64.3	14.4	4.5

Table 8.6 Variation of Critical Strain Energy Release Rate with CSF Content (CCS, a=30 mm).

w/d	a/d	k ($m^{-3/2}$)
0.15	0.30	12.0
	0.35	14.1
0.20	0.30	11.0
	0.35	13.2

Table 8.7 Comparison of k Values for the Geometries Considered in Section 8.5.2 (DNASS) - Rectangular Elements.

Mix Ref.	CSF (%)	w/d	a/d	Failure Load (kN)		V (%)	k_c ($MNm^{-3/2}$)
R1	0	0.15	0.30	83.8 71.5 83.7	79.7	8.9	0.95
			0.35	58.1 60.0 67.1	61.7	7.7	0.87
		0.20	0.30	79.2 75.0 70.0	74.7	6.2	0.82
			0.35	55.0 65.5 64.5	61.7	9.4	0.81
R2	12	0.15	0.30	82.9 87.5 75.7	82.0	7.3	0.98
			0.35	57.0 77.6 71.8	68.8	15.4	0.97
		0.20	0.30	86.0 81.5 89.5	85.7	4.7	0.94
			0.35	73.0 67.0 62.0	67.3	8.2	0.89
R3	16	0.15	0.30	87.0 88.5 99.2	91.6	7.2	1.10
			0.35	74.0 58.0 77.0	69.6	14.6	0.98
		0.20	0.30	101.0 70.3 101.0	90.8	19.5	1.00
			0.35	54.5 63.0 68.0	61.8	11.0	0.95

V = Coefficient of Variation

Table 8.8 Failure Loads and Fracture Toughness Values (DNASS) - Mixes R1-R3, 20° C Curing.

Mix Ref.	CSF (%)	w/d	a/d	Failure Load (kN)		V (%)	k_c ($MNm^{-3/2}$)
R4	20	0.15	0.30	70.2 62.7 85.4	72.8	15.9	0.87
			0.35	47.0 50.0 53.7	50.2	6.7	0.71
		0.20	0.30	77.8 78.8 78.7	78.4	0.8	0.86
			0.35	84.6 69.0 75.2	76.3	10.3	1.01
R5	24	0.15	0.30	83.0 87.8 84.4	85.1	2.9	1.02
			0.35	70.1 54.0 55.7	59.9	14.7	0.84
		0.20	0.30	81.5 58.3 88.3	76.0	20.6	0.84
			0.35	77.0 80.0 69.3	75.4	7.3	0.99
R6	28	0.15	0.30	69.8 67.2 59.8	65.6	7.9	0.79
			0.35	69.7 67.7 48.7	62.0	18.7	0.87
		0.20	0.30	66.0 62.5 75.0	67.8	9.5	0.75
			0.35	73.8 62.5 55.1	63.8	14.8	0.84

V = Coefficient of Variation

Table 8.9 Failure Loads and Fracture Toughness Values (DNASS) - Mixes R4-R6, 20° C Curing.

Mix Ref.	CSF (%)	w/d	a/d	Failure Load (kN)		V (%)	k_c ($MNm^{-3/2}$)
R1	0	0.15	0.30	59.3 48.0 51.5	52.9	10.9	0.64
			0.35	54.8 59.7 64.0	59.5	7.9	0.84
		0.20	0.30	83.4 79.9 86.6	83.3	4.0	0.91
			0.35	70.2 69.0 69.5	69.6	0.9	0.92
R2	12	0.15	0.30	76.5 71.2 85.0	77.6	9.0	0.93
			0.35	55.0 54.7 56.0	55.2	1.2	0.78
		0.20	0.30	84.8 94.0 86.0	88.3	5.7	0.97
			0.35	79.0 83.8 89.2	84.0	6.0	1.11
R3	16	0.15	0.30	70.4 72.3 68.1	70.2	3.0	0.84
			0.35	75.0 68.2 60.3	67.8	13.6	0.96
		0.20	0.30	98.3 102.0 80.1	93.4	12.6	1.03
			0.35	84.5 82.0 98.2	88.2	9.9	1.16

V = Coefficient of Variation

Table 8.10 Failure Loads and Fracture Toughness Values (DNASS) - Mixes R1-R3, 50° C Curing.

Mix Ref.	CSF (%)	w/d	a/d	Failure Load (kN)		V (%)	k_c ($MNm^{-3/2}$)
R4	20	0.15	0.30	92.0 73.2 85.8	83.7	11.6	1.00
			0.35	63.8 67.2 70.3	67.1	4.8	0.95
		0.20	0.30	102.6 94.9 99.8	99.1	3.9	1.09
			0.35	85.1 97.1 91.8	91.3	6.6	1.21
R5	24	0.15	0.30	75.0 78.0 74.0	75.7	2.8	0.91
			0.35	59.4 62.3 54.3	58.7	6.9	0.83
		0.20	0.30	87.5 87.0 96.2	90.2	5.6	0.99
			0.35	79.3 76.9 76.8	77.7	1.8	1.03
R6	28	0.15	0.30	56.3 49.5 49.5	51.8	7.6	0.62
			0.35	54.6 49.4 52.6	52.0	4.5	0.73

V = Coefficient of Variation

Table 8.11 Failure Loads and Fracture Toughness Values (DNASS)- Mixes R4-R6, 50° C Curing.

Sample No.	Notch Type	L (mm)	Failure Load (kN)	k_c ($MNm^{-3/2}$)
1	Blunt	150	85.2	1.23
2		200	99.6	1.43
3		250	102.6	1.48
4		280	108.9	1.57
5		330	107.1	1.54
1	Sharp	150	79.8	1.15
2		200	92.5	1.33
3		230	98.3	1.42
4		280	105.2	1.51
5		330	105.7	1.52

Table 8.12 Variation of Fracture Toughness with Specimen Length (SNASS, a=100 mm, w=25 mm) - Mix 1.

Geometry	Failure Load (kN)		V (%)	k_c ($MNm^{-3/2}$)
CCS a=30 mm 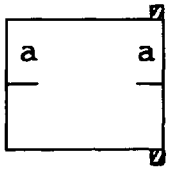	7.51 7.30 7.63	7.48	2.2	0.90
DNASS a=30 mm 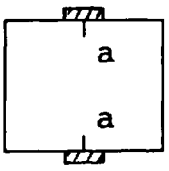	87.6 91.1 83.0	87.2	4.7	0.96
3-PBS a=50 mm 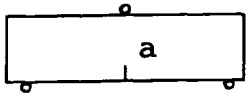	2.77 2.89 2.79	2.82	2.3	1.07

Table 8.13 Comparison of k_c Values Using Different Geometries.

Mix Ref	Temp. (° C)	f_t (MN/m^2)	$E(x10^3)$ (MN/m^2)	G_c (Nm/m^2)	BN Eqn 8.3	k_c ($MNm^{-3/2}$)	BN Eqn 8.6
R1	20	4.3	42.6	69.8	0.6	0.79	3.1
R2		4.7	43.1	60.8	0.8	0.93	2.7
R3		5.0	44.2	55.8	1.0	0.92	3.1
R4		4.2	40.8	58.5	0.7	0.97	2.0
R5		4.3	42.1	55.0	0.8	0.93	2.2
R6		4.6	41.4	46.1	1.1	0.90	2.7
R1	50	3.8	42.5	60.7	0.6	0.72	2.9
R2		4.2	42.9	48.0	0.9	0.83	2.7
R3		4.5	45.0	42.1	1.1	0.85	2.9
R4		3.8	42.7	49.0	0.7	0.79	2.4
R5		4.2	39.8	60.4	0.7	0.78	3.0
R6		4.4	37.6	64.3	0.8	0.75	3.6

Table 8.14 Brittleness Numbers (CCS, a=30 mm).

Mix Ref	Temp. (° C)	k_c ($MNm^{-3/2}$)	BN
R1	20	0.86	2.6
R2		0.95	2.6
R3		1.01	2.6
R4		0.86	2.5
R5		0.92	2.3
R6		0.81	3.3
R1	50	0.83	2.2
R2		0.95	2.0
R3		1.00	2.1
R4		1.10	1.3
R5		0.94	2.1
R6		0.67	4.4

Table 8.15 Brittleness Numbers (DNASS, Averaged)

Material	f_c (MN/m^2)	E($x10^3$) (MN/m^2)	f_t (MN/m^2)	G_c (Nm/m^2)	k_c ($MNm^{-3/2}$)	l_{ch} (m)	Reference
Ref. Concrete	74-77	42-43	3.8-4.3	60-70	0.7-0.8	0.2	Present
CSF Concrete	80-110	37-45	3.8-5.0	40-65	0.7-1.0	0.1	
Concrete	38-62	35-43	3.3-4.6	60-100	-	0.25	[45]
Concrete	-	30	3	60	1.3	0.2	[136]
Cement Paste	-	7	4	20	0.4	0.01	
Dense SC Paste	-	25	20	20	0.7	0.001	[137]

SC = Silica Cement

Table 8.16 Comparison of Mechanical and Fracture Properties of Various Cement Based Materials.

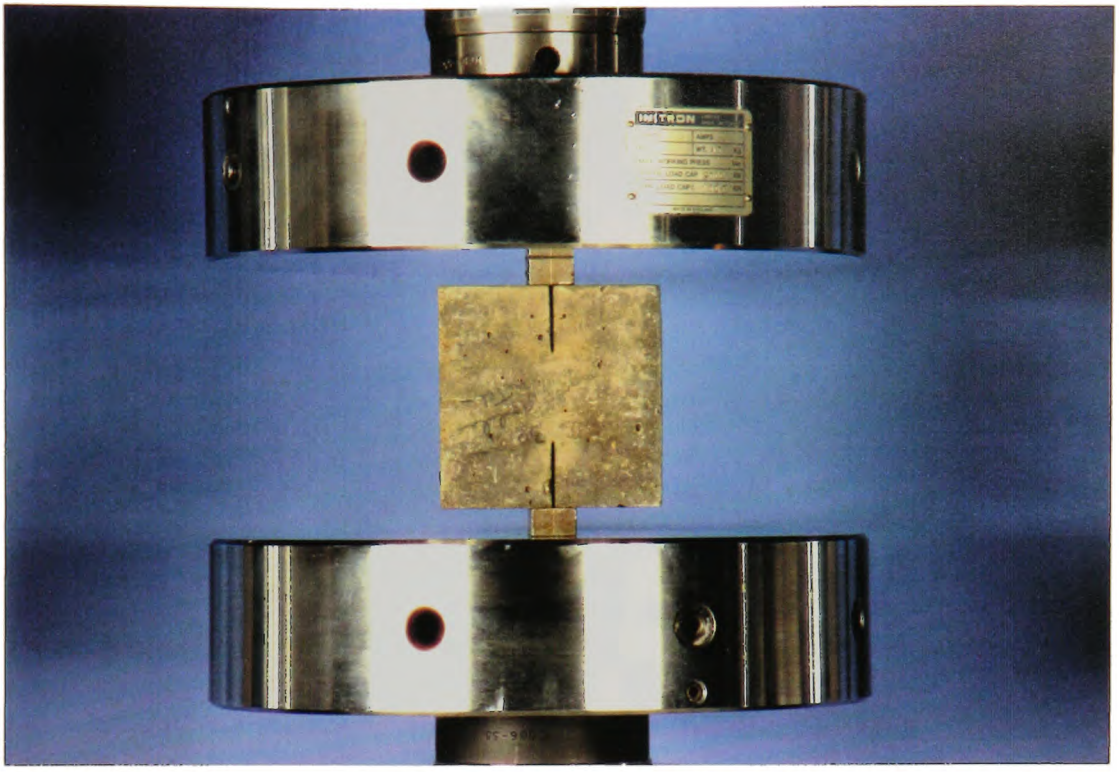

Plate 8.1 Specimen in Position Ready for Testing (DNASS).

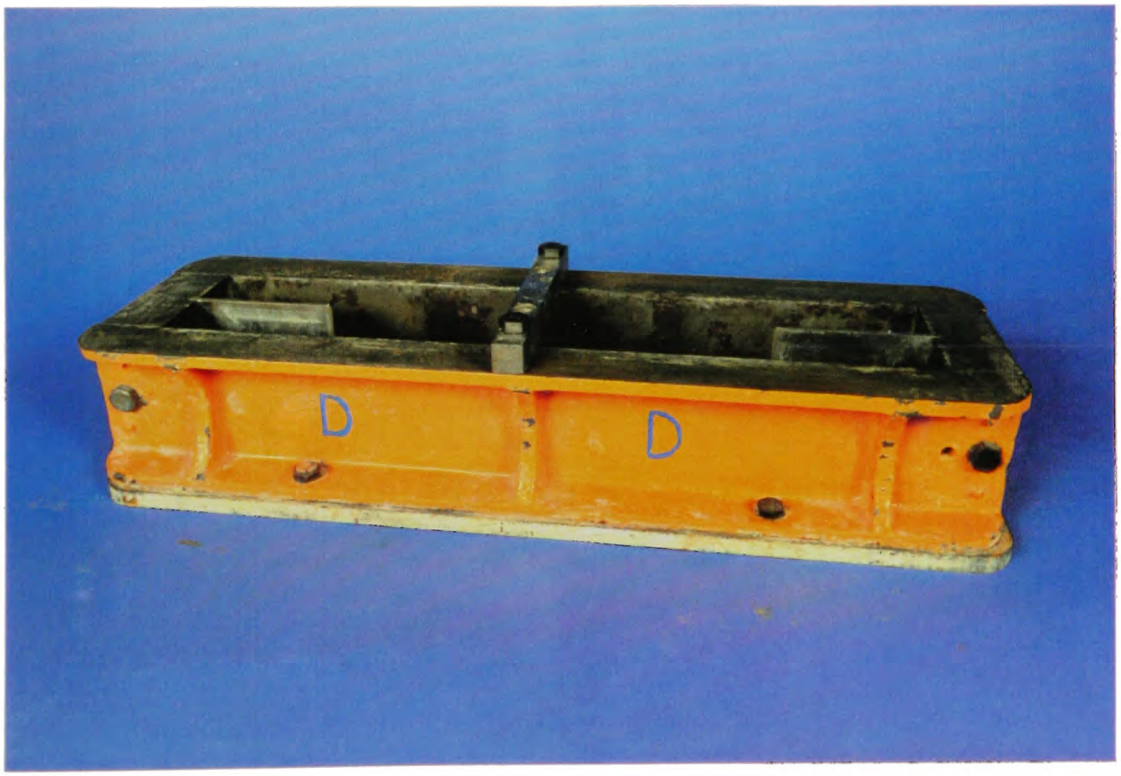

Plate 8.2 The 500 mm Prism Mould with Adjustable Plate.

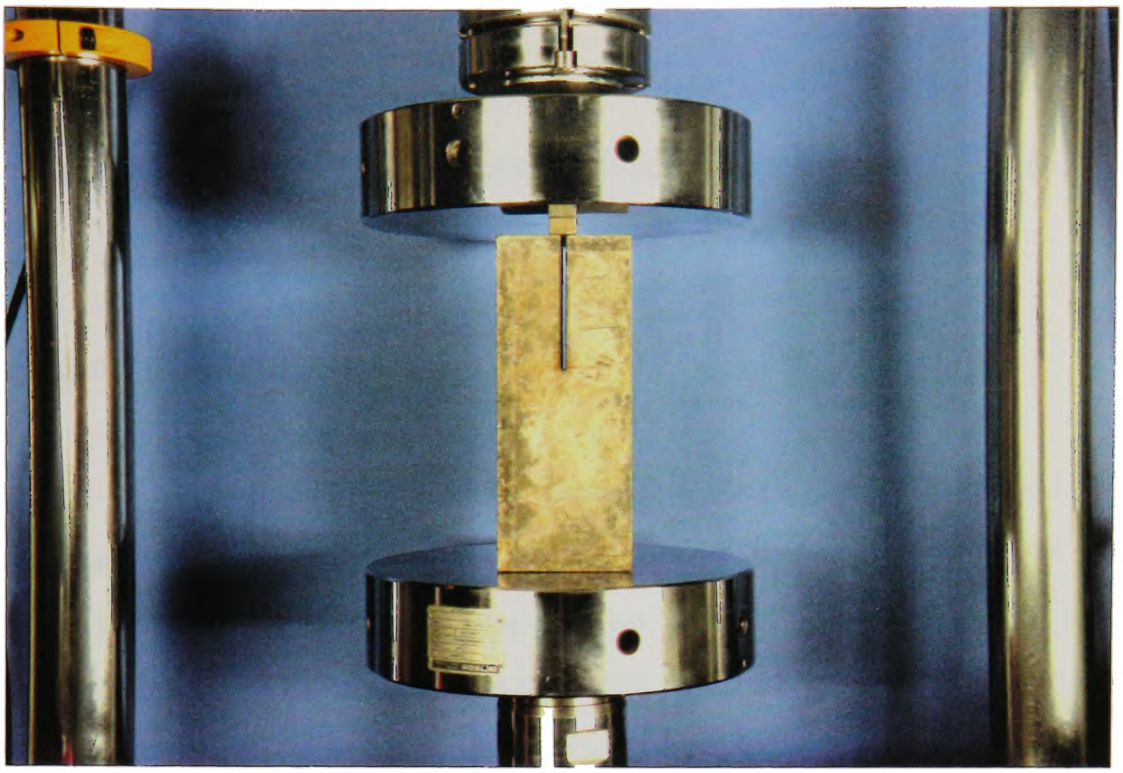

Plate 8.3 Specimen in Position Ready for Testing (SNASS).

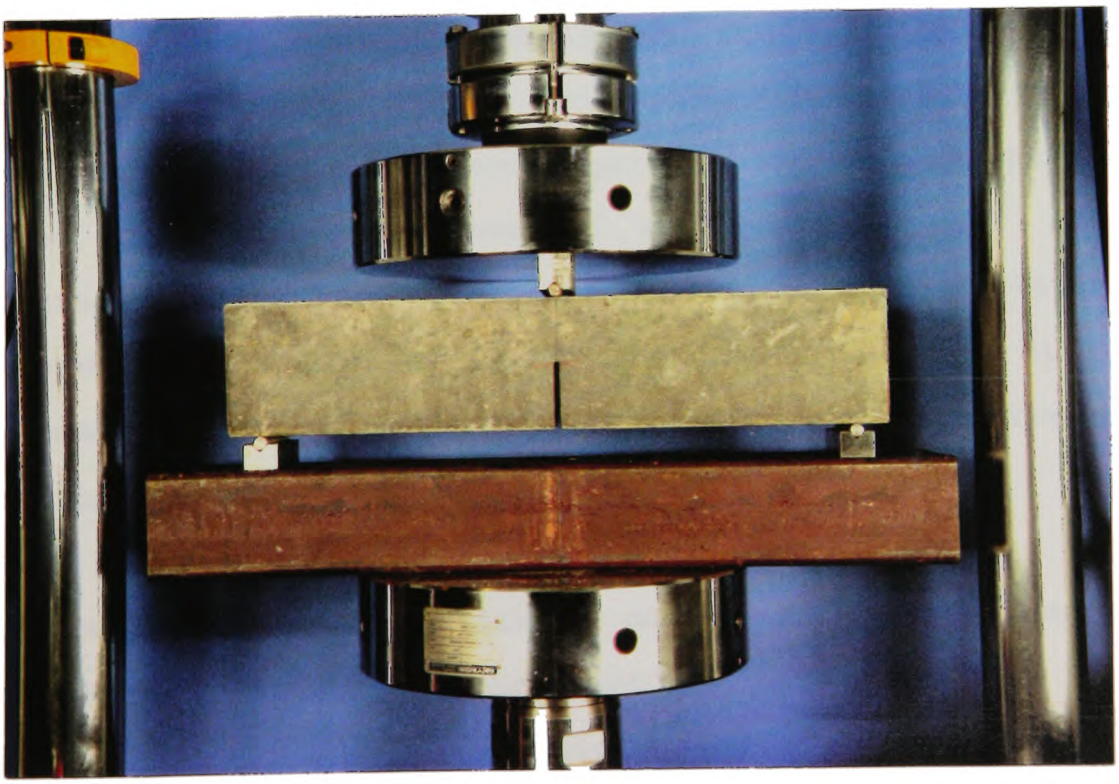

Plate 8.4 The 3-Point Bend Specimen in Position Ready for Testing.

CHAPTER NINE

CRITICAL DISCUSSION, CONCLUSIONS AND SUGGESTIONS FOR FUTURE WORK

Critical Discussion

In the work reported in this thesis a detailed numerical and experimental program aimed at a better understanding of the mechanical and fracture properties of CSF concrete has been carried out. This chapter provides a critical assessment of the results and presents the final conclusions.

The numerical work comprised finite element (FE) analyses of three fracture geometries, namely the Compact Compression Specimen (CCS) and the Singly and Doubly Notched Axial Splitting Specimens (SNASS and DNASS). The analyses were carried out using a commercial program (PAFEC) employing 6-noded triangular isoparametric elements, as well as a program (STRESS) utilising 8-noded quadrilateral isoparametric elements. Using the former package, it was demonstrated that the mode of failure in each geometry was that of the opening mode.

FE analysis of the CCS with 30 mm symmetrical notches was carried out using program PAFEC. The results of this analysis were employed to determine the stress intensity factor k by the displacement extrapolation (DE) and conic section simulation (CSS) methods. Two meshes having 952 and 3664 degrees of freedom (d.o.f.) were employed. Using these

two idealisations, the results obtained for k by the DE method were within 3% of each other. The CSS method did not give a constant value for k and an extrapolation process was necessary in order to achieve reasonable accuracy.

In analysing fracture problems using PAFEC, the program outputs results for the J-integral computed along an unidentified contour through elements close to the crack tip. No control over the choice of the contour path is facilitated for and such results should be treated with care. Furthermore, when symmetry conditions are utilised to reduce the size of the problem, the results for the J-integral are erroneous since the computations involved are valid only for cases where the full geometry of the crack is modelled. Although commercial software and the graphics facilities they offer can be of great help to the analyst, such considerations highlight the problems faced by the inexperienced user.

Next the above geometry was analysed using program STRESS. In evaluating k the DE and CSS methods together with the strain energy release rate (SERR) and J-integral methods were employed. Again two mesh idealisations were used. In the first, which had a total of 326 d.o.f., the elements surrounding the crack tip were arranged in a fan-like pattern. This arrangement of elements necessitated a manual input of all element topologies and required a considerable amount of data. In the second idealisation an arrangement of regular rectangular elements, which were constructed using

an automatic mesh generation scheme, was employed. In this idealisation, several meshes with varying total number of d.o.f. were employed in order to carry out convergence studies. Using the DE method it was found that the k value obtained by the fan mesh was overestimated by 9.2% when compared to that obtained by the regular mesh with similar total number of d.o.f. Using a regular mesh with 720 d.o.f., both the SERR and J-integral methods yielded values for k which were within 1% of that obtained by program PAFEC with 3664 d.o.f.

By varying the size of the notches, analysis of a total of 17 geometries of the CCS were carried out using different FE idealisations. In all cases excellent convergence of the results were obtained and a converged solution (using a 1% convergence criterion) was achieved with as few as 720 d.o.f. Expressions for k for the symmetrically notched specimens were obtained using the FE results. These expressions give values for k which are within 1% of the FE results.

The SNASS was next analysed using triangular isoparametric elements. When comparing the results for k with those obtained by the analytical solution, it was found that the DE method yielded results which were in closer agreement than those obtained by the CSS method. The SNASS geometry was also analysed using rectangular isoparametric elements. It was shown that using 1778 d.o.f. greater accuracy for k was obtained than that yielded by the analysis using

triangular elements with 6158 d.o.f. For all the notch sizes considered, the results were in close agreement with those obtained by the analytical solution.

A parametric study of the SNASS indicated that the stress intensity factor k decreased with increasing loading platen width and increased with increasing notch size. Furthermore it was confirmed that k was independent of the specimen length as suggested by the analytical solution.

A modified version of the SNASS in the form of a 100 mm cube containing an additional notch on the opposite face (DNASS) was presented and analysed. The FE analysis of this geometry established that the mode of failure was that of the opening mode. A comparison of the maximum stresses revealed that the modified specimen was more susceptible to tensile failure than the SNASS.

A detailed experimental investigation was carried out to examine the mechanical and fracture properties of CSF concrete. Tests were conducted to determine the compressive strength, tensile splitting strength and the static modulus of elasticity for concretes with varying CSF contents. Fracture tests were conducted to complement the numerical work described above in order to assess the fracture characteristics of the concretes employed. The results were presented on the basis of two classes of concretes according to the compressive strength achieved at 28 days. An arbitrary cut-off point of 70 N/mm^2 was used to distinguish

between the two classes, namely the normal concrete and high strength concrete. The normal concrete was produced using a w/c ratio of 0.47 with cement replacement by CSF of up to 12%. In this category strengths up to 64.8 N/mm^2 were obtained. The high strength concrete was achieved by employing a lower w/c ratio of 0.35 and cement replacements by CSF of up to 28%. The strengths obtained ranged between 74.0 and 110.5 N/mm^2.

It was found that high temperature curing (50° C) increased the 4- and 7-day strengths of all the concretes investigated. Beyond this age concretes cured at 20° C with CSF contents up to 16% showed higher compressive strengths than those cured at 50° C. Further examination of the results revealed a significant drop in the early age strength of the 20° C cured concrete when the CSF content was increased from 16% to 20%. This was attributed to the possible reduction in the hydration products at some levels of CSF replacement leading to reduced amounts of calcium hydroxide available for reaction with CSF. It is suggested that the abundance of CSF particles at the higher levels (> 20%) may lead to greater dispersal of cement particles and, therefore, increased reaction rates thus producing more cementitious gel.

The tensile splitting strength and the static modulus of elasticity were largely unaffected by the curing temperature. The latter, however, showed a marked reduction at CSF replacement levels beyond 16%. This finding was

unexpected and could only be explained if the re-distribution of the pore size as a result of the increase in CSF content is coupled with an increase in the porosity. This increase in porosity may be partly responsible for the reductions in the densities which accompanied increasing CSF contents.

LEFM was employed to evaluate the fracture toughness k_c from the numerical work and the fracture tests. Using the CCS it was found that, for normal concrete, k_c did not increase appreciably with increasing CSF content. However, in the case of the high strength concrete, k_c decreased significantly with increasing CSF contents beyond 16%.

It was generally observed that k_c increased with increasing notch size up to 30 mm and then decreased. Whereas for normal concrete the values for k_c were in the range 0.54-0.74 $MNm^{-3/2}$, those for the high strength concrete were in the range 0.79-0.97 $MNm^{-3/2}$. It was found that increasing the curing temperature from 20° C to 50° C led to small reductions in k_c.

The fracture energy G_c was evaluated using the load-displacement relationships obtained from the CCS tests. In this evaluation allowance was made for the interaction that takes place between the specimen and the testing machine. As no allowance was made for the tortuosity of the fracture path the values obtained using this approach were considered to be overestimated.

G_c was re-evaluated indirectly from the k_c and E values obtained from the laboratory tests. This approach led to values for G_c which were several times smaller than those obtained directly from the areas under the load-displacement graphs. The difference was considered to be due to the tortuosity of the fracture path. The tortuosity factor (TF) was estimated as the ratio of the two G_c values and was found to be in the range 2-5. Furthermore the G_c values calculated from k_c and E did not show a significant variation as the compressive strength increased. This was expected as both k_c and E decreased with increasing compressive strength. The variation in G_c with notch depth was similar to that obtained for k_c. For normal concrete G_c was in the range 9.3-17.5 Nm/m^2 and for high strength concrete the range was 11.7-22.6 Nm/m^2. Again high temperature curing caused a small decrease in G_c.

Polypropylene fibres were employed in some of the fracture tests and the post-cracking performance was assessed using a toughness index calculated from the area under the load-displacement graphs. The addition of fibres caused slight reductions in the values of the compressive strength as well as the fracture toughness. Although the fibres imparted residual strength to the specimen after first failure, this was sustained at only 20% of the maximum load. This renders the fibres used during the course of this investigation of little practical benefit.

k_c was also evaluated by means of the DNASS tests. Using this geometry, k_c for the high strength concrete was found to be in the range 0.71-1.10 $MNm^{-3/2}$. These results are in close agreement with those obtained by the CCS tests and demonstrate the validity of the tests employed in the present work.

The degree of brittleness of the concrete was assessed by a non-dimensional parameter called the brittleness number (BN). The BN was evaluated using the results for k_c obtained from the CCS and DNASS tests. Both tests yielded similar results, with the BN being in the range 1.3-4.4. The brittleness number increased significantly beyond strength levels of about 90 N/mm^2.

Conclusions

From the above and the work described throughout this thesis the following specific conclusions may be made.

1. The numerical and experimental work confirm the suitability of the compact compression specimen (CCS) and the doubly notched axial splitting specimen (DNASS) for the evaluation of the fracture toughness of concrete.

2. The 8-noded rectangular isoparametric finite element is more efficient than the 6-noded triangular element in analysing the fracture problems considered in the present investigation. In the absence of analytical solutions it is

necessary to carry out several analyses, using different FE idealisations, to ensure convergence to the correct solution.

3. In evaluating the stress intensity factor k, the conic section simulation (CSS) method has no advantage over the displacement extrapolation (DE) method. The methods preferred in the present work are the J-integral and strain energy release rate (SERR).

4. OPC replacements by condensed silica fume (CSF) up to 28% improve the long-term compressive strength of concrete. Such concretes benefit from the application of heat curing during early ages, up to 7 days.

5. The tensile splitting strength and the static modulus of elasticity are largely unaffected by high temperature curing.

6. The modulus of elasticity of high strength concrete decreases with strengths beyond 90 N/mm^2 (> 16% CSF).

7. The fracture toughness k_c for concretes with compressive strengths < 70 N/mm^2 is not affected by the CSF content. For high strength concrete, however, k_c decreases with increasing CSF content beyond 16%.

8. In all cases the fracture toughness initially increases and then decreases with increasing notch size.

9. The fracture energy G_C evaluated from the area under the load-displacement graphs shows a consistent decrease with increasing notch size. These G_C values are several times greater than those obtained using k_C and the appropriate relationship. Although the results are generally in agreement with those reported by other workers, as no allowance was made for the tortuosity of the cracked surface, the k_C approach is considered to be more reliable in the present work. The G_C values obtained by the two approaches were utilised to estimate the degree of tortuosity of the fracture path. It was found that in both plain and fibre concretes the true fracture area is of the order 2-5 times the theoretical value. This factor increased with increasing notch size.

10. The two fracture geometries, i.e. CCS and DNASS, yield similar values for k_C.

11. The brittleness of CSF concrete increases significantly beyond strengths of about 90 N/mm^2.

Suggestions for Future Work

It was pointed out earlier that the residual strength imparted by the fibres to the matrix after first failure occurred at much reduced loads. One reason for this may be the fact that the fibres employed in this work were only 8-10 mm long and perhaps not capable of providing a

significant bridging mechanism against crack propagation. It would be interesting to see the effect of longer fibres on the fracture energy in a future study.

The tortuosity of the fracture surface was estimated from the calculated values of the critical strain energy release rate G_C. It would be of particular interest to develop a means for the physical measurement of the actual fracture area using techniques such as polymer impregnation.

Finally the limitations of the testing arrangement in employing the machine displacements in the direct evaluation of fracture energy may be overcome by employing a more sophisticated testing procedure. This may involve the use of linearly varying displacement transducers (LVDT) in controlling the straining rate. Such an arrangement would be essential if stable crack propagation, for example in the SNASS tests, is sought for. This may be the subject of a future investigation.

REFERENCES

1. **Yogendran, V., Langan, B.W., Haque, M.N. and Ward, M.A.,** Silica fume in high-strength concrete, American Concrete Institute Materials Journal, Vol. 84, No. 2, 1987, pp. 124-129.

2. **Wilson, H.S. and Malhotra, V.M.,** Development of high strength lightweight concrete for structural applications, The International Journal of Cement Composites and Lightweight Concrete, Vol. 10, No. 3, 1988, pp. 79-90.

3. **Ohama, K., Demura, K. and Muranishi, R.,** Development of super-high-strength concrete made with silica fume addition and polymer impregnation, American Concrete Institute, Special Publication, Vol. 89, 1985, pp. 231-247.

4. **Carette, G.G. and Malhotra, V.M.,** Silica fume in concrete- Preliminary investigation, Report No. 82-1E, CANMET Energy Mines and Resources, Ottawa, 1982.

5. **Radjdy, F.F. and Loland, K.E.,** Microsilica concrete: A breakthrough commercialized, Proceedings of the Materials Research Society, Vol. 42, 1984, pp. 305-312.

6. **State-of-Art Report:** Condensed Silica Fume in Concrete, Thomas Telford Publishers, 1988.

7. **Ronne, M.,** Effect of condensed silica fume and fly ash on compressive strength development of concrete, Proceedings of the 3rd CANMET/ACI International Conference on fly ash, silica fume, slag and natural pozzolans in concrete, Trondheim, Norway, 1990, pp. 175-189.

8. **Aitcin, P.C. and Laplante, P.,** Long-term compressive strength of silica fume concrete, Journal of Materials in Civil Engineering, Vol. 2, No. 3, 1990, pp. 164-170.

9. **Loland, K.E. and Hustad, T.,** Silica in Concrete-Mechanical properties, Report STF65 A81031, Norwegian Institute of Technology, Trondheim, Norway, 1981.

10. **Maage, M. and Hammer, T.A.,** Modifisert portlandsement delrapport 3 fasthetsutvikling og E-modulus, Report STF65 A85041, Norwegian Institute of Technology, Trondheim, Norway, 1985.

11. **Carrasquillo, R.L., Nilson, A.H. and Slate, F.O.,** Properties of high strength concrete subjected to short-term loads, Journal of the American Concrete Institute, Vol. 78, No. 3, 1981, pp. 171-178.

12. **Ahmad, S.H. and Shah, S.P.,** Properties of high strength concrete for structural design, Proceedings of the Materials Research Society, Vol. 42, 1984, pp. 169-181.

13. **Jerath, S. and Yamane, L.C.**, Mechanical properties and workability of superplasticized concrete, Cement, Concrete and Aggregates, Vol. 9, No. 1, 1987, pp. 12-19.

14. **John, R. and Shah, S.P.**, Fracture mechanics analysis of high strength concrete, Journal of Materials in Civil Engineering, Vol. 1, No. 4, 1989, pp. 185-198.

15. **Dewar, J.D.**, The indirect tensile strength of concretes of high compressive strength, Technical Report No. 42-377, Cement and Concrete Association, 1964.

16. **Teychenne, D.C., Parrott, L.J. and Pomeroy, C.D.**, The estimation of the elastic modulus of concrete for the design of structures, Current Paper 23, Building Research Establishment, Watford, 1978.

17. Building code requirements for reinforced concrete, American Concrete Institute Journal, No. 318, 1983.

18. **Swamy, R.N.**, Properties of high strength concrete, Cement, Concrete and Aggregates, Vol. 8, No. 1, 1986, pp. 33-41.

19. **Ahmad, S.H. and Shah, S.P.**, Complete triaxial stress-strain curves for concrete, Proceedings of the American Society of Civil Engineers, Special Publication, Vol. 108, No. 4, 1982, pp. 728-742.

20. **Loland, K.E.**, Fasthets og deformasjonsegenskaper i herdnet tilsand- herdebetingelser, Seminar Bruk av Silika Betong. Norsk Sivilingeniorers Forening, Oslo, Norway, 1983.

21. **Giaccio, G., Violini, D., Zappitelli, J. and Zerbino, R.**, Compressive strength and elastic properties of fly ash concrete elaborated with different cement types, Proceedings of the 3rd CANMET/ACI International Conference on fly ash, silica fume, slag and natural pozzolans in concrete, Trondheim, Norway, 1990, pp. 188-202.

22. **Kaar, P.H., Hanson, N.W. and Capell, H.T.**, Stress-strain characteristics of high strength concrete, Proceedings of the Douglas McHenry International Symposium on Concrete and Concrete Structures, Detroit, U.S.A., 1978, pp. 161-185.

23. **Ahmad, S.H.**, Properties of confined concrete subjected to static and dynamic loading, PhD thesis, University of Illinois at Chicago Circle, 1981.

24. **Swamy, R.N.**, Influence of slow crack growth on the fracture resistance of fibre composites, International Journal of Cement Composites, Vol. 2, No. 1, 1980, pp. 43-53.

25. **Welch, G.B. and Haisman, B.**, The application of fracture mechanics to concrete and measurement of fracture toughness, Materials and Structures, Vol. 2, 1969, pp. 171-177.

26. **Ewalds, H.L. and Wanhill, R.J.H.**, Fracture Mechanics, Edward Arnold Publishers, 1986.

27. **Modeer, M.**, A fracture mechanics approach to failure analysis of concrete materials, Report TVBM-1001, Division of Building Materials, University of Lund, Sweden, 1979.

28. **Dugdale, D.S.**, Yielding of steel sheets containing slits, Journal of Mechanics and Physics of Solids, No. 8, 1960, pp. 100-104.

29. **Kesler, C.E., Naus, D.J. and Lott, J.L.**, Fracture mechanics - Its applicability to concrete, Proceedings of the International Conference on Mechanical Behaviour of Materials, Vol. IV, Japan, 1972, pp. 113-124.

30. **Lott, J.L. and Kesler, C.E.**, Crack propagation in plain concrete, Proceedings of the Symposium on Structure of Portland Cement Paste and Concrete, Washington, U.S.A., 1966, pp. 204-218.

31. **Hillerborg, A., Modeer, M. and Petersson, P.E.**, Analysis of crack formation and crack growth in concrete by means of fracture mechanics and finite elements, Cement and Concrete Research, Vol. 6, No. 6, 1976, pp. 773-782.

32. **Bazant, Z.P. and Oh, B.H.**, Concrete fracture via stress-strain relations, Report 81-10/665c, Centre for Concrete and Geomaterials, Northwestern University, U.S.A., 1981.

33. **Wecharatana, M. and Shah, S.P.**, Predictions of nonlinear fracture process zone in concrete, Journal of Engineering Mechanics, Vol. 109, No. 5, 1983, pp. 1231-1246.

34. **Bazant, Z.P., Kim, J.K. and Pfeiffer, P.A.**, Nonlinear fracture properties from size effect tests, Journal of Structural Engineering, Vol. 112, No. 2, 1986, pp. 289-307.

35. **Saouma, V.E., Ingraffea, A.R. and Catalano, D.M.**, Fracture toughness of concrete - k_{1c} revisited, Journal of Engineering Mechanics Division, American Society of Civil Engineers, Vol. 108, No. EM6, 1982, pp. 1152-1166.

36. **Swartz, S.E.**, Fracture toughness testing of concrete at Kansas State University: Is LEFM acceptable?, Proceedings of the International Conference on Fracture Mechanics of Concrete, Lausanne, Switzerland, 1985, pp. 359-362.

37. **Swamy, R.N.**, Fracture mechanics applied to concrete, Developments in Concrete Technology, Applied Science Publishers, 1979, pp. 221-281.

38. **Barr, B.I.G. and Bear, T.**, A simple test for fracture toughness, Concrete, Vol. 10, No. 4, 1976, pp. 25-27.

39. **Barr, B.I.G., Evans, W.T. and Dowers, R.C.**, Fracture toughness of polypropylene fibre concrete, International

Journal of Cement Composites and Lightweight Concrete, Vol. 3, No. 2, 1981, pp. 115-122.

40. Karihaloo, B.L., Fracture toughness of plain concrete from compression splitting tests, The International Journal of Cement Composites and Lightweight Concrete, Vol. 8, No. 4, 1986, pp. 251-259.

41. Mindess, S., The effect of specimen size on the fracture energy of concrete, Cement and Concrete Research, Vol. 14, No. 3, 1984, pp. 431-436.

42. Nallathambi, P., Karihaloo, B.L. and Heaton, B.S., Effect of specimen and crack sizes, water/cement ratio and coarse aggregate texture upon fracture toughness of concrete, Magazine of Concrete Research, Vol. 36, No. 129, 1984, pp. 227-236.

43. Barr, B.I.G. and Sabir, B.B., Fracture toughness testing by means of the compact compression specimen, Magazine of Concrete Research, Vol. 37, No. 131, 1985, pp. 88-94.

44. Gjorv, O.E., Sorensen, S.I. and Arnesen, A., Notch sensitivity and fracture toughness of concrete, Cement and Concrete Research, Vol. 7, No. 3, 1977, pp. 333-344.

45. Petersson, P.E., Fracture energy of concrete: Practical performance and experimental results, Cement and Concrete Research, Vol. 10, No. 1, 1980, pp. 91-101.

46. Carpinteri, A., Static and energetic fracture parameters for rocks and concrete, Materials and Structures, Vol. 14, No. 81, 1981, pp. 151-162.

47. Pak, A.P. and Trapeznikov, L.P., Experimental investigations based on the Griffith-Irwin theory processes of the crack development in concrete, The 5th International Conference on Fracture, Cannes, France, 1981, pp. 1531-1539.

48. Hillemeier, B. and Hilsdorf, H.K., Fracture mechanics studies on concrete compounds, Cement and Concrete Research, Vol. 7, No. 5, 1977, pp. 523-536.

49. Kitagawa, H. and Suyama, M., Fracture mechanics study on the size effect for the strength of cracked concrete materials, The 9th Japanese Congress on Materials Research, Tokyo, Japan, 1976, pp. 156-159.

50. Brandt, A.M., Crack propagation energy in steel fibre reinforced concrete, International Journal of Cement Composites, Vol. 2, No. 1, 1980, pp. 35-42.

51. Yokomichi, H., Fujita, Y. and Saeki, N., Experimental researches on crack propagation of plain concrete, Revised 27th General Meeting, The Cement Association of Japan, Tokyo, 1973, pp. 144-147.

52. **Mazars, J.,** Existence of a critical strain energy release rate for concrete, Proceedings of the 4th International Conference on Fracture, Canada, Vol. 3, 1977, pp. 1205-1209.

53. **Desayi, P.,** Fracture of concrete in compression, Materials and Structures, Vol. 10, No. 57, 1977, pp. 139-144.

54. **Nallathambi, P., Karihaloo, B.L. and Heaton, B.S.,** Various size effects in fracture of concrete, Cement and Concrete Research, Vol. 15, No. 1, 1985, pp. 117-126.

55. **Barr, B.I.G., Hasso, E.B.D. and Sabir, B.B.,** The effect of test specimen size on the fracture toughness of concrete, Cement and Concrete Research, Vol. 15, No. 5, 1985, pp. 833-841.

56. **Jenq, Y.S. and Shah, S.P.,** A two parameter fracture model for concrete, Journal of Engineering Mechanics, American Society of Civil Engineers, Vol. 111, No. 10, 1985, pp. 1227-1241.

57. **Nallathambi, P. and Karihaloo, B.L.,** Influence of slow crack growth on the fracture toughness of plain concrete, Proceedings of the International Conference on Fracture Mechanics of Concrete, Lausanne, Switzerland, 1985, pp. 271-280.

58. **Barsom, J.M. and Rolfe, S.T.,** Fracture and fatigue control in structures, Prentice Hall Publishers, 1987.

59. **American Concrete Institute Committee 544,** Measurement of properties of fibre reinforced concrete, Journal of the American Concrete Institute, Vol. 75, No. 7, 1978, pp. 283-289.

60. **Johnston, C.D.,** Definition and measurement of flexural toughness parameters of fibre reinforced concrete, Cement, Concrete and Aggregates, Vol. 4, No. 2, 1982, pp. 53-60.

61. **Barr, B.I.G., Liu, K. and Dowers, R.C.,** A toughness index to measure the energy absorption of fibre reinforced concrete, The International Journal of Cement Composites and Lightweight Concrete, Vol. 4, No. 4, 1982, pp. 221-227.

62. **Purkiss, J.A.,** Toughness measurements on steel fibre concrete at elevated temperatures, International Journal of Cement Composites and Lightweight Concrete, Vol. 10, No. 1, 1988, pp. 39-47.

63. **Chan, S.K., Tuba, I.S. and Wilson, W.K.,** On the finite element method in linear fracture mechanics, Engineering Fracture Mechanics, Vol. 2, No. 1, 1970, pp. 1-17.

64. **Kobayashi, A.S., Maiden, D.E., Simon, B.J. and Iida, S.,** Application of finite element analysis method to two-

dimensional problems in fracture mechanics, American Society of Mechanical Engineers, 1968.

65. Dixon, J.R. and Strannigan, J.S., Determination of energy release rates and stress intensity factors by the finite element method, Journal of Strain Analysis, Vol. 7, No. 2, 1972, pp. 125-131.

66. Pian, T.H.H. and Moriya, K., Three-dimensional fracture analysis by assumed stress finite elements, Proceedings of the 1st International Conference on Numerical Methods in Fracture Mechanics, Swansea, U.K., 1978, pp. 363-373.

67. Byskov, E., The calculation of stress intensity factors using the finite element method with cracked elements, International Journal of Fracture Mechanics, Vol. 6, No. 2, 1970, pp. 159-167.

68. Muskhelishvili, N., Some Basic Problems of the Mathematical Theory of Elasticity, Noordhoff Publishers, 1963.

69. Wilson, W.K., Some crack tip finite elements for plane elasticity, Proceedings of the National Symposium on Fracture Mechanics, American Society for Testing and Materials, Special Technical Publication, No. 513, 1972, pp. 90-105.

70. Williams, M.L., On the stress distribution at the base of a stationary crack, Journal of Applied Mechanics, Vol. 24, No. 1, 1957, pp. 109-114.

71. Tracey, D.M., Finite elements for determination of crack tip elastic stress intensity factors, Engineering Fracture Mechanics, Vol. 3, No. 3, 1971, pp. 255-266.

72. Zienkiewicz, O.C., The Finite Element Method, 3rd Edition, McGraw-Hill Publishers, 1986.

73. Sabir, B.B., The application of the finite element method to fracture mechanics problems, PhD thesis submitted to the C.N.A.A., U.K., 1980.

74. Henshell, R.D. and Shaw, K.G., Crack-tip finite elements are unnecessary, International Journal for Numerical Methods in Engineering, Vol. 9, No. 3, 1975, pp. 495-507.

75. Barsoum, R.S., On the use of isoparametric finite elements in linear fracture mechanics, International Journal for Numerical Methods in Engineering, Vol. 10, No. 1, 1976, pp. 25-37.

76. Barsoum, R.S., A degenerate solid element for linear fracture analysis of plate bending and general shells, International Journal for Numerical Methods in Engineering, Vol. 10, No. 3, 1976, pp. 551-564.

77. **Birch, J.M., Wilshire, B., Owen, D.J.R. and Shantaram, D.,** The influence of stress distribution on the deformation and fracture behaviour of ceramic materials under compression creep conditions, Journal of Material Science, Vol. 11, No. 10, 1976, pp. 1817-1825.

78. **Barsoum, R.S.,** Triangular quarter point elements as elastic and perfectly plastic crack-tip elements, International Journal for Numerical Methods in Engineering, Vol. 11, No. 1, 1977, pp. 85-98.

79. **Bleackley, M.H. and Luxmoore, A.R.,** An investigation of numerical errors in finite element elastic plastic crack extension models, Proceedings of the 1st International Conference on Numerical Methods in Fracture Mechanics, Swansea, U.K., 1978, pp. 508-524.

80. **Lynn, P. and Ingraffea, A.R.,** Transition elements to be used with quarter point crack-tip elements, International Journal for Numerical Methods in Engineering, Vol. 12, No. 6, 1978, pp. 1031-1036.

81. **Griffith, A.A.,** The phenomena of rupture and flow in solids, Proceedings of the 1st International Congress on Applied Mechanics, Delft, Holland, 1920, pp. 163-198.

82. **Irwin, G.R.,** Analysis of stresses and strains near the end of a crack traversing a plate, Journal of Applied Mechanics, Vol. 24, No. 3, 1957, pp. 361-364.

83. **Westergaard, H.M.,** Bearing pressures and cracks, Journal of Applied Mechanics, Vol. 61, No.1, 1939, pp. 49-53.

84. **Chow, C.L. and Lau, K.J.,** Finite element analysis of cracked bodies to determine stress intensity factors, Journal of Strain Analysis, Vol. 11, No. 1, 1976, pp. 18-25.

85. **Sneddon, I.N. and Lowengrub, M.,** Crack Problems in the Classical Theory of Elasticity, J. Wiley and Sons Publishers, 1970.

86. **Chow, C.L. and Lau, K.J.,** On the finite element method for calculating stress intensity factors with a modified elliptical model, International Journal of Fracture, Vol. 12, No. 1, 1976, pp. 59-69.

87. **Woo, C.W. and Kuruppu, M.D.,** Use of finite element method for determining stress intensity factors with a conic section simulation model for crack surface, International Journal of Fracture, Vol. 20, No. 3, 1982, pp. 163-178.

88. **Paris, P.C. and Sih, G.C.,** Stress analysis of cracks, American Society for Testing and Materials, Special Technical Publication, No. 381, 1965.

89. **Parks, D.M.,** A stiffness derivative finite element technique for determination of elastic crack tip stress

intensity factors, International Journal of Fracture, Vol. 10, No. 4, 1974, pp. 487-502.

90. Hellen, T.K., On the method of virtual crack extensions, International Journal of Numerical Methods in Engineering, Vol. 9, No. 1, 1975, pp. 187-208.

91. Rice, J.R., A path independent integral and the approximate analysis of strain concentrations by notches and cracks, Journal of Applied Mechanics, Vol. 35, No. 2, 1968, pp. 379-386.

92. Phillips, H.B., Vector Analysis, J. Wiley Publishers, 1959.

93. Asili, M., Finite element analysis of annular plates subjected to in-plane loading, MSc thesis submitted to the University of Wales, U.K., 1986.

94. Sabir, B.B. and Barr, B.I.G., New finite elements for fracture analysis, Proceedings of the 2nd International Conference on Numerical Methods in Fracture Mechanics, Swansea, U.K., 1980, pp. 25-39.

95. Levy, N., Marcal, P.V., Ostergren, W. and Rice, J., Small scale yielding near a crack in plane strain: A finite element analysis, International Journal of Fracture Mechanics, Vol. 7, No. 2, 1971, pp. 143-157.

96. Tracey, D.M. and Cook, T.S., Analysis of power type singularities using finite elements, International Journal of Numerical Methods in Engineering, Vol. 11, No. 8, 1977, pp. 1225-1235.

97. Blackburn, W.S., Calculation of stress intensity factor at crack tips using special finite elements, Mathematics of Finite Elements, Academic Press, 1973, pp. 327-336.

98. Owen, D.R.J. and Fawkes, A.J., Engineering Fracture Mechanics: Numerical Methods and Applications, Pineridge Press, 1983.

99. PAFEC Program, PAFEC Ltd, Strelley Hall, Strelley, Nottingham, U.K.

100. Sabir, B.B., On the reliability of finite element J-integral evaluation in fracture analysis, Proceedings of the 7th European Conference on Fracture, Budapest, Hungary, 1988, pp. 187-195.

101. Brown W.F. and Srawley, J.E., Plane strain crack toughness testing of high strength metallic materials, American Society for Testing and Materials, Special Technical Publication, No. 410, 1966.

102. Sabir, B.B., Stress intensity factors using simple strain-based finite elements, Proceedings of the

International Conference on Computational Mechanics, Tokyo, Japan, 1986, pp. V99-V105.
103. Sabir, B.B., Asili, M. and Summerhayes, S.D., Fracture toughness of OPC/microsilica concrete, Proceedings of the International Conference on the Design and Construction of Non-Conventional Structures, Institution of Civil Engineers, London, U.K., 1987, pp. 215-222.

104. Carneiro, F.L.L.B., Concrete tensile strength, Union of Testing and Research Laboratories for Materials and Structures, No. 13, 1953.

105. Kendall, K., Transition between Cohesive and Interfacial Failure in a Laminate, Proceedings of the Royal Society, London, U.K., Vol. A344, 1975, pp. 287-302.

106. Karihaloo, B.L., A note on complexities of compression failure, Proceedings of the Royal Society, London, U.K., Vol. A368, 1979, pp. 483-493.

107. Karihaloo, B.L., Compressive fracture of brittle materials, Proceedings of the Royal Society, London, U.K., Vol. A396, 1984, pp. 297-314.

108. Kendall, K., Complexities of compression failure, Proceedings of the Royal Society, London, U.K., Vol. A361, 1978, pp. 245-263.

109. Guest, B.W. and Karihaloo, B.L., Fracture of glassy brittle materials, Journal of Material Science Letters, Vol. 4, No. 10, 1985, pp. 1285-1289.

110. Richart, F.E., Brandtzaeg, A. and Brown, R.L., Bulletin No. 185, Engineering Experiment Station, University of Illinois, U.S.A., 1928, 104 pp.

111. Kaplan, M.F., Crack propagation and the fracture of concrete, Journal of American Concrete Institute, Vol. 58, No. 5, 1961, pp. 591-610.

112. RILEM Technical Committee 50-FMC, Draft Recommendation, Determination of the fracture energy of mortar and concrete by means of three point bend tests on notched beams, Materials and Structures, Vol. 18, No. 106, 1985, pp. 287-290.

113. Sarkar, S.L. and Aitcin, P.C., Dissolution rate of silica fume in very high strength concrete, Cement and Concrete Research, Vol. 17, No. 4, 1987, pp. 591-601.

114. Burge, T.A., 14000 psi in 24 hours, Concrete International: Design and Construction, Vol. 5, No. 9, 1983, pp. 36-41.

115. Holland, T.C. and Gutschow, R.A., Erosion resistance with silica fume concrete, Concrete International, Vol. 9, No. 3, 1987, pp. 32-40.

116. **Swamy, R.N.,** Fibre reinforcement of cement and concrete, Materials and Structures, Vol. 85, No. 45, 1975, pp. 235-254.

117. **Goldfein, S.,** Fibrous reinforcement for Portland cement, Modern Plastics, 1965, pp. 156-159.

118. **Hannant, D.J.,** Fibre cements and fibre composites, J. Wiley and Sons Publishers, 1978.

119. **Teychenne, D.C., Franklin, R.E. and Erntroy, H.C.,** Design of Normal Concrete Mixes, Department of Environment, HMSO.

120. **Nallathambi, P. and Karihaloo, B.L.,** Determination of specimen-size independent fracture toughness of plain concrete, Magazine of Concrete Research, Vol. 38, No. 135, 1986, pp. 67-76.

121. **Swamy, R.N.,** Linear elastic fracture mechanics parameters of concrete, Fracture Mechanics of Concrete, Elsevier Science Publishers, 1983, pp. 411-461.

122. **Neville, A.,** Properties of Concrete, 3rd Edition, Longman Publishers, 1986.

123. **Hilsdorf, H.K. and Ziegeldorf, S.,** Fracture energy of concrete, Proceedings of the NATO Advanced Research Institute, 1980, pp. 101-124.

124. **Go, C.G. and Swartz, S.E.,** Energy methods for fracture-toughness determination in concrete, Experimental Mechanics, Vol. 26, No. 3, 1986, pp. 292-296.

125. **Skurdal, S.,** Egenskapsutvikling for silicabetong ved ulike forsekjellige herdetemperaturer, Report BML 82416, Norwegian Institute of Technology, Trondheim, Norway, 1982.

126. **Nadeau, J.S., Mindess, S. and Hay, J.M.,** Slow crack growth in cement paste, Journal of the American Ceramic Society, Vol. 57, No. 2, 1974, pp. 51-54.

127. **Mehta, P.K.,** Condensed silica fume, Cement Replacement Materials, Swamy, R.N. Ed., Surrey University Press, 1986, pp. 134-170.

128. **Hillerborg, A.,** Materialbrott, Report TVBM-3004, Division of Building Materials, University of Lund, Sweden, 1977.

129. **Bache, H.H.,** Fracture mechanics in design of concrete and concrete structures, Proceedings of the International Conference on Fracture Mechanics of Concrete, Lausanne, Switzerland, 1985, pp. 577-586.

APPENDIX I

Program PAFEC - Data File for the CCS (Fine Mesh)

The data file for the analysis of the CCS (a=c=30 mm) using the fine mesh in program PAFEC is presented below.

```
TITLE ECCENTRICALLY LOADED CUBE A=C=30 MM
CONTROL
FULL.CONTROL
PHASE=1,2,4,6,7,9
PLANE.STRAIN
CONTROL.END
NODES
AXIS=1
NODE   X   Y   Z
1   0.0      0.051
2   0.02     0.051
3   0.03     0.05
4   0.05     0.05
5   0.07     0.05
6   0.1      0.051
7   0.0      0.06
8   0.02     0.06
9   0.03     0.06
10  0.05     0.06
11  0.07     0.06
12  0.1      0.06
13  0.0      0.1
14  0.02     0.1
15  0.03     0.1
16  0.05     0.1
17  0.07     0.1
18  0.1      0.1
MATERIAL
MATERIAL.NUMBER E NU
11  30.0 0.2
PLATES.AND.SHELLS
MATERIAL.NUMBER THICKNESS
11  0.1
PAFBLOCKS
ELEMENT.TYPE=36110
BLOCK.NUMBER TYPE N1 N2 N3 TOPOLOGY
1   1   1 1 0    1 2 7 8
2   1   1 2 0    7 8 13 14
3   5   1 1 1    3 2 9 8
4   1   1 2 0    8 9 14 15
5   5   2 1 1    3 4 9 10
6   1   2 2 0    9 10 15 16
7   1   2 1 0    4 5 10 11
8   1   2 2 0    10 11 16 17
9   1   3 1 0    5 6 11 12
10  1   3 2 0    11 12 17 18
MESH
REFERENCE SPACING.LIST
1  4
2  8
3  6
```

```
LOADS
NODE.NUMBER DIRECTION.OF.LOAD VALUE.OF LOAD
1852 2 -1.0
RESTRAINTS
NODE PLANE DIRECTION
3 0 2
571 0 2
572 0 2
573 0 2
574 0 2
575 0 2
576 0 2
577 0 2
578 0 2
579 0 2
580 0 2
581 0 2
582 0 2
583 0 2
584 0 2
585 0 2
586 0 2
587 0 2
588 0 2
589 0 2
590 0 2
591 0 2
592 0 2
593 0 2
4 0 2
1160 0 2
1161 0 2
1162 0 2
1163 0 2
1164 0 2
1165 0 2
1166 0 2
1167 0 2
1168 0 2
1169 0 2
1170 0 2
1171 0 2
1172 0 2
1173 0 2
1174 0 2
5 0 2
1852 0 1
CRACK.TIP
LIST.OF.NODES
3
END.OF.DATA
```

APPENDIX II

Program STRESS - Data Preparation

The data preparation procedure for program STRESS is given below. The program employs the 8-noded isoparametric element for linear elastic stress analysis. Several methods may be used to evaluate the stress intensity factor for cracked geometries as shown below.

Data set 1 (1 line)

NKTYP Parameter indicating method to be employed in the stress intensity factor evaluation. This can have values between 1 and 5 according to the following:

1 Displacement extrapolation
2 Displacement extrapolation using singularity elements
3 Strain energy release rate
4 Virtual crack extension
5 J-integral

Data set 2 (1 line)

Problem title, limited to 72 alphanumeric characters.

Data set 3 (1 line)

Control parameters

NPOIN Total number of nodal points
NELEM Total number of elements
NVFIX Total number of restrained boundaries
NTYPE Problem type parameter:
1 Plain stress
2 Plain strain
NGAUS Order of quadrature for numerical integration:
2 Two point Gauss quadrature rule
3 Three point Gauss quadrature rule
NCTEL Crack tip singular element index:
0 No singularity elements to be included in the mesh
1 Singularity elements to be included in the mesh
NKTYP Stress intensity factor index as in data set 1
OUTPUT Type of output required:
0 Reduced output
1 Complete output

Data set 4 (1 line)

MESHTYP Type of mesh, whether FANMESH or UNIMESH

If MESHTYP is FANMESH, then

Data set 5

5(a)	Element data (1 line for each element, total of NELEM lines)
NUMEL	Element number
MATNO(NUMEL)	Material Property number
LNODS(NUMEL,1)	1st nodal connection number
.....	.....
LNODS(NUMEL,8)	8th nodal connection number
5(b)	Node data, one line for each node whose co-ordinates are to be input

IPOIN Nodal point number
COORD(IPOIN,1) x co-ordinate of the node
COORD(IPOIN,2) y co-ordinate of the node

If MESHTYP is UNIMESH, then
Data set 6 (3 lines)
6(a) Element data (1 line)
NELX Number of elements in x-direction
NELY Number of elements in y-direction

6(b) Node data (2 lines)
XSPCS Listing of all element dimensions along x-axis
YSPCS Listing of all element dimensions along y-axis

Data set 7 (1 line)
Scale factors for size effects
SCALEX Scale factor in the x-direction
SCALEY Scale factor in the y-direction

Data set 8 (NVFIX lines)
Restrained node data (1 line for each restrained node)
NOFIX Restrained node number
IFPRE Restraint code:
1,0 Nodal displacement restrained in the x-direction
0,1 Nodal displacement restrained in the y-direction
1,1 Nodal displacement restrained in both directions
DISPLX Prescribed nodal displacement in x-direction
DISPLY Prescribed nodal displacement in y-direction

Data set 9 (1 line)
Material data
NUMAT Material identification number
PROPS(1) Elastic modulus, E
PROPS(2) Poisson's ratio, μ
PROPS(3) Material thickness, t (=1.0 for plane strain)

Data set 10 (1 line)
TITLE Load case title, limited to 72 alphanumeric characters

Data set 11 (1 line)
Load control data
IPLOD Applied point load parameter:
IGRAV Gravity loading parameter:
IEDGE Distributed edge loading parameter:
0 No load to be input
1 Load to be input
The geometries considered in this thesis contained applied loading only.

Data set 12
Applied load data, one line for each loaded nodal point
LODPT Node number
POINT(1) Load component in x-direction
POINT(2) Load component in y-direction

Data set 13 (1 line)
Displacements output:

0 Not to be printed
1 To be printed

Data set 14 (1 line)
Stresses output:

0 Not to be printed
1 To be printed in full
11 Averaged values to be printed

If NKTYP=1 in data set 1, then
Data set 15 (3 lines)
Stress intensity factor by the displacement extrapolation

15(a)	Control data (1 line)
NINTP	Number of nodal points used in the extrapolation
15(b)	Nodal data (1 line)
LISTP(1)	1st nodal point number employed (crack tip node)
.....	.....
LISTP(L)	Last nodal point number employed
15(c)	Stress intensity data (1 line)
THETA	The angle Θ in degrees
MATIP	Material identification number of the crack tip

If NKTYP=2 in data set 1, then
Data set 16 (3 lines)
Stress intensity factor by the displacement extrapolation using singularity elements

16(a)	Control data (1 line)
NINTP	Number of nodal points to be used in the extrapolation process (=3)
LISTP(1)	1st nodal point number employed (crack tip node)
.....	.....
LISTP(3)	Last nodal point number employed
16(b)	Stress intensity data (1 line)
THETA	The angle Θ in degrees
MATIP	Material identification number of the crack tip

If NKTYP=3 in data set 1, then
Data Set 17 (3 lines)
Stress intensity factor by the strain energy release rate

17(a)	Control data (1 line)
NTOLD	Number of crack tip nodes released for extension
17(b)	Nodal list data (1 line)
NDREL(1)	1st crack tip nodal point released
NDREL(2)	2nd crack tip nodal point released
17(c)	Stress intensity data (1 line)
CREXT	The crack extension
MATIP	Material identification number of the crack tip
NSYMM	The symmetry factor:

1 Full modelling of the crack geometry
2 Half modelling of the crack geometry

If NKTYP=4 in data set 1, then
Data Set 18 (3 lines)
Stress intensity factor by the virtual crack extension

18(a)	Control data (1 line)
NLIST	Number of nodal points in mesh to be purturbated
18(b)	Nodal list data (1 line)
LISTP(1)	1st nodal point to be purturbated
.....	.....
LISTP(L)	Last nodal point to be purturbated
18(c)	Stress intensity data (1 line)
CREXT	The distance the crack length is to be extended
MATIP	As in data set 17
NSYMM	As in data set 17

If NKTYP=5 in data set 1, then
Data Set 19
Stress intensity factor evaluation by the J-integral

19(a)	Control data (1 line)
NPATH	Number of J-integral paths to be analysed
MATIP	As in data set 17
NSYMM	As in data set 17
19(b)	Type of mesh (1 line)
MESHTYP	Type of mesh, whether FANMESH or UNIMESH

If MESHTYP=FANMESH in 19(b), then NPATH pairs of lines

19(c)	Control data (1 line)
NJIEL	Number of elements through which the contour passes
NPXSI	Gauss point index- value of 1, 2 or 3 corresponding to the integrating positions for the 2 or 3 point quadrature
19(d)	Element data (1 line)
LISTE(1)	1st element number on the J-contour path
.....	.....
LISTE(L)	Last element on the J-contour path

If MESHTYP=UNIMESH in 19(b) then, NPATH + 1 lines

19(e)	Element data (1 line)
NELX	Number of elements in x-direction
NELY	Number of elements in y-direction
19(f)	Node data (NPATH lines, one for each node)
NPXSI	As above
LISTP(1)	1st nodal point
LISTP(2)	2nd nodal point
LISTP(3)	3rd nodal point
LISTP(4)	4th nodal point

APPENDIX III

Program STRESS - Data File for the CCS (Fan Mesh)

A typical data file for the analysis of the CCS (a=c=30 mm) using program STRESS and the J-integral method of analysis is given below.

```
5
ECCENTRICALLY LOADED CUBE
163,44,5,2,2,0,5,0
FANMESH
1,1,3,31,47,46,45,30,1,2
2,1,5,32,49,48,47,31,3,4
3,1,7,33,51,50,49,32,5,6
4,1,9,34,53,52,51,33,7,8
5,1,11,35,55,54,53,34,9,10
6,1,13,36,57,56,55,35,11,12
7,1,15,37,59,58,57,36,13,14
8,1,17,38,74,64,59,37,15,16
9,1,19,39,76,75,74,38,17,18
10,1,21,40,78,77,76,39,19,20
11,1,23,41,80,79,78,40,21,22
12,1,25,42,82,81,80,41,23,24
13,1,27,43,84,83,82,42,25,26
14,1,29,44,86,85,84,43,27,28
15,1,49,50,51,60,66,65,47,48
16,1,53,61,68,67,66,60,51,52
17,1,55,62,70,69,68,61,53,54
18,1,57,63,72,71,70,62,55,56
19,1,59,64,74,73,72,63,57,58
20,1,47,65,66,87,98,97,45,46
21,1,66,67,68,88,100,99,98,87
22,1,68,69,70,89,102,101,100,88
23,1,70,71,72,90,104,103,102,89
24,1,72,73,74,91,106,105,104,90
25,1,74,75,76,77,78,92,106,91
26,1,78,79,80,93,108,107,106,92
27,1,80,81,82,94,110,109,108,93
28,1,82,83,84,95,112,111,110,94
29,1,84,85,86,96,114,113,112,95
30,1,110,111,112,116,120,119,118,115
31,1,112,113,114,117,122,121,120,116
32,1,110,115,118,124,129,128,127,123
33,1,118,119,120,125,131,130,129,124
34,1,120,121,122,126,133,132,131,125
35,1,45,97,98,135,147,146,145,134
36,1,98,99,100,136,149,148,147,135
37,1,100,101,102,137,151,150,149,136
38,1,102,103,104,138,153,152,151,137
39,1,104,105,106,139,155,154,153,138
40,1,106,107,108,140,157,156,155,139
41,1,108,109,110,123,127,141,157,140
42,1,127,128,129,142,159,158,157,141
43,1,129,130,131,143,161,160,159,142
44,1,131,132,133,144,163,162,161,143
1,0.0,0.0
3,12.0,0.0
```

```
5,20.0,0.0
7,25.0,0.0
9,30.0,0.0
11,35.0,0.0
13,40.0,0.0
15,45.0,0.0
17,54.0,0.0
19,65.0,0.0
21,70.0,0.0
23,75.0,0.0
25,80.0,0.0
27,90.0,0.0
29,100.0,0.0
45,0.0,20.0
47,12.0,11.0
49,20.0,5.0
51,25.0,5.0
53,30.0,5.0
55,35.0,5.0
57,40.0,5.0
59,45.0,5.0
66,20.0,15.0
68,29.3,15.0
70,35.8,15.0
72,44.3,15.0
74,54.0,11.0
76,65.0,5.0
78,70.0,5.0
80,75.0,5.0
82,80.0,5.0
84,90.0,10.0
86,100.0,10.0
98,14.0,28.0
100,28.0,30.0
102,37.0,30.0
104,50.0,28.0
106,60.0,22.0
108,72.0,20.0
110,82.0,20.0
112,90.0,20.0
114,100.0,20.0
118,88.0,34.0
120,94.0,34.0
122,100.0,34.0
127,80.0,40.0
129,88.0,44.0
131,94.0,44.0
133,100.0,44.0
145,0.0,50.0
147,14.0,50.0
149,28.0,50.0
151,37.0,50.0
153,50.0,50.0
155,60.0,50.0
157,72.0,50.0
159,88.0,50.0
161,94.0,50.0
163,100.0,50.0
```

```
1.0,1.0
15,0,1
16,0,1
17,0,1
18,0,1
19,0,1
1,30.0,0.2,1.0,0.0,0.0
POINT LOAD
1,0,0
161,0.0,-1.0
163,0.0,0.0
0
0
2,1,2
FANMESH
10,1
8,19,24,39,38,37,36,35,20,1
8,1
8,19,24,23,22,21,20,1
```

APPENDIX IV

Program STRESS - Data File for the CCS (Regular Mesh)

A typical data file for the analysis of the CCS (a=c=30 mm) using the J-integral method in program STRESS is presented below.

```
5
ECCENTRICALLY LOADED CUBE
198,55,11,2,2,0,5,0
UNIMESH
11,5
21.0,6.0,2.0,1.0,1.0,2.0,6.0,10.0,21.0,25.0,5.0
1.0,2.0,6.0,10.0,31.0
5,1,12,23,34,45
4
1.0,1.0
9,0,1
10,0,1
11,0,1
12,0,1
13,0,1
14,0,1
15,0,1
16,0,1
17,0,1
18,0,1
19,0,1
1,30.0,0.2,1.0,0.0,0.0
POINT LOAD
1,0,0
196,0.0,-1.0
198,0.0,0.0
0
0
2,1,2
UNIMESH
11,5
1,9,53,45,1
2,9,53,45,1
```

LIST OF PUBLICATIONS

Sabir, B.B., Summerhayes, S.D. and Asili, M., The fracture toughness of fibre reinforced concrete, Proceedings of the International Symposium On Fibre Reinforced Concrete, Madras, India, 1987, pp. 1173-1184.

Sabir, B.B., Asili, M. and Summerhayes, S.D., Fracture toughness of OPC/microsilica concrete, Proceedings of the International Conference on the Design and Construction of Non-conventional Structures, Institution of Civil Engineers, London, U.K., 1987, pp. 215-222.

Sabir, B.B. and Asili, M., A compression splitting test for fracture toughness of concrete, Proceedings of the 7th European Conference on Fracture, Budapest, Hungary, 1988.

Sabir, B.B. and Asili, M., The toughness characteristics of fibre reinforced concrete, Proceedings of the International Conference on Computational Engineering Science, Atlanta, U.S.A., 1988.

Sabir, B.B. and Asili, M., Strength and fracture properties of condensed silica fume concrete with and without polypropylene fibre reinforcement, Proceedings of the 3rd International Conference on the Use of Fly Ash, Silica Fume, Slag and Natural Pozzolans in Concrete, Trondheim, Norway, 1989, pp. 444-458.

Asili, M. and Sabir, B.B., The use of microsilica concrete, Proceedings of the 3rd International Iranian Congress of Civil Engineering, Shiraz, Iran, 1990.